Multiscale mathematical models for simulation and scale-up of green processes in the perspective of industrial sustainability

Ph.D. in Mathematical Engineering & Simulation

Matteo Neviani

Supervisor: Professor O. Paladino
Professor R. Cianci

Department of Mechanical, Energy, Management and Transportation Engineering (DIME)
University of Genoa, Polytechnic School

This dissertation is submitted for the degree of
Doctor of Philosophy

University of Genoa XXXI cycle

ABSTRACT

The present work presents research studies aimed at developing tools useful to design engineering solutions moving in the direction of industrial sustainability. The investigations hereinafter discussed regard an extraction process of active compounds – polyphenols – from agro-food industry wastes (olive and grape pomaces) and a biorefinery exploiting waste frying oil, solid organic wastes and algal biomass to produce biofuels. In particular, for the former topic, a procedure aimed at the evaluation of the technological feasibility at pilot scale of said process is discussed. The proposed approach takes into consideration the extended kinetic route coupled with mathematical simulation. Detailed physically-based dynamic mathematical models, taking into account mass and energy balance equations, are adopted to describe both the lab-scale and the pilot-scale reactors. Chemical physical parameters appearing in the models are estimated from the experimental data at lab-scale or are partially taken from literature. Different heating systems are designed for the pilot scale reactor and their performance is tested by simulation. Characteristic times are evaluated also during start-ups and different control loops are analyzed in order to set-up the best process and operating variables. Average yields in polyphenols are finally evaluated for both the batch and the continuous operated pilot reactor, by considering feed variability and fluctuations of process parameters.

For what concerns the biorefinery, special attention was devoted to the modeling of the airlift reactor, its most delicate and complex component. In fact, to optimize this interesting microalgae cultivation system, a precise description of the moving interfaces formed by the liquid and gas phase is critical. In this study, coupled front capturing methods (standard and conservative level set methods) and finite difference method are used to simulate gas bubbles dynamics in a pilot-scale external loop air-lift photobioreactor in which microalgae are used to capture CO_2 from flue gas and to treat wastewater. Numerical simulations are carried out on rectangular domains representing different sections of the vertical axis of the riser. The data employed was either acquired from previous experimental campaigns carried out in the airlift reactor or found in the literature. The rise, shape dynamics and coalescence process of the bubbles of flue gas are studied.

Moreover, for each analyzed applications, a procedure based on Buckingham π-theorem to perform a rigorous scale-up is proposed. In this way, scale-invariant dimensionless groups describing and summarizing the considered processes could be identified. For the research focused on the scale-up of photobioreactors used to cultivate *Chlorella Vulgaris*, an experimental campaign at three levels was designed and carried out to evaluate the characteristic dimensionless numbers individuated by the theoretical formulation. Since scale-up regards both geometrical dimensions and type of reactor, passing from lab-scale stirred tanks to pilot scale tubular and airlift, particular attention was devoted to define characteristic lengths inside the dimensionless numbers.

PREFACE

This thesis deals with issues related to environmental and energy engineering pursuing a mathematical modeling perspective. This latter was obtained through the extensive use of physically-based models, a macroclass of models chosen due to the fact that they typically involve physically interpretable parameters, allowing deeper insights into system performance and better predictions with respect to phenomenological models. The studies carried out did not focus on a single topic, but rather tackled different problems. In particular, two can be distinguished: the first is related to the valorisation of agro-food waste, while the second concerns the design of a closed-loop integrated pilot plant, pressing markedly on its most complicated component, i.e. the photobioreactor.

The works published and/or submitted to international scientific journals and congresses that constitute the framework on which this thesis was drafted, are explicitly referenced in the pertinent chapters and summarized in the continuation of the present preface.

In summary, the structure of the thesis is organized in such a way as to lend itself to a dual mode of reading: by applications and methodologies, meaning, in a way, by rows and columns. The reader in fact can either proceed sequentially through each chapter, which concerns the methodology/topic (introduction, modeling and scale-up), or skim through different chapters and follow the discussion about the application (mainly photobioreactors and process for the valorisation of agro-food waste).

A brief overview of the different parts of the thesis is presented below.

- **Introduction.** The purpose of this first chapter is to provide a cohesive and comprehensive framework in which the research carried out is to be inserted. The problems and their origins are then presented, subsequently speaking about the technologies and resources used to address them. To this end, inspiration was drawn from:
  - Hodaifa G., Paladino O., Malvis A., Seyedsalehi M., Neviani M. (2019). Green Techniques for Wastewaters. In G. Z. Kyzas (Ed.), Advanced low-cost separation techniques in interface science. London, UK: Elsevier.

Two technological examples are discussed more in depth, while their modeling and simulation is left for subsequent chapters. The work on these latter processes and devices were reported in the following scientific papers:

  - Neviani M., Aliakbarian B., Perego P., Paladino O. (2019). Extraction of polyphenols from olive pomace: mathematical modelling and technological feasibility in a high temperature and high pressure stirred reactor. Chem. Eng. Res. Des. 141, pp- 32-46.
  - Paladino O., Neviani M., (2018). A closed loop biowaste to biofuel integrated process fed with waste frying oil, organic waste and algal biomass: feasibility at pilot scale. Renew. Energy. 124, pp. 61–74.
  - Paladino O., Neviani M., Moranda A., (2016). Feasibility Study of a Pilot scale Integrated Biowaste to Biofuel System fed with Waste Frying Oil, Organic Waste and Algal Biomass. Proceedings of the 6th International Symposium on energy from Biomass and Waste, Venice, Italy.

- **Dynamic modeling.** Chapter 2 hinges on the development of mathematical models for the simulation of the extraction of active compounds (polyphenols) from olive and grape industry organic waste. Hence, dynamic models of discontinuous and continuous reactors are presented and discussed.

  The results are presented mainly in the article:

  - Neviani M., Aliakbarian B., Perego P., Paladino O. (2019). Extraction of polyphenols from olive pomace: mathematical modelling and technological feasibility in a high temperature and high pressure stirred reactor. Chem. Eng. Res. Des. 141, pp- 32-46.

  Also, some aspects of the process there discussed and modeled are treated in:

  - Neviani, M., Paladino, O., An approach based on the π-theorem for the scale-up of polyphenols extraction for wide-ranging waste in a stirred reactor. Intended for submission.

- **Local modeling apt to phenomenology study and control.** In Chapter 3 a key component of a closed-loop integrated process for waste valorization is investigated under a modeling perspective. The behavior of such device, an external loop airlift photobioreactor, is analyzed through numerical methods.

  The reference paper for this research is:

  - Bagnerini M., Neviani M, Paladino O., (2019). Simulation of the rising of gas bubbles in a pilot-scale external loop airlift photobioreactor. Proceedings of the SUPEHR'19 – SUstainable PolyEnergy generation and HaRvesting Conference, Savona, Italy.
  - Neviani M., Bagnerini P., Paladino O., (2018). A level set approach for computation of bubble dynamics in airlift reactors. ISCRE25, Florence, Italy.

  whilst theories and concepts taken up and organized in

  - Paladino O., Hodaifa G., Neviani M., Seyedsalehi M., Malvis A. (2019). Modelling in Environmental Interfaces. In G. Z. Kyzas (Ed.), Advanced low-cost separation techniques in interface science. London, UK: Elsevier.

  are used.

- **Theoretical scale-up.** Chapter 4 briefly introduce the theoretical foundation on which the scientific scale-up is built, successively presenting their application to the polyphenols extraction process discussed in Chapter 1 and 2, and to the algaculture system comprised in the closed-loop biorefinery examined in Chapter 1.

  To this end, extensive reference has been made to:

  - Paladino O., Neviani M. Scale-up of photo-bioreactors for microalgae cultivation by π-theorem. Under review.
  - Neviani, M., Paladino, O., An approach based on the π-theorem for the scale-up of polyphenols extraction for wide-ranging waste in a stirred reactor. Intended for submission.

- **Conclusions.** In this last chapter conclusions are drawn and horizons for new research activities are discussed.

Appendix A show experimental data relative to the lab-scale polyphenols extraction process.

In Appendix B, detailed information on the materials employed for the experimental campaigns related to the study of the scale-up of photobioreactors for the cultivation of microalgae are presented. This information is contained in the following papers:

- Paladino O., Neviani M. Scale-up of photo-bioreactors for microalgae cultivation by π-theorem. Under review.

- Paladino O., Neviani M. Set-up of operating conditions in airlift photo-bioreactors for microalgae cultivation in integrated energy production processes. Under review.
- Paladino O., Fissore F., Neviani M. A low-cost monitoring system and operating database for quality control in small food processing industry. Under review.

ACKNOWLEDGEMENTS

First of all, I would like to thank all the people that contributed, helped and influenced my work throughout my Ph.D. research studies.

To this end, I would like to start from my supervisor Professor Ombretta Paladino for her guidance, availability, patient support and kind advise. She was the first one to made me really savour the taste of research and laboratory investigation, offering me intellectual freedom in my work. I deeply appreciated your sharing your scientific knowledge with me, it was a privilege to keep on learning from you.

I also would like to acknowledge my co-supervisor Professor Roberto Cianci for his teachings and Professor Patrizia Bagnerini for her constructive suggestions and insightful comments, quintessential for completing my projects.

Besides them, my appreciations go to the whole ex-DIPTEM department section and in particular to my fellow Ph.D. colleagues for the consulting and the moments of lightness and laughter.

I cannot forget to externalize my appreciation for all my friends, old and new ones; each one of you shared moments, thoughts and a bit of your spirit with me, enriching me.

A special mention goes to Valentina, for her affectionate support throughout both joyous and tough times. Words can be empty, so I just say thank you, from the bottom of my heart.

At last but not least, my family. Their love and patience greatly supported me, pushing me to polish every aspect of myself, providing me with the tools to build my wings and leaving me free to spread them and fly as I see fit.

Matteo Neviani
XXXI cycle

TABLE OF CONTENTS

LIST OF FIGURES

LIST OF TABLES

Chapter 1: Introduction

1.1 Environmental challenges in the new millennium

Already at the dawn of the new millennium, the sociocultural landscape presented new awareness and attention to environmental issues. The connotation of “green” associated with various areas, from the economic one to energy production, had assumed a popular character, symptom of a greater impact and a broader dissemination of these topics on public opinion. These are real issues that have to be tackled, not fictitious nor exaggerated.

Although the seeds of modern globalization began to sprout as a result of the Industrial Revolution and in conjunction with nineteenth-century imperialism, often its initial phase is placed in the last decades of the 1900s.

The aftermath of World War II, primarily under American guidance with its recipe of *Rechtsstaat* (rule of law), capitalism, and orientation to the stipulation of treaties and community policies, represented the period of the definitive change of pace on this front, which roughly starts from the Bretton Woods conference in 1944.

Globalization means also, above all, interconnection of markets, investments, people, ideas. It means the development of similar economic, industrial and technological models, at least for what concerns the most advanced countries.

The post-war years had brought a state of economic expansion to many countries. The generalized economic boom was linked to the new trend of lowering barriers and to free trade, actions deemed possible thanks to international agreements such as the General Agreement on Tariffs and Trade (GATT) of 1947, as well as the establishment of governance institutions such as the World Bank and the International Monetary Fund (IMF).

Scientific and technological innovations also played a central role, on par with the development and growth of the international connective tissue of transport and telecommunications.

Productive growth did not cease, continuing until the 1970s in the wake of the process started before the outbreak of the war. Industrial automation began to be available to a more widespread audience; the lower cost of natural gas and oil (at least until the crisis of 1973) meant that these raw materials supplanted coal in many countries.

A key aspect of this phase of globalized development was the lack of attention to the impacts it had on the environment.

The first studies and timid interventions with a view to environmental management are datable at the beginning of the twentieth century. However, it is not until the 60s and 70s that the first environmental regulations were promulgated and the first specific entities were established. Among the latter stands the birth in 1970 of the American Environmental Protection Agency (EPA) under the Nixon presidency and that of the international agency called United Nations Environment Program (UNEP) in 1972. UNEP, assisted by the World Metereological Organization (WMO), formed under the aegis of the United Nations the Intergovernmental Panel on Climate Change (IPCC) in 1988, which is to date the most important group of studies in charge of a scientific and objective analysis on climate change and its social and economic repercussions.

Nowadays there is awareness of how environmental problems do not only concern anthropogenic climate change – which translates among other things (see Fig. 1.1) into global warming, alteration of the hydrological cycle (hence desertifications, areas with scarcity of water resources but also increase in frequency of extreme weather phenomena such as floods and tornado formation), global dimming, sea level rise and ocean acidification –, but are also linked to overpopulation (with consequences on biocapacity, land degradation, waste generation), to industrial production (in particular with regard to consumption energy, still mostly fueled by fossil fuels), and to pollution and depletion of environmental resources (fragmentation or destruction of habitats and ecosystems, overfishing, intensive livestock breeding and farming).

The term sustainable development has thus entered strongly in the dictionary of policy makers and stakeholders. According to the perspective originally proposed by the French economist René Passet (Passet, 1979), sustainable development rests on three pillars: environment, economy and society. Thus a mutual interdependence manifests itself, which is coupled with the interconnection of nations as a result of globalization. The result is the impossibility of dealing individually with the challenges of sustainable development.

In order for the earth system to resist shocks and alterations resulting from the advancement of human civilization, a paradigm shift is required. Rather than relying on the resilience of our planet, ideally we should recognize humankind as an integral part of the biosphere, in the perspective of a balanced and harmonious growth of our societies.

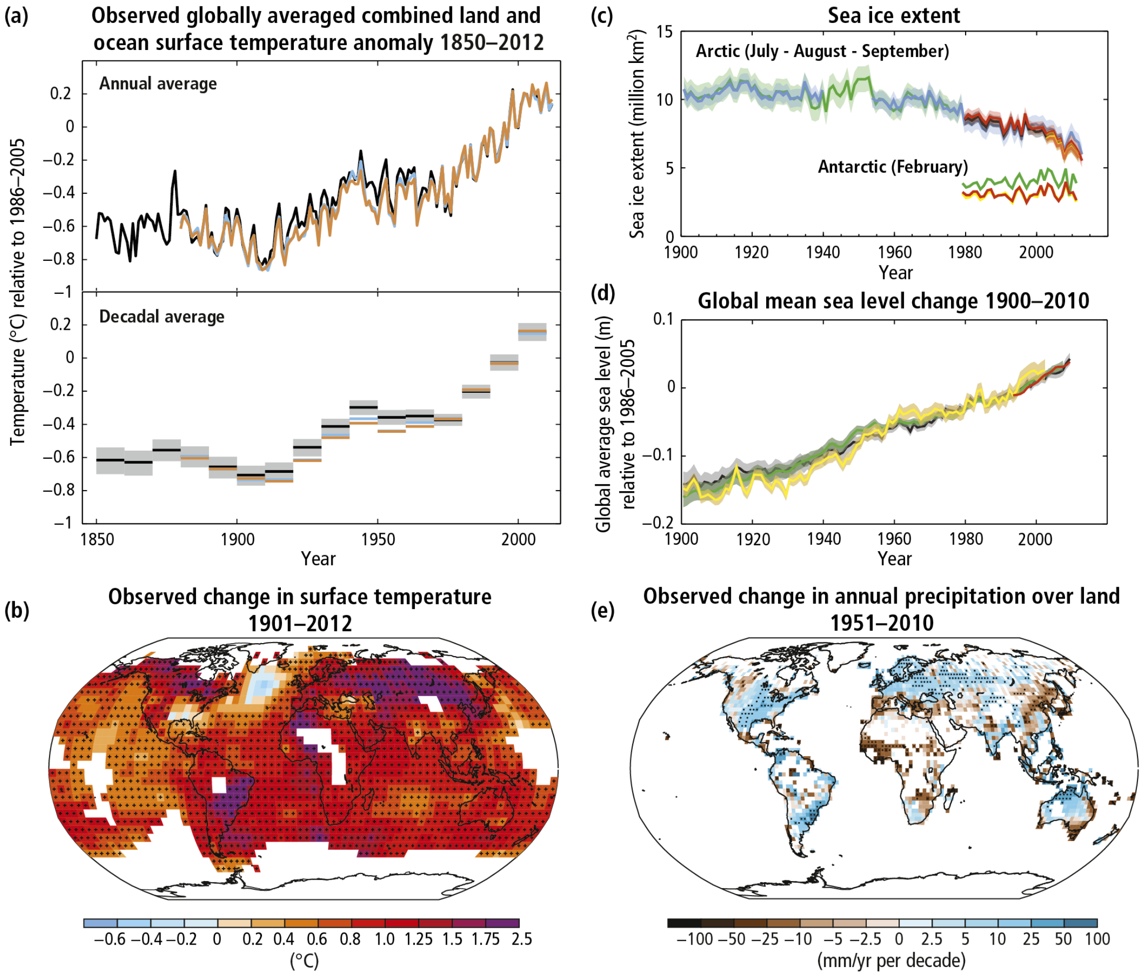

Fig. 1.1 Multiple observed indicators of a changing global climate system. (a) Observed globally averaged combined land and ocean surface temperature anomalies (relative to the mean of 1986 to 2005 period, as annual and decadal averages) with an estimate of decadal mean uncertainty included for one data set (grey shading). (b) Map of the observed surface temperature change, from 1901 to 2012, derived from temperature trends determined by linear regression from one data set (orange line in Panel a). Trends have been calculated where data availability permitted a robust estimate (i.e., only for grid boxes with greater than 70% complete records and more than 20% data availability in the first and last 10% of the time period), other areas are white. Grid boxes where the trend is significant, at the 10% level, are indicated by a + sign. (c) Arctic (July to September average) and Antarctic(February) sea ice extent. (d) Global mean sea level relative to the 1986–2005 mean of the longest running data set, and with all data sets aligned to have the same value in 1993, the first year of satellite altimetry data. All time series (coloured lines indicating different data sets) show annual values, and where assessed, uncertainties are indicated by colored shading. (e) Map of observed precipitation change, from 1951 to 2010; trends in annual accumulation calculated using the same criteria as in Panel b (IPCC, 2014).

Growth is the *mantra* repeated by every government. The role of science and technology also consists in trying to find solutions to continue to grow, allowing longer-lived lives in continuously improving conditions. This goal goes hand in hand with being compatible with the system that hosts us.

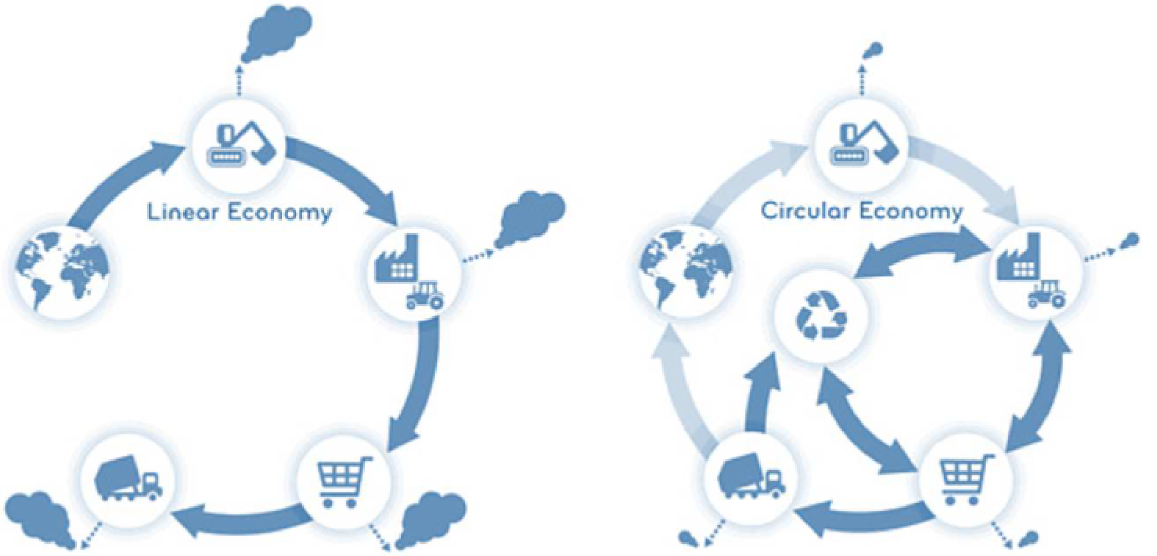

Fig. 1.2 Graphical representation of the concepts of linear and circular economy. Economic dynamics can be seen as a loop whose interactions with the planet are essential for the retrieval of natural resources and the absorption of waste and pollution. Endurance of the model is maintained until the load capacity of the planet is not exceeded. Whilst linear economy (left) neglects the environmental impacts deriving from the aforementioned interactions, taking on a segment characterization with a beginning (extraction) and an end (disposal), the circular one (right) also considers the consumption of resources and the waste flows towards the environment. Circular economy contemplates the material symbiosis between vastly different production processes and activities, emphasizing how the continuous exchanges with the various environmental matrices lead to further closed alternative cycles, proposing to optimize the use of virgin resources and reduce pollution as far as feasible (adapted from Sauvé et al., 2016).

On the other hand, the need to address issues together rather than individually also creates opportunities. Where this is probably most evident is in the waste sector. They are seen in a new light, as a potential resource. This new concept fits perfectly into that, now in the foreground as evidenced effectively by the recent policies of China (Geng et al., 2013), European Community (European Commission, 2015)) and other Asian states (Andersen, 2007), of a circular economy replacing the dominant open-ended linear model (see Fig. 1.2), also known as "take, make and dispose" development model (Ghisellini et al., 2016). In fact, circular economy is a locution that defines "an economic system that replaces the 'end-of-life' concept with reducing, alternatively reusing, recycling and recovering materials in production/distribution and consumption processes by operating at the micro level (products, companies, consumers), meso level (eco-industrial parks) and macro level (city, region, nation and beyond) with the aim to accomplish sustainable development, thus simultaneously creating environmental quality, economic prosperity and social equity, to the benefit of current and future generations" (Kirchherr et al., 2017).

As evidence of the mentioned emergence of new opportunities following a more holistic approach on environmental challenges, one can think of the topic of biofuels. With the documented recognition of anthropogenic climate change, the search for alternative and greener energy supply sources has become more intense. Among the alternatives, biofuels are back in vogue. In a first phase (first generation), they were synthesized from food crops such as corn, soybean, palm and sugar cane, giving rise to an ethical debate. In order to overcome this major limitation, i.e. the creation of a potential competition for agricultural products between the energy and food production sectors, it was decided to exploit the biomass of agricultural residues as raw material, reaching the so-called second generation biofuels.

Subjects related to recycling and biofuels will be explored more in depth in Sections 1.2 and 1.3 respectively.

Section 1.5 deals with the issue of biofuel production through biorefineries and, more generally, the importance of creating closed-loop systems that follow the precepts of the circular economy, exploiting as much as possible any flow that interests them. In this regard the discussion on conversion processes operating thanks to biomass aimed at the production not only of fuels but also of energy, heat and added-value chemicals will be introduced. The technical study of one of the crucial and also delicate components of a particular closed-loop pilot plant of this kind will then be presented in detail in Chapter 3 whilst details on aspects relative to this plant can be found in Appendix B.

1.2 Reduce, reuse and recycle

Although a univocal definition of circular economy is still absent (the one previously provided is an attempt to standardize by drawing on various different definitions), it is widely believed that it interweaves different concepts including industrial ecology, the life cycle approach and the 3R principle.

Industrial ecology draws a parallel between industrial systems and ecosystems, emphasizing the flows of matter and energy and how in networks of biological systems they tend to form feedback loops, recycling nutrients and energy in an integrated way (Hu et al., 2011).

The development of innovative systems that incorporate the vision of the circular economy also depends on the availability of tools apt to evaluate their potential and performance: in this sense, the currently most accepted methodology is the Life Cycle Assessment (LCA),with which the energy and environmental loads associated with a product are quantified, considering all the stages of his life (Lijò et al., 2018).

Finally, the last mentioned ingredient is the so-called principle of the 3Rs, which stands for Reduce, Reuse and Recycle. Originally introduced as an answer to the management of Municipal Solid Waste (MSW), it is also taking hold in other areas, such as energy and industrial productions.

Imagining what this principle implies is easy: reduction implies putting the emphasis on the parsimony with which resources are exploited, as well as their careful choice, in order to minimize the waste products generated. Reusing means finding applications for which wastes or parts of them can be used, as such, again. Finally, recycling aims to enhance waste to create added value, by seeing them as raw material. Following the procedure just described, the quantity of material to be transferred to final disposals is minimized (see Fig. 1.3).

The continuous increase of world population that according to the last projections (see Fig. 1.4), although slightly lower than previous estimates, should reach 8.6 billions in 2030 (United Nations, Department of Economic and Social Affairs, Population Division, 2017), has a clear correlation with production of waste (see Fig. 1.5).

Given the amount of material, the sense of the institution of a waste hierarchy, from which follows the ordering of the 3Rs transpires even more markedly: to implement preventive maneuvers (up-stream solutions) rather than end-of-pipe type (down-stream) ones affects both management costs (industrial symbiosis adding value to wastes and source reduction versus waste collection, disposal and remediations costs) and the environment (Mohanty, 2011). Nonetheless, relying too much on final recovery practices, such as waste-to-energy, may not be sufficient or advisable: incinerators release a wide variety of pollutants depending on the composition of the treated matrix, with possible repercussions on health and causing environment degradation (Sharma et al. al., 2013). Recycling large quantities of materials requires adequate facilities for capacity and technology, assisted by effective sorting systems. Prolonging the useful life of products, attacking planned obsolescence, digitizing and streamlining where possible, paying attention to new models such as the sharing economy while promoting the use of renewable energy sources are all actions referable to higher levels in the hierarchical pyramid of sustainable waste management.

Among the pioneers in the adoption of initiatives and policies centered on the 3Rs, following the agreement reached at the G8 Sea Island Summit in June 2004, is Japan (see in this regard the Basic Act for Establishing at the Sound Material-Cycle Society of 2000

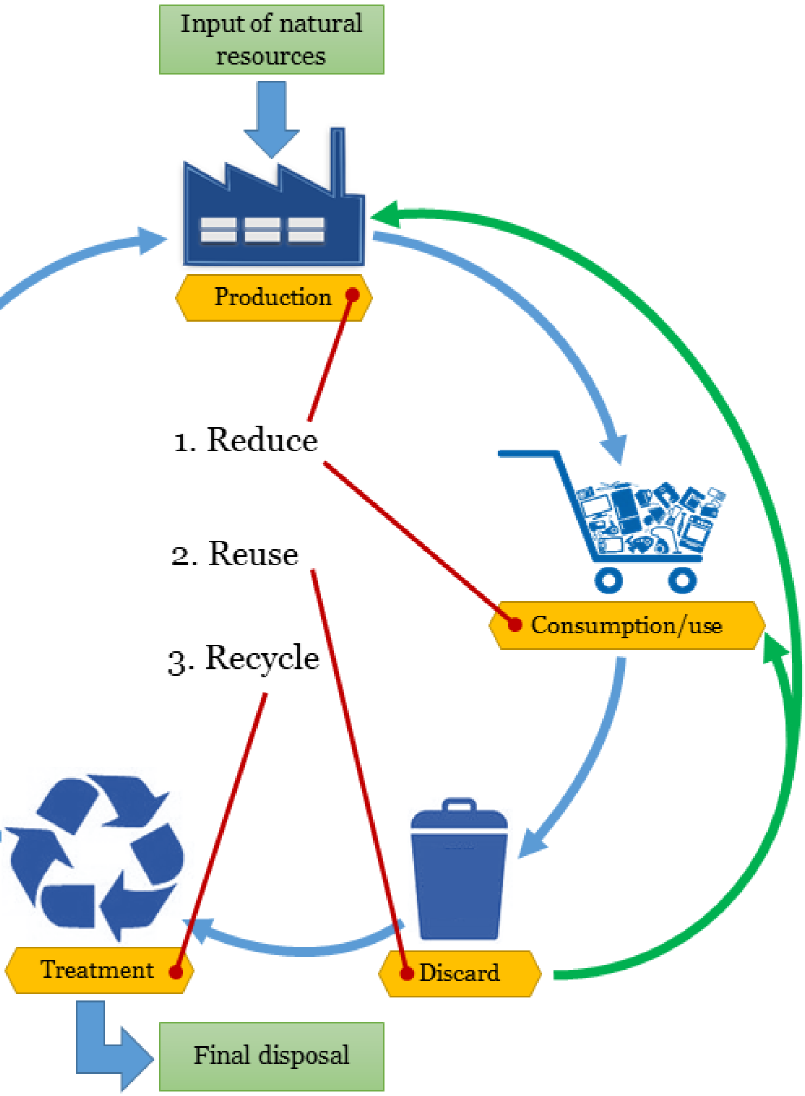

Fig. 1.3 The implementation of the 3Rs principle calls for three steps: the first is reduction, acting on both production (i.e. design, manufacturing, distribution, etc.) and consumption/use, then comes reuse, whose goal is to employ again discarded materials (or energy), and finally recycle. Recycle has an ambivalent meaning. It can refer both to the recovery of energy, where the waste to energy must be seen as the last resort, and to materials, which can not be re-used directly as raw materials.

implemented in 2003 with the Fundamental Plan (OECD, 2010), the 3R Initiative launched at Tokyo Conference in 2005 or the Kobe 3R Action Plan (Grosse, 2010)) but soon many other countries have begun to conform (Visvanathan and Kumar, 2007), at least for certain sectors (e.g. RRR Directive 2005/64/EC of the European Union on the recovery, reuse and recycling of motor vehicles). Even companies and corporations are following virtuous propositions, as witnessed for example by the announcement at the 2018 Word Economic Forum (WEF)

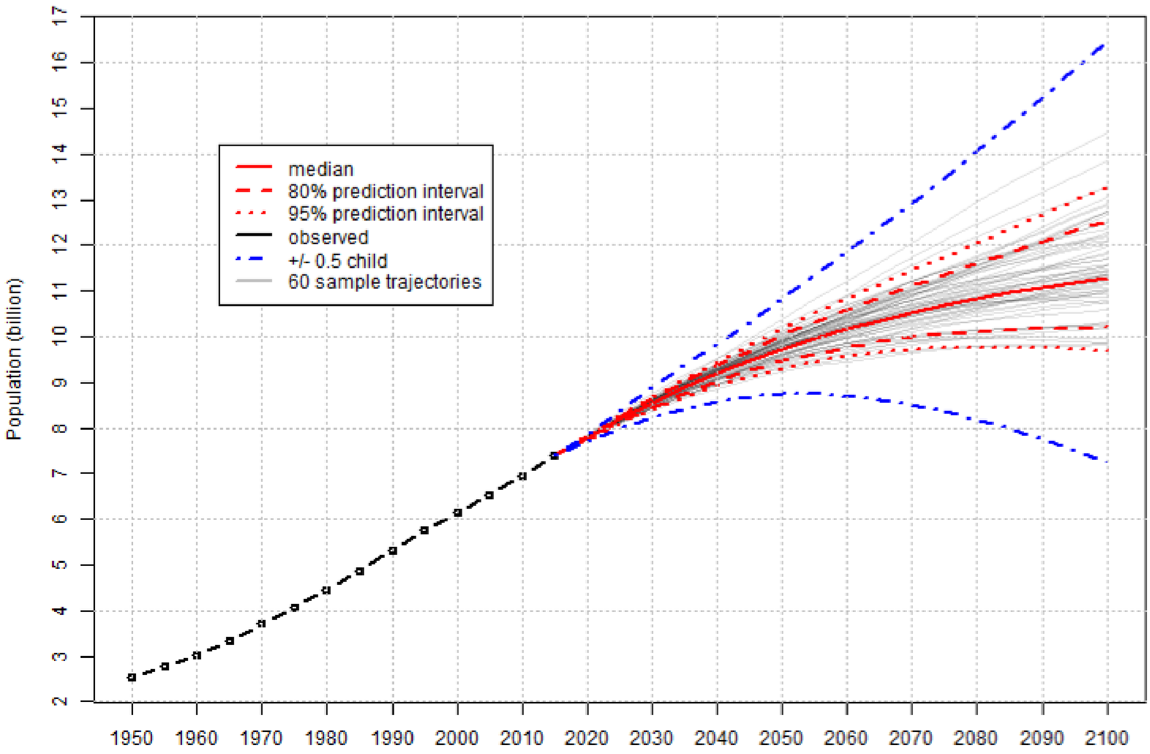

Fig. 1.4 Probabilistic projections of the world total population, built upon the probabilistic projections of total fertility and life expectancy at birth, based on estimates of the 2017 Revision of the World Population Prospects. These probabilistic projections of total fertility and life expectancy at birth were carried out with a Bayesian Hierarchical Model. The figures display the probabilistic median, and the 80 and 95 per cent prediction intervals of the probabilistic population projections, as well as the (deterministic) high and low variant (+/- 0.5 child) of the 2017 Revision of the World Population Prospects (United Nations, Department of Economic and Social Affairs, Population Division, 2017b).

that several giants such as The Coca-Cola Company, Walmart, PepsiCo and L'Oréal are committed to have all their packaging reused, recycled or composted by 2025.

Efforts to adopt a philosophy oriented to a cradle-to-cradle analysis of the various products are being spent in various fields: electrical and electronic waste, the aforementioned optimization of the life cycle of the products of the automotive industry, plastic waste management and so on.

The discipline of waste management, pursuing a pragmatic line, has established different degrees of priority based on the risk associated with each type of waste, taking into account proximity to the population and characteristics of the waste. If special attention is devoted to Municipal Solid Waste (MSW), waste management systems should therefore take into greater account the derivatives of all the life-cycle of products, intervening also on mining

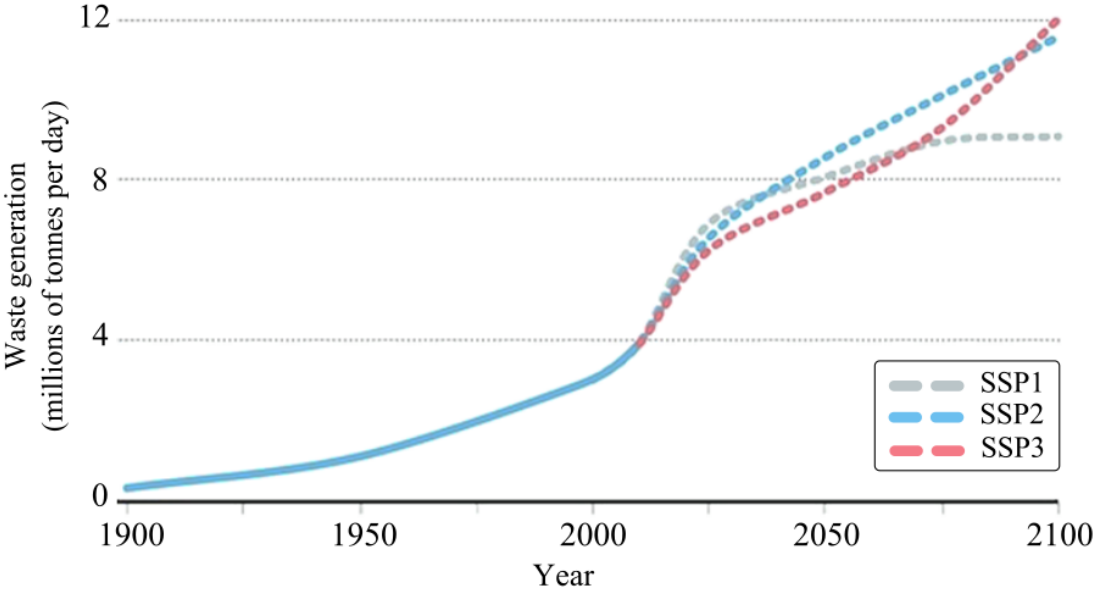

Fig. 1.5 Chart of global waste production with forecasts to 2100 that are based on three different scenarios. In the first Shared Socioeconomic Pathway scenario (SPP1) the world population stands at 7 billions, is 90% urbanized, more environmentally responsible, and boasts achievements of development targets, with reduction in the use of fossil fuels. The SSP2 projection considers a more conspicuous population, standing at 9.5 billions, inhabiting for the 80% in cities and does not consider large deviations from today's economic-industrial conditions. Finally, in SSP3, 70% of about 13.5 billions people live in an urban context of moderate wealth with pockets of extreme poverty and many rapidly growing demographic nations (adapted from (Hoornweg et al., 2013)).

and quarrying (extraction) wastes, byproducts of construction and demolition activities, agriculture and forestry wastes.

To this end, it is noted that, according to the Food and Agriculture Organization, 1.3 billion tons per year, roughly equivalent to one third of the food produced, turns into food waste. Being an organic material containing a wide range of compounds, this matrix is a useful resource for the production of value-added chemicals (Chen et al., 2017). In the following subsection, an idea that moves precisely in this sense is presented.

1.2.1 An example of waste valorisation: polyphenols extraction from agricultural waste

When talking about sustainability and focusing on the social aspects, health evidently holds a primary importance. It is common knowledge that diet plays a crucial role in this aspect. For example, Mediterranean diet is widely appreciated throughout the world also because of the low incidence of atherosclerotic diseases associated with it. Its high content of active ingredients, such as oleic acids and phenolic compounds, in particular those coming from olives and grapes, determines a significant antioxidant, anti-inflammatory, antimicrobial, cardioprotective and chemoprotective properties (Nassiri-Asl et al., 2016; Carluccio et al., 2003). In addition to the conspicuous ingestion of plant-based food, the moderate consumption of white and fish meat and the low intake of red meat, red wine and olive oil are in fact notable constituents this dietary pattern (Martínez-Huelamo et al., 2017).

The wine-making and oil mill industries are paramount standard bearers for the agro-industrial activity, and therefore for the economies, of the Mediterranean regions. To olive oil 30 million tons per year of waste by-products streams are due, the main exponent of which is olive pomace (Chandra and Sathiavelu, 2009), which has a heterogeneous solid nature. After milling, only 2% of the phenolic compounds in the olives are transferred to the oil. Hence, the olive pomace shows high concentrations of polyphenols (Di Nunzio et al., 2017).

Similar remarks can be made for the wine industry: as a result of practices such as pruning and exfoliation, vinification and distillation, the equivalent of almost 25% of the inputted grape is processed into grape pomace (Makris, 2018).

Recovery of phenolic compounds from this cheap and widely available biomass and their further application in food, cosmetic, and pharmaceuticals has been recognized as a valorization strategy for olive oil industries. Several processes have been examined for the extraction of polyphenols from olive pomace via conventional solid–liquid extraction or nonconventional techniques (Paini et al., 2016) and, among all, High-Pressure/High-Temperature Extraction (HPHTE) showed to be highly effective (Casazza et al., 2012).

The study of various operational parameters for the aforementioned type of extraction, already carried out for the olive pomace in a laboratory scale mixed reactor (Aliakbarian et al., 2011), has been extended to the case of extraction from grape pomace as well. Following these promising results and considering the industrial interest in the exploitation of pomaces, the feasibility study of up-scaling of the extraction technique using a mini-pilot reactor was conducted.

To do so, the extraction kinetic parameters were firstly estimated by the experimental extraction data, and a complete simulation model of the lab-scale reactor was tuned (heat transport and mixing parameters) in order to evaluate characteristic times at lab-scale.

A pilot scale mixed reactor was designed, and subsequently simulated with different possible heating systems and in different operating conditions, both in batch and in continuous. The dynamic behavior of the reactor was also studied by changing parameters values and simple control strategies were tested on the pilot-scale dynamic model. More details on this modeling and its results are given in Chapter 2.

As matrices from which to obtain the phenolic compounds, Taggiasca cultivar olive pomace supplied by a producer located in Liguria and Croatina cultivar grape pomace, provided by a Piedmontese winery have been employed. The grape pomace, collected after vinification and dried for 24 hours at 40 °C, subjected to grinding for 20 seconds in order to avoid heat generation and degradation of the polyphenols, was stored in a sealed container at $-20\,^{\circ}\mathrm{C}$. The olive pomace, deriving from three-phase oil extraction from a decanter, was instead stored at 20 °C before analysis.

At laboratory scale, the extraction process was carried out in a High-Pressure High-Temperature (HPHT) model 4560 (Parr Instruments Company, Moline, IL, USA) stirred discontinuous tank reactor. Its AISI 316 stainless steel cylindrical vessel, moveable and of tunable volume ($0.1\,\mathrm{L} \div 0.6\,\mathrm{L}$), is equipped with appropriate valves for the introduction and removal of gases inside the reaction chamber. As safety feature for pressure relief, a rupture disc is present. A pressure gauge and an internal thermocouple allows for temperature and pressure monitoring, while heating is achieved through a heating mantle. Temperature, along the entire duration of the extraction process, was maintained constant.

Every experimental test was carried out under nitrogen atmosphere so as to avoid the effect of an extractive atmosphere, meaning phenolic oxidation and gas phase extraction. Internal pressure was directly proportional to the required temperature to keep the solvent in liquid phase, so it was related to the chosen extraction solvent. Pressure of about 33 bar was measured at 180 °C by using methanol as a solvent, while a maximum pressure of 17 bar was measured at the same temperature using H_2O:ethanol (50:50).

Another feature of the compact reactor is that the inner liquid solution, mixed by a magnetic stirrer, can be recovered thanks to a liquid outlet valve.

Instead, at pilot scale, we availed ourselves of a 16 L stirred AISI 316 stainless steel reactor which can be operated either as a Discontinuous Stirred Tank Reactor (DSTR) or Continuous Stirred Tank Reactor (CSTR). Said reactor is geared with resistor wires, wrapped around and welded to the reactor lateral walls, that generate heat via Joule's effect. These wires are electrically insulated from external tubular sheaths in which they are inserted through the use of mineral insulation (magnesium oxide); this latter is also an excellent thermal conductor, aiding heat transmission to the outer tubular sheath. The system encompasses temperature self-regulation capability through a designated control system. While the resistor wires heating device is not suited for industrial scale reactors, it better approximates the heating system with which the lab-scale reactor is equipped, an important feature when considering testing scale-up results.

In order to gauge the Total Polyphenol (TP) concentration, a UV–Vis spectrophotometer (Model Lambda 25, Perkin Elmer, Wellesley, MA) at a wavelength of 725 nm and the colorimetric Folin–Ciocalteau assay (Swain & Hillis, 1959) were deployed. The calibration of the total polyphenol concentration, expressed as microgram of equivalent caffeic acid per grams of dried pomace, was carried out (coefficient of determination $R^2 = 0.999$) by means of standard methanolic solutions of caffeic acid ($10 \div 1000$ $\mu g_{CAE} mL^{-1}$). A summary of the experimental results is shown in Table A.1 and Table A.2 in Appendix A.

1.3 Biofuels

Another angle from which it makes sense to try to essay environmental challenges, especially for what concerns the development of reliable and sustainable energy sources, is the tangible implementation of biofuels in real economy.

The world energy demand is expected to continue to increase, with a growth rate estimated (Bosch et al., 2018) by the World Energy Council (WEC) and the International Energy Agency (IEA) of between 17 and 56% for the period $2015 \div 2050$ (from 563 EJ to between 663 and 879 EJ). Although fossil hydrocarbons and its derivatives are still predominant (and will probably be in the near future), the outlook sees a significant boost towards renewables, as shown by the IRENA data that estimate the transition of total installed power from renewable sources from 1058 GW in 2008 to 2179 GW in 2017 (IRENA, 2018).

In order to limit carbon dioxide (CO_2) emissions, the main contributor to the quantity of GreenHouse Gases (GHGs) released, we need to focus not only on power generation but also on the transport sector. In fact, since 1990, the emissions linked to it have increased by more than 50%, earning the primacy for fastest growing CO_2 source and weighing for 25% of the total emissions of carbon dioxide from combustion of fuels (Varone and Ferrari, 2015).

The major investments in the transition to renewables are focusing mainly on wind and solar. These technologies are intrinsically linked to a scarcely predictable and variable energy output due to the stochastic and intermittent nature of such energy sources. Therefore, they require the development of efficient electrical storage systems and a further increasing interpenetration of the various production systems in order to better balance the load on the supply grid. With regard to this point, digitalization is emerging as an important actor because the convergence in the use of artificial intelligence, cloud and Blockchain for energy systems seems to offer good promises in the key of smart grids, potentially expanding renewable energy from a niche resource to one with a wider pool of participation (prosumers) in the supply mix (WEC, 2018). From this it would seem to follow an electrification also of mobility and certainly many automotive brands are moving in this direction. Nevertheless, biofuels are seen by many as the key alternative for curbing the carbon footprint of the transport sector, at least in a medium-short horizon. Moreover, the main upside of biofuels is the possibility of exploiting the preexisting distribution and transport infrastructures, all without requiring alterations to the locomotion system, which remains the internal combustion engine nor prolongations of the refueling time (Brutschin and Fleig, 2018).

Taking as a reference the results of the mobility model presented by the IEA for its 2 °C scenario (in which a path for the energy system and a trajectory for the CO_2 emissions that would ensure at least a 50% probability of limiting the average global temperature increase of at 2 °C by 2100 is layed out), the biofuels' share of overall fuel consumption for transportation will amount to 30.7%, followed by 27% of electric vehicles. A similar future would require, considering the projections of the demand, a 10-fold increase in the production of biofuels (Oh et al., 2018).

Europe is at the forefront on this matter and, with the January 2018 amendments to its directive known as the post-2020 EU Renewable Energy Directive (RED II), imposes constraints with a dual purpose: phase out first generation biofuels that feast on edible biomass while promoting, with a binding mandate, the most advanced ones (second and third generation, possibly fourth). The limits for 2030 are thus set at 7% for first generation biofuels and 10% for those of subsequent generations (Doumax-Tagliavini and Sarasa, 2018). In this context, it should also be kept in mind that currently 90% of biofuels belong to the first generation.

Currently, the two most widely used biofuels are biodiesel and bioethanol: to offer some supporting data, of 126 billion liters of liquid biofuels produced in 2014, 78 were bioethanol and 32 biodiesel, with the United States and Brazil as the largest contributors (WBA, 2017). The former is mainly used as an additive in gasoline mixtures in different percentages: E15 (15% ethanol, remaining gasoline) and E85 (85% ethanol, 15% petrol) *in primis*. The conversion technology employed to synthesize it is function of the feedstock. However, bioethanol, nowadays produced primarily as a first-generation biofuel from corn (in China, USA and European Union) and sugarcane (in tropical countries), is obtained in most cases through a production process articulated in three fundamental phases: the first one consists in obtaining the solution containing fermentable sugars, followed by the conversion sugars into ethanol (CH_3CH_2OH) by fermentation and finally by the separation and purification of CH_3CH_2OH, generally by distillation, rectification and dehydration (Lin and Tanaka, 2006). Further details on bioethanol production can be found for example in (Vohra et al., 2014).

Biodiesel, on the other hand, is a fuel derived not necessarily from vegetal matrices: aside for vegetable oils, it can also be synthesized from animal fats. The key component of both these resources, which can not be used directly as fuels primarily due to damage that their high viscosity could cause to the engine, are triglycerides, or fatty acid esters. It follows that the most frequently followed route (Chakraborty et al., 2016) is that of Trans-Esterification

Table 1.1 Pros and cons of all the four generations of biofuels (Dutta et al., 2014).

Generation	**Advantages**	**Disadvantages**
1^{st}	GHG savings; Simple and low cost conversion technology.	Low yield; Cause food crisis as a large portion arable land required for growing crops.
2^{nd}	GHG savings; Utilize food wastes as feedstock; No food crop competition; Use of non-arable land for growing few energy crop.	Costly pretreatment of lignocellulosic feedstock highly advanced technology need to be developed for cost effective conversion of biomass to fuel.
3^{rd}	Easy to cultivate algae; Higher growth rate; Versatility: can use wastewater, seawater; No food crop competition.	More energy consumption for cultivation of algae (for mixing, filtration, centrifugation, etc.); Low lipid content or biomass contamination problem in open pond system; High cost of photo-bioreactor.
4^{th}	High production rate; High yield with high lipid containing algae; More CO_2 capture ability.	Initial investment is high; Research is at its primary stage.

(TE), assisted or not by heterogeneous, homogeneous or enzymatic catalysis, with which such drawbacks are obviated. Generally, this procedure give rise to a mixture of Fatty Acid Methyl Ester (FAME), whose quality must comply with appropriate standards (mainly the American standard, ASTM D-6751, or the European one, EN 14214). A less widespread alternative involves the use of pyrolysis (Sharma and Singh, 2009). For a review of the technologies for the production of biodiesel the work of (Abbaszaadeh et al., 2012) is suggested.

If it is true that first generation biofuels are predominant, more advanced alternatives are emerging. Numerous studies are focused on the exploitation of waste cooking oils, non-edible lignocellulosic biomass, microalgae, non-edible seed oils, and even manure (Gomaa and Abed, 2017). Nonetheless, research has yet to advance as even third and fourth generations present pros and cons. The main ones are listed in Table 1.1, while a more detailed discussion is reported in the following subsections.

1.3.1 The first generation

As mentioned earlier, biofuels that are produced from food crops, for animals or humans, are classified as belonging to the first-generation.

The renewable adjective is given to biofuels because the feedstocks necessary for their manufacture can be replenished way quicker than those of fossil fuels. Moreover, their use is said to reduce the emissions of GHGs not because their combustion does not release them but rather for an improvement by subtraction: feedstocks from which they are synthesized are an integral and active part of the carbon cycle. Plants, through photosynthesis, remove and sequester carbon dioxide from the atmosphere, which is released again during their combustion. On the contrary, using fossil fuels means introducing CO_2 from outside the carbon cycle, since it comes from reserves buried in Earth's crust for million of years. On closer inspection, however, the carbon footprint balance may not be so positive if a cradle-to-cradle approach is adopted. One of the main criticisms of first generation biofuels is that, when carbon dioxide output flows relative to the farming, transport and fertilizer production processes (which often rely on fossil fuels) are taken into consideration, the concept of carbon neutrality can become even significantly distant (Fargione et al., 2008).

The main downside of first generation biofuel implementation remains the one related to land use. Ceding plots of land to plants for fuel production raises obvious ethical questions. The repercussions in this sense are not only direct: fluctuations in demand, and therefore in prices, can push farmers towards the removal of portions of grasslands and forests to widen their agricultural fields and increase production, undermining biodiversity and the lunging capacity provided by plants. Some data, referred to 2014, is reported in Table 1.2 and Figure 1.6.

Table 1.2 Land use and shares of crops used for biofuel production (WBA, 2017).

Biofuel	Crop	Production (Mt)	Biofuels (Mt)	% of biofuels use
Bioethanol	wheat	720	2.62	0.4
	maize	1014	53.20	5.2
	other grains	299	4.16	1.4
	sugarbeet	257	1.11	0.4
	sugarcane	1812	25.3	1.4
Biodiesel	palm oil	61	23.2	37.9
	vegetable oils	114	14.1	12.4

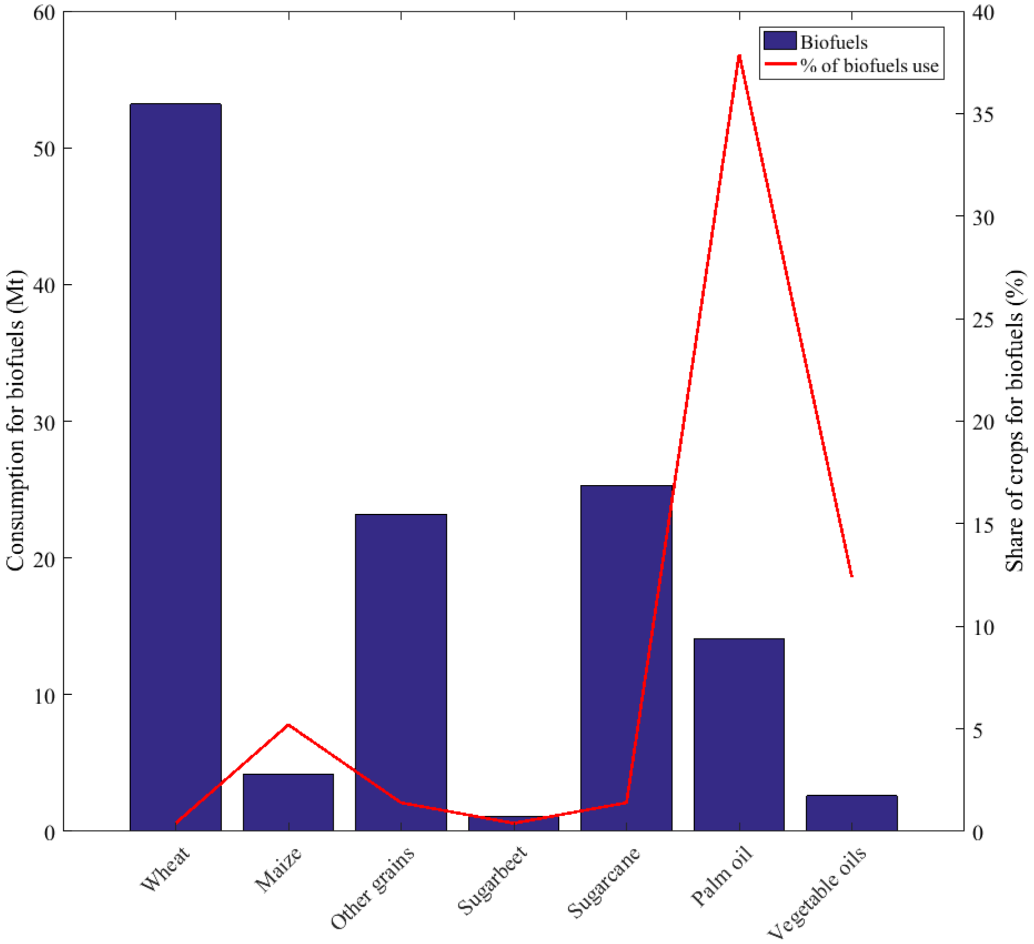

Fig. 1.6 Consumption of biofuels and shares of biofuels in major crops production (WBA, 2017).

First-generation bioethanol currently holds the record for production, with more than 85% of it deriving from wheat, maize and sugarcane (Table 1.2). Studies that have investigated the effectiveness of this latter feedstock for various maturity levels has shown that the best yields occur in the interval 300 ÷ 325 days after planting (Rolz and de León, 2011).

Biodiesel, which regardless of generation, is obtained primarily by trans-esterification through the use of methanol (CH_3OH) or, less commonly due to its higher price, ethanol (C_2H_5OH) to form Fatty Acid Methyl Esters (FAMEs) and Fatty Acid Ethyl Esters (FAEEs) respectively, has vegetable oils as its widest source. Considerable conversion yields have been reported, for example of 77% for its generation from cottonseed oil with 0.5% sodium hydroxide (NaOH) and 20% methanol (Nabi et al., 2009).

Another alternative, although much less adopted, is biogas, which can be obtained starting from anaerobic digestion of manure and other organic biomass (Naik et al., 2010).

1.3.2 The second generation

It is recognized that second generation biofuels offer numerous advantages not only with respect to fossil fuels but also to first generation biofuels. These include a better energy balance, a marked reduction in greenhouse gas emissions, overcoming the problem of competitiveness with food of the seasonality of production, with obvious positive influences on plant productivity (IEA Bioenergy, 2008).

Second-generation biofuels have evolved independently of previous generation biofuels. They instead represent products from new industrial dynamics, which have become part of the so-called bioeconomy, in which biomass-based products have been increasingly available as food, feed, energy and biomaterials. Second-generation biofuels can be a lower carbon option than first-generation biofuels in terms of their effects. According to the International Energy Agency (IEA), second-generation biofuels are produced from cellulose, hemicellulose or lignin. Such biofuels can be blended with petroleum-based fuels or used in adapted vehicles (Eisentraut, 2010). Cellulosic ethanol and Fischer-Tropsch fuels are an example of second generation biofuels. Second-generation biofuels yield greater energy output than fossil fuels, include a much larger array of feedstock options (Carriquiry et al, 2011), minimize competition on land and have much less environmental impacts.

Second generation biofuels are produced from non-edible ligno-cellulosic materials, entailing by-products such as forest residues (e.g. sawdust (Stoffel et al., 2017), bark (Frankó et al., 2015), hardwood chips (Perego et al., 1990)) and cereal straw (e.g. rice husk (Saha et al., 2005) and wheat straw (Hongzhang and Liying, 2007)), wastes, intended both as organic fraction of MSWs (food waste and paper sludge containing cellulose (Prasetyo et al., 2011) for example) and industrial wastes (e.g. spent grains from distilleries (Kricka et al., 2015)), and purpose grown energy crops (e.g. miscanthus (Lee and Kuan, 2015) and fast-growing poplar (Koukoulas, 2016)). The latter can be produced in marginal lands (Robak and Balcerek, 2018) but such a choice can affect yield, since it is obvious that a worse soil quality, in the absence of adequate supplies of water and nutrients, determines a yield declination over time. Regarding this aspect it is important to underline how, compared to first generation biofuels, lignocellulosic crops reach higher yields per unit area ($\mathrm{J\,ha^{-1}}$). The main constituents of lignocellulosic biomass are (Bajpai, 2016) cellulose ($40 \div 55\%$) and hemicellulose ($25 \div 40\%$), polysaccharides that embody an important pool of potential sugars. The hydrolysis of these two polymers compounds produces fermentable sugars, giving rise to one of the main methods for producing advanced biofuels. Following such a path allows the exploitation of the whole plant to obtain mixtures of fermentable sugars to be used as raw material in the production of advanced biofuels, whereas for first generation biofuels only a small fraction (cereals and seeds) of the biomass available is used. Direct fermentation is not practically feasible as grasses, wood and uneatable parts of the plants are tougher to break down and therefore require pre-treatments, categorized into four main groups: chemical, physical, physic-chemical and biological (Kumar et al. 2009).

Together (Luque et al., 2016) with the combination of hydrolysis and fermentation (biochemical route), the other main way to obtain second-generation biofuels is to follow the thermochemical route, i.e. high temperature heating of the biomass either in the absence (pyrolysis/torrefaction) or presence (gasification) of O_2, air and/or steam. Direct liquefaction and supercritical fluid extraction complete the picture of the exponents of this class (Demirbas, 2001).

Hydrolysis, be it acidic or enzymatic, preceded by pretreatment and followed by fermentation is the most common process for the production of bioethanol, in turn distinguishable in Simultaneous Saccharification and Fermentation (SSF), Separated Hydrolysis and Fermentation (SHF) or Simultaneous Saccharification and Co-Fermentation (SSCF) (Mohd Azhar et al., 2017). The constituents of cell walls of the plants, i.e. cellulose and hemicellulose, are separated from lignin and simple sugars are obtained from their hydrolysis; the subsequent stages of fermentation, distillation and refining follow those of the conventional bioethanol production process.

Following the thermochemical path allows for shorter conversion times and usually involves the generation of liquid fuels, hence the name Biomass-to-Liquid (BtL) synthesis, passing through an intermediate step of biomass to synthesis gas transformation. Important features of BtL biofuels are the low emissions of NO_x and CO_2, the adaptable quality of the products (cetane and octane number) and the complete elimination of emissions of particulate matter (Swain et al., 2011). Among the BtL processes, currently those that employ gasification or pyrolysis and the Fischer-Tropsch process are in the foreground (Ibarra-Gonzalez and Rong, 2018). The Fischer-Tropsch synthesis (FTS) consists of the production of single chain aliphatic hydrocarbons starting from a synthesis gas (syngas) derived from gasification, rich in carbon monoxide (CO) and hydrogen (H_2), with a reduction of the former by the H_2 in temperature conditions between $170 \div 220\,^{\circ}\mathrm{C}$ and pressure of $1 \div 10$ atmospheres. In this way, for example, FTS biodiesel is obtained. In addition to the aliphatic hydrocarbons, branched hydrocarbons, unsaturated hydrocarbons and primary alcohols, in lower quantities, are present in it as well (Bartocci and Cavalaglio, 2008). Biomethanol and bio-dimethyl ether (DME) are other biofuels obtainable from syngas. The former is produced by hydrogenating the carbon oxides present in the synthesis gas, derived from gasification or pyrolysis, in fixed bed reactors with pelletized catalyst (Cu/Zn/Al). The reactions are exothermic and determine a net decrease in the molar volume (Bartocci and Cavalaglio, 2008). On the other hand, DME (CH_3OCH_3) can be obtained either by the dehydration of methanol (and therefore also biomethanol) or by its direct generation starting from the syngas (Swain et al., 2011).

The lignocellulosic biomass can also be used for the purpose of biohydrogen synthesis. Again, different strategies can be adopted: single-step direct production is reported as the most cost effective and commercially viable. It is based on the action of thermophilic bacteria such as *Clostridium thermocellum* which produce hydrogen following the production of cellulolytic enzymes for effective hydrolysis (Cheng et al., 2011).

Other sources of primary importance in the discussion of second generation biofuels are vegetable oils, whether they come from inedible seeds, such as *Jatropha curcas*, or from animal and vegetable waste oils, Waste Cooking Oils (WCO) in particular (Bhatia et al., 2017). Typically, they assume the role of lipid sources for transesterification for the purpose of obtaining biodiesel and are available at low prices.

Finally, residues generated in the food industry and during the production of first generation biofuels can be employed as substrates for the synthesis of second generation ones. The case of glycerol, the main by-product of the biodiesel and bioethanol industries, is interesting in this sense (Yazdani and Gonzalez, 2007). Glycerol ($C_3H_8O_3$) can be fermented using microorganisms and used for bioethanol production. The fermentation is, for example, carried out by converting pyruvate or phosphoenolpyruvate (PEP), leading to a higher yield of bioethanol and content of reducing equivalents compared to the fermentation of xylose and glucose from the biomass (Robak and Balcerek, 2018). The advantages of a similar use of glycerol are the simplification of the process and the consequent cost reduction.

1.3.3 The third generation

Biofuels synthesized from lipids deriving from oleaginous microorganisms, such as bacteria, yeasts and fungi and algae form the third generation (Leong et al., 2018). Oftentimes, however, the latter is juxtaposed exclusively to the fuels produced by algal biomass, referring in particular to microalgae. In fact, the interest shown in the last few years is strongly referred to this organic matrix for a number of reasons: algae show better performances in terms of growth rate and photosynthesis compared to terrestrial plants, not suffering from the problems of the direct and indirect land use. They are able to metabolize water rich in nitrogen, phosphorus and heavy metal compounds, also supporting the use of brackish or saline water flows, decreasing the demand for freshwater, as well as the feeding of CO_2-rich gas (Correa et al., 2017). This is particularly useful because it allows to stem one of the main defects of algae fuels: the high water demand, which is also a function of the type of system used for the cultivation. In general, two types can be identified: open systems, oftentimes identified with open ponds, and photobioreactors (Vo et al., 2019). The former kind represents the most economical system for algae growth, as well as the cheaper one for both production and operation (an analysis of algae growth techniques is reported in Section 1.4). Leaving aside for now the strengths and weaknesses of these devices, it should be noted that between 11 and 13 millions liters per hectare per year are required (Chinnasamy et al., 2010): hence, it is clear how important it is to be able to reduce these freshwater volumes.

Linked to the choice of the growing system is also the discourse of the contingent areal space, which has been seen to be critical also with respect to the previous generations. Open ponds take less advantage of the space available to them, being less efficient than different solutions such as photobioreactors. Still, some studies (Chisti, 2007) express confidence in how microalgae represent the only source for the production of biofuels, biodiesel in particular, capable of satisfying the global demand for transport fuels. This is due to the fact that several species show excellent qualities of lipid accumulation, reaching up to 80% in dry mass. Nevertheless, it must be considered that the lipid productivity remains low even in such cases (Bellou et al., 2014). Chemical energy is stored in the form of oils when algae have to withstand adverse environmental conditions such as food deprivation or photo-oxidative stress; it can be used in the presence of short chain alcohols for transesterification to obtain biodiesel or catalytic deoxygenation/hydrogenation of fatty acids into linear hydrocarbons (Riazi and Chiaramonti, 2017). Overall, oil is produced by microalgae more efficiently than crop plantsOverall, oil is produced by microalgae more efficiently than crop plants, with yield per unit area way better than even the best oilseed crops (Rodolfi et al. 2009). Productions of bioethanol, biohydrogen and long-chain hydrocarbons from microalgae are possible as well, and are actually subject of investigations. Moreover, another pursuable route consists in converting algal biomass to biogas by the means of anaerobic fermentation (Wijffels and Barbosa, 2010). By the means of fermentation, one can recover the residual algal biomass resulting from oil extraction to obtain methane or ethanol, or alternatively exploit it as fertilizer or feed (Rodolfi et al. 2009). Other than water demand, the other main obstacle that prevents the declaration of the third generation as the biofuel of the future is the need of large amounts of nutrients, N and P in particular. This entails a two-fold problem: fertilizer production may end up releasing more GHGs emissions than those avoided by employing algae based biofuels, hindering the commercial viability as well due to costs higher than fuels derived from different sources, other than the high energy demand required for CO_2 transfer, water pumping, mixing and harvesting/dewatering. For example, with regard to open raceway ponds, in order to achieve a robust industrial scale production, downstream processing is reported to account for about 60% of the overall biodiesel production cost (Kim et al. 2013). Again, the need of integrating different processes in closed-loop cycles manifests itself.

Other shortcomings are related to the challenge of assuring the presence of appropriate conditions for the growth of the selected species, which should be identified between strains with lipid productivity as high as possible, and the lack of data regarding large-scale microalgae cultures (Rodolfi et al. 2009).

1.3.4 The fourth generation

In order to contain the costs related to algae-based biofuels, it is possible to intervene according to two philosophies: by evolving the technology behind the engineering of production processes, ideally optimizing both operating conditions and cost of the devices, or by improving biological efficiency, increasing the growth rate and lipid content inasmuch as possible (Davis et al., 2011). Pursuing this latter would lead to fourth generation biofuels. With this notion biofuels developed through the use of novel synthetic biology tools are identified. The predominant group is made up of biofuels synthesized from algae altered by the means of metabolic engineering and genome editing methods. Genome editing refers to an engineering technique capable of modifying the genomic DNA in a site-specific manner. To this class belongs genome editing systems based on Zinc-Finger Nuclease (ZFN), Transcription Activator-Like Effector Nucleases (TALEN) as well as the system acclaimed as revolutionary, the Clustered Regularly Interspaced Palindromic Sequences (CRISPR)/CRISPR-associated protein 9 (Cas9) (Maeda et al., 2018).

Employing tailor-suited biomass can markedly diminish processing costs associated with the harvest when compared with traditional approach. On the whole, notable production yields of genetically-modified algae with high lipid content, potentially better adaptivity and increased carbon capture capabilities are the main advantages of the fourth generation of biofuels. In contrast, the initial investment is very high, and research is still at its infant stage. To delve deeper into this interesting topic, see the review article by Aro (Aro, 2016).

1.4 Microalgae: a multipurpose environmental tool

Generally, the term algae refers to an artificial, non-cohesive and polyphyletic assembly of photosynthetic organisms, capable of tolerating a wide range of physiochemical conditions (temperature, pH values, light intensity, nutrient availability and salinity). This collection of life forms, which has no formal taxonomic standing, to thrive needs to be subjected to suitable biotic factors as well, including relations between algae and other organisms (e.g. competition within species for light, space, nutrients or other limiting sources), and biological interactions like symbiosis, parasitism and epiphytism (Barsanti et al., 2008).

Albeit no consensus is gained by a single systematic classification, three main classes (green algae – *Chlorophyta*, brown algae – *Phaeophyta* and red algae – *Rhodophyta*) can be identified, and further distinguishing can be carried out by the means of size, hence differentiating between microalgae and macroalgae. The latter, also referred to as seaweed, are macroscopic and multicellular whilst the former are unicellular and microscopic (Khan et al., 2018).

Microalgae share a number of the aspects of their physiology with seaweeds but to mass-produce these two kinds of algae, considerably dissimilar considerations are required (Williams and Laurens, 2010).

Microalgae, photoautotrophic organisms, can be subdivided in prokaryotic and eukaryotic. Prokaryotes are characterized by a cellular structure similar to that of bacteria, more primitive and simple; Eukaryotic microalgae present well defined, lipid membrane-bound organelles, such as nucleus, mitochondria and chloroplasts. Cyanobacteria, formerly known as blue-green algae, belong to the first group (Raja et al., 2014).

As seen, microalgae can be employed for various purposes: wastewater treatment, CO_2 biofixation and biofuels production. Although these represent the main reasons for their use and are consequently treated in more detail in the following subsections, other applications are identifiable (see Fig. 1.7). An in-depth analysis in this sense can be found for example in the review by Khan et al. (Khan et al., 2018) and relative bibliography.

In order to avoid repetitions, instead of resuming the discussion on microalgae biofuels, in Section 1.4.1.2 the main systems for the growth of microalgae mentioned above will be analyzed in more detail. Sections 1.4.2 and 1.4.3 regard wastewater treatment and carbon sequestration by means of microalgae use respectively.

1.4.1 Microalgae culture systems

In Section 1.3.3 it has been anticipated that systems employed for algaculture can be categorized into two classes: open and closed systems, which can be distinguished according to whether the dispersed solution of algae is in direct contact with the atmosphere or not, aspect that markedly impact the achievable level of algae cultivation control. The former systems are the simpler, more economic option (low energy demand, construction and maintenance costs), consisting of outdoor facilities covering even large areas and represent the most widely followed route for industrial scale microalgae growth (Costa and de Morais, 2014).

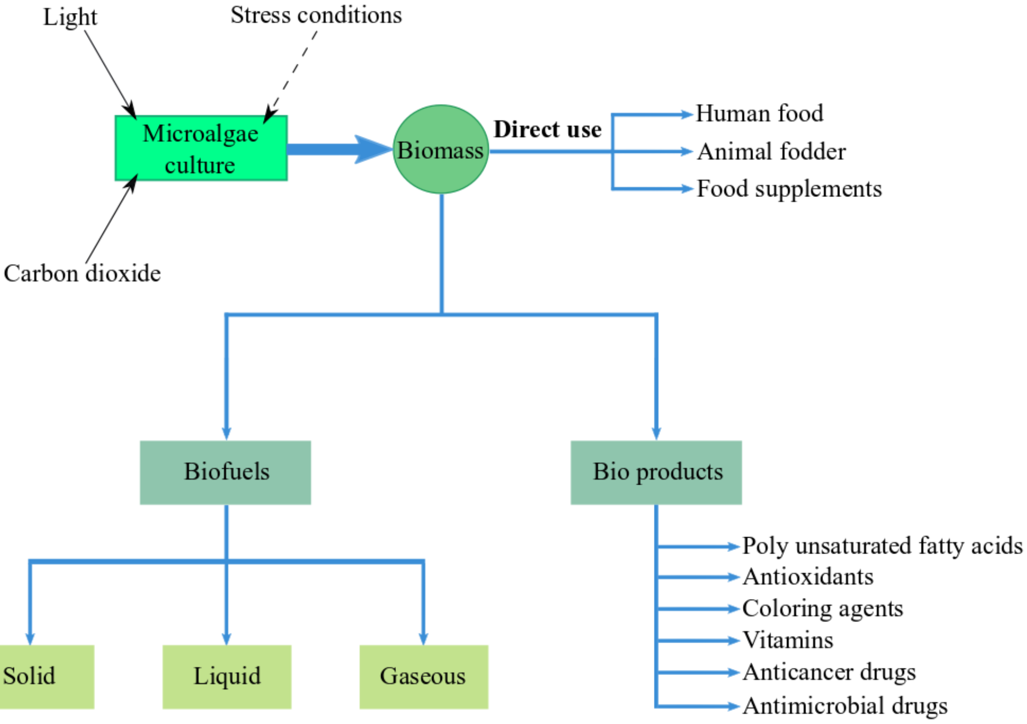

Fig. 1.7 Possible uses of biomass obtained from microalgae cultures. Adapted from Khan et al., 2018).

Nonetheless, weather conditions may pose a problem as the system is sensitive to them as culture conditions are not controllable (hence other issues are given by contamination by predators and other fast growing heterotrophs), and CO_2 diffusion to the atmosphere and suboptimal light utilization are some notable open ponds limitations (Ugwu et al., 2008).

Closed systems are transparent closed containers (tubes or vessels), subjected to either natural or artificial light irradiation, which are commonly grouped under the name photobioreactors. More technically complex, PhotoBioReactors (PBRs) are more versatile than open ponds, yield higher and more reliable biomass productivity, net of an higher initial investment and the need of a deeper knowledge on both production conditions and algae cultivation. The quality that makes them definitely stand out is given by their aptitude to be used as for synergic CO_2 removal and wastewater treatment applications (Razzak et al., 2013).

A synoptic view of the main microalgae cultivation systems is presented through Table 1.3.

Table 1.3 Main systems for microalgae cultivation: pros and cons. Adapted from (Hodaifa et al., 2019).

Culture system	Advantages	Disadvantages
Open systems	Low cost; low energy input; easy to clean.	Low biomass productivity; risk of contamination; large areal space is required; difficult control of operating conditions; limited to certain species; evaporation losses and CO_2 diffusion limitation.
Flat Plate PBRs	Low cost; high biomass productivity; high illumination area; easy to clean and sterilize; suitable for use indoor and outdoor use.	Difficult control of temperature; difficult to scale-up; hydrodynamic stress; biomass adhesion to the walls.
Tubular PBRs	Economic; high biomass productivity; easy to operate; high illumination area; suitable for use indoor and outdoor use.	Large areal space is required; generation of pH gradients; biomass adhesion to the walls.
Vertical columns	High mass transfer; low energy inputs; good mixing with low shear stress; easy to clean and sterilize.	Low illumination surface; algal cell sedimentation.
ALRs	High biomass productivity; efficient light utilization; simplicity; good mixing without high energy demand; relatively constant environment; many tunable process parameters.	Difficult to scale-up.

1.4.1.1 Open systems

To open systems belong both natural waters, i.e. lakes, lagoons and ponds, and artificial ponds and channels, like raceway and circular ponds or inclined systems.

There is a strong prevalence in the adoption of raceway systems and in general a preference for artificial systems rather than natural ones. The reasons are easy to guess: although natural open ponds represent the simplest and most economical alternative, the production is mono-specific, since the simultaneous protection from the impact due to the proliferation of bacteria, viruses and protozoa is not feasible for several different cultures, and the yields in terms of biomass produced are low, mainly due to the absence of mixing and the dissolution of CO_2 in the water. In fact, they consist of non-stirred ponds with mean depths lower inferior to 0.5 m, without mixing devices and subject to only minimal control of the environment (Razzak et al., 2013). Prime examples of natural ponds are given by the most extensive natural pond devoted to the commercial production of microalgae (*Dunaliella salina*), located in Australia, and the one used for the cultivation of *Spirulina* in El Caracol, Mexico (Richmond, 2008).

Circular ponds are circular reactors, quite similar to wastewater treatment ponds, which include the presence of feeding and carbon dioxide inlets, a harvesting outlet and a rotating arm pivoted to the center of the reactor acting as a stirrer moving in the axial direction (Chew et al., 2018). In order to achieve an efficient agitation, the diameter of these kind of ponds are prescribed to be inferior to 50 m whilst their depth usually ranges between 0.25 and 0.3 m (Razzak et al., 2013). Albeit circular ponds are not recommended for commercial-scale plants due to the high costs of operation and construction, they are adopted in Asia for the commercial production of *Chlorella* (Chew et al., 2018; Faried et al., 2017).

Rather, the choice usually made for commercial production falls on the raceways ponds (among the nurtured species one can cite *Chlorella sp.*, *Spirulina platensis*, *Dunaliella salina* and *Hematococcus sp.*). These are systems in which the dispersed phase, i.e. microalgae, is circulated around a cement racetrack with the aid of paddlewheels, devices apt to provide agitation to keep the microalgae in suspension and that also originate the turbulent mixing that facilitates the reception of solar radiation and the exchange of CO_2 with the atmosphere (Chew et al., 2018; Singh and Sharma, 2012). In order to maintain adequate light availability, as sunlight can only penetrate the pond water to a limited depth, the channel or group of channels (depending on the used system topology) are kept shallow, with depth usually comprised between 0.15 and 0.25 m (Razzak et al., 2013). In spite of being a simple growing technique, some bottlenecks are represented by the lower biomass productivity in comparison with closed PBRs and the large area required (Faried et al., 2017).

Inclined systems are a different type of open system that exploit the effect of gravity on a sloping surface to create turbulence and determine the continuous culture suspension flow from the top to the bottom of the tilted surface. Such technology offers both higher surface/volume ratio and cell concentrations in comparison with other systems but higher energy costs for the continuous pumping of the culture and cells sedimentation are significant drawbacks for their application (Richmond, 2008).

1.4.1.2 Photobioreactors

Photobioreactors constitute a cultivation system that allows to overcome some of the previously discussed problems associated with open systems (e.g. by minimizing water evaporation and reducing the exchange of contaminants such as dust or microorganisms between the culture and the atmosphere), with unparalleled performances in terms of control and regulation of all cultivation parameters as well as of yield, providing also the possibility of growing multiple species simultaneously. PBRs might be situated both indoors and outdoors, with the predilection usually being for the latter location as to exploit the free sunlight (Richmond, 2008; Molina Grima et al., 2003).

Closed systems can be classified according to their structure, for which case it is possible to distinguish between tubular, vertical column and flat plate PBRs (Faried et al., 2017).

Tubular PBRs are constituted by a series of plastic or glass transparent tubes of small diameter (≤ 0.1 m) that can be arranged in different orientations (vertical, horizontal, or near-horizontal) and inside which the medium is circulated while exposed to light. To maximize it, these cultivation vessels are design as to be present a large surface to volume ratio. At the bottom of the reactor oftentimes a sparger is attached to perform mixing, which is also aided by a circulation (mechanical or airlift) pump; the turbulent environment prevents the settling of algal biomass. Usually, the pump is used also to circulate back the medium to a reservoir. The operation of the reactor is continuous with a gas exchange vessel providing the inlet for nutrients, air and carbon dioxide and the oxygen removal point (Faried et al., 2017; Razzak et al., 2013).

Vertical column PBRs are cylinder-shaped columns made of polyethylene or glass, with a radius up to 0.2 m and height that can reach 4 m. The small radius is justified by the goal of increase the surface-to-volume ratio, whilst the height restriction is motivated by the strength of the transparent materials of which the columns are made and by the gas transfer limitations (Wang et al., 2012). In fact, with regard to this last aspect, it should be specified that the length of the columns is directly proportional to the residence time, and therefore to the oxygen generated by photosynthesis. It follows that, with tubes that are excessively long, O_2 could therefore accumulate up to the point of causing inhibitory effects. Moreover, too high column reactors could present CO_2 gradients, with consequent zones of starvation for microalgae as well as the establishment of pH gradients (Xu et al., 2009). Vertical column PBRs are probably the most popular closed system configuration, as they offer high mass transfer, good mixing with low shear stress, absence of wall growth and high efficiency of CO_2 (Moreno-Garcia, 2017; Ugwu et al., 2008). Within this group of PBRs, depending on their mode of aeration, two subcategories can be found: bubble columns and airlift reactors.

Bubble columns are multiphase reactors consisting of a column with an air injector at the bottom and a freeboard at the top apt to perform gas-liquid separation. The principle of operation on which they function is to use the bubbling of the gas mixture to achieve satisfactory mass transfer and mixing properties (Moreno-Garcia, 2017).

In a certain sense, AirLift Reactors (ALRs) represent the evolution of bubble columns, as they show superior performances in terms of microalgae cultivation in particular due to a homogeneous shear distribution throughout the ALR, translating in a relatively constant environment, with minimization of sharp changes in the mechanical forces acting on suspended particles (Merchuk et al., 2010; Xu et al., 2009). Additionally, ALRs exhibit the possibility of obtaining very fast photoperiods as well as good mixing without high energy demand. As a matter of fact, the interest in this type of PBR for microalgal culture is especially spiked by high yields net of energy consumption for medium/low mixing. The operating principle is based on the exploitation of the density difference to trigger a convective motion of natural circulation. The name of these reactors is due to the fact that the compressed gas bubbles generated by the gas insufflation, rise from the bottom, creating a tumultuous motion; by virtue of the pressure of the gas, which is greater on the bottom of the reactor, there is a difference in density (minor at the bottom of the reactor) which causes the liquid to rise (liquid air-lifting) and its mixing with the upper one. Accordingly, two main zones can be pinpointed in ALRs: the riser zone, where air is injected to move the liquid to the top zone, and the downcomer one, where liquid falls after been degassed at the top of the column. Based on structural morphology, ALRs can be further distinguished in internal and external loop reactors. The former kind is constituted by a transparent column with a smaller internal column equipped with an air injector at the bottom whilst external-loop ALRs present as a variant an external circulation column, with downcomer and riser connected by two horizontal collectors.

Finally, Flat Plate Reactors (FPRs) consist of a series of transparent narrow panels designed to achieve a high area-to-volume ratio for the efficient use of light (Carvalho et al., 2006). High photosynthetic productivities, resulting in high microalgae biomass concentrations are achieved thanks to the short light path and high illumination surface area (Ugwu et al., 2008). Among the main advantages of FPRs, simplicity, low cost and the suitability of FPR with suspended and immobilized cells are reported. On the other hand, this system shows some limitations such as the possibility of biomass adhesion to the walls of the panels as well as hydrodynamic stress caused by the aeration (Chew et al., 2018).

1.4.2 Wastewater treatment

The commercial use of microalgal cultures for wastewater treatment dates back approximately 75 years, most often as a tertiary process, meaning to remove phosphates and nitrates from the water supply, as well as other nutrients, organic ions, suspended solids, microorganisms and remaining pollutants, in order to attain a wastewater complying with the disposal regulations (Abdel-Raouf et al., 2012; Salgot and Folch, 2018). The amount of phosphates and nitrates in discharged water needs to be controlled as it can cause eutrophication and loss of aquatic life. However, microalgae can thrive even in extreme conditions, efficiently converting in biomass not only N and P but even heavy metals, as their cells present the ability to accumulate chromium (Cr), manganese (Mn), iron (Fe), cobalt (Co), nickel (Ni), copper (Cu), zinc (Zn), silver (Ag), cadmium (Cd), cesium (Cs), gold (Au) and mercury (Hg) (Moreno-Garcia, 2017). Among the most tolerant genera of microalgae *Chlorella*, *Scenedesmus* and *Chlamydomonas* are found and, because of that, they are widely employed for the treatment of different types of wastewaters (Wang et al., 2016). Several other beneficial characteristics ascribable to wastewater treatment with microalgae can be pinpointed and support the elevation of this type of treatment to a sustainable and attractive option: disinfecting effect, photosynthetic O_2 production as well as the capability to diminish chemical and biochemical O_2 demand (Abdel-Raouf et al., 2012). Moreover, as the small size of microalgae allows the formation of large surface areas, directly proportional to mass transfer rate, the nutrient uptake capacity is amplified (Mohd Udaiyappan et al., 2017). However, the main reason for the interest of these types of systems is given by the low cost, mainly due to the fact that the level of employed technology is lower when compared to the conventional chemical-based treatment methods, together with the production of high value added biomass (Pittman et al., 2011). As an example of the economic attractiveness of this kind of solutions, one can consider for example the case of the synthetic wastewater treatment with *Chlorella vulgaris*, discussed and analysed by Feng et al. (Feng et al., 2011). The cost analysis regarded a ratio of 1 t of algal biomass for 1443 m^3 of wastewater and showed that, for an estimated credit of 0.4 $\mathrm{US\$\,m^{-3}}$, a reduction of the price of 1 t of biomass from US$ 808.79 to US$ 231.59 could be achieved.

1.4.3 CO_2 sequestration

The approach that uses microalgae as a means of mitigating greenhouse gases is relatively recent. Following the principles underlying the 3R strategy, it is preferable to intervene in the sense of reducing the concentration of CO_2 in the atmosphere by reducing and/or controlling the emissions at source, developing alternatives to the fossil fuels and sequestering the existing carbon dioxide for long-term storage.

The different approaches for the CO_2 sequestration are organized in a structure that distinguishes two macro-groups: non-biological processes, in turn divided into chemical (chemical scrubber, carbonization) and physical (geological sequestration, ocean storage, bio-char burial) ones, and biological processes, cataloged in phytosequestration, terrestrial sequestration via soil carbon and oceanic fertilization (Kassim and Meng, 2017; Verma and Srivastava, 2018). Resorting to microalgal photosynthesis for biosequestration purposes is a rather novel and attractive solution, which is raising interest among researchers. A critical factor that justifies such application is that dried biomass from microalgae approximately contains 50% of carbon, linked to CO_2 capture capacity of 1.83 kg for each kilogram of algal biomass produced (Chisti, 2007). The key to understand this ability is given by the fact that many microalgae species, similarly to other photoautotrophs, developed Carbon Concentrating Mechanisms (CCMs). CCM is an environmental adaptation which enhance the accumulation of CO_2 at the site of RuBisCO (Ribulose Bisphosphate Carboxylase-Oxygenase) activity, an enzyme participating to the first step of the Calvin–Benson cycle that catalyzes the carboxylation of ribulose-1,5-bisphosphate, resulting in the diminution of the photorespiration and upsurge of photosynthetic rate (Zhao and Su, 2014). CCMs thus increases the rate of net carbon assimilation per unit rubisco and enable microalgae to grow under various CO_2 concentrations, even, theoretically, improving their growth rate by increasing the supply of carbon dioxide (Kassim and Meng, 2017). Clearly, not all the species of microalgae respond equivalently to the percentage of carbon dioxide present, and this, in conjunction with the adaptability to various other environmental factors previously treated (T, pH, illumination, mixing, aeration, nutrients availability, ...), determines the need to select strains of microalgae suitable for their use in the processes.

The most pressing challenge in this field seems to be given by the microalgae culture medium, as better efficacy in bio-fixing was recorded using photobioreactors, which also in this sector are better systems for the growth of these micro-organisms. Clearly, the associated shortcomings remain, that is the high economic investments associated with this technology so that it is competitive and the non-negligible demand for energy necessary for the bioreactors to function (Verma and Srivastava, 2018). This latter limitation is highlighted even in LCA studies and could reach a point such that it eliminates the positive effect of biosequestration. Once again, the research seems to point towards an integration of the different processes, so as to make concomitant the mitigation of CO_2 emissions, the generation of biofuels and the wastewater treatment (Lam et al., 2012).

1.5 Biorefineries

Biomass, which is the organic substances non-identifiable as fossil fuels and their derivatives, is the fourth energy source in terms of consumption in the world, behind petroleum, coal and natural gas, responsible for 14% of global primary energy use (Cao et al., 2017).

Like crude oil, it is characterized by a complex composition, differentiating itself from the latter due to different C:H:O:N ratios. At the base of the petrochemical industry is the intent of obtaining, from different hydrocarbon compounds, chemically pure products that are easy to handle and are well-defined. To do this, we resort to refineries articulated according to tree structures, through which basic chemicals, intermediate and advanced products are obtained (Kamm et al., 2008). Akin to the traditional concept of petroleum refinery is that of biorefinery, which detaches itself from the former, as well as for the raw materials used, also for the necessary technologies (albeit some of them are in common to both approaches) (Chew et al., 2017).

Dating back to the nineties, the term biorefinery has been defined in a variegated way. One of the first, of 1997, states: “green biorefineries represent fully integrated systems of sustainable, environmentally and resource-friendly technologies for the holistic material and energetic utilization as well as exploitation of biological raw materials in form of green and residue biomass from a targeted sustainable regional land utilization” (Kamm et al., 2008). The fulcrum of the concept, which over time has embraced different and variegated evolutions, is that they are systems that exploit biomass, whether it is a single or multiple feedstock, to produce energy, biofuels, chemicals and/or products with high added value, through environmentally friendly processes, usually aiming at minimizing the outgoing flows from the closed system (Naik et al., 2010; OECD, 2018; Pino et al., 2018).

Since 2009 in Europe there has been a clear push toward a transformation and rationalization of the refining system with various refineries being closed or being reduced in terms of refining capacity. In Italy, Eni’s Venice refinery was shut down in 2011 and converted into a green refinery that started its production in May 2014. Similar fate was shared by the Gela plant, with green fuel synthesis starting in 2017.

OECD suggested that economic viability of biorefineries raise with complexity, which in turn can obfuscate the delineation of economic and technological risks (OECD, 2018). The possibility of having more by-products opens the door to the maximization of the revenues obtainable from biomass feedstock, improving the economic performance of processes that would be less sustainable in many respects if they remained stand-alone.

In one of the latest issues of The Italian National Agency for New Technologies, Energy and Sustainable Economic Development (ENEA) periodical, it is stated that, even though significant breakthrough have been achieved in the sector of sustainable, bio-based production cascading approaches, there are still barriers to be broken and efforts in the R&D need to be lavished. One passage asserts that "development and demonstration of qualified innovative processes, technologies and components for the generation of both electric and thermal power in small-sized plants and the production of second-generation biofuels and sustainable biobased products, are the main challenges that needs to be addressed" (Braccio et al., 2017). In this perspective, the closed loop process presented and discussed for the first time in the publication (Paladino and Neviani, 2018) fits. Its schematic representation is shown in Fig. 1.8.

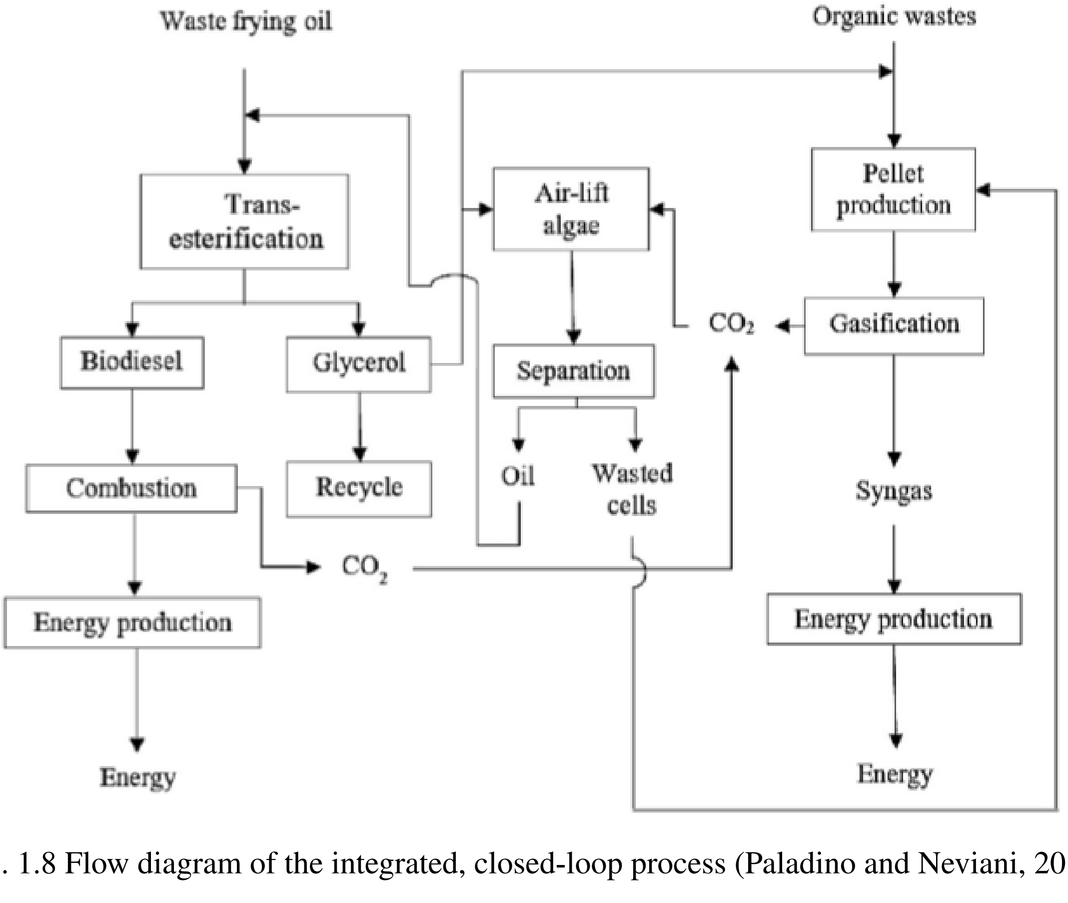

Fig. 1.8 Flow diagram of the integrated, closed-loop process (Paladino and Neviani, 2018).

Referring to the figure, one can see that the trans-esterification process is carried out in two steps: a first trans-esterification is realized in a stainless steel semi-batch reactor, followed by the separation carried out in a decanter; then the process involves a second trans-esterification, again in a stainless steel semi-batch reactor, with subsequent biodiesel washing realized in a second decanter.

Glycerol exiting from the first separation unit is sent to the gasification section where it is added to the solid-waste pellets in order to increase the Lower Calorific Value (LCV) and improve syngas quality. Glycerol exiting from the second separation unit and wastewater from bubble washing are sent to the airlift photo-bioreactors. Syngas exiting from gasifier and biodiesel obtained through trans-esterification are used in a combustion engine in order to produce energy.

In the original experimental campaign, biodiesel was mainly produced by waste frying oil whist syngas was mostly synthesized by wood pellets, wood chips and organic waste added with crude glycerol. The external loop airlift photobioreactors for microalgae production were self designed and constructed, and their best configuration were investigated in order to conduct the airlift battery as a part of the integrated biorefinery.

Each one of the three sub-processes were subjected to a thorough experimental analysis, both at laboratory and pilot scales.

Summing up, the process in question has been realized so that the following steps were carried out:

1. Trans-Esterification (TE) of waste frying oil (and olive oil, vegetable oil, seed oil for comparison) provided by the University Campus canteen, in batch reactors at lab scale and in semi-batch reactors at pilot scale. On-line measurements and self-developed control strategies were implemented and tested at pilot scale;

2. gasification of organic wastes/wood pellets collected in the campus park and organic wastes provided by the Campus canteen, also added with glycerol in a discontinuous fixed bed gasification/combustion unit (where syngas was directly burnt) at lab scale and in a downdraft automatized gasifier at pilot scale. On-line additional measurements were implemented at pilot scale;

3. microalgae growth in different operating conditions of temperature, pH, feed (glycerol percentage, flue gas composition), dark/light cycle in batch reactors at lab scale and in a set of airlift semi-continuous reactors at pilot scale. On-line measurements and self-developed control strategies were implemented and tested at pilot scale.

References

Abbaszaadeh, A., Ghobadian, B., Omidkhah, M.R., Najafi, G., 2012. Current biodiesel production technologies: A comparative review. Energy Convers. Manag., 10th International Conference on Sustainable Energy Technologies (SET 2011) 63, 138–148.

Abdel-Raouf, N., Al-Homaidan, A.A., Ibraheem, I.B.M., 2012. Microalgae and wastewater treatment. Saudi J. Biol. Sci. 19, 257–275.

Aliakbarian, B., Casazza, A.A., Perego, P., 2011. Valorization of olive oil solid waste using high pressure–high temperature reactor. Food Chem. 128, 704–710.

Andersen, M.S., 2007. An introductory note on the environmental economics of the circular economy. Sustain. Sci. 2, 133–140.

Aro, E.-M., 2016. From first generation biofuels to advanced solar biofuels. Ambio 45, 24–31.

Bajpai, P., 2016. Pretreatment of Lignocellulosic Biomass for Biofuel Production, SpringerBriefs in Molecular Science. Springer Singapore.

Barsanti, L., Coltelli, P., Evangelista, V., Frassanito, A.M., Passarelli, V., Vesentini, N., Gualtieri, P., 2008. Oddities and curiosities in the algal world, in: Evangelista, V., Barsanti, L., Frassanito, A.M., Passarelli, V., Gualtieri, P. (Eds.), Algal Toxins: Nature, Occurrence, Effect and Detection, NATO Science for Peace and Security Series A: Chemistry and Biology. Springer Netherlands, pp. 353–391.

Bartocci, P., Cavalaglio, G., 2008. Biocarburanti di seconda generazione. Ambiente Territ. Cult. Dellambiente E Sci. Territ. 2, 16–23.

Bellou, S., Baeshen, M.N., Elazzazy, A.M., Aggeli, D., Sayegh, F., Aggelis, G., 2014. Microalgal lipids biochemistry and biotechnological perspectives. Biotechnol. Adv. 32, 1476–1493.

Bhatia, S.K., Kim, S.-H., Yoon, J.-J., Yang, Y.-H., 2017. Current status and strategies for second generation biofuel production using microbial systems. Energy Convers. Manag. 148, 1142–1156.

Bosch, J., Staffell, I., Hawkes, A.D., 2018. Temporally explicit and spatially resolved global offshore wind energy potentials. Energy 163, 766–781.

Braccio, G., Cornacchia, G., De Bari, I., Pignatelli, V., 2017. Bioenergy, biorefineries and green chemistry: ENEA projects to advance a more sustainable economy. Energ. Ambiente E Innov. 2, 74–79.

Brutschin, E., Fleig, A., 2018. Geopolitically induced investments in biofuels. Energy Econ. 74, 721–732.

Cao, L., Zhang, C., Chen, H., Tsang, D.C.W., Luo, G., Zhang, S., Chen, J., 2017. Hydrothermal liquefaction of agricultural and forestry wastes: state-of-the-art review and future prospects. Bioresour. Technol. 245, 1184–1193.

Carluccio, M.A., Siculella, L., Ancora, M.A., Massaro, M., Scoditti, E., Storelli, C., Visioli, F., Distante, A., De Caterina, R., 2003. Olive oil and red wine antioxidant polyphenols inhibit endothelial activation: antiatherogenic properties of Mediterranean diet phytochemicals. Arterioscler. Thromb. Vasc. Biol. 23, 622–629.

Carriquiry, M.A., Du, X., Timilsina, G.R., 2011. Second generation biofuels: Economics and policies. Energy Policy, Special Section: Renewable energy policy and development 39, 4222–4234.

Carvalho, A.P., Meireles, L.A., Malcata, F.X., 2006. Microalgal Reactors: A Review of Enclosed System Designs and Performances. Biotechnol. Prog. 22, 1490–1506.

Casazza, A.A., Aliakbarian, B., Sannita, E., Perego, P., 2012. High-pressure high-temperature extraction of phenolic compounds from grape skins. Int. J. Food Sci. Technol. 47, 399–405.

Chakraborty, R., Chatterjee, S., Mukhopadhyay, P., Barman, S., 2016. Progresses in Waste Biomass Derived Catalyst for Production of Biodiesel and Bioethanol: A Review. Procedia Environ. Sci., Waste Management for Resource Utilisation 35, 546–554.

Chandra, M., Sathiavelu, S., 2009. Waste management in the olive oil industry in the Mediterranean region by composting. Clean Technol. Environ. Policy 11, 293–298.

Chen, S.S., Yu, I.K.M., Tsang, D.C.W., Yip, A.C.K., Khan, E., Wang, L., Ok, Y.S., Poon, C.S., 2017. Valorization of cellulosic food waste into levulinic acid catalyzed by heterogeneous Brønsted acids: Temperature and solvent effects. Chem. Eng. J. 327, 328–335.

Cheng, C.-L., Lo, Y.-C., Lee, K.-S., Lee, D.-J., Lin, C.-Y., Chang, J.-S., 2011. Biohydrogen production from lignocellulosic feedstock. Bioresour. Technol., Special Issue: Biofuels-III: Biohydrogen 102, 8514–8523.

Chew, K.W., Chia, S.R., Show, P.L., Yap, Y.J., Ling, T.C., Chang, J.-S., 2018. Effects of water culture medium, cultivation systems and growth modes for microalgae cultivation: A review. J. Taiwan Inst. Chem. Eng. 91, 332–344.

Chew, K.W., Yap, J.Y., Show, P.L., Suan, N.H., Juan, J.C., Ling, T.C., Lee, D.-J., Chang, J.-S., 2017. Microalgae biorefinery: High value products perspectives. Bioresour. Technol. 229, 53–62.

Chinnasamy, S., Bhatnagar, A., Hunt, R.W., Das, K.C., 2010. Microalgae cultivation in a wastewater dominated by carpet mill effluents for biofuel applications. Bioresour. Technol. 101, 3097–3105.

Chisti, Y., 2007. Biodiesel from microalgae. Biotechnol. Adv. 25, 294–306.

Correa, D.F., Beyer, H.L., Possingham, H.P., Thomas-Hall, S.R., Schenk, P.M., 2017. Biodiversity impacts of bioenergy production: Microalgae vs. first generation biofuels. Renew. Sustain. Energy Rev. 74, 1131–1146.

Costa, J.A.V., de Morais, M.G., 2014. An Open Pond System for Microalgal Cultivation, in: Pandey, A., Lee, D.-J., Chisti, Y., Soccol, C.R. (Eds.), Biofuels from Algae. Elsevier, Amsterdam, pp. 1–22.

Davis, R., Aden, A., Pienkos, P.T., 2011. Techno-economic analysis of autotrophic microalgae for fuel production. Appl. Energy, Special Issue of Energy from algae: Current status and future trends 88, 3524–3531.

Demirbaş, A., 2001. Biomass resource facilities and biomass conversion processing for fuels and chemicals. Energy Convers. Manag. 42, 1357–1378.

Di Nunzio, M., Picone, G., Pasini, F., Caboni, M.F., Gianotti, A., Bordoni, A., Capozzi, F., 2018. Olive oil industry by-products. Effects of a polyphenol-rich extract on the metabolome and response to inflammation in cultured intestinal cell. Food Res. Int. 113, 392–400.

Doumax-Tagliavini, V., Sarasa, C., 2018. Looking towards policies supporting biofuels and technological change: Evidence from France. Renew. Sustain. Energy Rev. 94, 430–439.

Dutta, K., Daverey, A., Lin, J.-G., 2014. Evolution retrospective for alternative fuels: First to fourth generation. Renew. Energy 69, 114–122.

European Commission, 2015. Circular Economy Closing the Loop (WWW Document). Eur. Comm. Press Release Database, accessed 9.10.18.

Fargione, J., Hill, J., Tilman, D., Polasky, S., Hawthorne, P., 2008. Land Clearing and the Biofuel Carbon Debt. Science 319, 1235–1238.

Faried, M., Samer, M., Abdelsalam, E., Yousef, R.S., Attia, Y.A., Ali, A.S., 2017. Biodiesel production from microalgae: Processes, technologies and recent advancements. Renew. Sustain. Energy Rev. 79, 893–913.

Feng, Y., Li, C., Zhang, D., 2011. Lipid production of Chlorella vulgaris cultured in artificial wastewater medium. Bioresour. Technol., Special Issue: Biofuels - II: Algal Biofuels and Microbial Fuel Cells 102, 101–105.

Frankó, B., Galbe, M., Wallberg, O., 2015. Influence of bark on fuel ethanol production from steam-pretreated spruce. Biotechnol. Biofuels 8, 15.

Geng, Y., Sarkis, J., Ulgiati, S., Zhang, P., 2013. Measuring China's Circular Economy. Science 339, 1526–1527.

Ghisellini, P., Cialani, C., Ulgiati, S., 2016. A review on circular economy: the expected transition to a balanced interplay of environmental and economic systems. J. Clean. Prod., Towards Post Fossil Carbon Societies: Regenerative and Preventative Eco-Industrial Development 114, 11–32.

Gomaa, M.A., Abed, R.M.M., 2017. Potential of fecal waste for the production of biomethane, bioethanol and biodiesel. J. Biotechnol. 253, 14–22.

Grosse, F., 2010. Is recycling "part of the solution"? The role of recycling in an expanding society and a world of finite resources. SAPIENS Surv. Perspect. Integrating Environ. Soc. 3.

Hodaifa, G., Paladino, O., Malvis, A., Seyedsalehi, M., Neviani, M., 2019. Green Techniques for Wastewaters, in: Kyzas, G.Z. (Ed.), Advanced Low-Cost Separation Techniques in Interface Science. Elsevier, London, UK.

Hongzhang, C., Liying, L., 2007. Unpolluted fractionation of wheat straw by steam explosion and ethanol extraction. Bioresour. Technol. 98, 666–676.

Hoornweg, D., Bhada-Tata, P., Kennedy, C., 2013. Environment: Waste production must peak this century. Nat. News 502, 615.

Hu, J., Xiao, Z., Zhou, R., Deng, W., Wang, M., Ma, S., 2011. Ecological utilization of leather tannery waste with circular economy model. J. Clean. Prod. 19, 221–228.

Ibarra-Gonzalez, P., Rong, B.-G., 2018. A review of the current state of biofuels production from lignocellulosic biomass using thermochemical conversion routes. Chin. J. Chem. Eng.

IEA Bioenergy, 2008. From 1st-to 2nd-Generation BioFuel technologies. An overview of current industry and RD&D activities. IEA-OECD.

IPCC, (Core Writing Team, R.K. Pachauri and L.A. Meyer eds.)., 2014. Climate Change 2014: Synthesis Report. Contribution of Working Groups I, II and III to the Fifth Assessment Report of the Intergovernmental Panel on Climate Change. IPCC, Geneva, Switzerland.

IRENA, 2018. Renewable Capacity Statistics 2018. International Renewable Energy Agency (IRENA), Abu Dhabi.

Kamm, B., Kamm, M., Gruber, P.R., Kromus, S., 2008. Biorefinery Systems – An Overview, in: Biorefineries-Industrial Processes and Products. John Wiley & Sons, pp. 1–40.

Kassim, M.A., Meng, T.K., 2017. Carbon dioxide (CO2) biofixation by microalgae and its potential for biorefinery and biofuel production. Sci. Total Environ. 584–585, 1121–1129.

Khan, M.I., Shin, J.H., Kim, J.D., 2018. The promising future of microalgae: current status, challenges, and optimization of a sustainable and renewable industry for biofuels, feed, and other products. Microb. Cell Factories 17.

Kim, J., Yoo, G., Lee, H., Lim, J., Kim, K., Kim, C.W., Park, M.S., Yang, J.-W., 2013. Methods of downstream processing for the production of biodiesel from microalgae. Biotechnol. Adv., "Bioenergy and Biorefinery from Biomass" through innovative technology development 31, 862–876.

Kirchherr, J., Reike, D., Hekkert, M., 2017. Conceptualizing the circular economy: An analysis of 114 definitions. Resour. Conserv. Recycl. 127, 221–232.

Koukoulas, A.A., 2016. A Critical Look at Cellulosic Ethanol and Other Advanced Biofuels: Biofuels Digest. Biofuels Dig., accessed 8.26.18.

Kricka, W., James, T.C., Fitzpatrick, J., Bond, U., 2015. Engineering Saccharomyces pastorianus for the co-utilisation of xylose and cellulose from biomass. Microb. Cell Factories 14, 61.

Kumar, P., Barrett, D.M., Delwiche, M.J., Stroeve, P., 2009. Methods for Pretreatment of Lignocellulosic Biomass for Efficient Hydrolysis and Biofuel Production [WWW Document].

Lam, M.K., Lee, K.T., Mohamed, A.R., 2012. Current status and challenges on microalgae-based carbon capture. Int. J. Greenh. Gas Control 10, 456–469.

Lee, W.-C., Kuan, W.-C., 2015. Miscanthus as cellulosic biomass for bioethanol production. Biotechnol. J. 10, 840–854.

Leong, W.-H., Lim, J.-W., Lam, M.-K., Uemura, Y., Ho, Y.-C., 2018. Third generation biofuels: A nutritional perspective in enhancing microbial lipid production. Renew. Sustain. Energy Rev. 91, 950–961.

Lijó, L., Frison, N., Fatone, F., González-García, S., Feijoo, G., Moreira, M.T., 2018. Environmental and sustainability evaluation of livestock waste management practices in Cyprus. Sci. Total Environ. 634, 127–140.

Lin, Y., Tanaka, S., 2006. Ethanol fermentation from biomass resources: current state and prospects. Appl. Microbiol. Biotechnol. 69, 627–642.

Luque, R., Lin, C.S.K., Wilson, K., Clark, J., 2016. Handbook of Biofuels Production, Second. ed, Energy. Woodhead Publishing.

Maeda, Y., Yoshino, T., Matsunaga, T., Matsumoto, M., Tanaka, T., 2018. Marine microalgae for production of biofuels and chemicals. Curr. Opin. Biotechnol., Energy biotechnology • Environmental biotechnology 50, 111–120.

Makris, D.P., 2018. Green extraction processes for the efficient recovery of bioactive polyphenols from wine industry solid wastes – Recent progress. Curr. Opin. Green Sustain. Chem. 13, 50–55.

Martínez-Huélamo, M., Rodríguez-Morató, J., Boronat, A., de la Torre, R., 2017. Modulation of Nrf2 by Olive Oil and Wine Polyphenols and Neuroprotection. Antioxidants 6.

Merchuk J.C., Garcia Camacho F., 2010. Bioreactors: Airlift Reactors, in: Encyclopedia of Industrial Biotechnology: Bioprocess, Bioseparation, and Cell Technology., Major Reference Works. American Cancer Society, pp. 887–953.

Mohanty, C.R.C., 2011. Reduce, reuse and recycle (the 3Rs) and resource efficiency as the basis for sustainable waste management, in: Proceedings of the Synergizing Resource Efficiency with Informal Sector towards Sustainable Waste Management. UNCRD, New York USA.

Mohd Azhar, S.H., Abdulla, R., Jambo, S.A., Marbawi, H., Gansau, J.A., Mohd Faik, A.A., Rodrigues, K.F., 2017. Yeasts in sustainable bioethanol production: A review. Biochem. Biophys. Rep. 10, 52–61.

Mohd Udaiyappan, A.F., Abu Hasan, H., Takriff, M.S., Sheikh Abdullah, S.R., 2017. A review of the potentials, challenges and current status of microalgae biomass applications in industrial wastewater treatment. J. Water Process Eng. 20, 8–21.

Molina Grima, E., Belarbi, E.-H., Acién Fernández, F.G., Robles Medina, A., Chisti, Y., 2003. Recovery of microalgal biomass and metabolites: process options and economics. Biotechnol. Adv. 20, 491–515. Moreno-Garcia, L., Adjallé, K., Barnabé, S., Raghavan, G.S.V., 2017. Microalgae biomass production for a biorefinery system: Recent advances and the way towards sustainability. Renew. Sustain. Energy Rev. 76, 493–506.

Nabi, M.N., Rahman, M.M., Akhter, M.S., 2009. Biodiesel from cotton seed oil and its effect on engine performance and exhaust emissions. Appl. Therm. Eng. 29, 2265–2270.

Naik, S.N., Goud, V.V., Rout, P.K., Dalai, A.K., 2010. Production of first and second generation biofuels: A comprehensive review. Renew. Sustain. Energy Rev. 14, 578–597.

Nassiri-Asl, M., Hosseinzadeh, H., 2016. Review of the Pharmacological Effects of Vitis vinifera (Grape) and its Bioactive Constituents: An Update. Phytother. Res. PTR 30, 1392–1403.

OECD, 2018. What is a biorefinery: Definitions, classification and general models, in: Meeting Policy Challenges for a Sustainable Bioeconomy. OECD Publishing, Paris, pp. 71–92.

OECD, 2010. Waste Management and the 3Rs (Reduce, Reuse, Recycle) 147–168.

Oh, Y.-K., Hwang, K.-R., Kim, C., Kim, J.R., Lee, J.-S., 2018. Recent developments and key barriers to advanced biofuels: A short review. Bioresour. Technol. 257, 320–333.

Paini, M., Casazza, A.A., Aliakbarian, B., Perego, P., Binello, A., Cravotto, G., 2016. Influence of ethanol/water ratio in ultrasound and high-pressure/high-temperature phenolic compound extraction from agri-food waste. Int. J. Food Sci. Technol. 51, 349–358.

Paladino, O., Neviani, M., 2018. A closed loop biowaste to biofuel integrated process fed with waste frying oil, organic waste and algal biomass: Feasibility at pilot scale. Renew. Energy, SI: Waste Biomass to Biofuel 124, 61–74.

Passet, R., 1979. L'Économique et le vivant. Payot.

Perego, P., Converti, A., Palazzi, E., Del Borghi, M., Ferraiolo, G., 1990. Fermentation of hardwood hemicellulose hydrolysate byPachysolen tannophilus, candida shehatae andPichia stipitis. J. Ind. Microbiol. 6, 157–164.

Pino, M.S., Rodríguez-Jasso, R.M., Michelin, M., Flores-Gallegos, A.C., Morales-Rodriguez, R., Teixeira, J.A., Ruiz, H.A., 2018. Bioreactor design for enzymatic hydrolysis of biomass under the biorefinery concept. Chem. Eng. J. 347, 119–136.

Pittman, J.K., Dean, A.P., Osundeko, O., 2011. The potential of sustainable algal biofuel production using wastewater resources. Bioresour. Technol., Special Issue: Biofuels - II: Algal Biofuels and Microbial Fuel Cells 102, 17–25.

Prasetyo, J., Naruse, K., Kato, T., Boonchird, C., Harashima, S., Park, E.Y., 2011. Bioconversion of paper sludge to biofuel by simultaneous saccharification and fermentation using a cellulase of paper sludge origin and thermotolerant Saccharomyces cerevisiae TJ14. Biotechnol. Biofuels 4, 35.

Raja, R., Shanmugam, H., Ganesan, V., Carvalho, I.S., 2014. Biomass from Microalgae: An Overview. J. Oceanogr. Mar. Res. 2, 1–7.

Razzak, S.A., Hossain, M.M., Lucky, R.A., Bassi, A.S., de Lasa, H., 2013. Integrated CO2 capture, wastewater treatment and biofuel production by microalgae culturing—A review. Renew. Sustain. Energy Rev. 27, 622–653.

Riazi, M.R., Chiaramonti, D., 2017. Biofuels Production and Processing Technology. CRC Press. Richmond, A., 2008. Handbook of Microalgal Culture: Biotechnology and Applied Phycology. John Wiley & Sons.

Robak, K., Balcerek, M., 2018. Review of Second Generation Bioethanol Production from Residual Biomass. Food Technol. Biotechnol. 56, 174–187.

Rodolfi, L., Zittelli, G.C., Bassi, N., Padovani, G., Biondi, N., Bonini, G., Tredici, M.R., 2009. Microalgae for oil: Strain selection, induction of lipid synthesis and outdoor mass cultivation in a low-cost photobioreactor. Biotechnol. Bioeng. 102, 100–112.

Rolz, C., de León, R., 2011. Ethanol fermentation from sugarcane at different maturities. Ind. Crops Prod. 33, 333–337.

Saha, B.C., Iten, L.B., Cotta, M.A., Wu, Y.V., 2005. Dilute acid pretreatment, enzymatic saccharification, and fermentation of rice hulls to ethanol. Biotechnol. Prog. 21, 816–822.

Salgot, M., Folch, M., 2018. Wastewater treatment and water reuse. Curr. Opin. Environ. Sci. Health 2, 64–74.

Sauvé, S., Bernard, S., Sloan, P., 2016. Environmental sciences, sustainable development and circular economy: Alternative concepts for trans-disciplinary research. Environ. Dev. 17, 48–56.

Sharma, Raman, Sharma, M., Sharma, Ratika, Sharma, V., 2013. The impact of incinerators on human health and environment. Rev. Environ. Health 28, 67–72.

Sharma, Y.C., Singh, B., 2009. Development of biodiesel: Current scenario. Renew. Sustain. Energy Rev. 13, 1646–1651.

Singh, R.N., Sharma, S., 2012. Development of suitable photobioreactor for algae production – A review. Renew. Sustain. Energy Rev. 16, 2347–2353.

Stoffel, R.B., Neves, P.V., Felissia, F.E., Ramos, L.P., Gassa, L.M., Area, M.C., 2017. Hemicellulose extraction from slash pine sawdust by steam explosion with sulfuric acid. Biomass Bioenergy 107, 93–101.

Swain, P.K., Das, L.M., Naik, S.N., 2011. Biomass to liquid: A prospective challenge to research and development in 21st century. Renew. Sustain. Energy Rev. 15, 4917–4933.

Ugwu, C.U., Aoyagi, H., Uchiyama, H., 2008. Photobioreactors for mass cultivation of algae. Bioresour. Technol. 99, 4021–4028.

United Nations, Department of Economic and Social Affairs, Population Division, 2017. World Population Prospects: The 2017 Revision, Volume II: Demographic Profiles.

Varone, A., Ferrari, M., 2015. Power to liquid and power to gas: An option for the German Energiewende. Renew. Sustain. Energy Rev. 45, 207–218.

Verma, R., Srivastava, A., 2018. Carbon dioxide sequestration and its enhanced utilization by photoautotroph microalgae. Environ. Dev. 27, 95–106.

Visvanathan, C., Kumar, S., 2007. 3Rs (Reduce, Reuse, and Recycle) Initiatives in Asia, in: Proceedings of the International Conference on Cleaner Technologies and Environmental Management (ICCTEM). Presented at the International Conference on Cleaner Technologies and Environmental Management (ICCTEM), Pondicherry, India.

Vo, H.N.P., Ngo, H.H., Guo, W., Nguyen, T.M.H., Liu, Yiwen, Liu, Yi, Nguyen, D.D., Chang, S.W., 2019. A critical review on designs and applications of microalgae-based photobioreactors for pollutants treatment. Sci. Total Environ. 651, 1549–1568.

Vohra, M., Manwar, J., Manmode, R., Padgilwar, S., Patil, S., 2014. Bioethanol production: Feedstock and current technologies. J. Environ. Chem. Eng. 2, 573–584.

Wang, B., Lan, C.Q., Horsman, M., 2012. Closed photobioreactors for production of microalgal biomasses. Biotechnol. Adv., Biorefining: Thermochemical and Enzymatic Biomass Conversion 30, 904–912.

Wang, Y., Ho, S.-H., Cheng, C.-L., Guo, W.-Q., Nagarajan, D., Ren, N.-Q., Lee, D.-J., Chang, J.-S., 2016. Perspectives on the feasibility of using microalgae for industrial wastewater treatment. Bioresour. Technol. 222, 485–497.

WBA, 2017. WBA Global Bioenergy Statistics 2017. World Bioenergy Association (WBA), Stockholm, Sweden.

WEC, 2018. 2018 World Energy Issues Monitor. London: World Energy Council (WEC).

Wijffels, R.H., Barbosa, M.J., 2010. An Outlook on Microalgal Biofuels. Science 329, 796–799.

Williams, P.J. le B., Laurens, L.M.L., 2010. Microalgae as biodiesel & biomass feedstocks: Review & analysis of the biochemistry, energetics & economics. Energy Environ. Sci. 3, 554–590.

Xu, L., Weathers, P.J., Xiong, X.-R., Liu, C.-Z., 2009. Microalgal bioreactors: Challenges and opportunities. Eng. Life Sci. 9, 178–189.

Yazdani, S.S., Gonzalez, R., 2007. Anaerobic fermentation of glycerol: a path to economic viability for the biofuels industry. Curr. Opin. Biotechnol., Energy biotechnology / Environmental biotechnology 18, 213–219.

Zhao, B., Su, Y., 2014. Process effect of microalgal-carbon dioxide fixation and biomass production: A review. Renew. Sustain. Energy Rev. 31, 121–132.

CHAPTER 2: DYNAMIC MODELING

2.1 Mathematical modeling of polyphenols extraction process

This chapter deals with the modeling of the polyphenols extraction process introduced in Section 1.2.1 .

The fundamental unit of said process is, as it is often the case, the chemical reactor. For the considered case, it is a Stirred Tank Reactor (STR) that could be operated either in discontinuous (DSTR) or continuous (CSTR).

This is a conventional choice, as it allows an accurate description of the transients, possibly including start-ups, shutdowns and transients related to emergency procedures. Furthermore, it allows to study the evolution of the system around nominal conditions and to calculate the time required to reinstate stationary (operating) conditions. Dynamic models are useful for stationary analyses as well, as they enable to optimize nominal operating conditions based on efficiency criteria or to evaluate plant performance in off-design situations. It is the way to go when the aim is to chose an effective control strategy, taking into account the characteristics of the plant that could limit its performance. Moreover, dynamic models are essential for control tuning, i.e. to choose parameters that minimize response times and variable instabilities.

A physically based, dynamic model was therefore constructed. Physically based models are derived from a thorough knowledge of the physics of the process, providing predictions of the output variables but also information on the state variables (white box), thus bearing a perceptible physical meaning. Built upon first principles, typically conservation laws and constitutive equations, they follow a hypothetical-deductive approach and can be written at each representation scale (Paladino et al., 2019).

Since the reactor used for the experimental tests at lab-scale can be considered a semi-ideal isothermal batch reactor and that employed at pilot-scale (Figure 2.1) is a SR identifiable as well-mixed, the common lumped system approximation was employed (Vojtesek and Dostal, 2012). This resulted in Ordinary Differential Equations (ODEs) type of models hinging on mathematical balances that include kinetic equations for extraction rates, heat transfer and equations representing property changes.

Fig. 2.1 Pilot scale STR, which can be used both in batch or continuous operation mode (Neviani et al., 2019).

In order to simulate the effect on possible noises or parameter estimation errors, some of the signals were perturbed. For actions of this kind, the possible data noise generation procedures are Pseudo Random Binary Sequences (PRBSs), Pseudo Random Sequences (PRSs) and Monte Carlo sequences. When using PBRS, for each input variable on which the noise is generated, the minimum and maximum values are identified (variation interval in which the steady state value is contained). The value of the input variable varies randomly between the two extra (min = 0, max = 1) according to a uniform distribution and the input variables can only take two values. The amplitude is sufficiently high with respect to the noise (fixed amplitude, usually 30% ÷ 50% less or more than the steady state value) and the noise, which is a white noise, is performed every n sampling times (equal to about 30% of the system response time). PRS sequences are analogous although the input variables can assume each value in the $[0, 1]$ range, the noise is not a white one and the amplitude of the interval is usually $20\% \div 30\%$ less or more than the plate (steady state) value. Also for Monte Carlo sequences the input minimum and maximum values on which to generate the disturbance for each variable are identified. The value of the input variable varies randomly (any value even outside the interval $(\min, \max)$) according to a Gaussian distribution in which the min/max values represent ($\pm 2\sigma$ or $\pm 3\sigma$) and can take all possible values. The width of the interval is slightly higher than the noise (usually $10\% \div 15\%$ less or more than the plate value) and the noise, as for PRSs, is not a white one.

2.1.1 Material balance for the reactor

The design of the optimal stirred reactor at pilot scale touches many different aspects but the main aim is to determine, at chosen and fixed process parameters, the time required to reach a specific yield, i.e. extraction time τ_e if it is operated in discontinuous, or space time τ_s and residence time τ_r in case of a CSTR (these two are equal for the ideal reactor). By considering the case where N_c components are contained in the reactor, the material molar balance equation for the i-th component can be written as:

$$\frac{\mathrm{d}n_i}{\mathrm{d}t} = W_{i,in} - W_{i,out} + \mathscr{R}_i \tag{2.1}$$

where $W_{i,in}$ and $W_{i,out}$ are, respectively, the incoming and outgoing molar flow rates ($\mathrm{mol\,s^{-1}}$) and $\mathscr{R}_i$ is the mole generation term for the i-th component ($\mathrm{mol\,s^{-1}}$). $\mathscr{R}_i$ is defined as the product of the reacting volume V_r for the specific mole generation term for the i-th component $\mathscr{R}_{i,\mathrm{spec}}$, in turn defined as:

$$\mathscr{R}_{i,\mathrm{spec}} = \sum_{j=1}^{\mathrm{NR}} \nu_{i,j} v_j \tag{2.2}$$

where, in case of generation terms due to chemical reactions, $\nu_{i,j}$ is the stoichiometric coefficient of the i-th component in the j-th reaction, NR is the overall number of reactions of the process and v_j is the reaction rate of the j-th reaction ($\mathrm{mol\,m^{-3}\,s^{-1}}$).

However, we can use the same formalism even in case of generation terms due to physical or mixed chemical-physical processes, as extraction is, by assigning to v_j the meaning of extraction rate. Hence:

$$\mathscr{R}_i = \mathscr{R}_{i,\mathrm{spec}} V_\mathrm{r} = V_\mathrm{r} \sum_{j=1}^{\mathrm{NR}} \nu_{i,j} v_j \tag{2.3}$$

When considering the lab-scale DSTR, equation Eqn. 2.1 can be simplified as:

$$\frac{\mathrm{d}n_i}{\mathrm{d}t} = \mathscr{R}_i = V_\mathrm{r} \sum_{j=1}^{\mathrm{NR}} \nu_{i,j} v_j \tag{2.4}$$

that can be rewritten in terms of concentration C of component $i =$ total polyphenols (specifically with the subscript S if they represent polyphenols contained in the solid phase dispersed in the fluid, with the assumption of homogeneous fluid, slurry reactor content) as:

$$\frac{\mathrm{d}V_\mathrm{r}C_i}{\mathrm{d}t} = V_\mathrm{r} \sum_{j=1}^{\mathrm{NR}} \nu_{i,j} v_j \tag{2.5}$$

Then, if the reacting volume into the reactor is constant, and the fluid inside the reactor is considered incompressible, Eqn. 2.5 is retooled as:

$$\frac{\mathrm{d}C_i}{\mathrm{d}t} = \sum_{j=1}^{\mathrm{NR}} \nu_{i,j} v_j \tag{2.6}$$

So, Eqn. 2.6 is valid if one considers only the fluid (slurry) phase, composed by incompressible solvents (in this case water/methanol/ethanol) and polyphenols (in both solid and liquid phases). Otherwise, equation Eqn. 2.5 must be used to describe the components mass balance inside the lab-scale DSTR.

The material balance equation of total polyphenols in the pilot-scale reactor can be written in general form as:

$$\frac{\mathrm{d}V_\mathrm{r}C_i}{\mathrm{d}t} = \sum_{k_{in}=1}^{\mathrm{NR}_\mathrm{in}} q_{k_\mathrm{in}} C_{k_\mathrm{in}} - \sum_{k_\mathrm{in}=1}^{\mathrm{NR}_\mathrm{out}} q_{k_\mathrm{out}} C_{k_\mathrm{out}} + V_\mathrm{r} \sum_{j=1}^{\mathrm{NR}} \nu_{i,j} v_j \tag{2.7}$$

where q_in and q_out are the input and output volumetric flowrates (solvent, slurry containing the vegetal) and the same assumptions can be made about the fluid phase.

2.1.2 Kinetics of polyphenols extraction

The set of mathematical models from which one can draw for the description of polyphenols extraction rates v_j is varied. One possibility is to to employ a pseudo first-order kinetic model to characterize a unique extraction rate. A valid alternative seems to be given by the model proposed by Peleg (Peleg, 1988).

Starting from a general reaction rate, written as follows:

$$v = \frac{k_1 \prod_{i=1}^{\mathrm{R}} C_{i,\mathrm{R}}^{\beta_i} - k_2 \prod_{i=1}^{\mathrm{P}} C_{i,\mathrm{P}}^{\gamma_i}}{1 + \prod_{i=1}^{\mathrm{R+P}} k_i C_i} \tag{2.8}$$

a pseudo-first order extraction model suggests that the extraction rate v_e can be reformulated as:

$$v_e = K c_{i,\mathrm{S}} \tag{2.9}$$

where $c_{i,\mathrm{S}}$ represents the mass concentration of total polyphenols contained in the solid phase dispersed in the fluid (slurry) ($\mathrm{mg_{TP,S0} mL^{-3}}$), and K is an effective extraction constant whose dependence on temperature could be expressed by the Arrhenius law.

By integrating equation Eqn. 2.6 for a DSTR with v_e expressed by equation Eqn. 2.9 and mass concentration expressed as $c_{i,\mathrm{S}}$, the variation of total polyphenols in time has the following form:

$$\frac{x_{i,\mathrm{S}}(t)}{x_{i,\mathrm{S0}}} = \exp(-Kt) \tag{2.10}$$

$x_{i,\mathrm{S}}(t)$ indicates the mass of TP in the solid phase at time t per dry matter basis, i.e. vegetable solid mass, ($\mathrm{mg_{TP,S} g_{DM}^{-1}}$) whilst $x_{i,\mathrm{S0}}$ represents the initial TP content per dry matter basis ($\mathrm{mg_{TP,S0} g_{DM}^{-1}}$). Consequently, $x_i(t)$, the TP in the liquid phase at time t per dry matter basis ($\mathrm{mg_{TP,L} g_{DM}^{-1}}$), can be inferred:

$$x_i(t) = x_{i0} + x_{i,\mathrm{S0}}(1 - \exp(-Kt)) \tag{2.11}$$

Bucić-Kojić suggested (Bucic-Kojic et al., 2007) that polyphenols extraction can be described by the extension of the model proposed by Peleg. Accordingly, the variation of total polyphenols in time can be inferred from Eqn. 2.12.

$$x_i(t) = x_{i0} + \frac{t}{K_1 + K_2 t} \tag{2.12}$$

K_1 is the modified Peleg's rate constant ($\mathrm{s\, g_{DM} mg_{TP}^{-1}}$) and K_2 is the modified Peleg's capacity constant ($\mathrm{g_{DM} mg_{TP}^{-1}}$).

The extraction rate, written as the rate of change in time of total polyphenol mass fraction, can be generally found by opportunely differentiating equation Eqn. 2.12 with respect to time:

$$\tilde{v}_e = \frac{K_1}{(K_1 + K_2 t)^2} \tag{2.13}$$

K_1 relates to the extraction rate $\tilde{v}_{e0}$. A rapid inspection of Eqn. 2.13, for $t = t_0$ shows that $\tilde{v}_{e0} = K_1^{-1}$. K_2, on the other hand, relates to maximum extraction yield, i.e. total polyphenols at equilibrium. Evaluating the limit of Eqn. 2.13 for $t \rightarrow +\infty$ one gets $x_{\text{eq}} = x_{i0} + K_2^{-1}$.

The extraction parameters K, K_1 and K_2 appearing in the two models, and consequently the extraction rates, are functions of temperature T. Arrhenius type equation could be used for the generic K in the pseudo first order extraction kinetics:

$$K = K_0 \exp\left(\frac{E_a}{R_u T}\right) \tag{2.14}$$

The parameters of constitutive equation 2.14 are a pre-exponential factor K_0, R_u is the universal gas constant ($8.314472\,\mathrm{J\,mol^{-1}\,K^{-1}}$) and T is the temperature of the process (K). Lastly, E_a ($\mathrm{J\,mol^{-1}}$) is similar to the activation energy but should be related to the solubility of the extracted product.

Through the fitting of the empirical data gathered at lab-scale in the DSTR with Eqn. 2.11 or Eqn. 2.12, extraction constants K or K_1 and K_2 can be estimated at fixed temperatures. Furthermore, Eqn. 2.14 or some polynomial functions offer the possibility to model of temperature on them.

2.1.3 Energy balance for the reactor

From the heat exchange standpoint and within its limits, a reactor can be operated isothermally (maximum heat exchange) or adiabatically (no heat exchange). Between these extremes lies the most common form of operation of the reactor, the non-isothermal regime. These three types of operating conditions correspond to different temperature profiles within the reactor; in this regard, it should be noted that the isothermal conditions are most advantageous for the measurement of the kinetic data. This is the reason why this condition is usually adopted at lab-scale during the experimental tests.

If a reactor works at non-isothermal or adiabatic conditions, then the material balance equation needs to be expressed as a function of temperature T, as the formulation of the reaction rate (in this case the extraction rate) comprises the independent variable T. It follows that the material balance equation can be solved only with the simultaneous solution of the energy balance. Thus, for non-isothermal reactor descriptions, energy and material balances must be coupled (Davis and Davis, 2012). This is the case of the pilot-scale reactor, that have to be equipped with a device properly designed for heat exchange so as to realize the reactor initial heating, the development of the extraction phase and the final cooling. Typically, pursuable solutions for medium heat loads (for this process, internal temperature could be between 120 °C and 180 °C) consist in an external coil or in a jacketed reactor heated and cooled through vapor, oil or water at defined pressures.

In case of a small reactor volume, some electrical heaters can be used whilst cooling could be assured by external heat exchange; this is the case of the lab-scale reactor.

The energy balance for a generic CSTR employed to realize a single-reaction process can be expressed in terms of enthalpy (assumption legitimized by the fact that the process under study is carried out at constant pressure, thus allowing the use of enthalpy instead of internal energy) as:

$$V_\mathrm{r}\rho c_p \frac{\mathrm{d}T}{\mathrm{d}t} = \dot{H}_\mathrm{in} - \dot{H}_\mathrm{out} - V_\mathrm{r}\Delta H_r v - \dot{Q}_\mathrm{syst} - \dot{Q}_\mathrm{loss,t} - \dot{Q}_\mathrm{loss,b} \tag{2.15}$$

In Eqn. 2.15, V_r is the reaction volume m^3, ρ is the mean density of the liquid phase – averaged on temperature and components – ($\mathrm{kg\,m^{-3}}$), c_p is the specific heat capacity at constant pressure of the fluid contained in the reactor – averaged on temperature and components – ($\mathrm{J\,kg^{-1}\,K^{-1}}$), T is the temperature inside the reactor – considered uniform since the reactor is well mixed – (K), $\dot{H}_\mathrm{in}$ and $\dot{H}_\mathrm{out}$ are, respectively, the rates of enthalpy entering the system by inflow and leaving it by outflow ($\mathrm{J\,s^{-1}}$), ΔH_r is the reaction enthalpy (in this case the extraction process) at temperature equal to T ($\mathrm{J\,mol^{-1}}$) and pressure p, v is the reaction rate – thus, for the process under examination $v = v_e$ – ($\mathrm{mol\,mol^{-3}\,s^{-1}}$) and $\dot{Q}_\mathrm{syst}$ represents heat flux exchanged with the heating/cooling system with which the reactor vessel is equipped (W). $\dot{Q}_\mathrm{loss,t}$ and $\dot{Q}_\mathrm{loss,b}$ are the heat fluxes flowing out of the reactor from the lid and from the reactor bottom respectively (W).

The main simplifying assumptions made in Eqn. 2.15 are that the reaction volume V_r and both ρ and c_p are not considered time dependent, and that the heat of mixing of the components and the contribute of the reactor mixer on enthalpy balance are neglected.

For an extraction process, since the standard enthalpy of formation is almost equal to zero (no chemical reaction), only second-order thermal effects should be considered in ΔH_r. Inasmuch the required heat to keep the reactor at the optimal process temperature (120 °C $\div$ 180 °C) is greater than these effects, this term into Eqn. 2.15 can be taken equal to zero.

Various structural solutions for reaching the desired temperature inside the reactor can be adopted. If resistor wires are welded to the reactor lateral walls, $\dot{Q}_\mathrm{syst}$ can be written as:

$$\dot{Q}_\mathrm{syst} = U_\mathrm{rw} S_\mathrm{rw} (T - T_\mathrm{rw}) \tag{2.16}$$

where S_rw is the heat transfer area of the warming system (m^2), T_rw is the temperature of the copper conductor (K) and U_rw is the overall heat transfer coefficient relative to the heat transfer control system ($\mathrm{W\,m^{-2}\,K^{-1}}$). This latter parameter measures the overall tendency of series of materials, seen as conductive or convective barriers to heat transfer. Besides, it can be thought in terms of R-value $R_{\mathrm{th,overall}}$, so that:

$$R^{-1}_{\mathrm{th,overall}} = \frac{1}{U_{\mathrm{rw}} S_{\mathrm{rw}}} = \frac{1}{h_{\mathrm{mix}} S_{\mathrm{mix}}} + \frac{\ln\left(\dfrac{r_{\mathrm{w}} + \delta_{\mathrm{w}}}{r_{\mathrm{w}}}\right)}{2\pi \lambda_{\mathrm{w}} L_{\mathrm{w}}} + \frac{\ln\left(\dfrac{r_{\mathrm{w}} + \delta_{\mathrm{w}} + \delta_{\mathrm{ins,w}}}{r_{\mathrm{w}} + \delta_{\mathrm{w}}}\right)}{2\pi \lambda_{\mathrm{ins,w}} L_{\mathrm{w}}} \tag{2.17}$$

where h_{mix} is the convective heat transfer coefficient between the fluid inside the reactor and the inner side of the reactor wall ($\mathrm{W\,m^{-2}\,K^{-1}}$), δ_{w} and $\delta_{\mathrm{ins,w}}$ are respectively the thickness of the reactor wall (m) and that of the insulating material wrapped around the electrical wiring, λ_{w} and $\lambda_{(\mathrm{ins,w})}$ the corresponding thermal conductivities ($\mathrm{W\,m^{-1}\,K^{-1}}$), L_{w} is the vertical height of the portion of reactor enveloped in resistor wires (m), S_{mix} is the inner outer surface area of the reactor ($\mathrm{m^2}$) and r_{w} is the inner radius of the reactor wall (m).

The use of Eqn. 2.17 for the overall heat transfer coefficient is due to the conformation of the heating system: the resistive wires produce heat when current runs through them because of Joule's effect and they are electrically insulated from external tubular sheaths in which they are inserted due to the use of mineral insulation (e.g. magnesium oxide). This latter also ensures excellent heat transfer to the outer tubular sheath as it has high thermal conductivity. Since the characteristic heating time of the heater container is smaller than the reactor heating time, in calculations the mass of the heater container can be neglected, T_{rw} transients are very fast and no energy balance for the heating system is considered. Moreover, for the lab-scale isothermal DSTR, T_{rw} is considered a constant and Eqn. 2.15 is used only to simulate the reactor heating start-up.

Another possibility to assure heat exchange consists in deploying jacketed or coil reactors. Heat transfer fluid passes through the jacket or coils to add or remove heat. In this case:

$$\dot{Q}_{\mathrm{syst}} = U_{\mathrm{f}} S_{\mathrm{f}} (T - T_{\mathrm{f}}) \tag{2.18}$$

Saturated vapor or a proper heating fluid (usually a mineral oil) can be employed. If the heating fluid remains in liquid phase, the following enthalpy balance has to be added for the heating fluid:

$$\frac{\mathrm{d}T_{\mathrm{f}}}{\mathrm{d}t} = \frac{c_{p_{\mathrm{f,in}}} \rho_{\mathrm{f,in}} q_{\mathrm{f,in}} T_{\mathrm{f,in}}}{V_{\mathrm{f}} \rho_{\mathrm{f}} c_{p_{\mathrm{f}}}} - \frac{c_{p_{\mathrm{f,out}}} \rho_{\mathrm{f,out}} q_{\mathrm{f,out}} T_{\mathrm{f,out}}}{V_{\mathrm{f}} \rho_{\mathrm{f}} c_{p_{\mathrm{f}}}} + \frac{U_{\mathrm{f}} S_{\mathrm{f}} (T - T_{\mathrm{f}})}{V_{\mathrm{f}} \rho_{\mathrm{f}} c_{p_{\mathrm{f}}}} - \frac{U_{\mathrm{jct}} S_{\mathrm{jct}} (T_{\mathrm{f}} - T_{\mathrm{amb}})}{V_{\mathrm{f}} \rho_{\mathrm{f}} c_{p_{\mathrm{f}}}} \tag{2.19}$$

where $q_{\mathrm{f,in}}$ and $q_{\mathrm{f,out}}$ are, respectively, the volumetric flow rate of the heating fluid entering and leaving the heating system ($\mathrm{m^3\,s^{-1}}$) while T_{amb} is the ambient air temperature (K). Subscripts in and out have the same meaning for all the quantities in Eqn. 2.19. T_{f} is a chosen average temperature for the heating fluid. If the system is modeled as a heat exchanger, the logarithmic mean temperature difference has to be considered.

The thermal resistances relative to Eqn. 2.19 are:

$$R_{\mathrm{th,f}}^{-1} = \frac{1}{U_{\mathrm{f}}S_{\mathrm{f}}} = \frac{1}{h_{\mathrm{mix}}S_{\mathrm{mix}}} + \frac{\ln\left(\frac{r_{\mathrm{w}}+\delta_{\mathrm{w}}}{r_{\mathrm{w}}}\right)}{2\pi\lambda_{\mathrm{w}}L_{\mathrm{w}}} + \frac{1}{h_{\mathrm{f}}S_{\mathrm{ew}}} \tag{2.20}$$

$$R_{\mathrm{th,jct}}^{-1} = \frac{1}{U_{\mathrm{jct}}S_{\mathrm{jct}}} = \frac{1}{h_{\mathrm{air}}S_{\mathrm{ins}}} + \frac{\ln\left(\frac{r_{\mathrm{ew}}+\delta_{\mathrm{ew}}+\delta_{\mathrm{ins}}}{r_{\mathrm{ew}}+\delta_{\mathrm{ew}}}\right)}{2\pi\lambda_{\mathrm{ins}}L_{\mathrm{ew}}} + \frac{\ln\left(\frac{r_{\mathrm{ew}}+\delta_{\mathrm{ew}}}{r_{\mathrm{ew}}}\right)}{2\pi\lambda_{\mathrm{ins}}L_{\mathrm{ew}}} + \frac{1}{h_{\mathrm{f}}S_{\mathrm{ew}}} \tag{2.21}$$

Subscript ins stands for thermal insulator while ew for external reactor wall.

In general, the heat transfer design for agitated vessels is not trivial. In the case at hand here, if one chose a jacketed solution, the temperature range would be conceivably small. Even though that would simplify the modeling as the overall heat transfer coefficient for the external side could be assumed constant and an average jacket temperature can be employed for determining cooling/heating time, the internal, process-side has to be considered as well. This translates in the need of turbulent heat transfer correlations. The most common mathematical expressions for determining the appropriate heat transfer coefficient when working with jacketed vessels or immersed tubes and coils hinge on the use of adimensional groups like Reynolds, Nusselt and Prandtl numbers (most correlations take the “Nusselt form”), linked through empirical exponent coefficients. Moreover, the overall disquisition prefigures the usage of correction and fouling factors. Typical examples of such correlations are given by the Dittus-Boelter equation, the Colburn one or the Sieder-Tate equation (Bin et al., 2009).

Finally, as reactors are not fully wrapped in heating systems and insulators, losses from the top and the bottom need to be accounted for, as shown in Eqn. 2.15. In particular,

$$\dot{Q}_{\mathrm{loss,t}} = U_{\mathrm{t}}S_{\mathrm{t}}(T - T_{\mathrm{amb}}) = \frac{T - T_{\mathrm{amb}}}{R_{\mathrm{th,t}}} \tag{2.22}$$

$$\dot{Q}_{\mathrm{loss,b}} = U_{\mathrm{b}}S_{\mathrm{b}}(T - T_{\mathrm{amb}}) = \frac{T - T_{\mathrm{amb}}}{R_{\mathrm{th,b}}} \tag{2.23}$$

S_{t} and S_{b} are the surface area of the reactor lid and of its bottom respectively (m^2). Moreover,

$$R_{\mathrm{th,t}}^{-1} = \frac{1}{U_{\mathrm{t}}S_{\mathrm{t}}} = \frac{\delta_{\mathrm{t}}}{\lambda_{\mathrm{w}}S_{\mathrm{ti}}} + \frac{1}{h_{\mathrm{li}}S_{\mathrm{ti}}} + \frac{1}{h_{\mathrm{lo}}S_{\mathrm{to}}} \tag{2.24}$$

$$R_{\mathrm{th,b}}^{-1} = \frac{1}{U_{\mathrm{b}}S_{\mathrm{b}}} = \frac{\delta_{\mathrm{b}}}{\lambda_{\mathrm{w}}S_{\mathrm{bi}}} + \frac{1}{h_{\mathrm{bi}}S_{\mathrm{bi}}} + \frac{1}{h_{\mathrm{bo}}S_{\mathrm{bo}}} \cong \frac{\delta_{\mathrm{b}}}{\lambda_{\mathrm{w}}S_{\mathrm{bi}}} + \frac{1}{h_{\mathrm{bo}}S_{\mathrm{bo}}} \tag{2.25}$$

being δ_{t} and δ_{b} the thicknesses of the lid and of the floor respectively (m), h_{li} the convective heat transfer coefficient between the mixture and the inner surface of the lid ($\mathrm{W\,m^{-2}\,K^{-1}}$), h_{lo} the convective heat transfer coefficient between the outer surface of the lid and ambient air, h_{bi} the convective heat transfer coefficient between the mixture and the inner surface of the reactor bottom and h_{bo} the convective heat transfer coefficient between the outer surface of the reactor bottom and ambient temperature. The terms S_{ti} and S_{to} represent the inside and outside areas of the lid (m^2, while S_{bi} and S_{bo} the equivalents for the bottom of the reactor.

The approximation in Eqn. 2.25 is due to the fact that, when stirring is applied inside the reactor, thermal energy is carried from the mixture to the reactor bottom via forced convection which results are much more noteworthy than the heat transfer mode between the reactor floor and the surroundings at ambient temperature, i.e. natural convection (Burdock et al., 2008). To actually perform the computation, Eqn. 2.26 comes in handy as it describes the convective heat transfer coefficient for a heated plate facing downward in natural convection conditions (Holman, 2009):

$$h_{\mathrm{bo}} = 0.59 \left(\frac{T_{\mathrm{b}} - T_{\mathrm{amb}}}{L_{\mathrm{b}}} \right)^{1/4} \tag{2.26}$$

T_{b} is the temperature of the outside surface of the reactor bottom (K) and L_{b} is the diameter of the reactor floor (m). Similarly, the relation for a heated plate facing upward helps evaluating h_{lo}:

$$h_{\mathrm{lo}} = 1.32 \left(\frac{T_{\mathrm{l}} - T_{\mathrm{amb}}}{L_{\mathrm{t}}} \right)^{1/4} \tag{2.27}$$

being T_{l} the temperature of the outside surface of the lid (K) and L_{t} the diameter of the reactor lid (m).

2.2 Simulation of the polyphenols extraction process

2.2.1 Data-analysis and estimation of the extraction parameters

The global kinetics has been evaluated through numerical interpolation techniques both for the extraction process performed using olive pomace as dry basis and for that produced using grape pomace. In fact, although the latter is not used in the research presented in this chapter, the scale-up of the process discussed in Chapter 4 will require knowledge of the kinetic parameters and, since the method for their estimation is the one described below, it is preferred do not split the discussion.

Experimental tests were carried out until reaching residence times greater than the optimal extraction time in order to detect the maximum achievable concentration of polyphenols. This value is used as guess value for parameters estimation. Obviously, both the pseudo first-order and the Peleg kinetic models cannot describe the mechanisms related to polyphenols degradation, after the optimal extraction time.

Kinetics parameters estimation was carried out under the assumption of explicit exact models. This means that the adopted objective function represents the estimated experimental error, regardless model uncertainty. In case of chemical kinetics parameters, a Maximum Likelihood method reduces, under some assumptions (Catania et al., 2006), to weighted or non-weighted least-squares. They represent a different choice about the experimental error, often due to different analytic instrumentation or experimental conditions: by weighted least squares a multiplicative error is used, i.e. a residual proportional to the measured concentration is assigned. For this study, it consists in keeping more accuracy in measuring low levels of polyphenols. In non-weighted least-squares an additive error is adopted, and its meaning is to keep the same characteristics of random error on all the measures of concentration. Since polyphenols concentrations were measured by multiple procedures, each of them with its proper experimental error, we supposed an additive experimental error.

By considering the pseudo-first order extraction rate described by Eqn. 2.11 with $x_{\mathrm{TP},0} = 0$,

$$x_{\mathrm{TP}}(t) = x_{\mathrm{TP,s0}}^{T_{\max}} \alpha (1 - \exp(-Kt)) \tag{2.28}$$

and where

$$\alpha = \frac{x_{\mathrm{TP,s0}}^{T}}{x_{\mathrm{TP,s0}}^{T_{\max}}} \tag{2.29}$$

the values of the two parameters K and α were determined at fixed temperatures by the non-weighted least squares method. Least squares were applied to data obtained from the quasi-isothermal DSTR lab-scale reactor.

Since $x_{\mathrm{TP,s0}}$ for each sample is unknown, the maximum value of $x_{\mathrm{TP}}(t)$ reached during polyphenols extraction in the experimental campaign was chosen as its estimate. In this way, the parameter α could represent the effect of limiting phenomena on the extraction process due to temperature.

The Levenberg-Marquardt (NLS-LMA) algorithm was used and results are reported in 2.1 and in Figure 2.2 and Figure 2.3.

Table 2.1 Pseudo-first order extraction rate: estimated parameters at different temperatures. Case of olive pomace (O.P.), dry mass : solvent ratio = 1 : 10 (Neviani et al., 2019).

Reactants	K (s^{-1})	T (°C)	$x_{TP,s0}^{T}$ ($mg_{TP}\ g_{DM}{}^{-1}$)	α (-)	$x_{TP,s0}^{T_{max}}$ ($mg_{TP}\ g_{DM}{}^{-1}$)	$\mathscr{E}$ (-)	R^2 (-)
O.P. & methanol	0.0011	100	11.6494	0.2577	45.2	0.0376	0.7404
	0.0015	150	23.0522	0.5100	45.2	0.0257	0.7719
	5.297×10^{-4}	180	42.1125	0.9317	45.2	0.0672	0.7981
O.P. & ethanol - H_2O (50:50)	7.921×10^{-7}	120	14.7667	0.7310	20.2	0.0325	0.9654

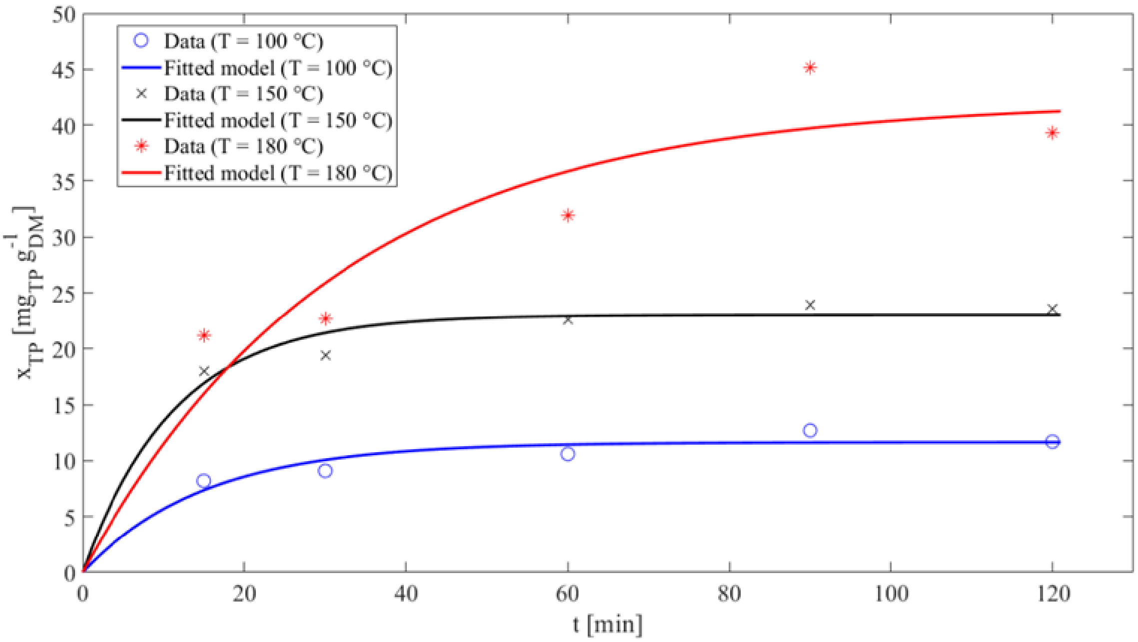

Fig. 2.2 Pseudo-first order extraction rate using olive pomace and methanol at different extraction temperatures (Neviani et al., 2019).

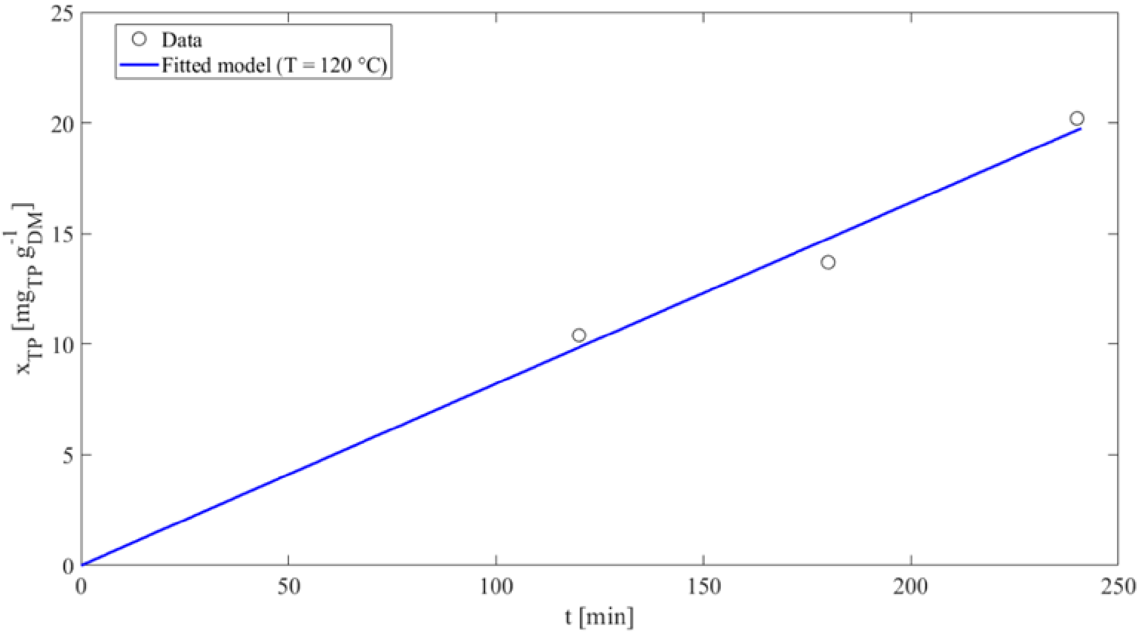

Fig. 2.3 Pseudo-first order extraction rate using olive pomace and ethanol - H_2O (50:50) at different extraction temperatures (Neviani et al., 2019).

Mean error $\mathscr{E}$ was defined as:

$$\mathscr{E} = \frac{1}{n}\sqrt{\sum_{i=1}^{n}\left(\frac{x_{\mathrm{TP}}^{\mathrm{obs}}(t_i) - x_{\mathrm{TP}}^{\mathrm{model}}}{x_{\mathrm{TP}}^{\mathrm{obs}}}\right)^2} \tag{2.30}$$

and R^2 is the coefficient of determination.

The obtained results can be considered good for the experimental lab-scale tests conducted with both methanol and water-ethanol as solvents. It should be noted that each experimental test is interrupted every time that polyphenols concentration is measured in the liquid phase at a selected experimental time; for this reason, the number of data is limited for each run. The use of this limited number of data to estimate kinetics is justified by the main goal of our study, that was to define the best extraction time in order to design the residence time in the continuous unit. Of course, uncertainty on kinetic parameters was embedded into simulations taking into account the results of the minimum least square regression.

The extraction rate constant K does not always show the dependence on temperature described by the Arrhenius law, but since K is an effective extraction constant, temperature dependence is also encountered in the parameter α.

The experimental data were then also fitted by means of the Peleg model, expressed by Eqn. 2.12. Table 2.2, Fig. 2.4 and Fig. 2.5 show the respective results.

Table 2.2 Peleg extraction rate: estimated parameters at different temperatures. Case of olive pomace (O.P.), dry mass : solvent ratio = 1 : 10 (Neviani et al., 2019).

Reactants	T (s g_{DM} $mg_{TP}{}^{-1}$)	K_1 (g_{DM} $mg_{TP}{}^{-1}$)	K_2 (-)	$\mathscr{E}$ (-)	R^2 (-)
O.P. &	100	47.1011	0.0768	0.0261	0.8550
&	150	15.7429	0.0400	0.0143	0.9293
methanol	180	33.9826	0.0192	0.0581	0.8212
O.P. & ethanol - H_2O (50:50)	120	766.8659	-0.000029	0.0343	0.9670

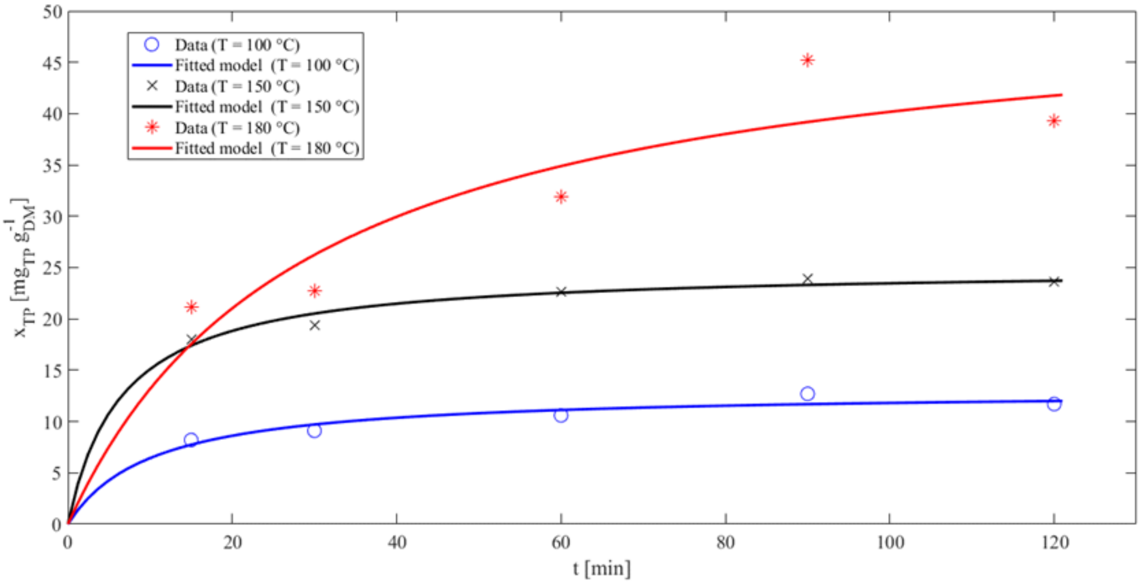

Fig. 2.4 Peleg extraction rate using olive pomace and methanol at different extraction temperatures (Neviani et al., 2019).

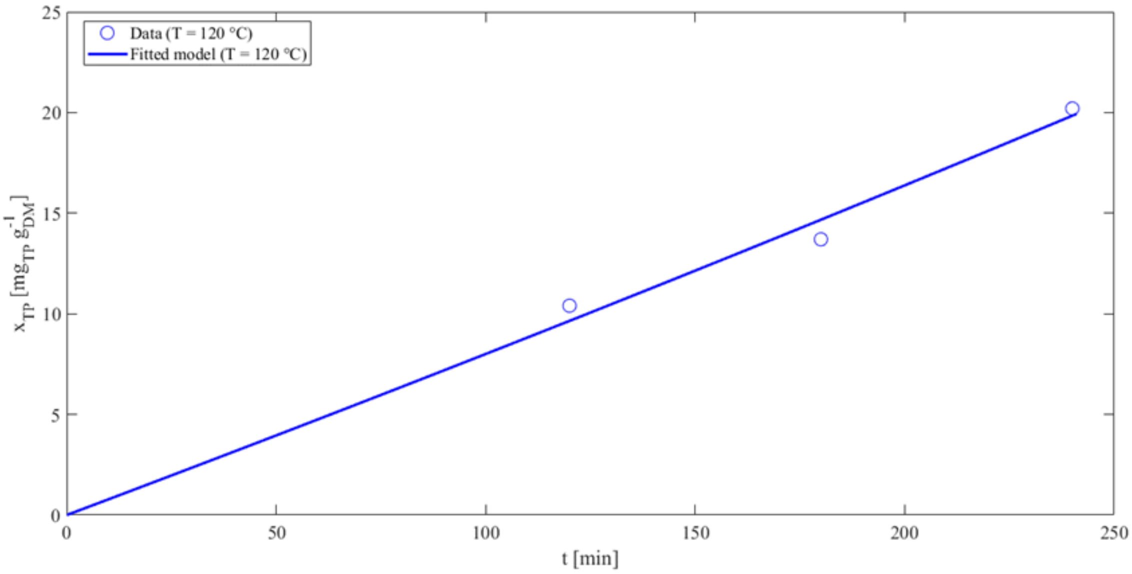

Fig. 2.5 Peleg extraction rate using olive pomace and ethanol - H_2O (50:50) at different extraction temperatures (Neviani et al., 2019).

Also in this case the obtained results can be considered good for the experimental lab-scale tests conducted with both methanol and water-ethanol as solvent.

Since the Peleg model contains the two constants K_1 and K_2, it also succeeds in the description of polyphenols extraction from olive pomace by ethanol - H_2O (50:50): the algorithm reaches the minimum for a value of K_2 equal to zero. As Peleg's capacity constant K_2 relates to maximum extraction yield, i.e. total polyphenols at equilibrium, this means that the experimental test of polyphenols extraction from olive pomace by ethanol - H_2O (50:50) at $T = 120$ °C is very far from the equilibrium and process temperature should be increased. Due to the fact that the experimental tests at $T = 180$ °C (runs $17 \div 20$ of Table A.1) were not sufficient to estimate kinetics, some new experimental tests have been carried out.

As finally regards the dependence of the constants K_1 and K_2 on temperature, by looking at Table 2.2 it can be observed that constant K_2 is always decreasing with increasing temperature, while constant K_1 has a minimum at $T = 150$ °C for olive pomace and methanol. The interpretation of this fact could be very interesting in process scale-up: since K_1 relates to the extraction rate at the very beginning, where $v_{e0} \rightarrow K_1^{-1}$, this means that $T = 150$ °C is the optimal temperature for polyphenols extraction from olive pomace with methanol and higher temperatures do not increase extraction rate.

2.2.1.1 Effects of solvents on polyphenols extraction rate

Methanol is probably the best solvent to be used in polyphenols extraction. Nevertheless, since ethanol is not toxic, it was used as a pure solvent or mixed with water. Even in spite of lower extraction yields, its use could be economically advantageous for the elimination of the product purification costs. Furthermore, experimental results on the analyzed process shows a noteworthy difference in terms of required pressure: about 17 bar (or 1.7×10^6 Pa in SI units) when using the ethanol - water blend versus about 30 bar when employing methanol. Results from extraction tests conducted at different temperatures and different ethanol - water ratios are summarized in Fig. 2.6.

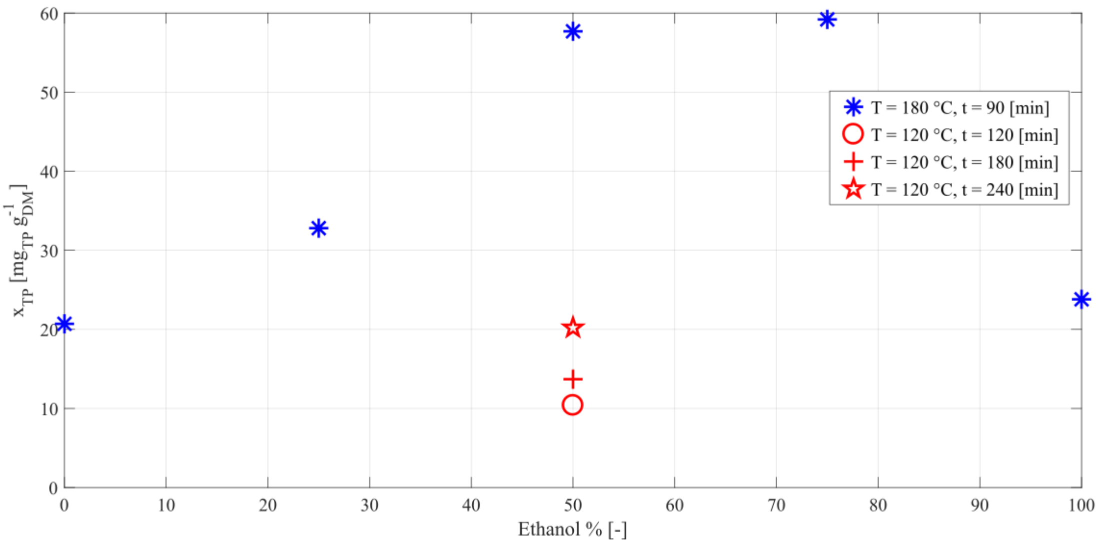

Fig. 2.6 Effects of solvents ratio on polyphenols extraction (Neviani et al., 2019).

Tests at $T = 180$ °C (at higher temperatures the product degrades) were conducted in order to define the maximum extraction yield with the proposed solvent ratio. It is easily observable that the best result is for ethanol - water (75:25). On the other hand, the value of x_{TP} for ethanol - water (50:50) is only slightly less. It follows that, by taking into account ethanol costs, the optimal solvent ratio is certainly (50:50).

Tests carried out with solvent ratio (50:50) (red dots in Fig. 2.6) are those from which data used in Fig. 2.3 and Fig. 2.5 were learnt and confirm what stated in the previous paragraph: the three points are close enough to each other but away from the blue dot. This means that temperature should be increased in order to reach acceptable yields. These considerations suggested to acquire more data. Hence, some new experimental tests for polyphenols extraction with the use of (50:50) ethanol - H_2O at $T = 180$ °C were conducted.

Table 2.3 Extraction parameters and mean error estimate for olive pomace and ethanol-H_2O (50:50) relative to the experimental run at $T = 180\,°C$ (Neviani et al., 2019).

Reactants	K [s^{-1}]	$x^{T}_{TP,s0}$ [$mg_{TP}\ g_{DM}^{-1}$]	α	$x^{T_{max}}_{TP,s0}$ [$mg_{TP}\ g_{DM}^{-1}$]	ε	R^2	T [°C]
Olive pomace & ethanol/H_2O (50:50). Dry biomass=4[g], solvent=40[ml]	$3.747 \cdot 10^{-4}$	61.2	0.9162	66.8	0.0264	0.8194	180
	K_1 [$s\ g_{DM}\ mg_{TP}^{-1}$]		K_2 [$g_{DM}\ mg_{TP}^{-1}$]		ε	R^2	T [°C]
	27.9699		0.0109		0.0292	0.7777	180

Extraction rates, estimated kinetic parameters and mean errors are reported in Figure 2.7, Figure 2.8 and Table 2.3.

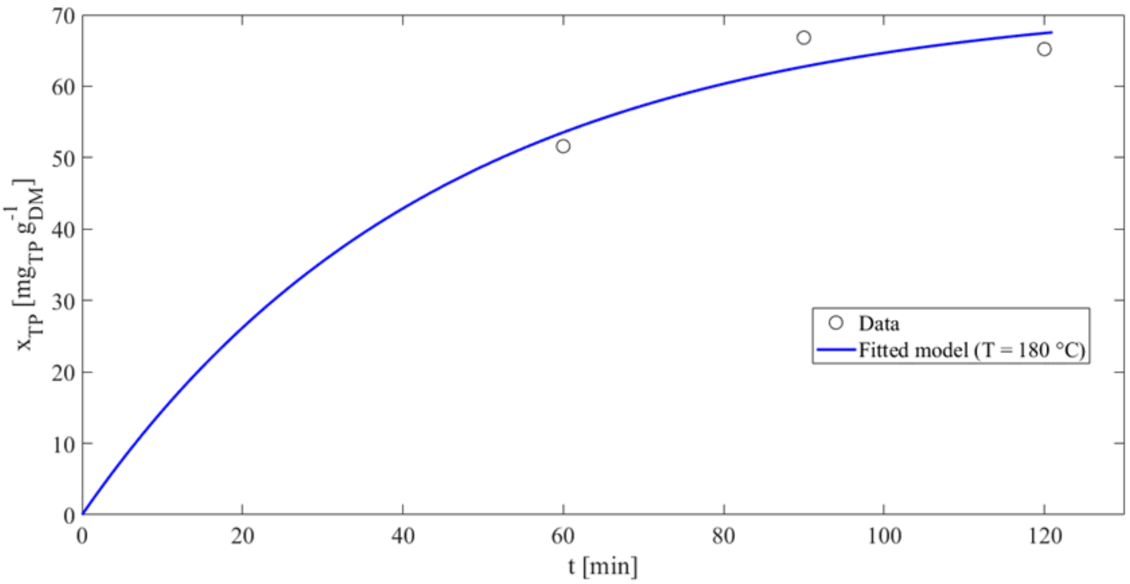

Fig. 2.7 Pseudo-first order extraction rate using olive pomace and ethanol-H_2O(50:50) at $T = 180\,°C$ (Neviani et al., 2019).

By observing the new experimental data (or by looking at Fig. 2.8), one can infer that, for $T = 180$ °C, an extraction time of 90 minutes suffices as after 120 minutes total polyphenols are diminished.

Hence, the following operating conditions are chosen: $T = 180$ °C, $t = 90$ min, ratio between solvent (ethanol - water (50:50)) and initial raw material feed concentration of $100\,g\,l^{-1}$. Some refinements in design optimal values of operating variables can be carried out by using Response Surface Methodology (RSM) as in (Aboelazayem et al., 2017).

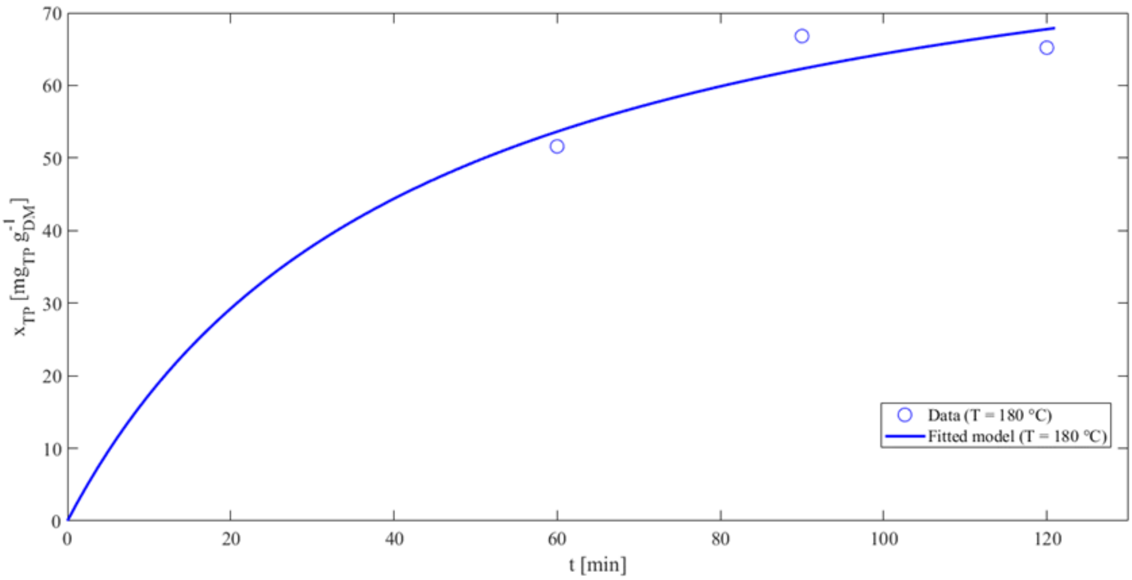

Fig. 2.8 Peleg extraction rate using olive pomace and ethanol-H_2O(50:50) at $T = 180\,°C$ (Neviani et al., 2019).

Table 2.4 Pseudo-first order extraction rate: estimated parameters at different temperatures. Case of grape pomace (G.P.), dry mass:solvent ratio = 1:5.

Reactants	K (s^{-1})	T (°C)	$x^{T}_{TP,s0}$ (mg_{TP} $g_{DM}{}^{-1}$)	α (-)	$x^{T_{max}}_{TP,s0}$ (mg_{TP} $g_{DM}{}^{-1}$)
G.P. & methanol	9.383×10^{-4}	30	10.8975	0.1563	69.7
	7.707×10^{-4}	120	34.7717	0.4989	69.7
	8.398×10^{-4}	150	61.8032	0.8867	69.7

2.2.1.2 Estimation of extraction parameters for the process using grape pomace

According to the same procedure followed for the extraction process employing olive pomace, the extraction kinetic constants were estimated for the very same process carried out using grape pomace as the dry matter basis and methanol as the solvent. These choices are motivated in Section 4.4.

On another note, in this case it was decided to resort only to the pseudo first-order kinetic model. In fact, the chosen kinetics matches satisfactorily the experimental data and, for the purpose of the process of scale-up, the choice of this model do not conceptually affect the discussion.

In conclusion, the results are summarized in Table 2.4 whilst extraction rate profiles are shown in Figure 2.9.

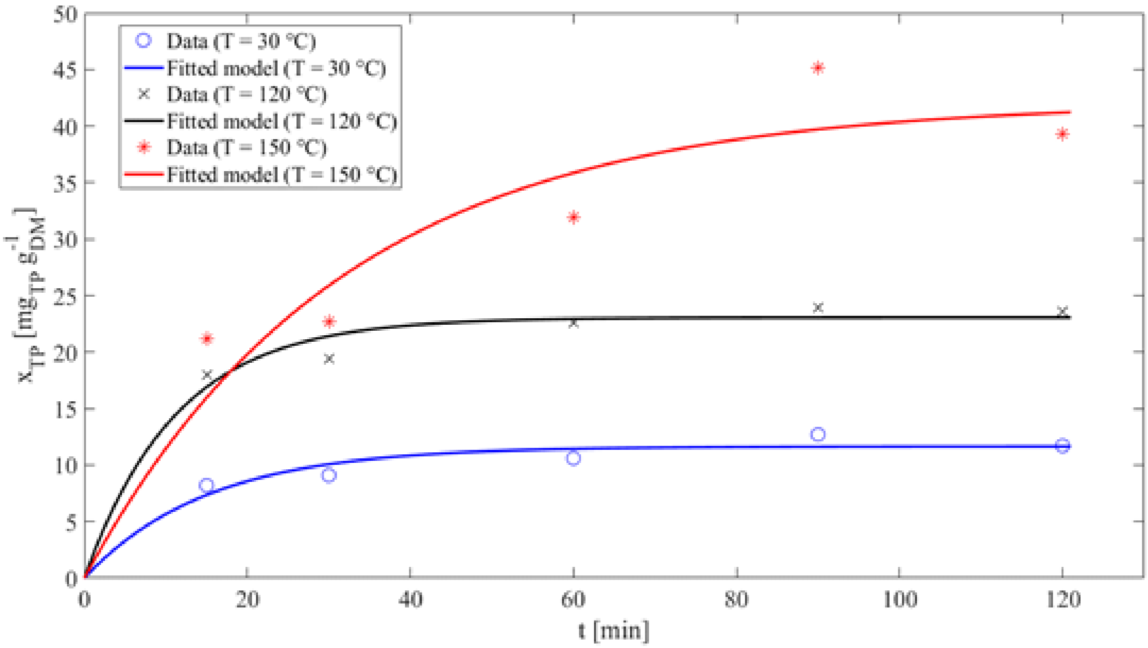

Fig. 2.9 Pseudo-first order extraction rate using grape pomace and methanol at different extraction temperatures.

2.2.2 Development of the simulation model

The system was described by four ordinary differential equations representing:

I. the total material balance of the liquid phase transformed in a volume balance, since the fluid (slurry) is considered incompressible and a regulation system that uses nitrogen is adopted to keep a constant pressure in the reactor (Eqn. 2.31);

II. the material balance for total polyphenols (Eqn. 2.32);

III. the energy balance of the reacting volume (Eqn. 2.33);

IV. the energy balance of the heating system (Eqn. 2.33).

plus one algebraic nonlinear equation describing the extraction rate (Eqn. 2.35).

The pilot reactor of Figure 2.1, equipped with resistor wires and a similar jacketed reactor that uses mineral oil as heating fluid was simulated. In the former case $\dot{Q}_{\mathrm{syst}}$ in Eqn. 2.33 is calculated by Eqn. 2.16, while equation (34) becomes an algebraic equation from which the fixed temperature of the heating system $T_{\mathrm{hs}} = T_{\mathrm{rw}}$ can be calculated (auto-regulating wires at constant temperature).

For the jacketed reactor $\dot{Q}_{\mathrm{syst}}$ in Eqn. 2.33 is computed by Eqn. 2.18 and $T_{\mathrm{hs}} = T_{\mathrm{f}}$ in both Eqn. 2.33 and Eqn. 2.34.

The ODEs system is:

$$\frac{\mathrm{d}V}{\mathrm{d}t} = q_{\mathrm{in}} - q_{\mathrm{out}} \tag{2.31}$$

$$\frac{\mathrm{d}x_{\mathrm{TP}}}{\mathrm{d}t} = q_{\mathrm{in}} \frac{x_{TP,in}}{V_{\mathrm{r}}} - q_{\mathrm{out}} \frac{x_{TP,out}}{V_{\mathrm{r}}} + \tilde{v}_e \tag{2.32}$$

$$\frac{\mathrm{d}T}{\mathrm{d}t} = \frac{q_{\mathrm{in}} c_{p_{\mathrm{in}}} \rho_{\mathrm{in}} T_{\mathrm{in}}}{V_{\mathrm{r}} \rho c_p} - \frac{q_{\mathrm{out}} c_{p_{\mathrm{out}}} \rho_{\mathrm{out}} T_{\mathrm{out}}}{V_{\mathrm{r}} \rho c_p} - \frac{\dot{Q}_{\mathrm{syst}}}{V_{\mathrm{r}} \rho c_p} - \frac{\dot{Q}_{\mathrm{loss,t}}}{V_{\mathrm{r}} \rho c_p} - - \frac{\dot{Q}_{\mathrm{loss,b}}}{V_{\mathrm{r}} \rho c_p} \tag{2.33}$$

$$\frac{\mathrm{d}T_{\mathrm{hs}}}{\mathrm{d}t} = \frac{q_{\mathrm{f,in}} c_{p_{\mathrm{f,in}}} \rho_{\mathrm{f,in}} T_{\mathrm{f,in}}}{V_{\mathrm{f}} \rho_{\mathrm{f}} c_{p_{\mathrm{f}}}} - \frac{q_{\mathrm{out}} c_{p_{\mathrm{out}}} \rho_{\mathrm{out}} T_{\mathrm{out}}}{V_{\mathrm{f}} \rho_{\mathrm{f}} c_{p_{\mathrm{f}}}} - \frac{\dot{Q}_{\mathrm{syst}}}{V_{\mathrm{f}} \rho_{\mathrm{f}} c_{p_{\mathrm{f}}}} - \frac{U_{\mathrm{jct}} S_{\mathrm{jct}} (T_{\mathrm{hs}} - T_{\mathrm{amb}})}{V_{\mathrm{f}} \rho_{\mathrm{f}} c_{p_{\mathrm{f}}}} \tag{2.34}$$

where x_{TP} is the mass fraction of total polyphenols in liquid phase and

$$\tilde{v}_e = \frac{K_1(T)}{(K_1(T) + K_2(T)t)^2} \tag{2.35}$$

To obtain the total polyphenols mass concentration c_{TP} ($\mathrm{mg_{TP}\ m^{-3}}$), it is sufficient to use the Eqn. 2.36:

$$c_{\mathrm{TP}} = \frac{x_{\mathrm{TP}}}{V_{\mathrm{r}}} m_{\mathrm{DM}} \tag{2.36}$$

where m_{DM} is the dry mass ($\mathrm{g_{DM}}$) dispersed in the slurry.

2.2.2.1 Parameter values used in simulation

The volume and area of the pilot-scale reactor are supplied by its design data. It has a total volume of 15 L, so we considered a theoretical reacting volume (slurry = liquid extracting phase plus solid phase) $V_{\mathrm{r}} = 0.012\ \mathrm{m}^3$, with the remaining volume being occupied by nitrogen. Lid and bottom surfaces are equal to $0.0314\ \mathrm{m}^2$, whilst the heat transfer area S_{mix} inside the reactor amounts to $0.2513\ \mathrm{m}^2$. $S_{\mathrm{w}} = 0.2639\ \mathrm{m}^2$, $S_{\mathrm{ew}} = 0.3267\ \mathrm{m}^2$ and $S_{\mathrm{ins}} = 0.3292\ \mathrm{m}^2$.

The initial temperature of the fluid inside the reactor is assumed equal to 25 °C, so as the external air temperature. The initial dry pomace was 1200 g in 12 L of total solvent mixture.

The values of c_p for each solvent were identified through empirical correlations (Perry et al., 2007) and DIPPR105 equation was used for evaluating liquid density of pure components:

$$\rho = \frac{\mathrm{A}}{\mathrm{B}^{1+\left(1-\frac{T}{\mathrm{C}}\right)^{\mathrm{D}}}} \tag{2.37}$$

in which A, B, C and D are empiric constants relative to the considered substance.

The contribute of the solid phase on both c_p and ρ was not considered and this assumption must be validated. Values for a given solvent mixture are evaluated at a certain temperature by weighting the different solvent values.

We considered two possibilities for the pilot-scale reactor: equipped with resistor wires or jacketed and heated by a mineral oil in liquid phase. The reactor of Figure 2.1 refers to the first case. It is made in stainless steel (AISI 316) with a wall thickness $\delta_{\mathrm{w}} = 0.005\,\mathrm{m}$, whereas the thickness $\delta_{\mathrm{ins,w}}$ of the magnesium oxide layer wrapped around each coil is 0.001 m and the one of the external insulating material is $\delta_{\mathrm{ins}} = 0.030\,\mathrm{m}$.

A thermal conductivity of stainless steel of $\lambda_{\mathrm{w}} = 16\,\mathrm{W\,m^{-1}\,K^{-1}}$ at 25 °C was considered, whilst λ_{ins} of the mineral wool composing the insulating layer is about $0.04\,\mathrm{W\,m^{-1}\,K^{-1}}$ at the same temperature of 25 °C. Thermal conductivity $\lambda_{\mathrm{ins,w}}$ of the magnesium oxide ranges between $30\,\mathrm{W\,m^{-1}\,K^{-1}}$ and $60\,\mathrm{W\,m^{-1}\,K^{-1}}$. Given the data relative to thermal conductivities of those materials at different temperature, linear interpolation was adopted inside the simulator to have values at intermediate temperatures.

In order to compute the overall heat transfer coefficient of the reactor, the convective heat transfer coefficients h_{mix} must be defined. It depends on variables such as the surface geometry, the nature of the fluid motion, the bulk fluid velocity and the properties of the fluid. As mentioned before, some form of Nusselt correlation has to be employed in order to determine it. In the simulation, a value of $368\,\mathrm{W\,m^{-2}\,K^{-1}}$ was adopted.

In case of a similar but jacketed reactor the enthalpy balance of the jacket must be considered as well. Consequently, h_{f} and h_{air} have to be defined. h_{air} was found in literature (it usually ranges between $10\,\mathrm{W\,m^{-2}\,K^{-1}}$ and $100\,\mathrm{W\,m^{-2}\,K^{-1}}$) while a suitable value of $h_{\mathrm{f}} = 770\,\mathrm{W\,m^{-2}\,K^{-1}}$ was assumed by considering natural convection and the properties of commonly used mineral oils.

A suitable operating temperature T_{rw} of the coils equal to $220\,^{\circ}\mathrm{C} = 493\,\mathrm{K}$ was designed. On the other hand, in presence of heating fluid, initial operating $T_{\mathrm{f,in}}$ was chosen to be 265 °C. Said value was inferred by observing how, after imposing equilibrium with the reactor for $T = 180\,^{\circ}\mathrm{C}$, $T_{\mathrm{f,out}} = 521\,\mathrm{K} = 248\,^{\circ}\mathrm{C}$ while the fluid flowrates $q_{\mathrm{f,in}} = q_{\mathrm{f,out}}$ are equal to $6.098 \times 10^{-5}\,\mathrm{m^3\,s^{-1}} = 3.7\,\mathrm{L\,min^{-1}}$.

Simulations were performed with a PI controller on the reactor temperature, using respectively the temperature of the coils or the warming fluid flowrate as the manipulated variable.

2.2.3 Scale-up results via simulation model

As a very important constraint for the correct scale-up regards the experimental procedure conducted at lab-scale, all the experimental data used to estimate kinetics were taken in isothermal condition. This means that time is equal to zero when the DSTR lab-scale reactor is at the requested temperature, reported in Table A.1. Since during the heating of the lab-scale reactor some polyphenols extraction can occur, it is important that the heating time of the pilot DSTR reactor is maintained equal to the corresponding heating time in the lab-scale reactor, otherwise the estimated kinetics cannot be extended at the pilot scale. This heating time varied from 22 to 30 min, respectively for runs at $T = 100\,°\mathrm{C}$ and $T = 180\,°\mathrm{C}$. The first step of scale-up was the simulation of the lab scale DSTR, in order to validate the dynamic model with the experimental data. In particular, the robustness of the interpolation functions adopted for describing the variation with temperature of the chemical-physical parameters (ρ, c_p) and the estimated parameters (K_1 and K_2) was checked.

The second step was the simulation of the pilot-scale DSTR. A filling time of about 5 min was obtained with the design input flowrate of $3\,\mathrm{L\,min^{-1}}$ (at completely open valve), by considering a parabolic valve opening model. A relay block was used to simulate the valve closure.

The resistor wires heating system performed as expected, reaching the operating temperature of 180 °C after 30 min. A relay block was used to simulate the stop of the heating transient. After this time, the complete pilot DSTR dynamic model can start (with also mass balances running), and the PI model is inserted in the simulator. A simulation with the operating PI (Proportional–Integral) controller also during the heating transient is shown in Fig. 2.10. The heating time in this case is greater than in the previous one since the controller varies the temperature of the resistor wires during the transient.

Since the reactor discharge cannot be performed at high temperature and pressure, the cooling transient of the batch reactor was simulated. The time to reach ambient temperature without a fast cooling system was about 28 min.

A Pseudo Random Sequence (PRS) was used to simulate noise in the operating variables (input flowrate and wires temperature) during the filling and heating transients with extremes at $\pm 20\%$ of the target values. No particular problems were detected during transients and the variation in both heating and filling times was not appreciable.

Errors in the estimated values of the Peleg's constants K_1 and K_2 were simulated with Monte Carlo sequences, taking into account both the error values reported in Table 2.3 and the errors introduced in the model adopted to compute the dependence of the Peleg's constants with temperature (obtained by interpolation of the few experimental data). The minimum value of the yield obtained after 90 minutes was $60\,\mathrm{mg_{TP}\,g_{DM}^{-1}}$.

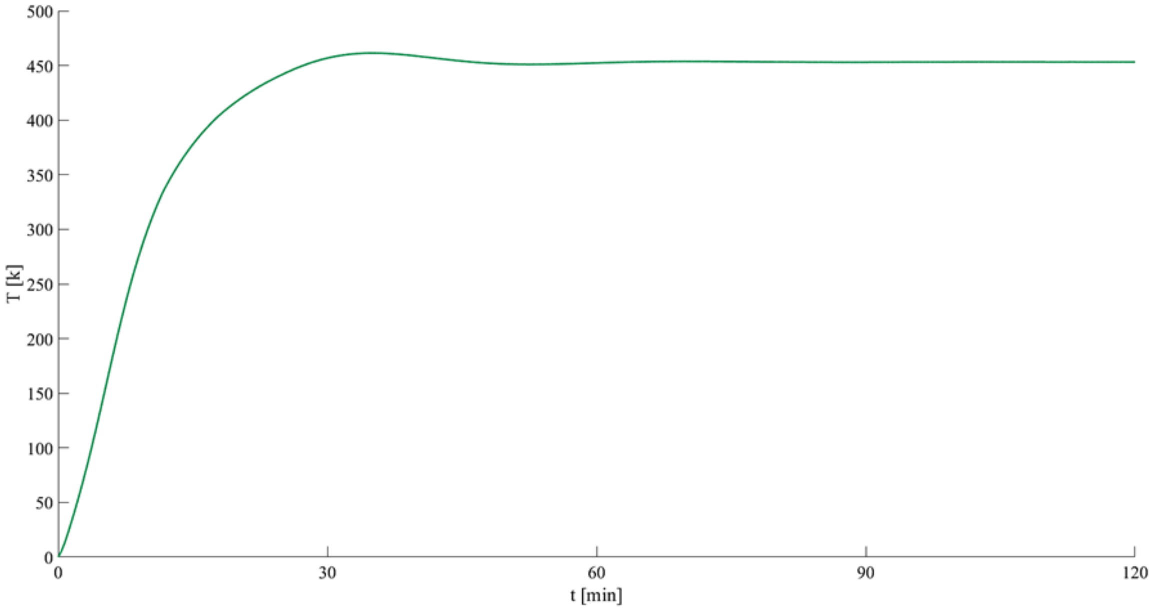

Fig. 2.10 Temperature trend of the mixture inside the pilot reactor operated as a batch and heated through resistor wires with PI controller (Neviani et al., 2019).

As the residence time is imposed to be $\tau_r = 90\,\text{min}$, the total polyphenols yield for batch operation at pilot scale was confirmed as $60\,\text{mg}_{\text{TP}}\ \text{g}_{\text{DM}}^{-1}$. That means a production of about 72 g of polyphenols for each batch, for a total of about $216\,\text{gd}^{-1}$ of polyphenols produced for a pilot scale production without turnover.

Simulation of the jacketed pilot DSTR was carried out by testing different commercial heating fluids (Paratherm$^{\text{TM}}$ NF heat transfer fluid, an hydrotreated mineral oil with high naphthenic content, DelcoTerm®S DbT, a synthetic diathermic oil and DelcoTerm®M 32, a paraffinic based mineral oil).

Input temperature and operating jacket flowrate were chosen, by considering the fluid heat transport properties, so as the heating time of the pilot DSTR reactor, which is equal to the corresponding heating time of the lab-scale reactor. A PID (Proportional–Integral-Derivative) controller manipulating the jacket flowrate was tested.

The third step was the simulation of the pilot reactor operated in continuous. Since we know that the total of the simulated filling + heating + cooling + discharging times for the pilot DSTR was about 70 min, we started the pilot CSTR simulation by choosing an apparent residence time equal to the pilot-DSTR operating time (residence + total $= 90+70$) residence time, keeping in mind that this time can be decreased till the pilot-DSTR residence time.

The evaluated minimum flowrate of the fluid (slurry) in input at the pilot-CSTR for this limit residence time was:

$$q(\tau_r = 90 \ \ \mathrm{min}) = \frac{V_\mathrm{r}}{\tau_r} = 2.222 \times 10^{-6} \ \ \mathrm{m^3 s^{-1}} \tag{2.38}$$

All the input variables, i.e. incoming reactor flowrate and temperature, outcoming reactor flowrate, input and output temperature of the heating fluid, were perturbed with PRS signals (Fig. 2.11). This translates in an oscillating value of the reacting volume resulting from Eqn. 2.31 and showed in Fig. 2.12. The use of a PI controller on the incoming flowrate, with V_r as the controlled variable, was not considered as necessary.

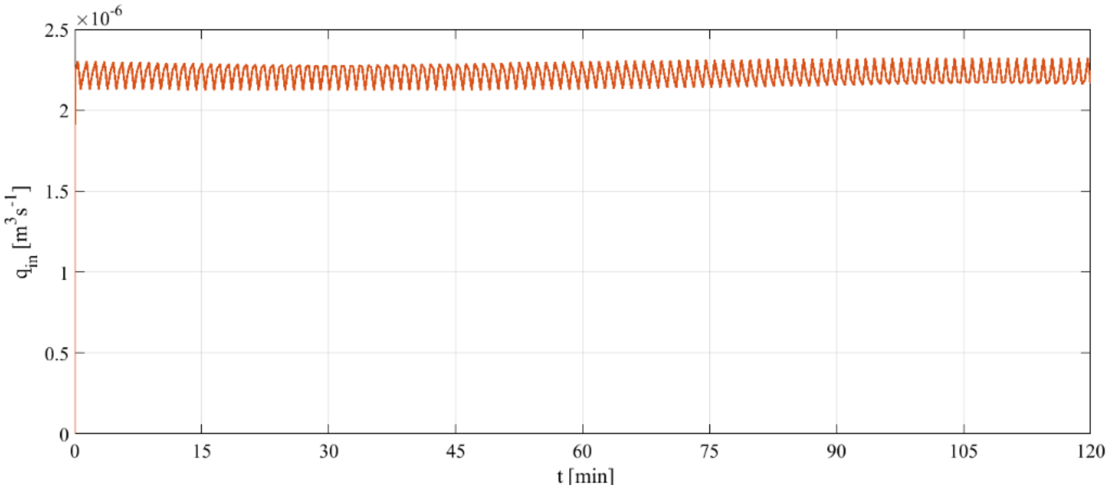

Fig. 2.11 PRS on q_in ($\pm$ 19×10^{-7} $\mathrm{m^3\,s^{-1}}$).

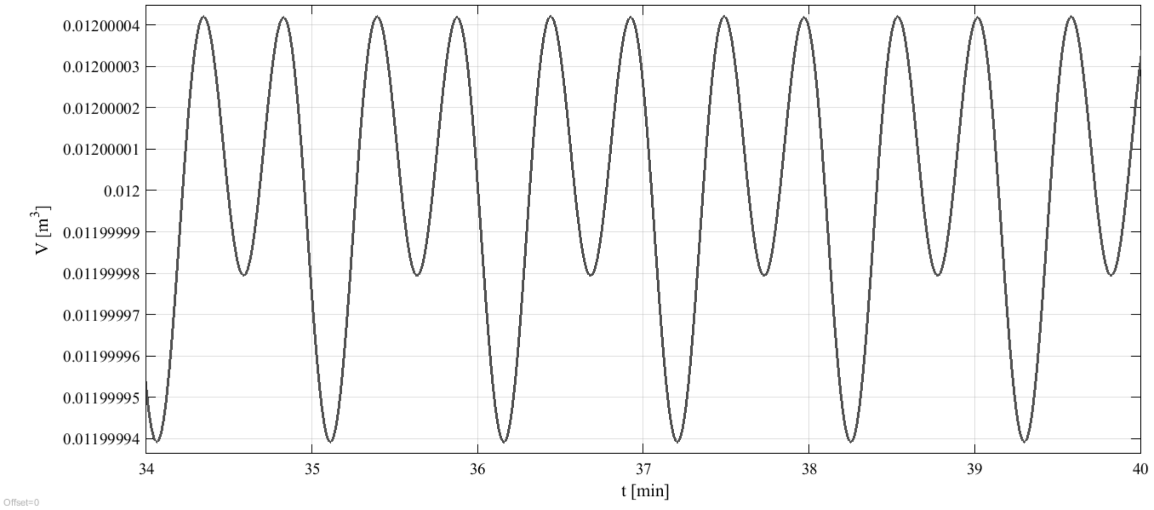

Fig. 2.12 Volume oscillations trend (oscillations $\cong \pm 5 \times 10^{-8}$ $\mathrm{m^3}$) (Neviani et al., 2019).

The incoming jacket flowrate was chosen as the manipulated variable (PID controller) and the reactor temperature was the controlled one. In addition, some parameters values (heat transport coefficients) were perturbed by Pseudo Random Binary Sequences (PBRS).

Overall, the total polyphenol yield (CSTR warm startup simulation) is characterized by the trend presented in Fig. 2.13.

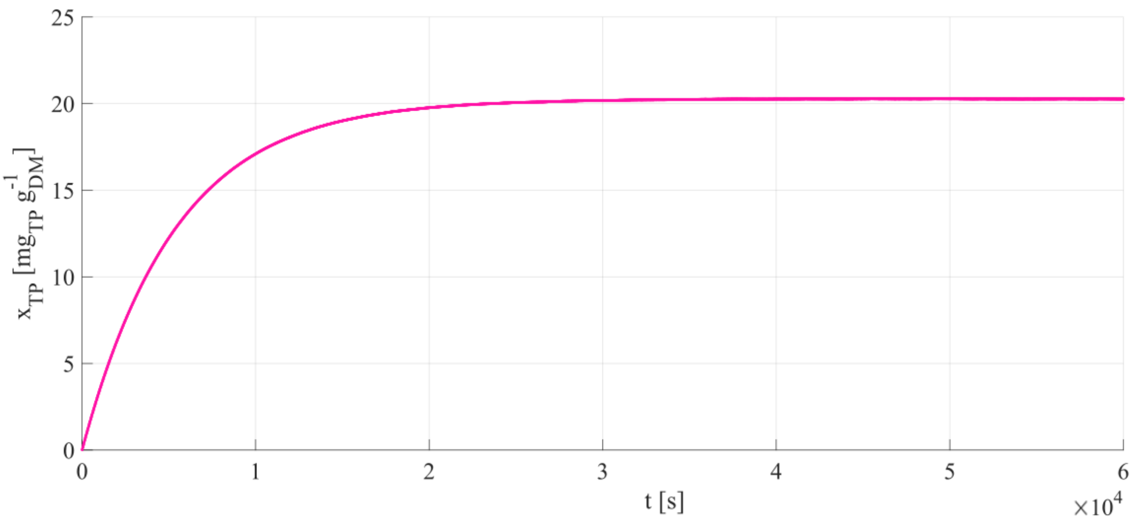

Fig. 2.13 Total polyphenols yield trend for the pilot-scale reactor operated as a CSTR (Neviani et al., 2019).

where noise is amplified in Fig. 2.14.

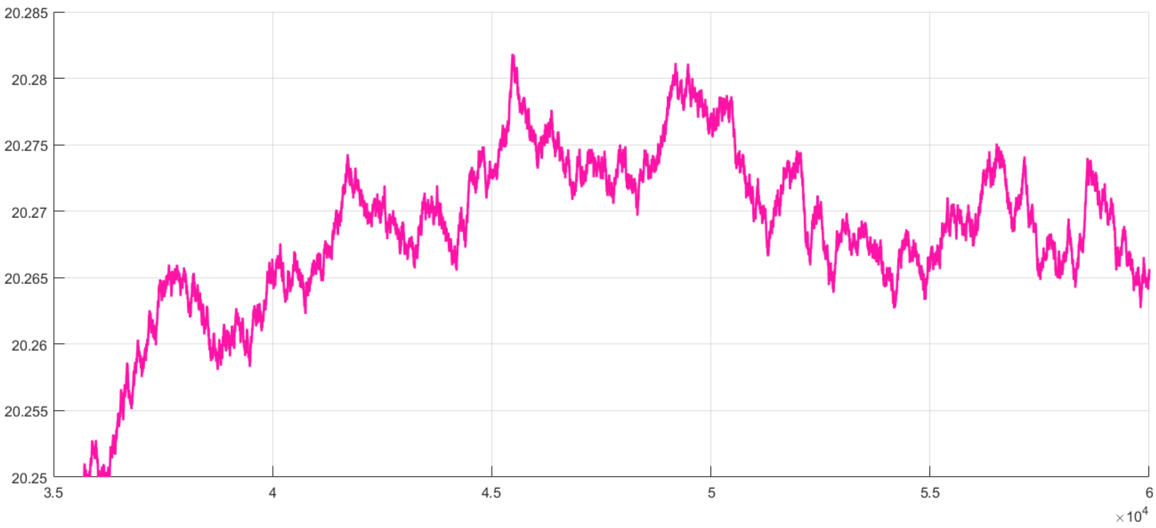

Fig. 2.14 Zoom of the noise in the total polyphenols yield trend in CSTR simulation (Neviani et al., 2019).

Finally, the temperature of the fluid (slurry) being controlled through the PID controller and the temperature of the heating fluid in output, are shown in Fig. 2.15. The offset of the PID controller can be eliminated by gains optimization.

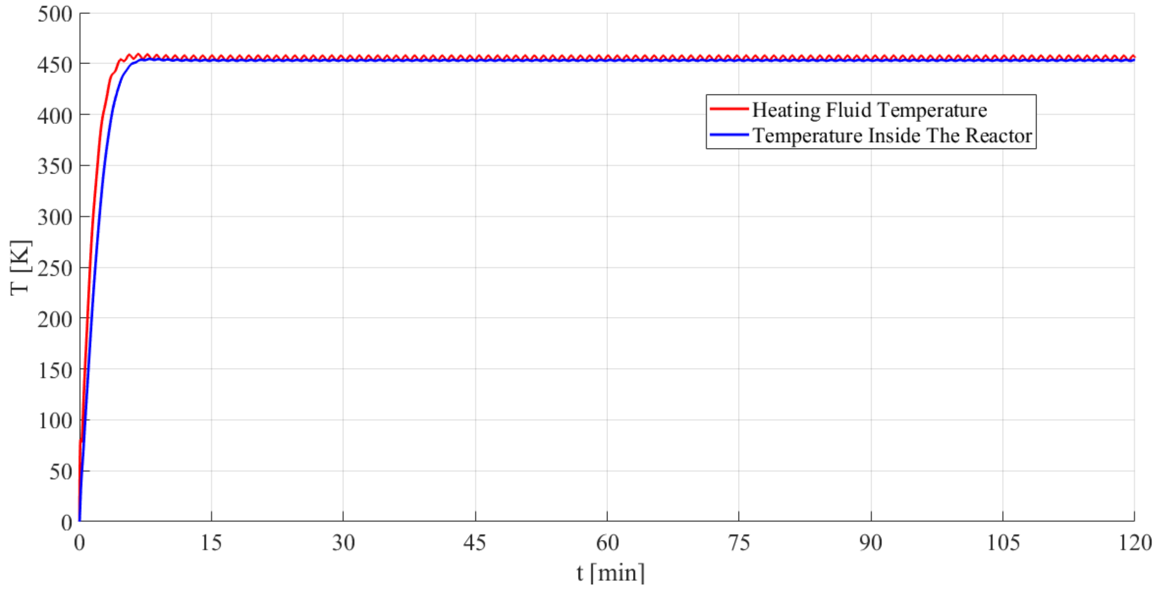

Fig. 2.15 Temperature trends of the mixture inside the reactor operated as a CSTR and of the heating fluid in exit (Neviani et al., 2019).

As the flowrate in input to the pilot CSTR is equal to about $8\,\mathrm{L\,h^{-1}}$ (see Eqn. 2.38), $800\,\mathrm{g_{dry\ pomace}}\,\mathrm{h^{-1}}$ can be processed and a production of $16\,\mathrm{g\,h^{-1}}$ of polyphenols can be estimated, for a total of about $350\,\mathrm{g\,d^{-1}}$, by considering $350\,\mathrm{d\ year^{-1}}$ of continuous operation (Neviani et al., 2019).

References

Aboelazayem, O., Gadalla, M., Saha, B., 2018. Biodiesel production from waste cooking oil via supercritical methanol: Optimisation and reactor simulation. Renewable Energy, SI: Waste Biomass to Biofuel 124, 144–154.

Bin, L., Yu-ting, W., Chong-fang, M., Meng, Y., Hang, G., 2009. Turbulent convective heat transfer with molten salt in a circular pipe. International Communications in Heat and Mass Transfer 36, 912–916.

Bucić-Kojić, A., Planinić, M., Tomas, S., Bilić, M., Velić, D., 2007. Study of solid–liquid extraction kinetics of total polyphenols from grape seeds. Journal of Food Engineering 81, 236–242.

Burdock, T.J., Giffin, A.H., Brooks, M.S., Ghaly, A.E., 2008. Heat Balance Analysis During the Production of Jadomycin C. American Journal of Biochemistry and Biotechnology 4, 7–18.

Catania, F., Massabò, M., Paladino, O., 2006. Estimation of transport and kinetic parameters using analytical solutions of the 2D advection-dispersion-reaction model. Environmetrics 17, 199–216.

Davis, M.E., Davis, R.J., 2012. Fundamentals of Chemical Reaction Engineering. Courier Corporation, USA. Green, D.W., Perry, R.H., 2007. Perry's Chemical Engineers' Handbook, 8th ed. ed. McGraw Hill Professional.

Holman, J.P., 2009. Heat Transfer, 10th ed. ed. McGraw-Hill Education.

Neviani, M., Aliakbarian, B., Perego, P., Paladino, O., 2019. Extraction of polyphenols from olive pomace: Mathematical modeling and technological feasibility in a high temperature and high pressure stirred reactor. Chemical Engineering Research and Design 141, 32–46.

Paladino, O., Hodaifa, G., Neviani, M., Seyedsalehi, M., Malvis, A., 2019. Modelling in Environmental Interfaces, in: Kyzas, G.Z. (Ed.), Advanced Low-Cost Separation Techniques in Interface Science. Elsevier (in press), London, UK.

Peleg, M., 1988. An Empirical Model for the Description of Moisture Sorption Curves. Journal of Food Science 53, 1216–1217.

Vojtesek, J., Dostal, P., 2012. Use of Differential Equations In Modeling and Simulation of CSTR, in: Advances in Mathematical and Computational Methods, Mathematics and Computers in Science and Engineering Series. Presented at the 14th WSEAS International Conference on Mathematical and Computational Methods in Science and Engineering (MACMESE 12), WSEAS Press, Sliema, Malta, pp. 264–269.

CHAPTER 3: LOCAL MODELING APT TO PHENOMENOLOGY STUDY AND CONTROL

3.1 Mathematical modeling of the ALR riser

The key role played by the hydrodynamics of the multi-phase flow for the proper operation of ALRs recommends a detailed modeling of this aspect. In fact, it affects the shape and trajectory of the bubbles in the riser, which in turn significantly influence the mass transfer between gas and microalgae and hence the growth of the latter.

One way to tackle this problem is to resort to physically based models. These establish their roots in first principles, i.e. conservation laws, which are used in synergy with constitutive relations characterizing the specific nature of materials or substances, as keystones to structure models that delve deeper on a priori information about the system/process.

The detailed analysis of bubble dynamics incarnates a classical example of problem requiring the simulation of Environmental Interfaces (EIs). As such, it demands the consideration of transport phenomena, and the balance equations on which build the mathematical models usually include those of mass, energy and momentum. As anticipated, a study of this kind it involves multiple phases of which are not quiescent fluids; fluid flows comprising free moving interfaces are thus of the utmost importance. Flows of bubbles in a liquid environment can be considered, in essence, biphasic immiscible fluid flows (Smolianski, 2001). The architecture of a physically based simulation model for said moving EIs rests on the conjunction between conservation of mass and energy with conservation of momentum, under constitutive equations prescribing the characteristics of superficial stresses that, in the case of Newtonian fluids, lead to the well-known Navier-Stokes equations (Paladino et al., 2019).

In order to describe a dynamic system subject to the action of a flow field, it is necessary to pick a reference frame. As fluid dynamics illustrates, whenever the specification can falls on a point of view integral with a fluid particle, we talk about the Lagrangian approach whilst, when the point of view focuses on a portion of space in which the fluid flows over time, of the Eulerian approach. When attacking multiphase flow problems, the options are distinguished between Eulerian-Eulerian (E-E) and Eulerian-Lagrangian (E-L). In nutshell, in the E-L paradigm the flow is described as a continuous fluid matrix in an Eulerian perspective whilst the dispersed phase, consisting of discrete elements, is followed in a Lagrangian manner. On the contrary, in E-E simulations both the carrier and dispersed phases are treated following an Eulerian point of view. In other terms, these different classifications arise from the difference in the treatment of the characteristics of the dispersed phase and the adoption of a Lagrangian or Eulerian specification of the dispersed phase field, having marked repercussions on the mathematical formulation, determines differences also in the numerical constraints and techniques to be adopted (Paladino et al., 2019).

When talking about simulation techniques, one has to bear in mind that conservation laws are, in general, nonlinear hyperbolic Partial Differential Equations (PDEs). Thus, global classical solutions oftentimes are not discernible and one can either resort to weak formulations or to numerical methods. Navier-Stokes equations are once again a prime example, as the existence of a global solution of them is one of the seven Millennium Prize Problems. Their importance is indisputable: they constitute the foundations of almost the totality of the mathematical models nowadays used in Computational Fluid Dynamics (CFD), a now computer-aided branch of fluid mechanics that exploit numerical analysis methods to simulate the behavior of various physical properties for fluid flows (Paladino et al., 2019).

Due to the complexity in their design and operation, related to the interconnection between physical phenomena, with transport phenomena and fluid dynamics at the forefront, ALRs pose a daring challenge to modelers. To carry out a detailed simulation of biochemical reactions and mass transport processes inside the reactor is a tall task, frequently avoided to focus on the mass transfer (e.g. (Zhang et al., 2006)) or hydrodynamics (e.g. (AL-Mashhadani et al., 2015)) separately. Furthermore, a gleaning limitation of both multifluid and mixed Eulerian-Lagrangian methods regards the accurate descriptions of shapes and behavior of the elements of the dispersed phases, spelling trouble when the focus falls on deformable interface dynamics, e.g. for the study of the behavior of bubbles. In this case, two classes of strategies could represent better alternatives: Front-Tracking (FT) and Front-Capturing (FC) methods. FT methods explicitly track the interface (front) through marker particles, requiring the continuous update of the mesh as the flow evolves, whilst FC methods hinge on the advection of implicit marker functions on fixed spatial domains.

Consequently, the former can be considered as belonging to the Lagrangian class whereas the latter exploit the Eulerian framework. Common to both FC and FT methods is the so-called one-fluid formulation according to which properties like density and viscosity, on the whole computational domain, are assimilated to discontinuous fields. In fact, the general structure that essentially distinguishes all the FC and FT algorithms relies primarily on a flow solver that uses some projection technique to solve the Navier-Stokes equations and usually a Poisson pressure equation on an Eulerian mesh. On the other hand, it is necessary to take into account the different material characteristics of the phases involved, essentially contained in the density and viscosity scalar fields, as well as interfacial phenomena, such as the onset of surface forces that translate into surface tension. By crossing the front that separates two phases, the change of the values of the aforesaid scalar fields will ideally manifest itself with jump discontinuities, due to the theoretically negligible thickness of the interface. The one-fluid formulation allows to keep the notation compact, ideally combining the various multiphase equations in a single equation including the jump conditions at the interface (Paladino et al., 2019). Practically, the modelling of the interfacial terms concentrated on the front is carried out with Dirac delta distribution δ whilst the discontinuity in material properties is conveyed through the Heaviside step function H (Prosperetti and Tryggvason, 2009).

Hereinafter, a FC method called level set method will be employed. In brief, such a choice was motivated by the main advantage of these techniques, i.e. the possibility to handle implicitly the changes of topologies, without the need of detecting and reconstructing the merging or splitting of fronts.

Summarizing, in order to build an appropriate model for the ALR riser, one must take into account two essential phenomena: viscous fluid flow and moving interfaces, in addition to their mutual influence. Fluid flow is described by the non-dimensional form of the incompressible Navier-Stokes equations (see Section 3.1.1) whereas interfaces are described through an implicit representation by resorting to the level set approach (see Section 3.1.2). The link between the two equation systems is offered by the formulation of physical properties of the considered fluids, i.e. density ρ, dynamic viscosity μ and surface tension, all described as functions of the level set function ϕ.

3.1.1 Navier-Stokes equations

The local formulation of the Navier-Stokes equations, obtained from momentum balance by resorting to the divergence theorem in conjunction with Reynolds transport theorem, illustrates how (Batchelor, 2000; Chorin and Marsden, 1990)

$$\rho\frac{\mathrm{D}\mathbf{u}}{\mathrm{D}t} = -\nabla p + \left(\zeta + \frac{1}{3}\mu\right)\nabla(\nabla\cdot\mathbf{u}) + \mu\nabla^2\mathbf{u} + \mathbf{F}_b \tag{3.1}$$

where the ratio $\frac{\mathrm{D}\mathbf{u}}{\mathrm{D}t}$ denotes the material derivative of the velocity $\mathbf{u}$ (given any tensor field T dependent on space and time, it is defined that $\frac{\mathrm{D}\mathsf{T}}{\mathrm{D}t} = \frac{\partial\mathsf{T}}{\partial t} + \mathsf{T}\cdot\nabla\mathsf{T}$). Moreover, ρ is the density, p the pressure of the fluid, μ the dynamic viscosity while ζ represents the volume viscosity (also known as second viscosity coefficient) and $\mathbf{F}_b$ other body forces (per unit volume) such as gravitational force per unit volume ρg.

As it is well known, for Newtonian, incompressible fluids, the continuity equation applies. It describes the velocity field $\mathbf{u}$ as a solenoidal vector field:

$$\nabla\cdot\mathbf{u} = 0 \tag{3.2}$$

It follows that, if one considers $\mathbf{F}_b = \rho g$ as it is often the case,

$$\frac{\mathrm{D}\mathbf{u}}{\mathrm{D}t} = -\frac{1}{\rho}\nabla p + \mathbf{g} + \frac{\mu}{\rho}\nabla^2\mathbf{u} = -\frac{1}{\rho}\nabla p + \mathbf{g} + \nu\nabla^2\mathbf{u} \tag{3.3}$$

having introduced the kinematic viscosity $\nu = \mu\rho^{-1}$ as well.

Frequently, it is useful to massage transport differential equations like Eqn. 3.3 and write them in non-dimensional form. Among the reasons, one can cite the possibility to assess the relative importance of terms in the model equations and the generalization of the problem that becomes scale-independent.

To do so, one can introduce suitable non-dimensional variables (hereinafter marked by the $\star$ superscript) by specifying a characteristic length L and velocity U so that:

$$\mathbf{x} = \mathbf{x}^\star \mathrm{L}, \qquad \mathbf{u} = \mathbf{u}^\star \mathrm{U}, \qquad \mathbf{g} = \hat{\mathbf{e}}_g = \mathbf{g}^\star \mathrm{g} \tag{3.4}$$

The selection of a proper pressure scale is not a foregone conclusion: a possibility, advisable for the cases in which dynamic effects are dominant, consists in obtaining the non-dimensional pressure $p^\star$ as the ratio

$$p^\star\rho\mathrm{U}^2 = p \tag{3.5}$$

In addition, it is easy to observe how

$$\nabla^\star = \mathrm{L}\nabla \tag{3.6}$$

and that the introduction of L and U naturally leads to the identification of the time scale, since

$$\mathrm{T} = \frac{\mathrm{L}}{\mathrm{U}} \tag{3.7}$$

where T is the convective time. It follows that one can define $t^{\star}$ as

$$t^{\star} = \frac{t}{\mathrm{T}} \tag{3.8}$$

L and U are quantities adopted to assemble dimensionless quantities which are useful to analyze the similarity of different systems. For the similarity constraint to be satisfied, geometrical similarity, as well as similarity of boundary conditions and equality of each of these dimensionless groups are required. Generally speaking, characteristic physical quantities are liable to arbitrary choice, provided that they are well defined and referred to the same geometrical locations for every system (Pnueli and Gutfinger, 1997).

Rearranging these latter mathematical expressions defining the non-dimensional quantities and plugging them in Eqn. 3.3 leads to

$$\frac{\mathrm{U}^2}{\mathrm{L}}\frac{\mathrm{D}\mathbf{u}^{\star}}{\mathrm{D}t^{\star}} = -\frac{1}{\rho}\frac{\rho\mathrm{U}^2}{\mathrm{L}}\nabla^{\star}p^{\star} + \mathbf{g}^{\star}g + \nu\frac{\mathrm{U}}{\mathrm{L}^2}\nabla^{2\star}\mathbf{u}^{\star} \tag{3.9}$$

being $\nabla^{2\star}$ the non-dimensional Laplacian, i.e. the square of $\nabla^{\star}$.

To complete the non-dimensionalization of the NSE, as it deducible from dimensional analysis, it is necessary to multiply both sides of Eqn. 3.9 by the constant term LU^{-2}, hence obtaining the non-dimensionalized Navier–Stokes equations for an incompressible, isothermal, Newtonian fluid.

$$\frac{\mathrm{D}\mathbf{u}^{\star}}{\mathrm{D}t^{\star}} = -\nabla^{\star}p^{\star} + \frac{g\mathrm{L}}{\mathrm{U}^2}\hat{\mathbf{e}}_g + \frac{\nu}{\mathrm{LU}}\nabla^{2\star}\mathbf{u}^{\star} \tag{3.10}$$

Two well-known similarity numbers, i.e. dimensionless groups, emerge in this way: the Reynolds number Re and Froude number Fr.

$$\mathrm{Re} = \frac{\mathrm{LU}}{\nu} \tag{3.11}$$

$$\mathrm{Fr} = \frac{\mathrm{U}}{\sqrt{g}\mathrm{L}} \tag{3.12}$$

Eqn. 3.10 can therefore be condensed in

$$\frac{\mathrm{D}\mathbf{u}^{\star}}{\mathrm{D}t^{\star}} = -\nabla^{\star}p^{\star} + \frac{1}{\mathrm{Fr}^2}\hat{\mathbf{e}}_g + \frac{1}{\mathrm{Re}}\nabla^{2\star}\mathbf{u}^{\star} \tag{3.13}$$

What has been written up to this point in the present section on the Navier-Stokes equations is valid for the study of the fluid dynamics of single-phase systems. When the number of phases involved increases, as occurs in bubble columns and airlift reactors, the changes in the properties of the fluids must be considered, even when they are considered constant and uniform for each of them, as well as other forces, surface tension in particular. The first of the two aspects can be addressed through techniques that follow the one-fluid approach, like the level set method, which in turn influences the modeling of the surface tension term, to be introduced in the NSE.

3.1.2 The level set method

The level set method is based upon a rather simple idea: the interface can be implicitly thought of as the zero iso-contour of a signed distance field $\phi(\mathbf{x},t)$ called level set function (see Fig. 3.1).

Having called $\Omega \subset \mathbb{R}^n$ the space domain and $\mathscr{T}$ the final time, the level set function $\phi : \Omega \times [0,\mathscr{T}] \to \mathbb{R}$ is the solution of the Hamilton-Jacobi (HJ) equation

$$\begin{cases} \dfrac{\partial \phi(\mathbf{x},t)}{\partial t} = \mathbf{u}(\mathbf{x},t)\|\nabla\phi(\mathbf{x},t)\| \\ \phi(\mathbf{x},0) = \phi_0(\mathbf{x}) \end{cases} \tag{3.14}$$

where $\|\cdot\|$ is the Euclidean norm, $\phi_0 : \Omega \to \mathbb{R}$ a given initial condition and $\mathbf{u} : \Omega \times [0,\mathscr{T}] \to \mathbb{R}$ is the speed vector field.

The zero level of ϕ_0 coincides with the initial location of the front and can therefore be set to the signed distance to it, meaning that the domain Ω is subdivided in two distinct regions Ω^+ and Ω^- ($\Omega^+ \cap \Omega^- = \emptyset$) by the boundary Γ between Ω^+ and Ω^- ($\Gamma \notin \{\Omega^+,\Omega^-\}$), i.e. the zero level of ϕ_0.

$$\begin{cases} \phi(\mathbf{x},t) > 0 & \text{if } \mathbf{x} \in \Omega^+ \\ \phi(\mathbf{x},t) = 0 & \text{if } \mathbf{x} \in \Gamma \\ \phi(\mathbf{x},t) < 0 & \text{if } \mathbf{x} \in \Omega^- \end{cases} \tag{3.15}$$

The level set approach presupposes the computation of the latter at each time step, following the resolution of Eqn. 3.14, in order to obtain the front propagation. However, an anticipated consequence of the convection term in Eqn. 3.14 is the need of re-initialization of the distance profile, as a loss in smoothness of field ϕ is to be expected. In fact, ϕ is generally initialized into the signed distance function $D(x,t) = \min_{\mathbf{x}_\Gamma \in \Gamma} |\mathbf{x} - \mathbf{x}_\Gamma|$, with $\mathbf{x}_\Gamma$ being the closest point of the front from $\mathbf{x}$: in the probable event that the speed function $\mathbf{u}$ is not constant, ϕ can become either very flat or steep. Sussman et al. (Sussman et al., 1994) proposed an iterative reinitialization of ϕ by reformulating $D(x,t)$, i.e. the unique viscosity solution of the Eikonal equation $|\nabla\phi| = 1$ anchored at ϕ_0, by solving another Hamilton-Jacobi PDE (Eqn. 3.16) in an artificial time reference $\tilde{\tau}$.

$$\frac{\partial \phi(\mathbf{x},t)}{\partial \tilde{\tau}} + \mathscr{S}(|\nabla\phi(\mathbf{x},t)| - 1) = 0 \tag{3.16}$$

where $\mathscr{S}$ is a modified signed function (Hartmann et al., 2008). Albeit subject to Courant–Friedrichs–Lewy (CFL) condition limitations, this procedure is widely employed as it translates in an accurate reconstruction of the distance profile.

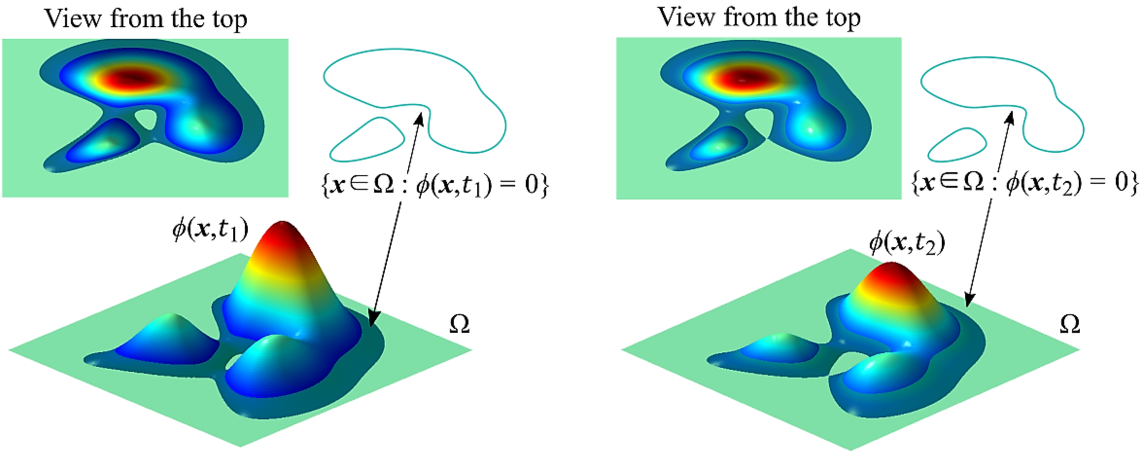

Fig. 3.1 Graphical illustration of the level set method (Paladino et al., 2019).

In a nutshell, the application of LSM to fluid dynamic problems hinges on three mathematical functions: other than the level set function ϕ, Dirac delta δ and Heaviside step function H play a crucial role. Even though the thickness of the interface may be inconsiderable from a physical perspective, LSM calls for the prescription of a fixed and numerically relevant front thickness as a mean to alleviate numerical difficulties that may arise due to sharp changes of the considered physical properties across Γ.

To avoid jump discontinuities, sharp changes in the properties of Ω^+ and Ω^- regions are smudged by the means of a smoothed Heaviside function $H_\varepsilon(\phi)$, whilst mollified delta function $\delta_\varepsilon(\phi)$ is employed to analogously model the surface tension force (Sharma, 2015).

Specifically, Osher and Fedkiw (Osher and Fedkiw, 2003) report the definition of $H_\varepsilon(\phi)$ (see Fig. 3.2a) as

$$H_\varepsilon(\phi) = \begin{cases} 0 & \text{if } \phi < -\varepsilon \\ \dfrac{1}{2} + \dfrac{\phi}{2\varepsilon} + \dfrac{1}{2}\sin\left(\dfrac{\pi\phi}{\varepsilon}\right) & \text{if } -\varepsilon \le \phi \le \varepsilon \\ 1 & \text{if } \varepsilon < \phi \end{cases} \tag{3.17}$$

where ε is a parameter influencing the numerical smearing – usually of the same order of magnitude as the interface thickness –, and $\delta_\varepsilon(\phi)$ (see Fig. 3.2b) as:

$$\delta_\varepsilon(\phi) = \begin{cases} 0 & \text{if } \phi < -\varepsilon \\ \dfrac{1}{2\varepsilon} + \dfrac{1}{2\varepsilon}\cos\left(\dfrac{\pi\phi}{\varepsilon}\right) & \text{if } -\varepsilon \leq \phi \leq \varepsilon \\ 0 & \text{if } \varepsilon < \phi \end{cases} \tag{3.18}$$

LSM is a front capturing method, depicting a picture in which coordinates are fixed in space, i.e. an Eulerian method. In the perspective of the simulation of a system that involves bubble motion within a liquid domain and requires a high degree of precision considering the importance of their shape, Eulerian methods seem to be preferable. In fact, having an external stationary reference frame at one's disposal offers undeniable advantages in the delineation of bubble shape evolution: it enables to take into account topology variations whereby bubbles may coalesce and break up. Moreover, Lagrangian methods prove to be ill-suited to cope with such problems since, while they preserve a sharp interface representation, they demand re-meshing when large deformations manifest and are subjected to mesh tangling and numerical inaccuracy due to highly irregular meshes (Dukowicz, 1981), being prone to blow up.

Among other virtues of LSM, its ability to naturally determine intrinsic geometrical properties of the moving interfaces such as their normal vector $\hat{\mathbf{n}}$ turns out to be very advantageous also in the perspective of dealing with physical properties such as surface tension. Simply by differentiation of ϕ, one is in fact able to infer both $\hat{\mathbf{n}}$ and the curvature κ:

$$\hat{\mathbf{n}} = \frac{\nabla\phi}{\|\nabla\phi\|} \tag{3.19}$$

$$\kappa = \nabla\cdot\hat{\mathbf{n}} \tag{3.20}$$

To recap, in order to build an adequate computational model for the problem at hand, it is necessary to take into account three essential elements: the velocity field, a description of the moving fronts and the coupling between interface tracking and the velocity field.

The link between the equations for the velocity field (NSE) and the interface tracking (realized thanks to an implicit representation obtained through the LSM) is offered by the formulation of the physical properties of the considered fluids (e.g. density and viscosity) as functions of the level set function ϕ, according to the one-fluid formulation. When multiphase flows are considered, jump discontinuities are commonly encountered across the fronts due to the diversity in those physical properties. To this end, the use of the smoothed Heaviside

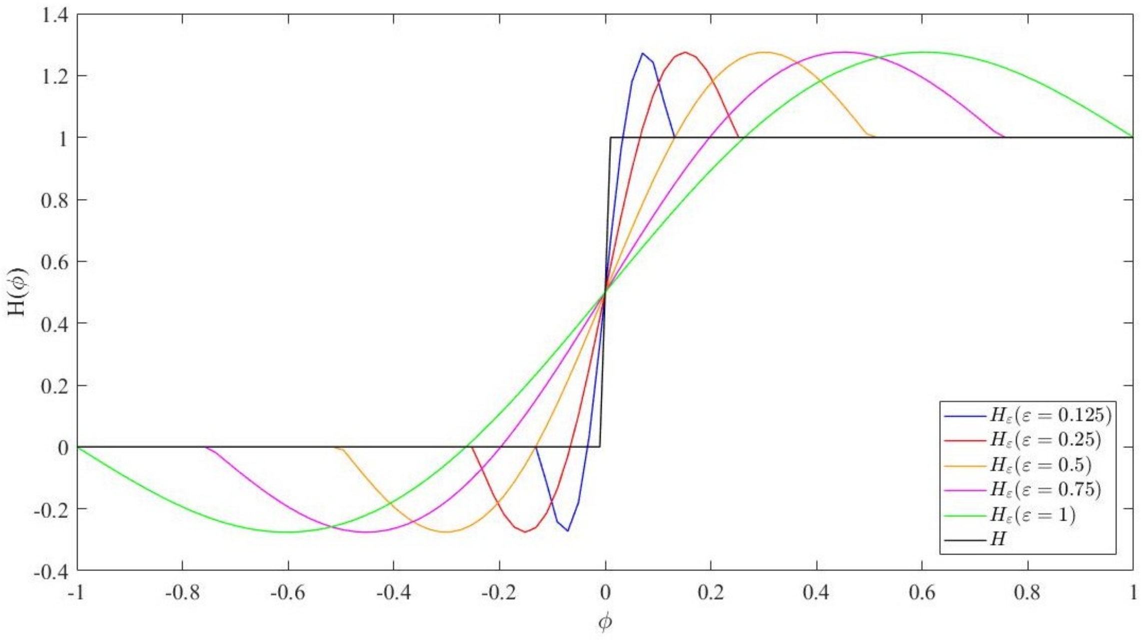

(a) Comparison between H and H_ε.

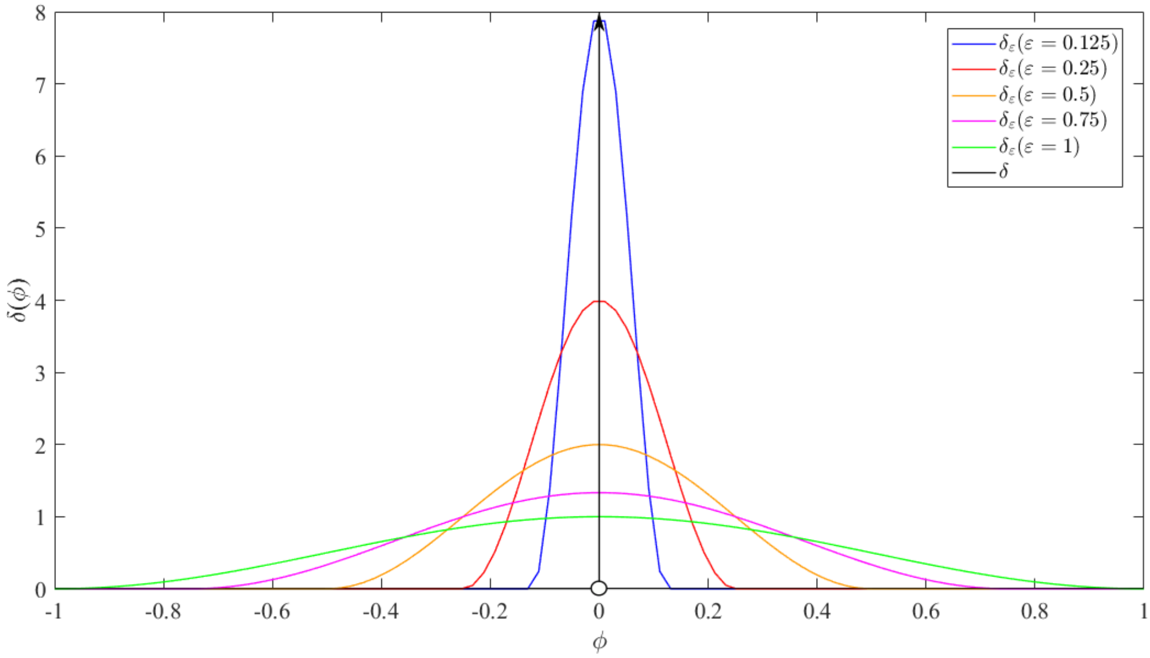

(b) Comparison between δ and δ_ε.

Fig. 3.2 Analytic and numerical representations of Heaviside step function and Dirac delta distribution.

function H_ε comes in handy, allowing the definition of the density and of the kinematic viscosity of the two-phase flow system of incompressible fluids in a compact way.

$$\rho = \rho_{\mathrm{G}} + (\rho_{\mathrm{L}} - \rho_{\mathrm{G}})H(\phi) \cong \rho_{\mathrm{G}} + (\rho_{\mathrm{L}} - \rho_{\mathrm{G}})H_{\varepsilon}(\phi) \tag{3.21}$$

$$\nu = \nu_{\mathrm{G}} + (\nu_{\mathrm{L}} - \nu_{\mathrm{G}})H(\phi) \cong \nu_{\mathrm{G}} + (\nu_{\mathrm{L}} - \nu_{\mathrm{G}})H_{\varepsilon}(\phi) \tag{3.22}$$

being the subscripts G and L tags referring to the gas and liquid phases respectively.

The other quintessential ingredient to model multiphase flows is the surface tension force.

The surface tension is due to the forces of cohesion between the molecules of a fluid. Analyzing the case of air bubbles in a liquid, the net force acting on a molecule due to its neighbors is zero within the bubble. On the other hand, this force, on the surface, is directed radially inward, causing the combined effect of the radial force components across the whole spherical surface to contract this latter, whereby increasing the pressure on the concave side of the surface. The superficial force that fulfills the role of maintaining equilibrium in such situations is precisely the superficial tension, balancing the radially inward inter-molecular attractive force with the radially outward pressure gradient force across the surface. Where two distinct fluid phases can be distinguished, one of which does not take the form of spherical bubbles, the action of surface tension is aimed at minimizing free energy going to reduce the interface area.

Since the surface-tension force is a singular force active only at the location of the phase interface Γ, formally, it can be expressed as the integral over the entire front, thereby adding the delta functions together to create a force that is concentrated at the interface, but smooth along the front. $\mathbf{x}$ is the point at which the equation is evaluated and $\mathbf{x}_{\Gamma}$ is the position of the front (Loth, 2016).

$$\mathbf{F}_{ST} = \int_{\Gamma} \sigma \kappa \hat{\mathbf{n}} \delta(\mathbf{x} - \mathbf{x}_{\Gamma})\, \mathrm{d}\Gamma \tag{3.23}$$

This is a volumetric formulation, obtained by resorting to the first Frenet formula for parametric curves to handle Young's formulation of $\mathbf{F}_{ST}$ (for a constant surface tension coefficient). Young's model describes the two-dimensional tension as a force per unit length tangential to the curve $\sigma\hat{\mathbf{t}}$, where σ is the coefficient of surface tension and $\hat{\mathbf{t}}$ is the unit tangent vector (Fritsching and Li, 2016). Eqn. 3.23 is the surface tension term reformulated according to the Continuum Surface Force (CSF) model (Brackbill et al., 1992), one of the two most widely employed model, together with the Continuous Surface Stress (CSS) model. Volumetric formulations hinge on a numerical approximation surface delta function that permits a direct calculation of the volumetric force (Popinet, 2018). Both techniques provide for a discretization of the Dirac distribution that usually entails the spread of the surface tension force into a small neighborhood normal to the interface of the phase (Fritsching and Li, 2016). An issue common to both these models, mainly due to discretization errors, is the introduction of spurious (also known as parasitic) currents at the interface, small but growing vortical flows caused by the imbalance of the surface tension force and the pressure gradient that affect the front shape and may lead to unphysical results (Seifollahi et al., 2008).

CSS model represents $\mathbf{F}_{ST}$ in a conservative manner as the divergence of a surface-tension tensor, avoiding the explicit computation of curvature. However, since in the present work the computation of κ is easy due to the use of the LSM, it was decided to rely on the more widely used CSF model. According to it, $\mathbf{F}_{\mathrm{ST}}$ is expressed by using a Dirac delta function that, for the LSM, has ϕ as its argument:

$$\mathbf{F}_{\mathrm{ST}} = \sigma\kappa\hat{\mathbf{n}}\delta(\phi) \tag{3.24}$$

where for computational purposes, one can use the mollified delta function $\delta_\varepsilon(\phi)$ instead of $\delta(\phi)$.

Then, having considered what has been said so far, it is possible to rewrite the NSE for a multiphase flow as:

$$\frac{\mathrm{D}\mathbf{u}^\star}{\mathrm{D}t^\star} = -\nabla^\star p^\star + \frac{1}{\mathrm{Fr}^2}\hat{\mathbf{e}}_g + \frac{1}{\mathrm{Re}}\nabla^{2\star}\mathbf{u}^\star + \frac{\sigma\kappa\hat{\mathbf{n}}\delta_\varepsilon}{\rho}\frac{\mathrm{L}}{\mathrm{U}^2} \tag{3.25}$$

In many instances, Eqn. 3.25 is reported in a slightly different form (see Eqn. 3.28), that can be obtained by resorting to the definition of Weber number We,

$$\mathrm{We} = \frac{\rho \mathrm{L}\mathrm{U}^2}{\sigma} \tag{3.26}$$

and by defining

$$\kappa^\star = \kappa\mathrm{L}, \qquad \delta^\star = \delta\mathrm{L} \tag{3.27}$$

In fact, by doing so, one obtains that

$$\frac{\mathrm{D}\mathbf{u}^\star}{\mathrm{D}t^\star} = -\nabla^\star p^\star + \frac{1}{\mathrm{Fr}^2}\hat{\mathbf{e}}_g + \frac{1}{\mathrm{Re}}\nabla^{2\star}\mathbf{u}^\star + \frac{\kappa^\star\hat{\mathbf{n}}\delta_\varepsilon^\star}{\mathrm{We}} \tag{3.28}$$

3.2 Development of the computational model of the ALR riser

The simulator rests on a cascade model, developed in MATLAB environment. The algorithm articulates in three main steps (Fig. 3.3): a first resolution of the flow field modeled with the Navier-Stokes PDEs system is carried out, after which the the Hamilton-Jacobi equation

(Eqn. 3.14) is solved. The zero level set of the level set function is then evaluated to infer the position and shape of the fronts. Accordingly, the material properties are updated and the algorithm starts with the subsequent iteration.

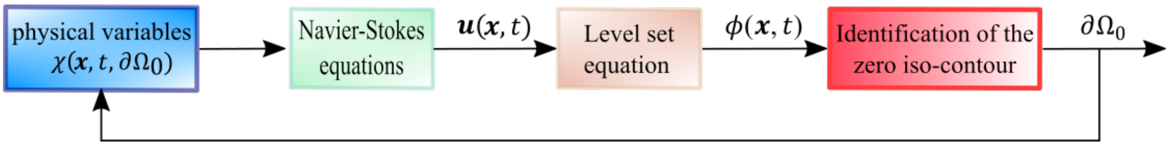

Fig. 3.3 Flowchart of the algorithm used for the numerical simulation of the hydrodynamics in the riser of the airlift photobioreactor.

In particular, two-dimensional NSE in non-dimensional form are solved by employing Chorin's projection (Chorin, 1968) on a Marker-and-Cell (MAC) staggered grid (Fig. 3.4).

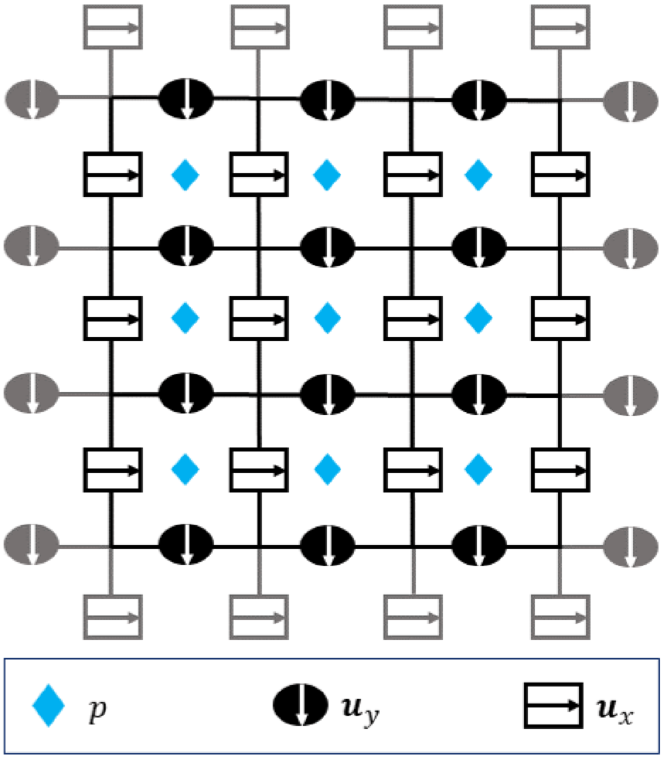

Fig. 3.4 Marker-and-Cell staggered grid with boundary cells.

Chorin's projection method is a fractional step technique built on Helmholtz decomposition which states that any vector field can be split in the sum of a curl-free (irrotational) field and a divergence-free (solenoidal) one. This operator splitting method comprises three steps: the nonlinear convection term $\mathbf{u}^{\star} \cdot \nabla^{\star}\mathbf{u}^{\star}$ (in the material derivative) is processed with an explicit scheme while the diffusion term $\nabla^{2\star}\mathbf{u}$ with an implicit one, finding an intermediate velocity field that do not abide by the incompressibility constraint. The final passage consists in projecting this tentative velocity onto the space of solenoidal fields, thus imposing continuity through the Poisson equation (Eqn. 3.2) and finding the corrected velocity by adding the pressure gradient.

The relative code is based on the NS solver programmed by Seibold (Seibold, 2008) and utilizes a three-steps semi-implicit scheme for time discretisation. It is based on the theory discussed in (Strang, 2007) proceeds to perform three consequent refinements per time step to adjust numerical approximation of dimensionless velocity field (for the considered two dimensional case denoted as (U,V)).

If one considers the n-th time step, corresponding to the instant t, under the constraint provided by the continuity equation, the splitting method, starting from the matrices U^n and V^n allows to derive those at the time step $(n+1)$ corresponding to the instant $t+\Delta t$ through the use of two dummy vectors, respectively indicated with $*$ and $**$ superscripts. The algorithm is summarized below (Saci and Nouri, 2013; Seibold, 2008).

- **Step 1: treatment of nonlinear terms**. The nonlinear terms are handled explicitly. This entails a double effect: it allows to circumvent the solution of a nonlinear system but at the price of introducing a CFL condition that limits the time step by a constant times the spatial resolution.

$$\frac{\mathsf{U}^* - \mathsf{U}^n}{\Delta t} = -((\mathsf{U}^n)^2)_x - (\mathsf{U}^n\mathsf{V}^n)_y \tag{3.29}$$

$$\frac{\mathsf{V}^* - \mathsf{V}^n}{\Delta t} = -(\mathsf{U}^n\mathsf{V}^n)_x - ((\mathsf{V}^n)^2)_y \tag{3.30}$$

- **Step 2: implicit treatment of viscosity terms**. Viscosity terms are added and treated implicitly to find another intermediate solution. Opting for an explicit approach would entail a a time step restriction proportional to the square of the spatial discretization. The other side of the coin is that the resolution of two linear systems is required in each time step.

$$\frac{\mathsf{U}^{**} - \mathsf{U}^*}{\Delta t} = \frac{1}{\mathrm{Re}}(\mathsf{U}^{**}_{xx} + \mathsf{U}^{**}_{yy}) \tag{3.31}$$

$$\frac{\mathsf{V}^{**} - \mathsf{V}^*}{\Delta t} = \frac{1}{\mathrm{Re}}(\mathsf{V}^{**}_{xx} + \mathsf{V}^{**}_{yy}) \tag{3.32}$$

- **Step 3: pressure correction**. The intermediate velocity field U^{**} (V^{**}) is corrected by the gradient of a (dimensionless) pressure P^{n+1} in order to enforce incompressibility and obtain the solenoidal field U^{n+1} (V^{n+1}). To do so, Chorin's projection method comes in handy. Recalling Helmoltz decomposition, since pressure is irrotational as the curl of any gradient is zero as long as the commutative property of the partial derivative holds, one can infer (since any vector field $U^{**} = U_{\text{irrotational}} + U_{\text{solenoidal}}$) that:

$$\frac{\mathsf{U}^{n+1} - \mathsf{U}^{**}}{\Delta t} = -(\mathsf{P}^{n+1})_x \tag{3.33}$$

$$\frac{\mathsf{V}^{n+1} - \mathsf{V}^{**}}{\Delta t} = -(\mathsf{P}^{n+1})_y \tag{3.34}$$

being,

$$\mathsf{U}_{\text{irrotational}} = -\Delta t \nabla^{\star} \mathsf{P}^{n+1} \tag{3.35}$$

The pressure field P^{n+1} is given only implicitly and is obtained from a Poisson equation. In vector notation, the correction of velocity fields through the pressure gradient can be written in the form

$$\frac{1}{\Delta t}\mathsf{U}^{n+1} - \frac{1}{\Delta t}\mathsf{U}^{n} = -\nabla^{\star}\mathsf{P}^{n+1} \tag{3.36}$$

which, by applying the divergence to both sides of the equation, yields the linear system

$$-\frac{1}{\Delta t}\nabla^{\star} \cdot \mathsf{U}^{n} = -\nabla^{2\star}\mathsf{P}^{n+1} \tag{3.37}$$

The spatial discretization for the portion of the model that concerns the resolution of the HJ equation for computing the zero level set is performed by an upwind second-order Essentially Non-Oscillatory (ENO) scheme whilst time discretization is carried out with a three-steps, second-order Total Variation Diminishing (TVD) Runge-Kutta scheme. The choice of upwind approximations is motivated by the hyperbolic nature of the PDE to avoid numerical instabilities.

Albeit LSM can be used with finite volume schemes, here all the equations were treated by relying on finite difference approximations.

The MATLAB code for the implementation of level set method was written using Mitchell's LSM toolbox (Mitchell, 2008) as a mold.

The system equations were numerically solved in the spatial domain $\Omega = [-\frac{d_r}{2}, \frac{d_r}{2}] \times [-\frac{L_r}{2}, \frac{L_r}{2}]$, where L_r is the length of the ALR riser, equal to 0.78 m, and d_r is its diameter, equal to 0.11 m.

Ω was discretised to form a mesh grid of rectangular cells, made up of 300 nodes in each dimension.

Another possibility, actually employed later in this research work (see Section 3.5), consists in focusing on the bottom section of the airlift reactor, with the diffuser diameter (equal to the riser diameter) as the characteristic length. Since the collector diameter d_c is about half the riser diameter (d_c =0.05 m), in this case a square domain $\Omega = d_r \times d_r$ could

Table 3.1 Data gathered in the experimental campaigns, from (Paladino and Neviani, 2018).

Geometric data	**Value**
Length of the riser	0.780 m
Diameter of the riser	0.110 m
Length of the downcomer	0.780 m
Diameter of the downcomer	0.050 m
Length of the horizontal collectors	0.385 m
Diameter of the horizontal collectors	0.050 m
Operating variables	**Value**
Temperature	293 K
Pressure	3÷4 bar
NaCl pulse injection	1÷10 g l^{-1}
Measured variables	**Value**
Gas velocity	0.57÷0.64 m s^{-1}
Liquid velocity (in the riser)	0.06÷0.14 m s^{-1}
Liquid velocity (in the downcomer)	0.17÷0.39 m s^{-1}
(min, average, max) bubble diameter	(0.003, 0.007, 0.020) m

better capture both bubble shape modifications and initial behavior in the inlet section, where the diffuser is highly influenced by the lateral collector.

Referring for now to the first instance, i.e. Ω as rectangular domain, the boundary conditions employed to evaluate the velocity field were of the Dirichlet type. No-slip conditions were imposed on three sides of the domain, both in the x and y direction. The right-side wall, on the contrary, was modeled as to consider the inflow and outflow determined by the presence of the horizontal collectors. Hence, in correspondence of the openings, a noise-imposed, fairly flat profile velocity distribution typical of the turbulent fluid flow was adopted, while no-slip conditions were used elsewhere.

For what regards the simulation data, aside for the dynamic parameters measured in the experimental campaign (Paladino and Neviani, 2018) and the ALR dimensions (Table 3.1), the remaining data used in simulations were retrieved from literature (Table 3.2).

3.3 Grace's diagram and the shapes of bubbles

In order to maximize mass transfer, the maximum surficial area of exchange is required. Also, it is self-evident that the longer the transport phenomenon lasts, the better it is.

Table 3.2 Physico-chemical data found in literature and employed in the simulations.

Physico-chemical parameters	**Value**
Specific gas constant (CO_2)	$188.9\,\mathrm{J\,kg^{1}\,K^{-1}}$
Surface tension coefficient (CO_2)	$72.86 \times 10^{-3}\,\mathrm{N\,m^{-1}}$
Liquid velocity (H_2O)	$997\,\mathrm{kg\,m^{-3}}$
Liquid dynamic viscosity (H_2O)	$1.002 \times 10^{-3}\,\mathrm{Pa\,s}$
Gas dynamic viscosity (CO_2)	$1.470 \times 10^{-5}\,\mathrm{Pa\,s}$

Referring this notion to the problem under examination, this means that, in addition to needing suitable forms of the bubbles, it is also necessary to optimize their residence time in the riser. That is, to ensure that appropriate trajectories are achieved. Hydrodynamics of multiphase flow thus holds a controlling influence on mass transport phenomena.

As long as the gas inlet velocity is maintained below a threshold value, dependent on the tube geometry, bubbles rise almost individually without significant interactions between them and with narrow bubble size distribution. In this flow condition, known as bubble or homogeneous flow, values of the diameter of the bubble d_b (taken equal to the diameter of a sphere having the same volume as the bubble) generally fall within the range $1\,\mathrm{m} \div 7\,\mathrm{m}$. The ascent path is mostly rectilinear, with minor transverse and axial oscillations (Abdulmouti, 2014). Whenever the gas phase velocity exceeds the aforementioned threshold, the density of the gaseous fraction in the liquid gradually increases, resulting in a greater interaction between the bubbles, with collisions, clusters formation and the occurrence of coalescence phenomena. The consequential appearance of larger bubbles significantly alters the hydrodynamic scenario, with the concomitant presence of large (more than 20 mm) and small bubbles. These latter rise rather fast ($1\,\mathrm{m\,s^{-1}} \div 2\,\mathrm{m\,s^{-1}}$) stirring the liquid. The name of churn flow (also known as heterogeneous flow) is due to the fact that the larger bubbles tend to churn up the liquid (Krishna and Van Baten, 2001). In this state, as the corresponding Reynolds numbers prove to be higher, spiraling and zigzagging motions can be observed. Moreover, due to this rather turbulent environment, large bubbles often do not count on a clear definition of their form which rather fluctuates quite casually. Nevertheless, some characteristic shapes can be identified, since the morphology of the bubbles is particularly a function of the diameter, speed and properties of the system. The work carried out by Grace (Grace, 1973) produced a well-known generalized graphical correlation (Fig. 3.5) that depicts the individual geometry of a single rising bubble in terms of three dimensionless numbers: Reynolds number, Eötvös number Eo and Morton number Mo.

$$\mathrm{Eo} = \frac{g(\rho_{\mathrm{L}} - \rho_{\mathrm{G}})d_b^2}{\sigma} \tag{3.38}$$

$$\mathrm{Mo} = \frac{g\mu_{\mathrm{L}}^4(\rho_{\mathrm{L}} - \rho_{\mathrm{G}})}{\rho_{\mathrm{L}}^2\sigma^2} \tag{3.39}$$

Note that, in this context, the characteristic length required to compute Reynolds number is d_b.

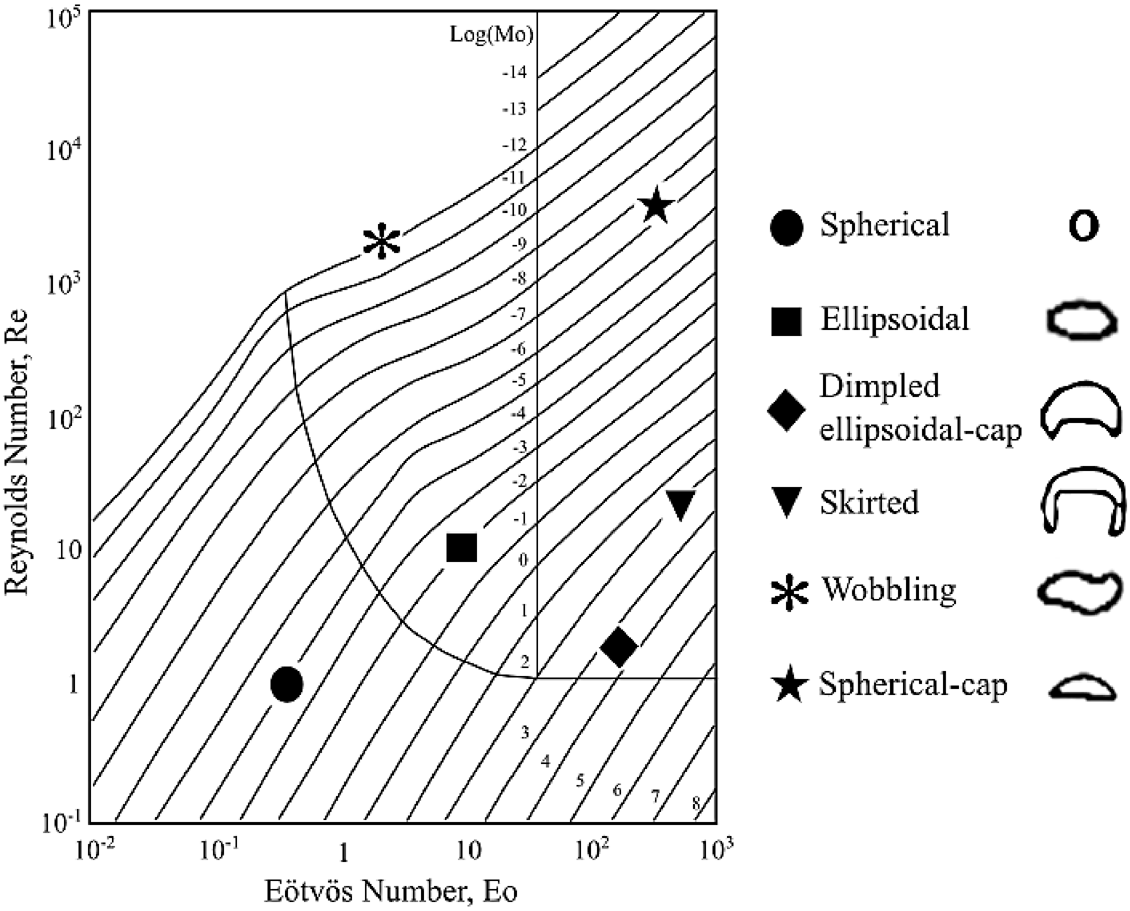

Fig. 3.5 Grace’s diagram (adapted from (Grace, 1973)).

By analyzing the diagram of Fig. 3.5, oftentimes called Grace’s diagram, one can surmise that the preferable shape is that of a spherical cap, given the high ratio between the exchange surface and the occupied volume. Proceeding with the reasoning, a zigzagging trajectory seems to be preferable, as it would extend the permanence time of the bubbles in the riser. The experimental survey reported bubbles having an average mean diameter of 7 mm with shapes that varied from spherical, especially at the bottom of the riser (as it is to be expected since the orifices from which gas is introduced are circular), to spherical caps. In Fig. 3.6, bubbles generated during one of the experimental runs are shown.

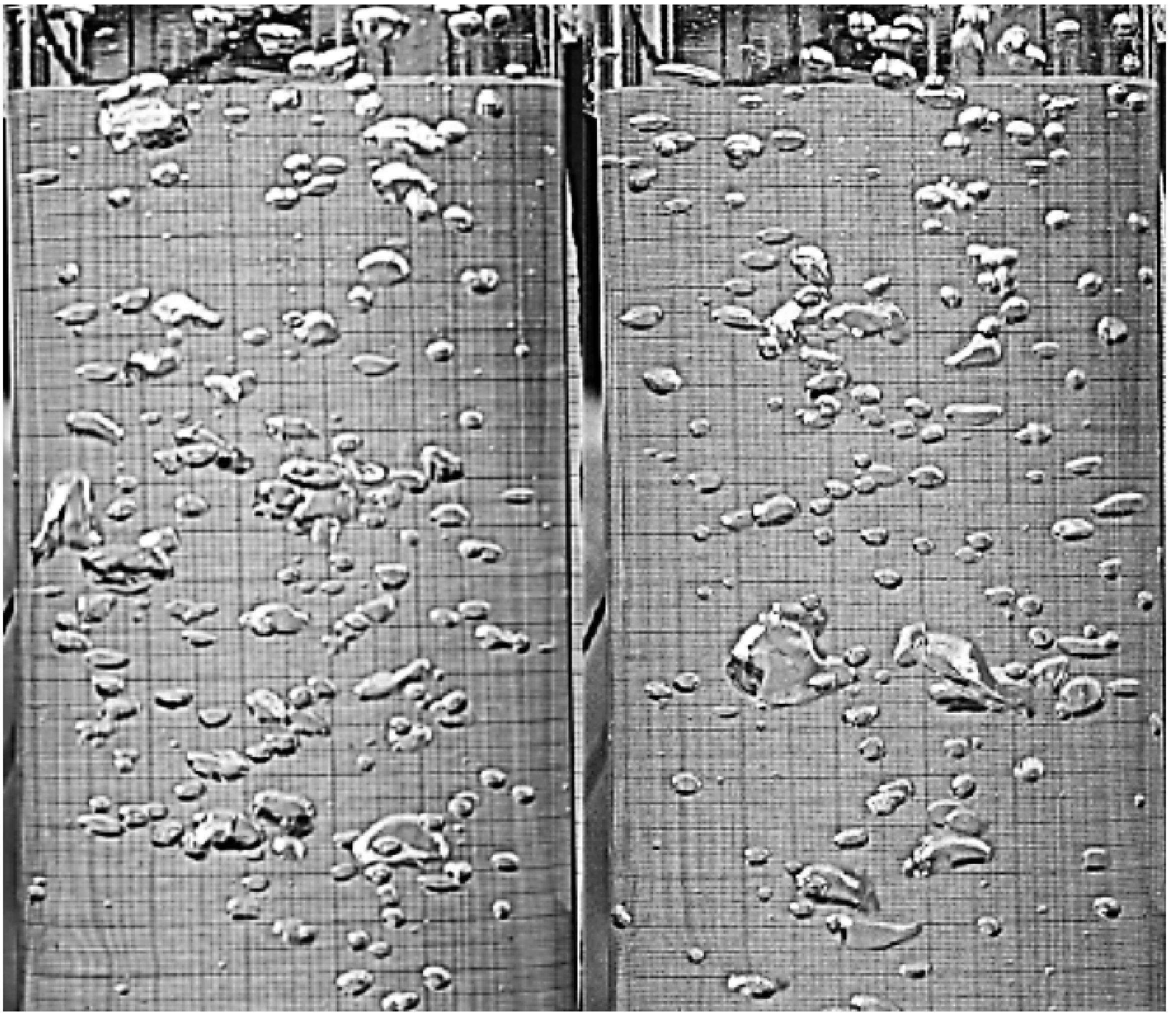

Fig. 3.6 Bubbles in the riser from the experimental campaign.

The overall computational model has been developed by gradually increasing the complexity of the simulated system: first, it followed a single bubble, with the final aim of considering multiple puffs of bubbles inserted in the computational domain at different times.

3.4 Simulation results with LSM

By virtue of the well-known volume loss problem by which the level set method is intrinsically affected, it has been necessary to introduce a correction apt to remedy such issue. With a mere relocation of the level set function, lowered or raised according to need, using a simple algorithm based on the bisection method, the simulation resulted more than satisfactory, as it can be noticed in Fig. 3.7.

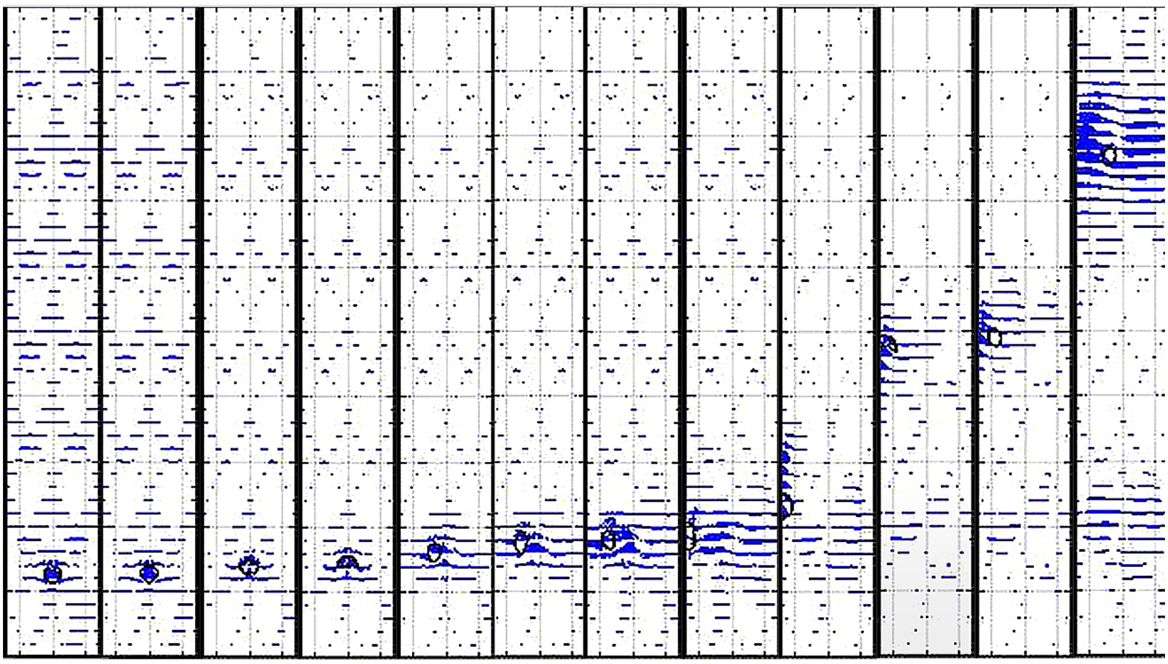

Fig. 3.7 Simulation of the single bubble dynamic in the riser with LSM modified relocation correction. On the background the speed plot of the liquid velocity field; vectors are auto-scaled as to not overlap.

Substantially, one can exploit the fact that, provided that the scheme for the convection of ϕ is sufficiently accurate, the error on the volume balance in each time step should be very small. In order to avoid the error accumulation, which instead leads to the significant observed losses, it is therefore advisable to apply the correction at each time step, at the same time paying attention not to alter the shape of the front. Presupposing a suitable rate of reinitialization of ϕ, in the proximity of the front, the level set function is the signed distance and therefore, in the vicinity of its zero iso-contour line, ϕ presents level sets approximately equidistant to each other. Then, by translating ϕ upward or downward by a signed constant ξ, which represents the distance between the original level set and the one after the translation, the volume (or area in two dimensions) occupied by the gas is conserved and the shapes of the interfaces are essentially unaltered (Fig. 3.8).

In order for this method to be reliable, ξ must be small (Smolianski, 2001). The algorithm counts the number of cells inside the interface at two successive times in order to judge if the latter has increased or decreased and therefore if it is necessary to lower or raise the zero-level set. The value of ξ is expected to be between zero and the maximum of the zero-level set, so one possibility is to use the bisection method within these two extremes.

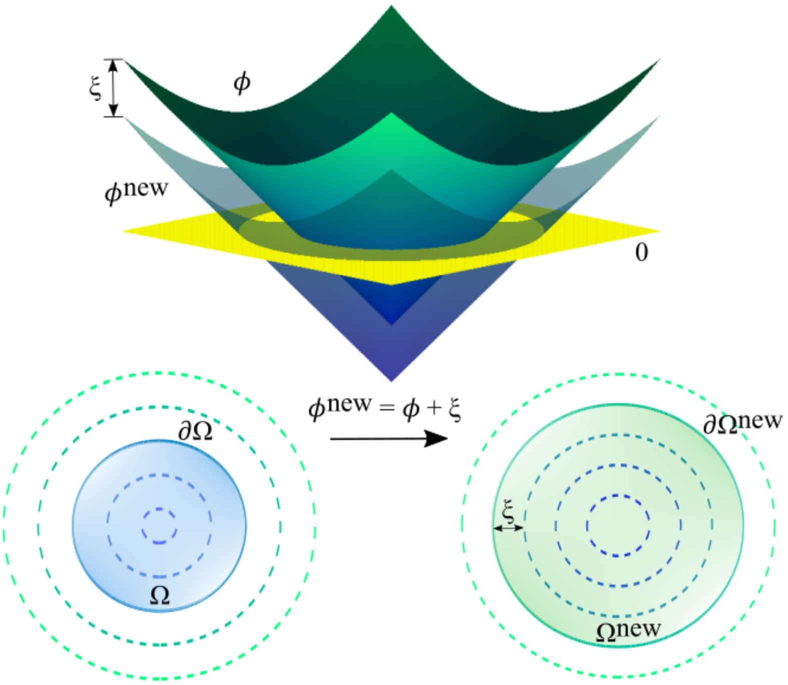

Fig. 3.8 Graphical illustration of the employed level set method correction strategy.

Although the precaution of inserting a correction on the balance of front volume worked just fine for the case of a single bubble, a further problem of distribution manifested in that of multiple bubbles: the number of grid cells standing within the fronts is preserved but the lost cells are typically added to the larger bubbles, without taking into account their position. The effect that follows is a sort of instantaneous transfer of matter, obviously devoid of physical meaning.

It is possible to circumvent this issue (Fig. 3.9a) as long as one simulates the evolution of multiple bubbles that begin their walk at the same time and the frequency with which the correction is performed is suitably reduced. In this way, it is even possible to achieve satisfying results, as evidenced by the good correspondence between the real picture and that obtained through simulation (Fig. 3.9b). Nevertheless, since this route is not sustainable, it is advisable to try to implement a different approach. With this in mind, the adoption of the so-called conservative level set method was decided.

3.5 Beyond LSM: the conservative level set method

The Conservative Level Set Method (CLSM), proposed by Olsson and Kreiss (Olsson et al., 2007; Olsson and Kreiss, 2005) entails the adoption of a different phase field function, employing ψ instead of ϕ, being

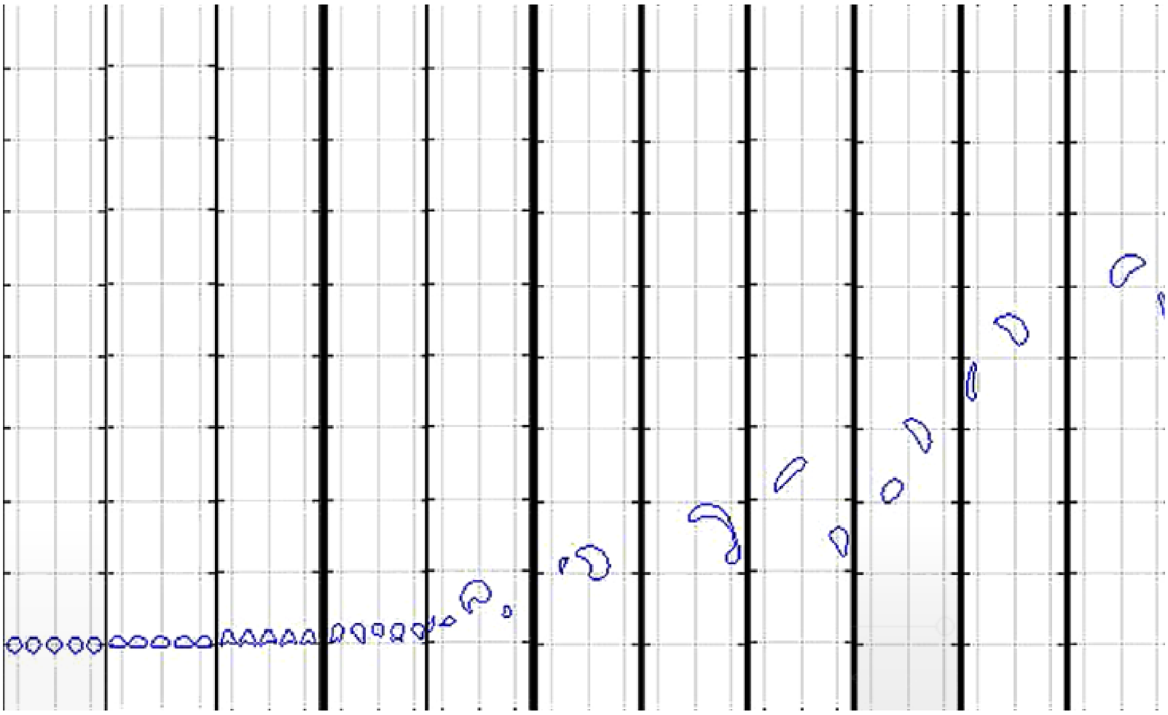

(a) Simulation of instantaneous puff behavior for a 5 bubbles flow inside the riser, with LSM modified with relocation correction. In order to obtain a clearer and more understandable picture of bubble dynamics, the quiver plot has been disabled.

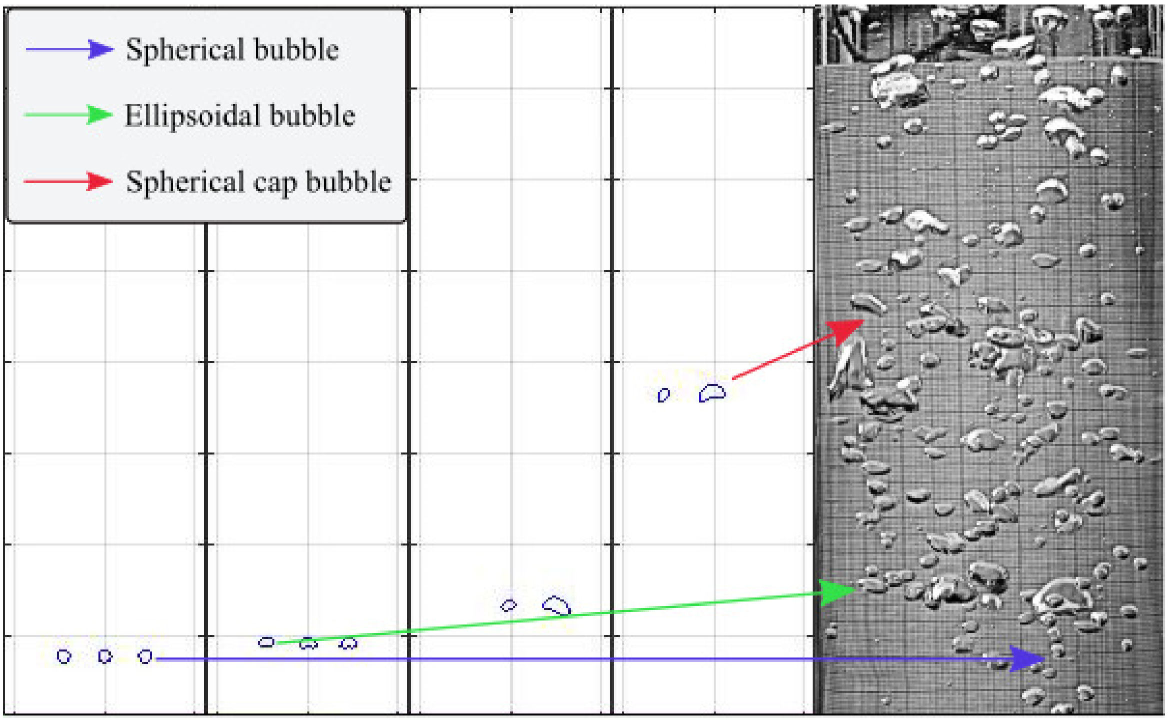

(b) Comparison between simulated bubbles (instantaneous puff behavior for a 3 bubbles flow) and experimental ones (Paladino et al., 2019).

Fig. 3.9 Simulation of multiple bubbles (LSM).

$$\psi(\mathbf{x},t) = H_\varepsilon(\phi(\mathbf{x},t)) \tag{3.40}$$

In this way, the position of the interface is implicitly represented, avoiding the need of computing both the step function and δ_ε. More importantly, if the advection of ψ is carried out in a conservative way, the volume bounded by the $\frac{1}{2}$ iso-surface is approximately preserved (exactly if one uses H instead of H_ε, but numerical issues would arise due to the nature of the sharp interface).

The function ψ is initialized as an hyperbolic tangent (Eqn. 3.41) of thickness ε as, for $\varepsilon \to 0$, it tends (Waclawczyk, 2015) to the exact Heaviside step function $H(\phi)$:

$$\psi(\mathbf{x},t) = \frac{1}{1+\exp\left(\dfrac{\phi(\mathbf{x},t)}{\varepsilon}\right)} = \frac{1}{2}\left(1+\tanh\left(\frac{\phi(\mathbf{x},t)}{2\varepsilon}\right)\right) \tag{3.41}$$

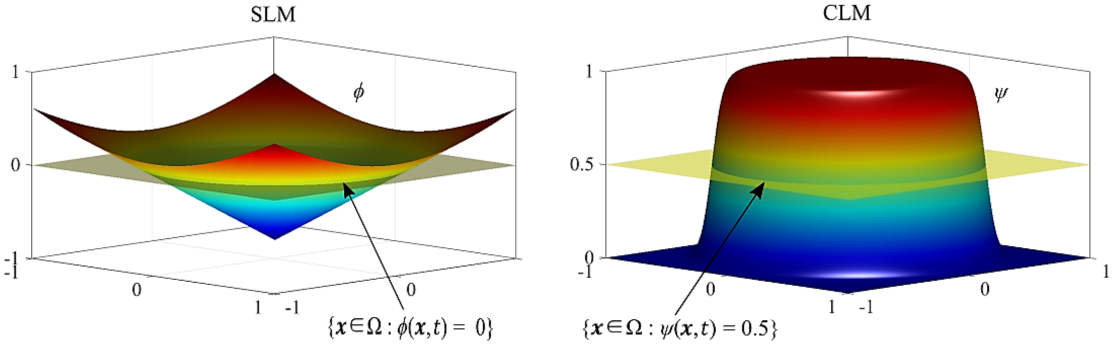

Fig. 3.10 LS (on the left) and CLS (on the right) functions.

The conservative level set method articulates in two steps. The first one, similarly to standard LSM, is the advection of the phase function, expressed as:

$$\frac{\partial\psi}{\partial t} + \mathbf{u}\cdot\nabla\psi = 0 \tag{3.42}$$

which, in the presence of a divergence-free flow field, one can reformulate as:

$$\frac{\partial\psi}{\partial t} + \nabla\cdot(\mathbf{u}\psi) = 0 \tag{3.43}$$

Eqn. 3.43 is a conservation equation and as such lends conservation properties to the algorithm.

The second step is the reinitialization, needed to regularize the shape of ψ and enhance numerical robustness. It consists in the resolution of the hyperbolic PDE Eqn. 3.44, comprised by a compressive limiter intended to sharpen the profile and a diffusive one in the normal direction, used to balance it and maintain the adequate interface thickness.

$$\frac{\partial \psi}{\partial \tau} + \nabla \cdot (\psi(1-\psi)\hat{\mathbf{n}}) = \varepsilon \nabla \cdot ((\nabla \psi \cdot \hat{\mathbf{n}})\hat{\mathbf{n}}) \tag{3.44}$$

The evolution equation Eqn. 3.44, reported in conservative form, has to be solved to steady state in an artificial time τ framework. CFL condition ensues for both advection and re-initialization steps.

In particular, when applying the artificial compression technique, Olsson and Kreiss (Olsson and Kreiss, 2005) suggested that

$$\Delta\tau \leq \frac{\mathrm{C}(\Delta x^2)}{\varepsilon} = 2\mathrm{C}(\Delta x)^{1+\varsigma} \tag{3.45}$$

with Courant number $\mathrm{C} = 0.25$, ε interface thickness and χ either 0 or very small (e.g. 0.1) for complicated flows. There, mesh size Δx was assumed uniform.

In the present research work, the choice was to use $\min(\Delta x, \Delta y)$ instead of Δx when dealing with the CFL condition in the rectangular space domain whilst exactly Δx when Ω is a square.

When implementing the CLSM, it was decided to precisely adopt this latter definition of Ω, for the reasons already explained in Section 3.2.

Besides, concerning the choice of the mesh size, a trade-off between volume conservation and accuracy emerges: if on the one hand smaller ε (Eqn. 3.46) implies better volume preservation and compliance with the CFL condition, on the other it entails a decrease in the order of accuracy. In fact, exceeding in setting ε to a small value can determine the formation of spurious oscillations, which in turn may damage the normal field by switching its direction.

$$\varepsilon = \frac{(\Delta x)^{1-\varsigma}}{2} \tag{3.46}$$

In their presentation of CLSM, Olsson and Kreiss (Olsson and Kreiss, 2005) attacked this problem by resorting to a second order TVD method with Superbee limiter; nevertheless in this way the overall accuracy of the method is affected (Chiodi and Desjardins, 2017).

As efficaciously explained by McCaslin and Desjardins (McCaslin and Desjardins, 2014), excessive re-initialization can damage the simulations results revealing equation stiffness. To relieve this degradation, Desjardins et al. (Desjardins et al., 2008) suggested a reconstruction of ϕ from ψ through Fast Marching Method (FMM), by which smooth normal field is obtained. Anyway, instead of resorting to this algorithm, called Accurate Conservative Level Set (ACLS), simplicity was here privileged over computational speed: we opted for a remapping of ψ by first restoring the steep profile of the Heaviside step function, and then smearing it out with a Gaussian filter (Fig. 3.11). Since this causes volume loss, in order not to waste the benefits of using CLSM, it was decided to couple it with the correction by translation of the level set function already used in the LSM.

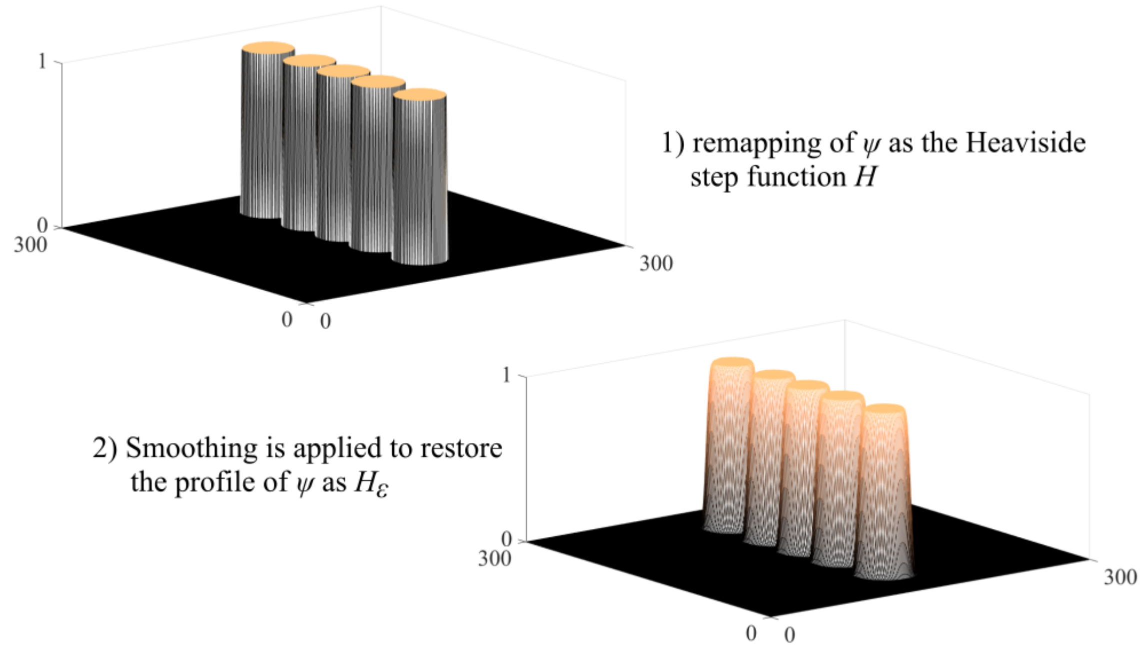

Fig. 3.11 Remapping of the CLSM function ψ.

Simulations were carried out on the regular square grid made up by 300 × 300 points, $\Omega = d_\mathrm{r} \times d_\mathrm{r}$, with Dirichlet boundary conditions for each edge of the computational domain. In particular, no-slip conditions were applied in both directions to the southern and western edges, to the upper half on the eastern boundary. The definition is instead trickier on the northern boundary. It was then decided to impose vertical component velocity of the same value of the mean liquid velocity measured experimentally in the riser $v_{\mathrm{L,r}}$ added with Gaussian White Noise (GWN, zero mean, $0.05 \cdot v_{\mathrm{L,r}}$ variance), whilst pure GWN was used to introduce small aleatory deviations in the x-direction. The same stratagem was employed to model the components of the imposed velocity profile on the eastern edge in the lower half. In particular, $\mathbf{u}_y$ is described as GWN and $\mathbf{u}_x$ the sum of mean liquid velocity in the collector $v_{\mathrm{L,c}}$ and GWN.

The resulting velocity field, for one of the simulated diffuser positions, is depicted in Fig. 3.12. Some snapshots of an exemplary simulation, referred to a puff of 5 initially spherical bubbles, are instead reported in Fig. 3.13.Indeed, the problem of the unphysical mass transfer has been overcome through the use of CLSM.

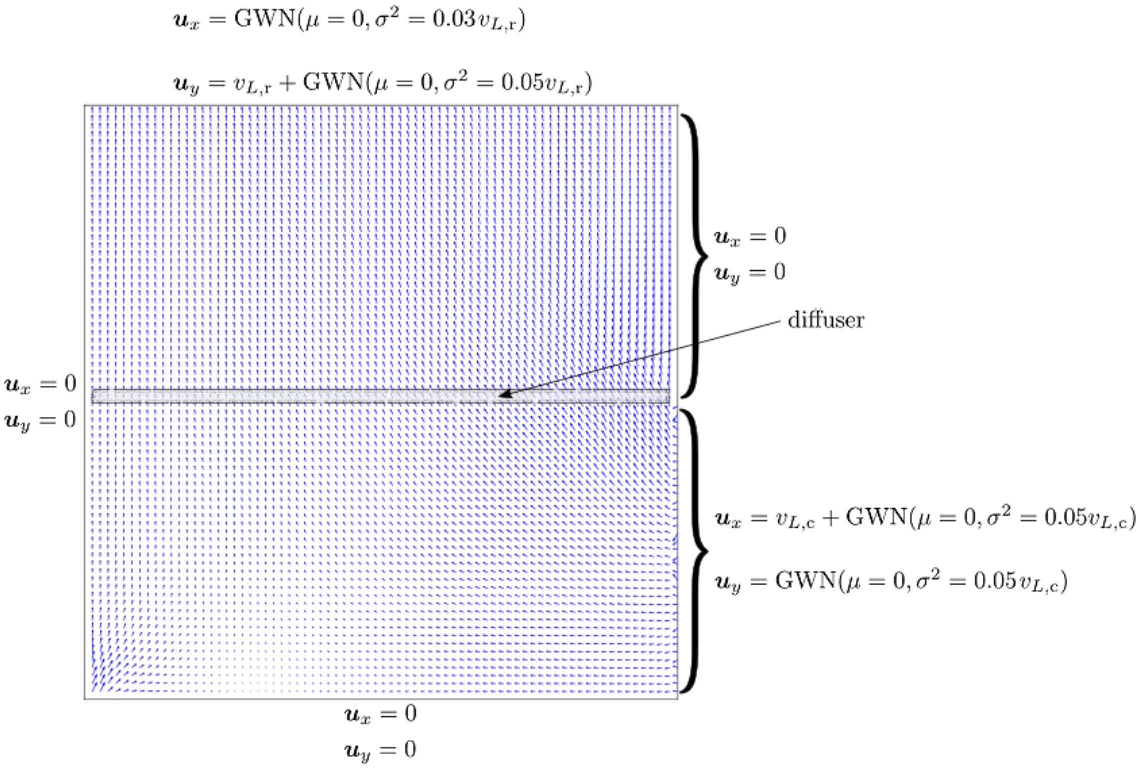

Fig. 3.12 Velocity field at simulation starting time. The position of the diffuser assumed for this simulation is highlighted. For the sake of clarity the grid is 150 × 150 instead of 300 × 300. In the figure, μ is the mean whilst σ^2 is the variance.

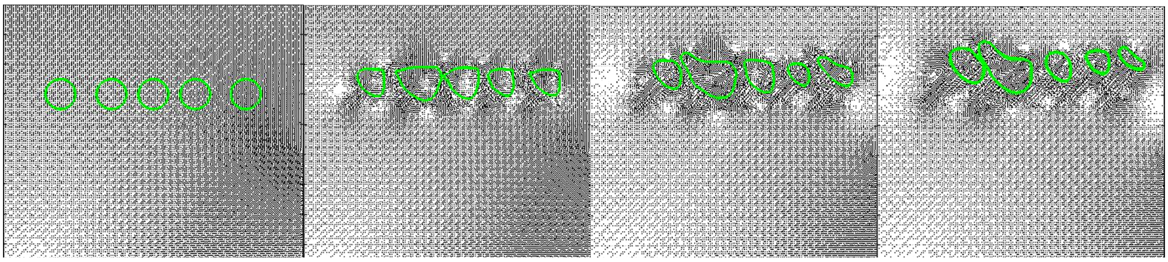

Fig. 3.13 Simulation of instantaneous puff behavior for a 5 bubbles flow inside the riser, with CLSM.

References

Abdulmouti, H., 2014. Bubbly Two-Phase Flow: Part I- Characteristics, Structures, Behaviors and Flow Patterns. American Journal of Fluid Dynamics 4, 194–240.

AL-Mashhadani, M.K.H., Wilkinson, S.J., Zimmerman, W.B., 2015. Airlift bioreactor for biological applications with microbubble mediated transport processes. Chemical Engineering Science 137, 243–253.

Batchelor, G.K., 2000. An Introduction to Fluid Dynamics. Cambridge University Press.

Brackbill, J.U., Kothe, D.B., Zemach, C., 1992. A continuum method for modeling surface tension. Journal of Computational Physics 100, 335–354.

Chiodi, R., Desjardins, O., 2017. A reformulation of the conservative level set reinitialization equation for accurate and robust simulation of complex multiphase flows. Journal of Computational Physics 343, 186–200.

Chorin, A.J., 1968. Numerical Solution of the Navier-Stokes Equations. Mathematics of Computation 22, 745–762.

Chorin, A.J., Marsden, J.E., 1990. A Mathematical Introduction to Fluid Mechanics, 2nd ed, Texts in Applied Mathematics. Springer-Verlag, New York.

Desjardins, O., Moureau, V., Pitsch, H., 2008. An accurate conservative level set/ghost fluid method for simulating turbulent atomization. Journal of Computational Physics 227, 8395–8416.

Dukowicz, J.K., 1981. Lagrangian fluid dynamics using the Voronoi-Delauanay mesh (No. LA-UR–81-1421). Los Alamos Scientific Lab., Los Alamos, NM.

Fritsching, U., Li, X., 2016. Spray Systems, in: Crowe, C.T. (Ed.), Multiphase Flow Handbook. CRC Press, New York, USA, pp. 1091–1249.

Grace, J.R., 1973. Shapes and Velocities of Bubbles Rising in Infinite Liquids. Transactions of the Institution of Chemical Engineering 51, 116–120.

Hartmann, D., Meinke, M., Schröder, W., 2008. Differential equation based constrained reinitialization for level set methods. Journal of Computational Physics 227, 6821–6845.

Krishna, R., Van Baten, J.M., 2001. Scaling up Bubble Column Reactors with the Aid of CFD. Chemical Engineering Research and Design, Particle Technology 79, 283–309.

Loth, E., 2016. Overview of Numerical Approaches, in: Crowe, C.T. (Ed.), Multiphase Flow Handbook. CRC Press, New York, USA, pp. 79–95.

McCaslin, J.O., Desjardins, O., 2014. A localized re-initialization equation for the conservative level set method. Journal of Computational Physics 262, 408–426.

Mitchell, I.M., 2008. The Flexible, Extensible and Efficient Toolbox of Level Set Methods. J Sci Comput 35, 300–329.

Olsson, E., Kreiss, G., 2005. A conservative level set method for two phase flow. Journal of Computational Physics 210, 225–246.

Olsson, E., Kreiss, G., Zahedi, S., 2007. A conservative level set method for two phase flow II. Journal of Computational Physics 225, 785–807.

Osher, S., Fedkiw, R., 2003. Level Set Methods and Dynamic Implicit Surfaces, Applied Mathematical Sciences. Springer-Verlag, New York.

Paladino, O., Hodaifa, G., Neviani, M., Seyedsalehi, M., Malvis, A., 2019. Modelling in Environmental Interfaces, in: Kyzas, G.Z. (Ed.), Advanced Low-Cost Separation Techniques in Interface Science. Elsevier, London, UK.

Pnueli, D., Gutfinger, C., 1997. Fluid Mechanics. Cambridge University Press.

Popinet, S., 2018. Numerical Models of Surface Tension. Annual Review of Fluid Mechanics 50, 49–75.

Prosperetti, A., Tryggvason, G., 2009. Computational Methods for Multiphase Flow. Cambridge University Press.

Saci, F., Nouri, F.Z., 2013. The projection method for fluid flows in complex geometries. Applied Mathematical Sciences 7, 4605–4615.

Seibold, B., 2008. A compact and fast Matlab code solving the incompressible Navier-Stokes equations on rectangular domains.

Seifollahi, M., Shirani, E., Ashgriz, N., 2008. An improved method for calculation of interface pressure force in PLIC-VOF methods. European Journal of Mechanics - B/Fluids 27, 1–23.

Sharma, A., 2015. Level set method for computational multi-fluid dynamics: A review on developments, applications and analysis. Sadhana 40, 627–652.

Smolianski, A., 2001. Numerical modeling of two-fluid interfacial flows (Ph.D. Thesis). University of Jyväskylä.

Strang, G., 2007. Computational Science and Engineering. Wellesley-Cambridge Press.

Sussman, M., Smereka, P., Osher, S., 1994. A Level Set Approach for Computing Solutions to Incompressible Two-Phase Flow. Journal of Computational Physics 114, 146–159.

Waclawczyk, T., 2015. A consistent solution of the reinitialization equation in the conservative level-set method. Journal of Computational Physics 299, 487–525.

Zhang, T., Zhao, B., Wang, J., 2006. Mathematical models for macro-scale mass transfer in airlift loop reactors. Chemical Engineering Journal.

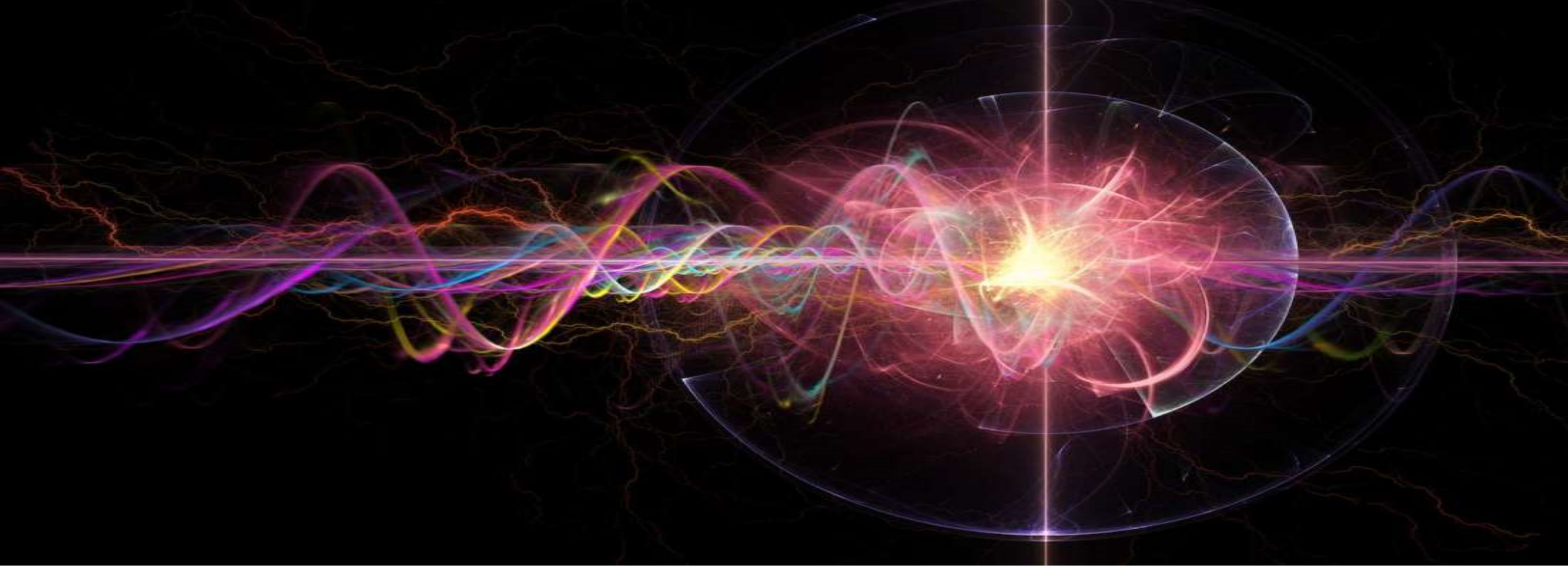

CHAPTER 4: THEORETICAL SCALE-UP

4.1 Theoretical background

In many fields of engineering, knowledge of the interdependence of the different parameters and quantities involved plays a major role in the resolution of design problems. In other terms, the determination of the function f which relates a certain physical quantity Q_0 to n others $Q_1, \ldots, Q_n$ is what is sought after.

$$Q_0 = f(Q_1, \ldots, Q_n) \tag{4.1}$$

Although in some cases it is possible to determine an analytic formulation of f by solving the equations that govern the phenomenon, this is not always true (or convenient); an extremely useful tool in the case of a more empirical study is the so-called Buckingham's π-theorem. In a nutshell, it asserts that it is possible to reformulate a physical law interconnecting some physical quantities as a function of dimensionless numbers, historically indicated as π (from which the name of the theorem derives) (Curtis et al., 1982). More precisely, it proclaims how the relation f that binds $n+1$ physical quantities can be rewritten as a new function $f^\star$ between $n+1-m$ pure numbers, being m the maximum number of dimensionally independent quantities that can be identified within the $n+1$ quantities $Q_1, \ldots, Q_n$.

$$\pi_0 = f^\star(\pi_1, \ldots, \pi_{n-m}) \tag{4.2}$$

Since m quantities are said to be dimensionally independent (fundamental quantities) whether having a dimensionless monomial $Q_1^\alpha Q_2^\beta \ldots Q_m^\omega$ implies $\alpha = \beta = \cdots = \omega = 0$, one can proceed to identify the monomial $Q_1^{\alpha_0} Q_2^{\beta_0} \ldots Q_m^{\omega_0}$ endowed with the same dimensions as Q_0 while imposing the condition that the exponents $\alpha_0, \ldots, \omega_0$ are not all zero. By dividing both members of the starting Eqn. 4.1 for this monomial, a dimensionless term is obtained:

$$\frac{Q_0}{Q_1^{\alpha_0} Q_2^{\beta_0} \dots Q_m^{\omega_0}} = f_0(Q_1, \dots, Q_n) = \pi_0 \tag{4.3}$$

An analogous thinking leads to realize that

$$\pi_0 = f_1(Q_1, \dots, Q_m, \pi_{m+1}, Q_{m+2}, \dots, Q_n) \tag{4.4}$$

since

$$\frac{Q_{m+1}}{Q_1^{\alpha_{m+1}} \dots Q_m^{\omega_{m+1}}} Q_1^{\alpha_{m+1}} \dots Q_m^{\omega_{m+1}} = \pi_{m+1} Q_1^{\alpha_{m+1}} \dots Q_m^{\omega_{m+1}} \tag{4.5}$$

By repeating this procedure for $Q_{m+2}, \dots, Q_n$, relation Eqn. 4.6 is attained.

$$\pi_0 = f_{n-m}(Q_1, \dots, Q_m, \pi_{m+1}, \dots, \pi_n) \tag{4.6}$$

Recalling that $Q_1, \dots, Q_m$ are dimensionally independent whilst $\pi_0, \pi_{m+1}, \dots, \pi_n$ are dimensionless, it can be inferred that f_{n-m} cannot explicitly depend on $Q_1, \dots, Q_m$, thus concluding that Eqn. 4.1 becomes Eqn. 4.2.

Since exploiting the condition on monomial exponents leads to the resolution of a homogeneous linear system, the process of π-numbers identification can be translated in the assembly and reduction of a $m \times n$ dimensional matrix $\mathbf{A}$, the elements of which are the dimensional exponents of the physical quantities pertinent to the considered problem. In fact, the homogeneous linear system can be obviously summarized as

$$\mathbf{A}\mathbf{x} = \mathbf{0} \tag{4.7}$$

where $\mathbf{x}$ is the $n \times 1$ column vector of the exponents of the considered physical quantities $Q_1, \dots, Q_n$ and $\mathbf{0}$ is the zero vector. Then, linear algebra comes in handy to better understand the meaning of the adimensionalization procedure. Given that any matrix represents a homomorphism between vector spaces and that the dimension of the kernel of $\mathbf{A}$, namely its nullity $\mathscr{N}(\mathbf{A})$, can be individuated by solving the homogeneous system Eqn. 4.7, as identifying the solutions allows to pinpoint a basis of $\ker(\mathbf{A})$, the rank-nullity theorem informs that $n = \mathscr{N}(\mathbf{A}) + \operatorname{rank}(\mathbf{A})$, being $\operatorname{rank}(\mathbf{A})$ the rank of $\mathbf{A}$. Note that in most cases $\operatorname{rank}(\mathbf{A}) = m$ (for an example where this characteristics does not hold see Section 7.1.11 of (Szirtes and Rózsa, 2007)); hence the widespread enunciation of Buckingham's theorem with reference simply to the number m of fundamental quantities. It follows that there is a $n - \operatorname{rank}(\mathbf{A})$ dimensional subspace of possible exponents $\mathbf{x}$ that constitutes a solution of

Eqn. 4.7, meaning that a basis of the null space of $\mathbf{A}$, composed by $n - \text{rank}(\mathbf{A})$ sets of exponents giving as many dimensionless groups π, can be determined. Obviously, since the definition of a basis of a vector space is not univocal, different dimensionless numbers may be identified depending on how the dimensional matrix was formed. Nevertheless, the pivotal point is that the space spanned by such vectors is scale invariant, laying the foundations of a reliable scaling.

4.2 Method of scale-up

According to Levin (Levin, 2001) and Zlokarnik (Zlokarnik, 2006) among others, the dimensional matrix can be thought as composed by two sub-matrices: the core matrix, which is a square one, and a residual matrix. Following this idea, it results that each element of the residual matrix will appear only in one dimensionless number whereas this restriction does not necessarily hold for the elements of the core matrix. Once the core matrix is completely reduced to the unit matrix $\mathbf{I}$ (by performing Gauss-Jordan reduction) π-numbers are obtained: each element of the residual matrix constitutes the numerator of the fractional dimensionless number whilst those of the core matrix, raised to the power indicated in the residual matrix, form the denominator, thus finding a relationship of the form of Eqn. 4.3.

Summarizing, performing dimensional analysis could be done by drafting a relevance list of all physical quantities – even constant ones – and variables for the considered process, followed by the assembly and reduction of the dimensional matrix.

In spite of the usefulness of scaling (in particular for the scale-up) performed by the means of the π-theorem, industries typically resort to other approaches. This is especially true for the chemical and petrochemical sectors, where oftentimes process modeling is viewed, possibly in synergy with piloting, as the primary scale-up tool. Such a choice is ideally corroborated by the record of success in applying such method. A more pragmatic interpretation on the lack of use of the π-theorem in industry field applications is just the difficulty in attacking scale-up problems with rigorous methodology, especially when phenomena underlying a process are complex. In this sense, a potential source of error can be identified in the selection of the main variables for the studied phenomena – a necessary step in performing accurate scale-up – since the task is not trivial. Nevertheless, a crucial virtue of performing theoretical scale-up lays in the fact that the definition of non-dimensional parameters allows an excellent generalizability of the developed model. This quality may very well end up in determining time and economic savings.

However, oftentimes, since establishing perfect similarity is highly improbable, partial similarities between systems at different scales are sought after, the main ones being geometric, kinematic and dynamic similarities. To do so for known phenomena and processes, one can rely on already identified dimensionless numbers, without passing through the application of the π-theorem.

In the following sections, the rigorous scale-up procedure just discussed will be shown as it was applied to both to microalgae growth in photobioreactors and to the polyphenols extraction process discussed in Chapter 2.

4.3 Scale-up of a microalgae cultivation system

In Chapter 1 the importance of a holistic view of interdependencies between waste flows and production processes for the purpose of implementing the circular economy was profusely discussed. In this sense, the leading role performed by the biorefineries and the potentialities of microalgae biomass have been highlighted. The concept of an integrated biorefinery that involves the cultivation of microalgae in airlift photobioreactors has therefore been presented. Of the three main sub-processes entailed by such a closed loop process, the one regarding microalgal biomass production in ALRs is the most critical one (see Section 1.4.1.2). Despite the fact that nowadays most scale-ups of reactors are executed with the aid of computers and simulative models, a complete simulation that simultaneously accounts for all the phenomena affecting the reactor behavior and its performance is challenging and, especially for ALRs, it is avoided. During operation, residence times into the different zones of the reactor must contemporary guarantee good mass transfer, the best CO_2 distribution and O_2 release possible on top of optimal light/dark cycles that can be guaranteed with part of the ALR made of not-transparent material. For these reasons, a pilot-scale experimental test planning is mandatory in order to correctly set up and tune process variables before the final plant installation. Moreover, even if design was optimized, in some cases the final operating conditions differ from the designed ones due to the biological nature of the reactants and the complexity of the system.

Even if theoretical scale-up procedures from batch mixed photobioreactors at lab-scale to ALRs at pilot scale are not usually carried out, the approach hereby adopted proposes to use the π-theorem to define the main dimensionless groups at lab scale and to keep their values as desired at pilot scale (Figure 4.1). Thus, since due to their hydrodynamics ALRs offer more degrees of freedom than Stirred Tank Reactors (STRs), some of these values can be tuned inside the identified ranges of the operating variables, then assuring a good continuous operation of the ALRs as components of the integrated pilot-scale biorefinery.

More details on the materials employed for the experimental test are provided in Appendix B.

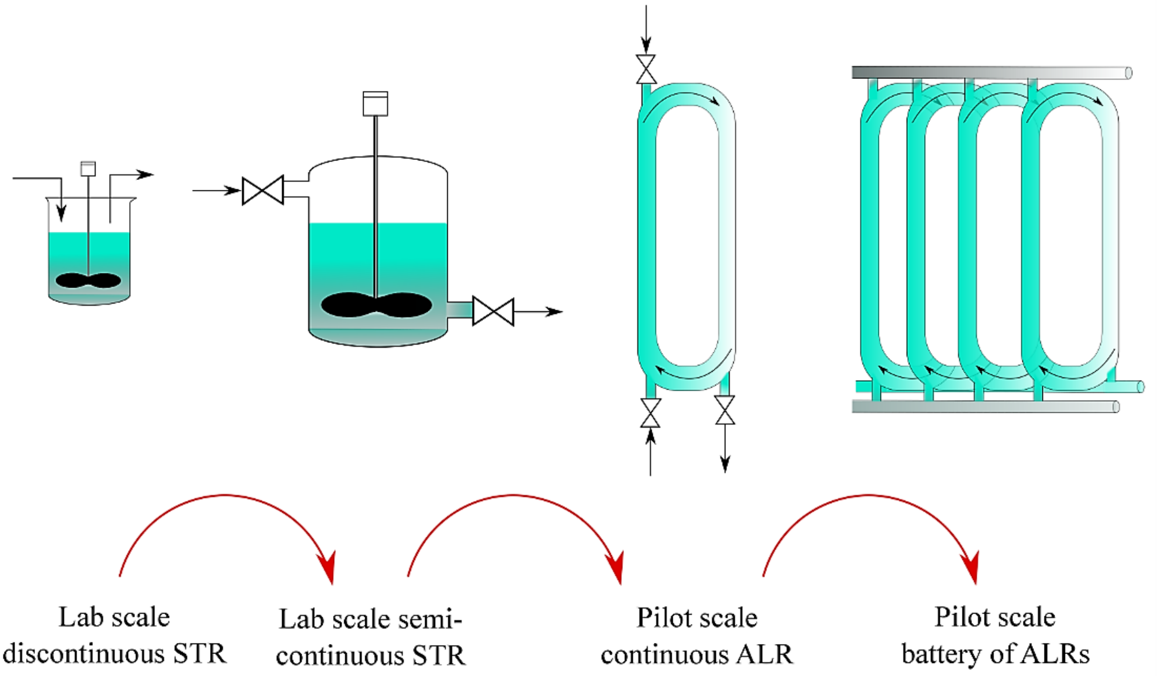

Fig. 4.1 Schematic representation of the microalgae culture process intended scale-up.

4.3.1 Outlining of the relevance list for batch microalgae growth in STRs

The relevance list has many common elements both for airlift photobioreactors and the lab-scale stirred ones, as the main aspects to cope with are fluid dynamics, mass transfer and light conditions. Moreover, geometric factors should be taken into account as well.

Generally speaking, from the point of view of dimensional analysis, chemical engineering problems refer to a 5-parametric dimensional system: [M, L, T, Θ, N] where [M] is mass, [L] is length, [T] is time, [N] is the amount of substance and [Θ] is temperature, 5 of the 7 base units of the International System of Units (SI). The whole list of such fundamental quantities is reported in Table 4.1.

While mass and heat transfer are scale dependent, the same cannot be said of thermodynamics laws and stoichiometry. A simplification is hereinafter employed, as the process of algae nurturing is assumed isothermal. This entails that the process relationships obtained though dimensional analysis are valid for any constant process temperature to which the numerical values of the physical properties are related.

In the first place, let us consider the problem of scaling up the lab scale cultivation of microalgae in a batch stirred reactor. Flow field characterization is inferable, in first approximation, on the base of two material properties, namely fluid density ρ and dynamic

Table 4.1 Base quantities and dimensions used in the SI (BIPM et al, 2008).

Base quantity	Symbol for dimension	SI base unit – symbol
Length	L	meter - m
Mass	M	kilogram - kg
Time	T	second - s
Electric current	I	Ampére - A
Temperature	Θ	Kelvin - K
Amount of substance	N	mole - mol
Luminous intensity	I_v	candela - cd

viscosity μ, two geometric parameters, i.e. the diameters of the reactor d and of the stirrer d_s, and a process one, the stirrer speed n. The list can be reduced by lumping together ρ and μ and considering in their place the kinematic viscosity $\nu = \mu\rho^{-1}$.

To identify the variables controlling the biochemical aspect of the process is more delicate. In order to try and develop a convincing mathematical description of microalgae growth, numerous studies have been carried out over the years, producing a wide cosmos of models, ranging from the well-known Monod equation to far more complex ones. A thorough review of such models is found in Lee et al. (Lee et al., 2015). However, it is known that microalgae growth depends on multiple factors, mainly temperature, pH, dissolved oxygen and CO_2 concentrations, availability of nutrients (in particular nitrogen and phosphorus) and light. It follows that the substrate concentration S can be added to the relevance list. Nevertheless, since T does not vary due to the adopted quasi-constant temperature condition, this parameter can be excluded from the relevance list as it does not directly alter the others.

Since pH is mathematically defined as the common logarithm of the reciprocal of the proton activity in an aqueous solution and activity is deemed a dimensionless number, pH is a dimensionless number as well. Thus, it can be considered as a π-number and be excluded from the list.

The concentration of dissolved oxygen (DO_x) in water is influenced by a number of factors, including water temperature, salinity and atmospheric pressure. As alkalinity of the aqueous solution is measured by pH and regulates chemical equilibrium, the aforementioned concentration can be thought of as functions precisely of pH other than the overall mass-transfer coefficient K_{OG} and oxygen concentrations. Ditto for dissolved CO_2 concentration. Carbon dioxide diffusion coefficient D is taken into account as well (diffusion coefficient in water, neglecting the effects of solutes dissolved in the culture medium). Hereinafter, CO_2 is assumed to be the only substrate. In addition, two more biotic factors should be accounted for: microalgae initial concentration and actual microalgae concentration, as the latter can indicate self-shading and thus autoinhibition.

To model algae growth, kinetic models oftentimes resort to a formulation comprising a pseudo-first order constant k_1, of dimension [T^{-1}], and a second kinetic constant related to the asymptotic behavior of the concentration, i.e. the maximum concentration obtainable [M L^{-3}]. Since Beruto's kinetic model (Beruto et al., 2014) will be used for estimating the global kinetics of *C. Vulgaris* (the cultivated microalgae species) growth, this second constant will hereinafter be denoted as k_a.

Finally, light plays a vital role, as luminous energy cannot be stored by microalgae and thus needs to be provided adequately. According to the Tamiya model (Tamiya et al., 1953), which is probably the most widely applied algae growth model among those taking light conditions into consideration, light-related parameter are a saturation constant K_I and the incident light intensity I. To be precise, however, incident light intensity on microalgae cells can be described by means of the Lambert-Beer law, which states that $I = I_0 \exp(-\varepsilon_a c l)$, where I_0 is the light intensity entering the material composing the reactor walls excluding surface reflection, ε_a is the absorption per concentration coefficient, c is the concentration of the absorbing material and l is the path length. In this case, one can assume that $l = d$.

Nevertheless, since the experimental campaign was conducted under controlled light conditions, the resulting dimensionless numbers, i.e. absorbance $\mathrm{A} = \varepsilon_a d c$ and the ratio $K_I I_0^{-1}$, are already fixed and thus not considered in this scale-up.

An additional operative hypothesis is that all parameters are uniform, i.e. perfect mixing is assumed.

Overall, the reference list for the scaling of microalgae farming in a stirred, transparent batch reactor is the one reported in Table 4.2.

4.3.2 Determination of the dimensionless numbers for batch microalgae growth in STRs

The relevance list consists of 14 parameters hinging on 4 SI base quantities: [L], [M], [T], [N]. It follows that $12 - 4 = 8$ non-dimensional numbers are to be expected. It has to be remembered though that pH was an important variable too but, due to its pure number character, it was enlisted in the π-number list a priori. Thus, the π-space will be spanned by 9 π-numbers. At least other 4 trivial dimensionless numbers can be pinpointed beforehand: the purely geometrical ratio $d_s d^{-1}$ and the ratios $\mathrm{DO_x} S^{-1}$, $c c_0^{-1}$ and the kinetic constant ratio $k_a c_0^{-1}$. Hence, 4 more π-numbers have to be ascertained.

Table 4.2 Relevance list for batch microalgae growth in STRs.

Geometric parameters		Diameter of the reactor d	[L]
		Diameter of the stirrer d_s	[L]
Physical properties	*Fluid dynamics*	Kinematic viscosity ν	[L^2T^{-1}]
	Mass transfer	Microalgae concentration c	[M^1L^{-3}]
		Microalgae initial concentration c_0	[M^1L^{-3}]
		Diffusion coefficient D	[L^2T^{-1}]
		Substrate concentration S	[$L^{-3}N^1$]
		Dissolved oxygen concentration DO_x	[$L^{-3}N^1$]
		Overall mass-transport coefficient K_{OL} or K_{OG}	[L^1T^{-1}]
		Maximum specific growth rate k_a	[T^{-1}]
		Grow rate k_1	[T^{-1}]
Process parameters		Stirrer speed n	[T^{-1}]

A final note regards the choice of the characteristic length inserted in the dimensional matrix. For an STR the usually adopted representative scale is the stirrer diameter, so it would make sense to use precisely that. However, when dealing with variations in type of employed devices, the need of using different characteristic lengths may arise (e.g. for an ALR, where the impeller is absent, one could focus on the sparger diameter or on bubble diameter). To keep the discussion more general, here the reactor diameter d was employed. This choice is not relevant from a theoretical perspective, since it is possible to switch a posteriori the characteristic lengths by conveniently combining dimensionless groups.

$$\begin{array}{|c|cccc|cccc|}
\hline
 & c & d & \mathrm{n} & S & \nu & D & K_{\mathrm{OL}} & k_1 \\
\hline
M & 1 & 0 & 0 & 0 & 0 & 0 & 0 & 0 \\
L & -3 & 1 & 0 & -3 & 2 & 2 & 1 & 0 \\
T & 0 & 0 & -1 & 0 & -1 & -1 & -1 & -1 \\
N & 0 & 0 & 0 & 1 & 0 & 0 & 0 & 0 \\
\hline
\end{array} \tag{4.8}$$

By the means of the Gaussian reduction algorithm, the matrix is easily found to be equivalent to:

$$\begin{array}{|c|cccc|cccc|}
\hline
 & c & d & \mathrm{n} & S & \nu & D & K_{\mathrm{OL}} & k_1 \\
\hline
M & 1 & 0 & 0 & 0 & 0 & 0 & 0 & 0 \\
L & 0 & 1 & 0 & 0 & 2 & 2 & 1 & 0 \\
T & 0 & 0 & 1 & 0 & 1 & 1 & 1 & 1 \\
N & 0 & 0 & 0 & 1 & 0 & 0 & 0 & 0 \\
\hline
\end{array} \tag{4.9}$$

The following π-numbers ensue:

$$\pi_1 = \frac{\nu}{d^2\mathrm{n}} = \frac{\mu}{\rho d^2\mathrm{n}} = \mathrm{Re}^{-1} \tag{4.10}$$

$$\pi_2 = \frac{D}{d^2\mathrm{n}} \tag{4.11}$$

$$\pi_3 = \frac{K_{\mathrm{OL}}}{d\mathrm{n}} \tag{4.12}$$

$$\pi_4 = \frac{k_1}{\mathrm{n}} \tag{4.13}$$

π_1 is the reciprocal of the impeller Reynolds number. The number π_2 can be rewritten in a different way resorting to π_4, gaining a different interpretation in the process; the reciprocal of the Damköhler number $\mathrm{Da}_{\mathrm{II}}$ appears:

$$\frac{\pi_2}{\pi_4} = \frac{D}{k_1} = \mathrm{Da}_{\mathrm{II}}{}^{-1} \tag{4.14}$$

Analogously, by combining π_2 and π_3, Sherwood number is found:

$$\frac{\pi_3}{\pi_2} = \frac{K_{\mathrm{OL}}d}{D} = \mathrm{Sh} \tag{4.15}$$

Concluding, the complete set of dimensionless groups describing the problem at hand is:

$$\left\{ \mathrm{Re}, \mathrm{Da}_{\mathrm{II}}, \mathrm{Sh}, \frac{k_1}{\mathrm{n}}, \mathrm{pH}, \frac{d_s}{d}, \frac{c}{c_0}, \frac{\mathrm{DO_x}}{S}, \frac{k_a}{c_0} \right\} \tag{4.16}$$

4.3.3 Outlining of the relevance list for microalgae growth in ALRs

When considering an external loop ALR, it is clear that the scaling hinges also on parameters that are different than those characterizing DSTRs. For one, no moving part is involved as they belong to the pneumatically agitated reactors. Since their functioning, much like bubble columns, rests on the exploitation of the density difference between gas and liquid phase to trigger a swirling motion of natural circulation, physical properties such as density and viscosity have to be taken into account for both phases. If the subscript G indicates the gas phase and L the liquid one, one can add to the relevance list the weight difference $g(\rho_{\mathrm{L}} - \rho_{\mathrm{G}}) = g\Delta\rho$ that set the circulation in motion. Moreover, surface tension, and hence its coefficient σ, cannot be overlooked.

Similarly to what has been said for stirred reactors, geometrical parameters need to be considered, all the more so that operation of ALRs pivots on the flow regimes of the involved phases. Column diameter and height probably are the first ones that come to mind although one should possibly consider the geometry of the system, meaning geometric parameters referred to riser, downcomer and the two horizontal collectors. On the top of that, gassed liquid height plays an important rule and is related to the gas hold-up ε, in turn linked to volumetric mass transfer coefficient k_{G} a through a direct proportionality relationship (Zlokarnik, 2006). ε is already dimensionless, thus it is legit to add it directly to the π-number list. Sparger nozzle diameter should be considered as well, since it is related to bubble equivalent diameter d_B, a crucial variable for the fluid dynamics inside the riser. Gas surficial velocity v_{G}, is enlisted as well.

The relevance list should contain then an unknown number ϖ apt to describe the coalescence behavior of finely dispersed gas bubbles and by this, indirectly, their hold-up in the liquid. Nevertheless, since such a number would be dependent on unknown properties of unknown dimension and number, it cannot be comprised in the dimensional matrix. However, this causes no issue since, with the known relevant physical properties ρ, μ and σ, one will always be able to transform ϖ to the dimensionless numbers $\varpi^{\star}$ (Zlokarnik, 2006).

The arguments made for the DSTR in Section 4.3.1 regarding light and algae growth parameters also apply to this case.

Table 4.3 shows the relevance list drafted for the microalgae growth process in an ALR.

4.3.4 Determination of the dimensionless numbers for microalgae growth in ALRs

Theoretically speaking, the relevance list should count more than 18 parameters that can be described through the use of 5 base quantities: length [L], mass [M], time [T], amount of substance [N] and luminous intensity [J]. On the other hand, due to the controlled light conditions, parameters functions of this latter aspect can be overlooked once again. ε was deemed a priori-known π-number, much like pH, while $\varpi^{\star}$ is a sort of unknown dimensionless group that cannot be precisely pinpointed. Moreover, the points of contact with the framework analyzed for the case of microalgae culture in DSTRs show the possibility to enrich such a list with, cc_0^{-1}, $k_a c_0^{-1}$, $\mathrm{DO_x}S^{-1}$, as well as with geometric ratios that are

Table 4.3 Relevance list for batch microalgae growth in an ALR.

Geometric parameters		Sparger nozzle diameter d_n	[L]
		Diameter of the column D_c	[L]
		Equivalent diameter of the bubbles d_b	[L]
Physical properties	*Fluid dynamics*	Gas viscosity μ_{G}	[$\mathrm{M}^1\mathrm{L}^{-1}\mathrm{T}^{-1}$]
		Liquid viscosity μ_{L}	[$\mathrm{M}^1\mathrm{L}^{-1}\mathrm{T}^{-1}$]
		Gas density ρ_{G}	[$\mathrm{M}^1\mathrm{L}^{-3}$]
		Liquid density ρ_{L}	[$\mathrm{M}^1\mathrm{L}^{-3}$]
		Surface tension coefficient σ	[$\mathrm{M}^1\mathrm{T}^{-2}$]
		Superficial gas velocity v_{G}	[$\mathrm{L}^1\mathrm{T}^{-1}$]
	Mass transfer	Microalgae concentration c	[$\mathrm{M}^1\mathrm{L}^{-3}$]
		Microalgae initial concentration c_0	[$\mathrm{M}^1\mathrm{L}^{-3}$]
		Diffusion coefficient D	[$\mathrm{L}^2\mathrm{T}^{-1}$]
		Substrate concentration S	[$\mathrm{L}^{-3}\mathrm{N}^1$]
		Dissolved oxygen concentration $\mathrm{DO_x}$	[$\mathrm{L}^{-3}\mathrm{N}^1$]
		Overall mass-transport coefficient K_{OL} or K_{OG}	[$\mathrm{L}^1\mathrm{T}^{-1}$]
		Maximum specific growth rate k_a	[T^{-1}]
		Grow rate k_1	[T^{-1}]
Process parameters		Weight difference $g\Delta\rho$	[$\mathrm{M}^1\mathrm{L}^{-2}\mathrm{T}^{-2}$]

different in the form but not in the essence. These are $d_n D_c^{-1}$ and $d_b D_c^{-1}$. On the top of that, it is straightforward to add $\mu_{\mathrm{G}}\mu_{\mathrm{L}}^{-1}$, $\rho_{\mathrm{G}}\rho_{\mathrm{L}}^{-1}$ and $c_0\rho^{-1}$.

Thus, $(18-8)-4=6$ π-numbers, albeit related to 3 base quantities ([M], [L] and [T]) since the dependence on [N] is contained in $\mathrm{DO_x}S^{-1}$, remain to be identified. After building the dimensional matrix

$$\begin{array}{|c|ccc|cccccc|}
\hline
 & \rho & D_c & v_{\mathrm{G}} & \mu & D & K_{\mathrm{OG}} & k_1 & \sigma & g\Delta\rho \\
\hline
M & 1 & 0 & 0 & 1 & 0 & 0 & 0 & 1 & 1 \\
L & -3 & 1 & 1 & -1 & 2 & 1 & 0 & 0 & -2 \\
T & 0 & 0 & -1 & -1 & -1 & -1 & -1 & -2 & -2 \\
\hline
\end{array} \tag{4.17}$$

and reducing it, obtaining

$$\begin{array}{|c|ccc|cccccc|}
\hline
 & \rho & D_c & v_{\mathrm{G}} & \mu & D & K_{\mathrm{OL}} & k_1 & \sigma & g\Delta\rho \\
\hline
M & 1 & 0 & 0 & 1 & 0 & 0 & 0 & 1 & 1 \\
L & 0 & 1 & 0 & 1 & 1 & 0 & -1 & 1 & -1 \\
T & 0 & 0 & 1 & 1 & 1 & 1 & 1 & 2 & 2 \\
\hline
\end{array} \tag{4.18}$$

it follows that the elicited π-numbers are:

$$\pi_{\mathrm{I}} = \frac{\mu}{\rho D_c v_{\mathrm{G}}} = \mathrm{Re}^{-1} = \pi_1 \tag{4.19}$$

$$\pi_{\mathrm{II}} = \frac{D}{D_c v_{\mathrm{G}}} = \pi_2 \tag{4.20}$$

$$\pi_{\mathrm{III}} = \frac{K_{\mathrm{OL}}}{v_{\mathrm{G}}} = \pi_3 \tag{4.21}$$

$$\pi_{\mathrm{IV}} = \frac{k_1 D_c}{v_{\mathrm{G}}} = \pi_4 \tag{4.22}$$

$$\pi_{\mathrm{V}} = \frac{\sigma}{\rho D_c v_{\mathrm{G}}^2} \tag{4.23}$$

$$\pi_{\mathrm{VI}} = \frac{g\Delta\rho D_c}{\rho v_{\mathrm{G}}^2} \tag{4.24}$$

As expected, some of the dimensionless groups correspond to those obtained for the scale-up of the same process but carried out in DSTRs. To them, Weber number We is added in the generating set of the π-space, as well as the Eötvös number: both of them can be obtained from the linear combination of others π-numbers relative to the process at hand.

$$\pi_{\mathrm{V}}\left(\frac{d_b}{D_c}\right)^{-1} = \frac{\sigma}{\rho d_b v_{\mathrm{G}}^2} = \mathrm{We}^{-1} \tag{4.25}$$

$$\frac{\pi_{\mathrm{VI}}}{\pi_{\mathrm{V}}}\left(\frac{d_b}{D_c}\right)^{2} = \frac{g\Delta\rho d_b^2}{\sigma} = \mathrm{Eo} \tag{4.26}$$

Overall, the set of generators of the π-space, that includes 16 elements ($18-4=14$ plus ph and ε), for the considered system is

$$\left\{\mathrm{Re}, \mathrm{Da_{II}}, \mathrm{Sh}, \mathrm{Eo}, \mathrm{We}, \frac{k_1 D_c}{v_{\mathrm{G}}}, \varepsilon, \mathrm{pH}, \frac{d_n}{D_c}, \frac{d_b}{D_c}, \frac{c}{c_0}, \frac{\mathrm{DO_x}}{S}, \frac{k_a}{c_0}, \frac{c_0}{\rho}, \frac{\mu_{\mathrm{G}}}{\mu_{\mathrm{L}}}, \frac{\rho_{\mathrm{G}}}{\rho_{\mathrm{L}}}\right\} \tag{4.27}$$

4.3.5 Methods for evaluating the π-numbers

By analysing the list 4.16, it is possible to single out three main categories of dimensionless numbers and group them in subcategories accordingly.

1. *Known dimensionless numbers.* To this group belong the Reynolds number, the Sherwood number and the second Damköhler number.
   Reynolds number, defined as the ratio between inertial and viscous forces, can be used to determine if the flow in which algae are dispersed is turbulent (strong prevalence of inertial forces) or laminar. Sherwood number compares convective mass transfer to the rate of diffusive mass transfer and for the considered application it can refer both to the dissolved CO_2 and O_2. $\mathrm{Da_{II}}$ is useful for determining whether diffusion or reaction is the controlling phenomenon. As regards microalgae growth, it compares the diffusion of the key reactant (CO_2) and the grow rate (k_1).

2. *Operational π-numbers.* Four of them can be individuated in set 4.16: cc_0^{-1}, $k_a c_0^{-1}$, $\mathrm{DO_x} S^{-1}$ and pH. The first three are related to characteristic process quantities as yield, maximum yield, ratio between key byproduct and key reactant, while pH is a process tuning parameter. They can be manipulated during continuous operation.

3. *Reactor-related π-numbers.* They encompass crucial data of the reactor, either geometric ($d_s d^{-1}$) and functional ($k_1 \mathrm{n}^{-1}$). They cannot be used if the shape or the structure of the reactor is changed.

According to what was said, dimensionless numbers Re, Sh and $\mathrm{Da_{II}}$ here listed contain the generally defined characteristic length d (diameter of the reactor). By combining the original dimensionless numbers with the reactor-related π-numbers they can be reformulated in order to encompass appropriate characteristic lengths, as d_s for STRs. As it is to be expected, by employing Buckingham's π-theorem for the up-scaling of ALRs, more dimensionless numbers emerge (like Weber and Eötvös numbers) as more phases are involved. Yet, these additional dimensionless groups only concern fluid dynamics and material properties of the gas and liquid phases and should be used to further scale-up ALRs. Moreover, in accordance to what has been said on reactor-related π-numbers, the two dimensionless groups of 4.16 related to the presence of the impeller disappear.

Concluding, at least two degrees of freedom remain and are exploitable.

The procedures and calculations employed to evaluate the identified dimensionless groups are presented in the following sections.

4.3.5.1 Fluid dynamics in STRs and hydro-bubble dynamics in ALRs

In order to choose the optimal impeller diameter and geometry at lab-scale some computer fluid dynamics simulations by SimScale Multiphase Flow was carried out. Only biphasic liquid systems as glycerol-water and dissolved carbon dioxide-water were simulated.

Microalgae fluid dynamics was not taken into consideration due to the required high computation time, even if SimScale allows it by using particle-flow approaches. From this study, the optimal dd_s^{-1} ratio and stirrer speed n were estimated in order to obtain in the STRs impeller related Reynolds numbers suitable for algae growth through Eqn. 4.28.

$$\mathrm{Re} = \frac{\rho d^2 \mathrm{n}}{\mu} \left(\frac{d_s}{d} \right)^2 \tag{4.28}$$

Strictly speaking, to perform the scale-up in STRs, this Reynolds number should be kept unaltered.

On the other hand, since the ALRs have a different morphology with respect to the lower scale reactors, some distinctions are necessary. In the first place, ALRs employed in this research are designed as to contain the bubble phase only in the riser, not in the downcomer. Consequently, considering the difference in their cross sections as well, it is evident that Re is nonequivalent in these two parts of the photobioreactor. Clearly, even the formulation of Re appears different: by making use of the π-theorem to derive dimensionless groups for the ALR, Reynolds number is obtained again but liquid velocity naturally substitute the velocity given by the product of stirrer diameter and impeller speed (Section 4.3.4). Besides, in order to optimize its operation, as specified in Section 3.3, the multiphase flow regime needs to be investigated. The preferential situation should be on the border between the heterogeneous (churn) and the homogeneous (bubble) regimes. It is here reminded that the former corresponds to an environment in which, due to the manifestation of clustering and coalescence, both small and large bubbles are present concomitantly; large bubbles can assume spherical cap shapes and zigzagging trajectories, providing better area-to-volume ratios and longer permanence times, subsequently entailing better G-L mass transfer. On the other hand, fluid velocities in the riser are higher, and turbulence phenomena can affect the integrity of microalgae cells. This critical issue is solved if the established regime is the homogeneous one. In this scenario, where fluid velocities are more modest, there are no substantial interactions between the bubbles to be reported, their ascending path is mostly straight and the bubble size distribution is narrow, with small diameters and prevalence of spherical shapes (Krishna and Van Baten, 2001). Hence, even if Reynolds numbers should be kept unaltered, for the aforementioned reasons it might not be possible and the optimal choice could be related to the desired contact time between microalgae and bubbles and to the right recirculation conditions that also assure convenient photoperiods.

The experimental campaign apt to examine the hydrodynamic picture inside ALRs was carried out on the EL-ALR fed with injected air and filled with water (see Appendix B). Liquid velocity was experimentally measured in the downcomer. The same was not feasible in the riser, as the formation of eddies at different scales, in conjunction with the fact that the hypothesis of unidirectional flow does not hold due to the presence of the bubbles. Instead, we availed ourselves of an empirical formula (Chisti, 1989) to calculate the average liquid velocity in the riser $v_{\mathrm{L,riser}}$ (Eqn. 4.29).

$$v_{\mathrm{L,riser}} = \sqrt{\frac{2g\mathrm{h}_{\mathrm{down}}(\varepsilon_{\mathrm{G,riser}} - \varepsilon_{\mathrm{G,down}}}{\vartheta\left(\frac{1}{(1-\varepsilon_{\mathrm{G,riser}})^2} + \frac{A_{\mathrm{riser}}}{A^2_{\mathrm{down}}} + \frac{1}{(1-\varepsilon_{\mathrm{G,down}})^2}\right)}} \tag{4.29}$$

Here, g represents the gravitational acceleration ($\mathrm{m\,s^{-2}}$), $\mathrm{h}_{\mathrm{down}}$ the downcomer height (m), ϑ the (dimensionless) friction loss coefficient, related to the geometrical parameters of the reactor, and A the cross-sectional area (m^2). Subscripts down and riser are used to refer the variables to the downcomer and riser respectively. Finally, $\varepsilon_{\mathrm{G,down}}$ denotes the gas hold-up (dimensionless), computed for the downcomer with Eqn. 4.30 and for the riser with Eqn. 4.31.

$$\varepsilon_{\mathrm{G,down}} = 0.79\varepsilon_{\mathrm{G,riser}} - 0.057 \tag{4.30}$$

$$\varepsilon_{\mathrm{G,riser}} = \frac{V_{\mathrm{G,riser}}}{V_{\mathrm{G,riser}} + V_{\mathrm{L,riser}}} \tag{4.31}$$

being $V_{\mathrm{G,riser}}$ the volume of the gas phase and $V_{\mathrm{L,riser}}$ that of the liquid phase, both in the riser (m^3).

PIV (Particle Image Velocimetry) analysis was used to gauge the gas velocity in the riser $v_{\mathrm{G,riser}}$ as well as microalgae motion, the latter with the aid of different tracers.

The results of the aforementioned investigations allows to calculate Re for the riser and the downcomer.

4.3.5.2 Mass transport

Carbon dioxide is the considered substrate in the relevance list, and oxygen is the product of photosynthesis, hence continuous operating in steady-state requests fixed ratio between them: this is the meaning of the operational π-number $\mathrm{DO_x}S^{-1}$ to be conserved during scale-up. Obviously, mass transport characteristics of the dissolved CO_2 to the suspended algae (and dissolved O_2 produced by them) in the liquid phase must be also kept into account during scale-up. With reference to the performance of the discontinuous and semi-continuous lab-scale stirred reactors it is necessary to evaluate the optimal average mass flux of the substrate to the algae. It depends on the bulk concentration of carbon dioxide, its diffusion coefficient in water, the dimension of microalgae, fluid properties as density and viscosity and algae velocity relative to the fluid.

The following assumptions are here adopted to scale-up from lab-scale to pilot-scale: the resistance to mass transport due to the cellular membranes do not change in scale-up and the algae clusters moving into the reactors (STRs and ALRs) have the same dimension. Since we decide to keep not very high Re in order to not damage algal cells and oxygen is rather soluble, liquid mass transport is the controlling phenomenon, and $K_{\mathrm{OL}} = k_{\mathrm{L}}$ (k_{L} is the liquid mass transfer coefficient). Dynamic experimental tests as discussed in (Garcia-Ochoa and Gomez, 2009) are then performed in the DSTRs and the volumetric mass transfer coefficient $k_{\mathrm{L}}a$ is obtained.

Let us consider the oxygen mass balance in the STR

$$\frac{\mathrm{d}C^{\mathrm{L}}_{A,\mathrm{bulk}}}{\mathrm{d}t} = k_{\mathrm{L}}a(C^{\mathrm{L}*}_{A} - C^{\mathrm{L}}_{A,\mathrm{bulk}}) \tag{4.32}$$

where $C^{\mathrm{L}*}_{A}$ is the saturation concentration in the liquid phase and $C^{\mathrm{L}}_{A,\mathrm{bulk}}$ is the measured concentration in the liquid phase. $k_{\mathrm{L}}a$ can be estimated by Eqn. 4.32 from the collected measures of $C^{\mathrm{L}}_{A,\mathrm{bulk}}$ during the dynamic physical test, being sure that the sensor response time is very small. A $k_{\mathrm{L}}a$ two-points estimate is easily calculated as:

$$k_{\mathrm{L}}a = \frac{1}{t}\log\left(\frac{C^{\mathrm{L}*}_{A} - C^{\mathrm{L}}_{A1,\mathrm{bulk}}}{C^{\mathrm{L}*}_{A} - C^{\mathrm{L}}_{A2,\mathrm{bulk}}}\right) \tag{4.33}$$

As regards ALRs, the volumetric mass transport coefficient $k_{\mathrm{L}}a$ could be experimentally determined in a similar manner or it can be computed by using correlations, e.g. as that reported for EL-ALRs in (Bello et al., 1985):

$$k_{\mathrm{L}}a = 0.79\left(1+\frac{A_{\mathrm{down}}}{A_{\mathrm{riser}}}\right)^{2} v^{0}_{\mathrm{G,riser}}.8 \tag{4.34}$$

Since many correlations are proposed for computing k_{L} and $k_{\mathrm{L}}a$ and sometimes it is difficult to distinguish between them, we verified the obtained experimental values also by directly calculating Sherwood number with the empirical correlation Eqn. 4.35 (Versteeg et al., 1987).

$$\mathrm{Sh} = 0.322\mathrm{Re}^{0.7}\mathrm{Sc}^{0.33} \tag{4.35}$$

where Sc is the Schmidt number, in this case equal to $\mathrm{Sc} = \mu\rho^{-1}D^{-1}$.

As regards ALRs, the specific surface of the bubbles a ($\mathrm{m}^2\,\mathrm{m}^{-3}$), i.e. the ratio between the sum of the surface of all the bubbles inside the ALR and the reactor volume is experimentally estimated by image acquisition.

4.3.5.3 Global kinetics of algae growth

Many kinetic models for microalgae growth are available in literature. It is possible (Lee et al., 2015) to distinguish between those which employ variations of Monod equation and consider a single substrate factor, the ones that take into account the effect of light, like the Tamiya model, and more complicated ones, like multiplicative and threshold models, that require multiple factors as to describe co-limitation of algal growth due to the presence of several nutrients and its effect on light availability. In this work, we decided to employ the kinetic model suggested by Beruto et al. as it allows to implicitly take into account different factors by following the perspective of cell mitosis. The advantage is that the concentration curve, of sigmoid shape, is obtained employing a rather streamlined equation (Eqn. 4.36).

$$c(t) = c_0 + \frac{k_a}{1+\dfrac{k_a - c_0}{c_0}\exp\left(-k_1 t\right)} \tag{4.36}$$

c_0 denotes the inoculum concentration ($\mathrm{g\,l^{-1}}$) at the initial time whilst k_a is a specific rate constant representing the total average probability that cells has to form clusters and, considering its limit for $t \to +\infty$, it can be viewed as the maximum increase in cell population ($\mathrm{g\,l^{-1}}$) in the reactor. k_1 is a specific kinetic rate constant ($\mathrm{s^{-1}}$) that can be computed through an Arrhenius-like equation as it is related to temperature, and accounts for the frequency of mitotic events and for the enthalpy barrier hindering cell duplication. Since the reactors are operated at pseudo-constant temperature, oscillating around 25 °C, the dependence of k_1 on T is neglected.

The Maximum Likelihood (ML) method is adopted to carry out parameter estimation. Under the assumption of explicit exact models, i.e. neglecting model uncertainty, the objective function with ML represents the estimated experimental error. This method reduces to un-weighted Non Linear Least-Squares (NLLS) or Weighted Non Linear Least Squares (WNLLS) if normally distributed and independent errors (Catania et al., 2006) are considered. The use of weighted or unweighted least-squares reflects a different choice about the experimental error due to the analytic instrumentation and the experimental conditions. If different accuracy is devoted in measuring low concentration and high concentration values, the residual is proportional to the measured concentration and weighted least squares are adopted with a multiplicative error. On the contrary, if the same random error is supposed for all the measures of concentration, unweighted least-squares with additive errors are adopted. Results obtained with both the approaches are here reported.

From the estimated values of the kinetic parameters both the $\mathrm{Da_{II}}$ number and the $k_a c_0^{-1}$ number can be computed. The same can be said of $k_1 n^{-1}$ at lab scale. Up-scaling to airlift, this number, as said previously, cannot be kept as it is and gas velocity, multiplied by a, could substitute n in its evaluation.

4.3.6 Computation of the π-numbers. Lab-scale STRs

4.3.6.1 Fluid dynamics

The impeller Reynolds number can be calculated according to Eqn. 4.28. For a STR operation at 60 rpm with a stirrer diameter of 0.04 m and at 150 rpm with a stirrer impeller of 0.10 m respectively, its values fall in the range $1.798 \times 10^3 \div 2.809 \times 10^4$. Consequently, the hydrodynamic environment in the reactors can be on average a turbulent one, and at least the regime is of transition to turbulence, since $\mathrm{Re} > 10^3$.

Simulation of the mixing conditions in STRs at lab scale was performed with SimScale for both 0.5 L and 2.5 L reactors, exploring the effect of different available impellers through their CAD design. The comparison of the results, in conjunction with the knowledge that high speeds could spell the damaging of microalgae, led to the choice of a radial impeller placed at 0.02 m from the bottom of the reactor, characterized by diameters of 0.08 m and 0.10 m respectively for the STRs of 0.5 L and 2.5 L, that operate at 90 rpm and 60 rpm respectively.

Re evaluated for the chosen conditions are approximately equal to 10800 for the lab-scale DSTRs and to 11.000 for the lab-scale semi-continuous reactors.

4.3.6.2 Mass transport

Experimental tests were carried out in lab-scale STRs to estimate the overall mass transport coefficient for different Reynolds numbers, modified through the variation of the stirrer speed,at different T and in both Bold's Basal Medium and pure water (concentration monitored by conductivity measures).

Due to the fact that, among the many variables influencing the value of K_{OL}, the effect of fluid velocity is the greater one, the results obtained for oxygen are considered valid for carbon dioxide as well.

The values of $k_{\mathrm{L}}a$ are slightly influenced by the medium. Results inferred by the means of Eqn. 4.33 for $T = 25\,^{\circ}\mathrm{C}$ are comprised between 4.3×10^{-4} and 7.5×10^{-4} for both the 0.5 L and 2.5 L STRs at their chosen stirrer speeds (i.e. 90 and 60 rpm respectively). The probe lag (polarographic $\mathrm{DO_x}$ measures) was gauged to be of 4 s and the acquired data was not subject to any correction.

The impeller Sherwood number is computed using these experimental data by applying the formula

$$\mathrm{Sh} = k_{\mathrm{L}} d_s^2 D^{-1} \tag{4.37}$$

instead of Eqn. 4.33 (where d_s replaces d in a way analogous to what was done with Eqn. 4.28), as it is often the case when experimental measures of $k_{\mathrm{L}}a$ are available (García-Ochoa and Gómez, 1998).

The computation of the Sherwood number with Eqn. 4.35 yields $\mathrm{Sh} = 1600$ whilst, following the $k_{\mathrm{L}}a$-evaluating route, it ranges between 1450 (smaller $k_{\mathrm{L}}a$ in DSTR) and 3950 (bigger $k_{\mathrm{L}}a$ in semi-continuous STR). As a reference for ALRS, an intermediate value can be considered.

4.3.6.3 Global kinetics of algae growth

Different variables were measured when operating the lab-scale DSTRs.

- 2 input variables: CO_2 and glycerol concentrations;
- 3 operating input variables: feeding time interval, stirrer speed and extraction time interval;
- 4 internal variables: temperature, conductivity, pH and dissolved oxygen;
- 2 output variables: dry cell mass weight and absorbance at different wavelengths λ_w.

Daily measurements of all the internal and output variables were carried out in six DSTRs. The experimental conditions of the first three DSTRs were defined in order to test the combined effects of the two chemical input variables, i.e. concentration of CO_2 and glycerol concentration, and of the two operating input variables (feeding time interval and extraction time interval) on microalgae growth. The values chosen for these input variables stand in the range of the possible process conditions. The third operating variable, stirrer speed, is kept fixed at a previously optimized value of 90 rpm for all the tests. The experimental operating conditions of DSTRs no. 4, 5, 6 are the same of DSTRs no. 1, 2, 3 for what concerns the input operating variables values, while the two input variables, (CO_2 and glycerol concentrations) are set to zero. By doing so, reactors no. 4, 5 and 6 are useful to evaluate kinetics when microalgae are fed only with nutrients (BBM medium), at different operating conditions.

The scheme of the experimental campaign, that lasted 90 days, is reported in Table 4.4.

Table 4.4 Experimental tests carried out at lab-scale in discontinuous mode.

Test number	**Reactor number**	**Glycerol** ($\mathrm{g\,L^{-1}}$)	**CO_2** (%)	**Feeding interval (days)**	**Extraction interval (days)**	**Cultivation time (days)**
1	1	5	5	3	3	10
2	1	15	5	3	4	10
3	1	20	5	3	3	10
4	1	0	5	4	7	15
5	1	0	15	4	7	15
6	1	10	10	4	7	15
7	1	0	20	5	5	15
8	2	0	30	5	5	20
9	2	30	0	5	5	20
10	2	30	30	6	3	20
11	2	30	15	6	5	30
12	3	15	30	6	5	30
13	3	15	18	5	6	30
14	3	20	18	6	6	30

The kinetic parameters inside the growth model provided with Eqn. 4.36 were estimated using concentration values derived by both dry-mass weight data and spectrophotometric data at different wavelengths, by the construction of proper calibration curves.

Kinetic parameters estimated through NLLS fitting. Some results obtained through the use of NLLS and WLNNS for tests no. 5 and 6 are shown in Table 4.5 and Table 4.6.

The fitted growth curves, referred to test no. 6, and computed by both NLLS and WNLLS, are finally presented for two wavelengths: $\lambda_w = 430\,\mathrm{nm}$ (Figure 4.2a) and $\lambda_w = 650\,\mathrm{nm}$ (Figure 4.2b).

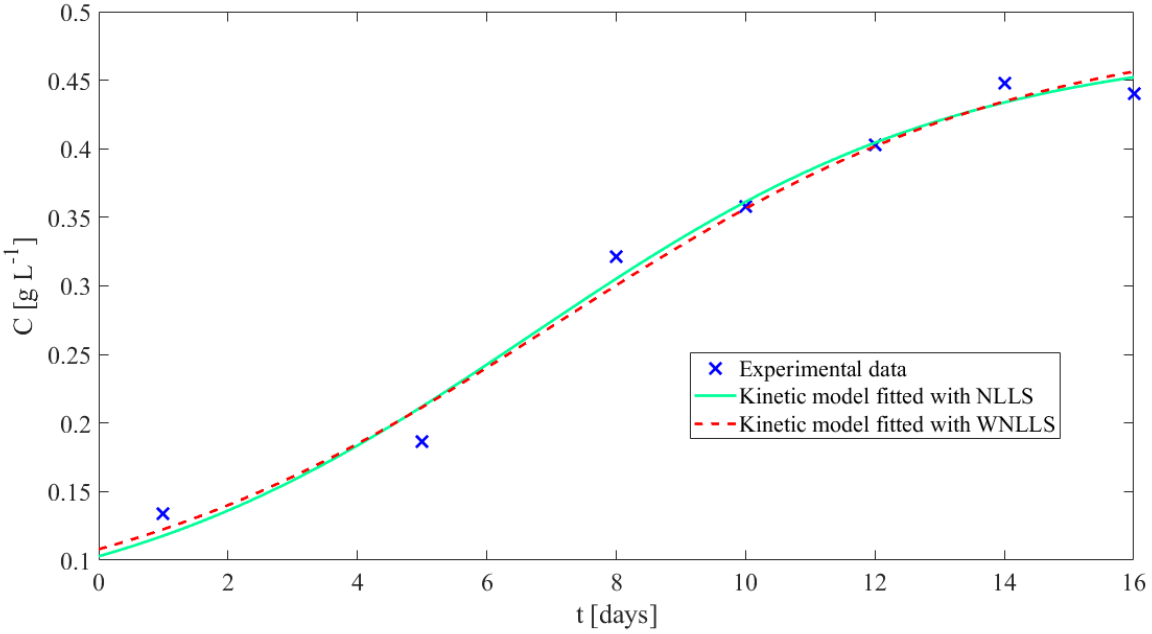

(a) $\lambda_w = 430\,\text{nm}$.

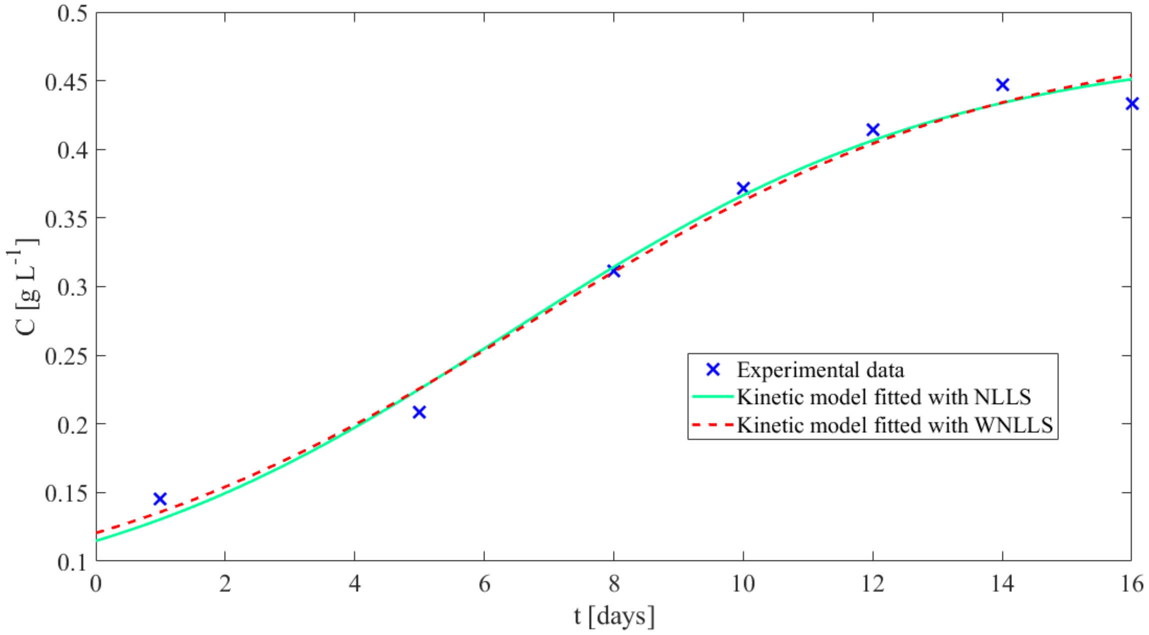

(b) $\lambda_w = 650\,\text{nm}$.

Fig. 4.2 Growth curves for Reactor 1, test no. 6, evaluated by the means of NLLS and WNLLS for two wavelengths.

Table 4.5 Results of the estimation of the kinetic parameters carried out through NLLS fitting.

NLLS	$\mathbf{c_0}$ $(\mathrm{g\,L^{-1}})$	$\mathbf{k_1}$ $(\mathbf{day^{-1}})$	$\mathbf{k_a}(\mathrm{g\,L^{-1}})$	$\mathscr{E}$	$\mathbf{R^2}$
$\lambda_w = 430\,\mathrm{nm}$	0.0605	0.2790	0.4296	0.0517	0.9323
$\lambda_w = 650\,\mathrm{nm}$	0.0683	0.2558	0.4375	0.0373	0.9338
Dry weight	0.0817	0.2000	0.6797	0.0517	0.9182
$\lambda_w = 430\,\mathrm{nm}$	0.0514	0.2967	0.4261	0.0279	0.9831
$\lambda_w = 650\,\mathrm{nm}$	0.0574	0.2880	0.4184	0.0200	0.9871
Dry weight	0.0573	0.2346	0.6123	0.0279	0.9180

Table 4.6 Results of the estimation of the kinetic parameters carried out through WNLLS fitting.

NLLS	$\mathbf{c_0}$ $(\mathrm{g\,L^{-1}})$	$\mathbf{k_1}$ $(\mathbf{day^{-1}})$	$\mathbf{k_a}(\mathrm{g\,L^{-1}})$	$\mathscr{E}$	$\mathbf{R^2}$
$\lambda_w = 430\,\mathrm{nm}$	0.0605	0.2790	0.4296	0.0517	0.9323
$\lambda_w = 650\,\mathrm{nm}$	0.0683	0.2558	0.4375	0.0373	0.9338
Dry weight	0.0817	0.2000	0.6797	0.0517	0.9182
$\lambda_w = 430\,\mathrm{nm}$	0.0514	0.2967	0.4261	0.0279	0.9831
$\lambda_w = 650\,\mathrm{nm}$	0.0574	0.2880	0.4184	0.0200	0.9871
Dry weight	0.0573	0.2346	0.6123	0.0279	0.9180

The data inferred for the lab-scale experimental tests with DSTRs provide a double effect: to reduce the costs for the measurements of the output variables and to restrict the range of the possible input conditions. Since tests no. 4, 5, 7 and 13 showed good yields, an investigation of the input conditions of these tests at semi-continuous lab-scale was deemed advisable.

The kinetic parameters estimated with concentration data coming from different measurement methods were in good accordance: at semi-continuous lab-scale, only spectrophotometric data can be used, also expecting to design an automated procedure for sample collection and related analysis. The expected error could be considered additive since R^2 computed by using NLLS was always higher than R^2 computed by WNLLS, even if the estimated parameters are very similar. The kinetic model is suitable and the estimation procedure is robust: at semi-continuous lab scale only one or two wavelength can be used to compute microalgae concentration.

The possible optimal operating conditions, resulting from the best kinetics among the experimental tests reported in Table 4.4, are summarized in Table 4.7. The corresponding ranges of internal variables, measured during the experimental tests, are also reported in Table 4.8.

Table 4.7 Optimal operating ranges of the input variables at DSTR lab-scale.

Glycerol ($\mathrm{g\,L^{-1}}$)	**$\mathrm{CO_2}$** (%)	**Feeding interval (days)**	**Extraction interval (days)**	**Cultivation time (days)**
$15 \div 20$	$15 \div 20$	$3 \div 5$	$5 \div 7$	$0 \div 15$

Table 4.8 Measured and optimal operating ranges of the internal variables at DSTR lab-scale.

	Temperature (K)	**pH** (-)	**Conductivity** (μS)	**$\mathrm{DO_x}$** ($\mathrm{mg\,L^{-1}}$)
Measured	$16 \div 28$	$7.5 \div 11$	$600 \div 2500$	$10 \div 21$
Optimal	$25 \div 28$	$7.5 \div 9$	$800 \div 1500$	$12 \div 20$

After analyzing the collected results, it was decided to investigate the scale-up of the reactor for the conditions of test no. 6. For this case, the four operational π-numbers can be directly inferred ($\mathrm{DO_x}S^{-1}$ and pH) or calculated. The ratio cc_0^{-1} ranges approximately between 6.3 and 8.8 whilst $k_a c_0^{-1}$ falls inside the interval $[6.4, 8.1]$.

The reactor-related geometric π-number $d_s d^{-1}$ is 0.80 and functional π-number $k_1 \mathrm{n}^{-1}$ assume values in $2.0 \times 10^{-6} \div 2.3 \times 10^{-6}$.

Finally, the calculated Damköhler number is in the range $10 \div 12$.

At semi continuous lab scale, the same variables studied at discontinuous lab scale were considered, with the one single difference: only one output variable (absorbance) was measured on a daily basis while the four internal variables were on-line measured.

Tests were carried out in two glass clamped top reactors: in one of them the tested conditions (test no. 6 of the previous scale) were used as reference and maintained within the interval of optimal operating ranges reported in Table 4.7 and Table 4.8. The other one was instead operated as control reactor with the two input variables related to feed set to zero.

The cultivation test lasted 90 days, and the automatic management of all the semi-continuous operations as feeding, extraction, brought to volume was performed by the self-built control tool developed on Labview 12 for the PXI National Instruments PXI system. Alarms for the internal variables were set on the MEMO HQ system (see Appendix B).

Growth curves were obtained for the many different wavelengths reported in Table 4.9. The estimated parameters gathered by resorting to both NLLS and WNLLS for two of those wavelengths (those that manifested the best results) are summarized in Table 4.10. Figure 4.3a shows the fitted growth curves for $\lambda_w = 430\,\mathrm{nm}$ whilst Figure 4.3b those for $\lambda_w = 650\,\mathrm{nm}$.

For this case as well. the four operational π-numbers can be directly calculated or inferred. $\mathrm{DO_x}S^{-1}$ is maintained similar in value to that of test no. 6 at discontinuous lab

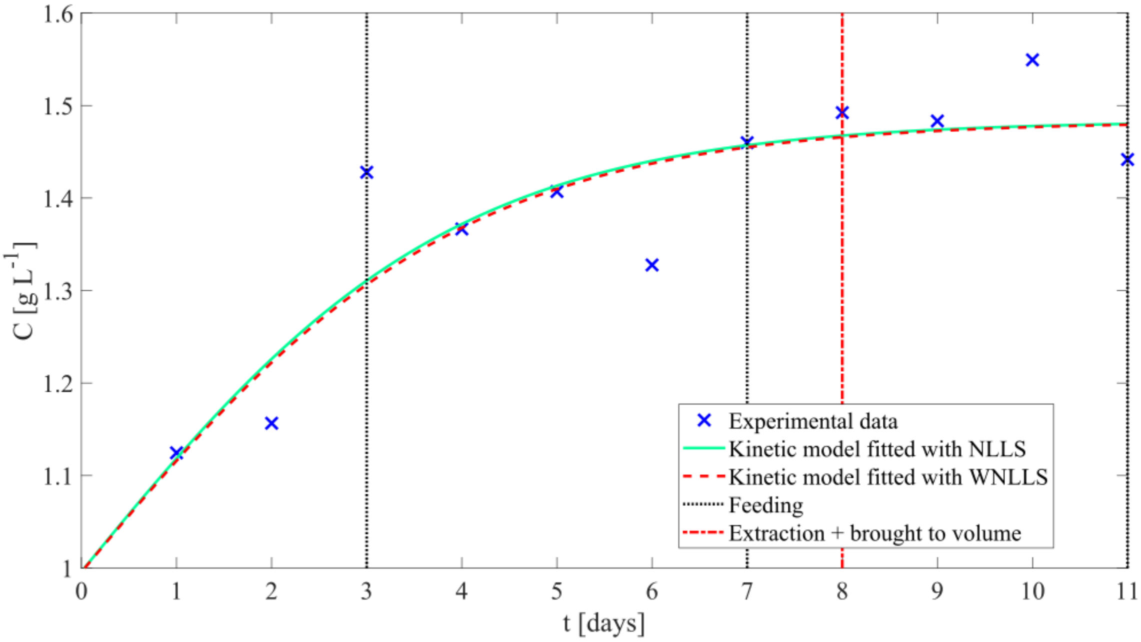

(a) $\lambda_w = 430\,\mathrm{nm}$.

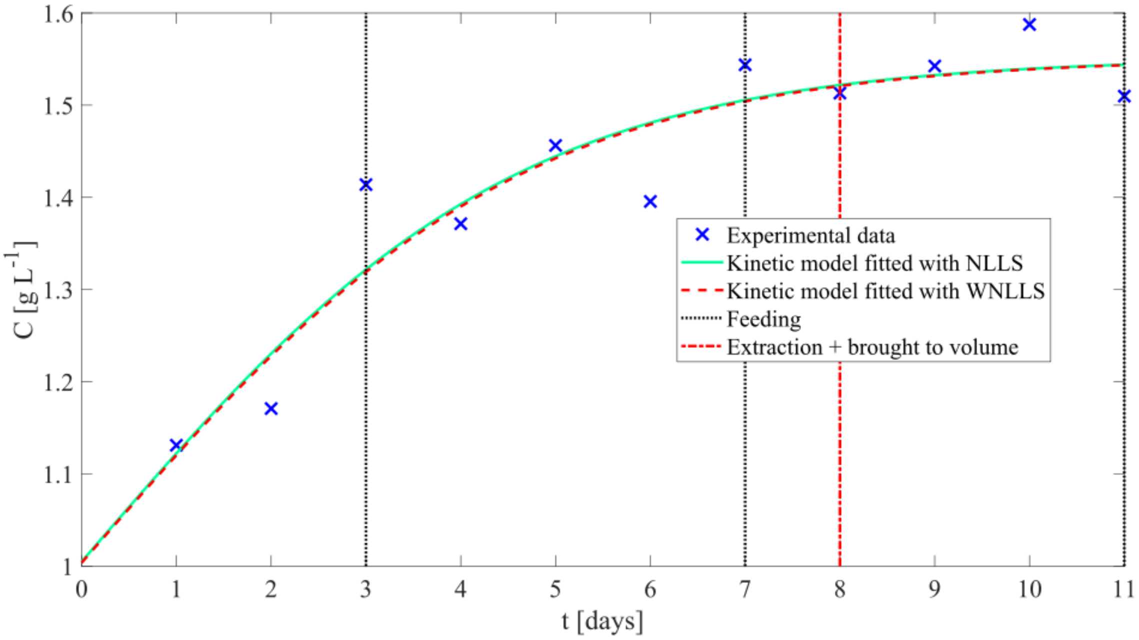

(b) $\lambda_w = 650\,\mathrm{nm}$.

Fig. 4.3 Growth curves for the tested semi continuous lab-scale reactor, evaluated by the means of NLLS and WNLLS for two wavelengths.

Table 4.9 Calibration curves at different wavelengths.

Wavelength (nm)	**Calibration curve regression equation**	$\mathbf{R^2}$
430	$y = 0.533x - 0.023$	0.997
434	$y = 0.523x - 0.021$	0.997
480	$y = 0.533x - 0.025$	0.997
550	$y = 0.716x - 0.050$	0.990
650	$y = 0.653x - 0.026$	0.997
663	$y = 0.613x - 0.018$	0.998
666	$y = 0.593x - 0.017$	0.998
680	$y = 0.554x - 0.021$	0.998
750	$y = 0.803x - 0.050$	0.989

Table 4.10 Results of the estimation of the kinetic parameters with NLLS and WNNLS fitting for semi-continuous operation.

	λ_w (nm)	$\mathbf{k_1}$ (day^{-1})	$\mathbf{k_a}$ (gL^{-1})	$\mathbf{c_0}$ (gL^{-1})	$\mathscr{E}$	$\mathbf{R^2}$
WNLLS	430	0.4999	0.9853	0.4978	0.0130	0.8462
	650	0.4482	1.0498	0.5018	0.0104	0.9199
NLLS	430	0.5087	0.9857	0.4980	0.0131	0.7890
	650	0.4516	1.0494	0.5024	0.0104	0.8884

scale, since CO_2 concentration is regulated and a mean value of 16% was measured for oxygen (Figure 4.4).

$k_a c_0^{-1}$ assumes values in $2.0 \div 2.1$ whilst cc_0^{-1} in $2.9 \div 3.0$. Not to be overlooked is the fact that the experimental growth conditions are different at semi-continuous lab scale with respect to those tested in the DSTRs. Through a comparative analysis of Figure 4.3 and Figure 4.2 it is noticeable how the kinetic curves estimated for the discontinuous case, starting from the inoculum, well describe the lag and the exponential phases of microalgae growth (Figure 4.5). On the contrary, the curves relative to the semi-continuous operation mode represent only the rapid growth phase until the stationary one; this is due to the fact that a great portion of the transferred cells were in the exponential growing phase (concentrated inoculum from past cultivation).

Then, attention must be payed when comparing kinetics related dimensionless numbers ($k_a c_0^{-1}$, $k_1 \mathrm{n}^{-1}$ and cc_0^{-1}) if the initial conditions at the different scales are not the same. To understand whether the STRs at the larger scale perform equally or better than the lab-scale DSTRs, the values here obtained must be correctly compared with those computed at the discontinuous lab scale but in the same growth phase. From the observation of Figure 4.2, it is

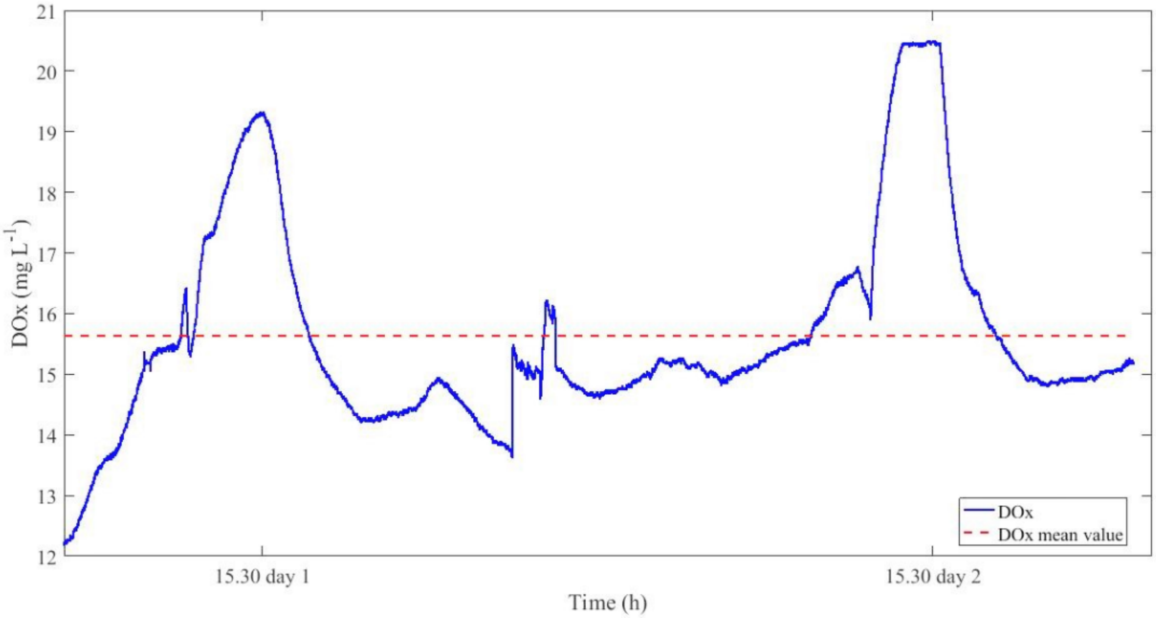

Fig. 4.4 Plot of the measure DO_x.

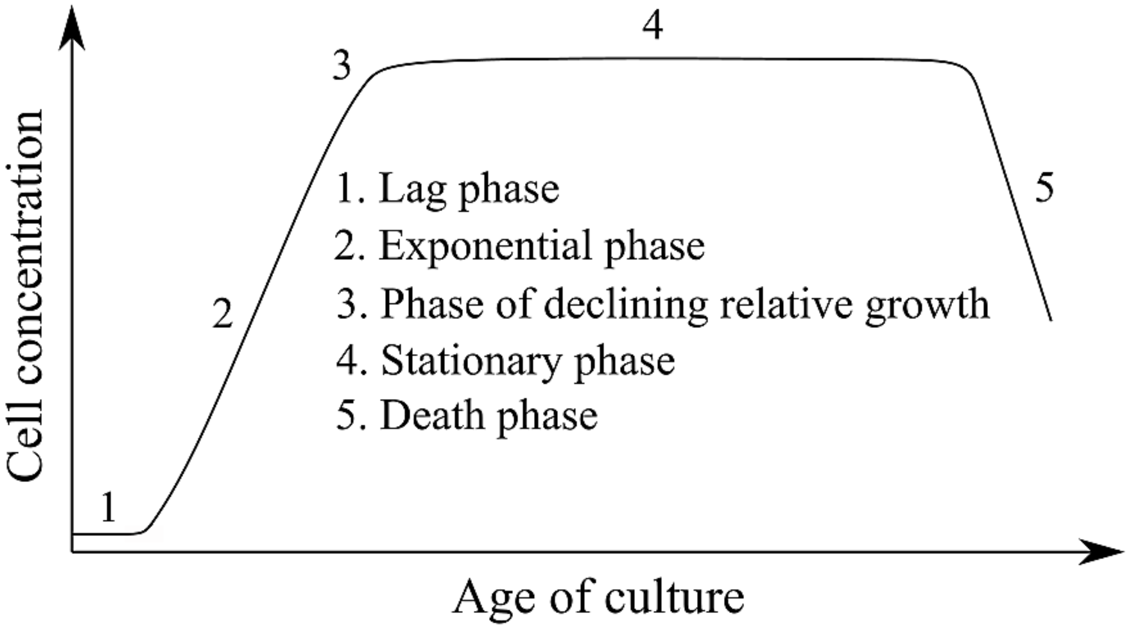

Fig. 4.5 Growth phases of microalgae cultures. Adapted from (Farag and Price, 2013).

noticeable that it happens at the inflection point of the kinetic curves, indicatively after 8 days of cultivation and with corresponding initial concentration of $0.3\,\mathrm{g\,L^{-1}}$ circa. Employing such c_0 value to recalculate the π-numbers, both $k_a c_0^{-1}$ and $c c_0^{-1}$ in semi-CSTRs are equal or better than the corresponding values in DSTRs.

Functional π-number $k_1 \mathrm{n}^{-1}$ and the reactor-related geometric dimensionless groups $d_s d^{-1}$ are respectively $5.2 \times 10^{-6} \div 5.9 \times 10^{-6}$ and 0.83.

$\mathrm{Da}_{\mathrm{II}}$ assumes values in the range $[27,31]$ depending on the considered k_1. Finally, the product $\mathrm{Da}_{\mathrm{II}}\mathrm{Sh}^{-1}$, useful to compare kinetics and overall mass transfer, is in the range $8 \times 10^{-3} \div 2 \times 10^{-2}$, thus underlining that the algae growth in the mixed conditions is still the controlling phenomenon.

4.3.7 Computation of the π-numbers. Pilot-scale ALRs

4.3.7.1 Fluid dynamics

The experimental runs were devised as to test both the bubble flow (Table 4.11) and churn regimes (Table 4.12). As regards the former, liquid velocity and related residence times in the downcomer were measured simultaneously using conductivity measurements of injected NaCl (tests no. $1 \div 3$) and solid particles as seeds (tests no. $4 \div 6$). Tests investigating churn regime were carried out only with NaCl.

Table 4.11 Main variables experimentally determined for the ALR operated in bubble flow. $\tau_{r,\mathrm{down}}$ is the downcomer residence time, while $\bar{d}_b$ is the mean bubble diameter.

Test no.	$v_{\mathrm{G,riser}}$ ($\mathrm{m\,s^{-1}}$)	$v_{\mathrm{L,down}}$ ($\mathrm{m\,s^{-1}}$)	$\tau_{r,\mathrm{down}}$ (s)	$\bar{d}_b$ (mm)	Bubbles per cross section	Bubbles in the riser	Average time cycle (s)
1	0.131	0.390	2.0	3	51	4505	21.2
2	0.111	0.357	2.2	4	45	3975	24.7
3	0.090	0.301	2.6	4	39	3445	21.9
4	0.131	0.367	2.1	3	51	4505	20.8
5	0.111	0.346	2.3	4	45	3975	19.9
6	0.090	0.325	2.4	4	39	3445	18.0

Table 4.12 Main variables experimentally determined for the ALR operated in churn flow.

Test no.	$v_{\mathrm{G,riser}}$ ($\mathrm{m\,s^{-1}}$)	$v_{\mathrm{L,down}}$ ($\mathrm{m\,s^{-1}}$)	$\tau_{r,\mathrm{down}}$ (s)	$\bar{d}_b$ (mm)	Average time cycle (s)
7	0.573	0.168	4.8	5	27.6
8	0.586	0.200	4.0	5	26.2
9	0.642	0.235	3.5	7	20.4

The estimated number of bubbles is not reported in Table 4.12 nor per cross section nor per riser volume, since, because of the complexity of heterogeneous flow, it was arduous to assess it without the aid of professional PIV instrumentation.

Instead of resorting to experimental tests, $v_{\mathrm{L,riser}}$ and Re for both the downcomer and the riser were respectively calculated according to the ALR version of Eqn. 4.28 and Eqn. 4.29. They are summarized in Table 4.13.

Table 4.13 Main hydrodynamic variables determined for the ALR by resorting to empirical correlations.

Test no.	$v_{\mathrm{G,riser}}$ ($\mathrm{m\,s^{-1}}$)	$\mathrm{Re_{riser}}$	$\mathrm{Re_{down}}$
$1 \div 4$	0.056	5244	$18843 \div 17731$
$2 \div 5$	0.057	5337	$17248 \div 16717$
$3 \div 6$	0.056	5244	$14543 \div 15219$
7	0.573	7865	9438
8	0.586	10300	11236
9	0.642	10955	13202

Fluid dynamics conditions in churn regime (Re) thus evidence a good correspondence with those at lab-scale.

4.3.7.2 Mass transport

The experimental data presented in Table 4.12 and Table 4.13 allows to calculate the specific surface of the bubbles a and the volume of the gas phase $V_{\mathrm{G,riser}}$. By employing Eqn. 4.34 with the data related to the bubble flow tests, values of $k_{\mathrm{L}}a$ in the range $0.08 \div 0.11$ were obtained whilst for churn regime $k_{\mathrm{L}}a$ they resulted to be in $[0.35, 0.38]$. In order to compute Sherwood number for the ALRs, a readaptation of Eqn. 4.37 can be used:

$$\mathrm{Sh} = k_{\mathrm{L}} a d_b^2 D^{-1} \tag{4.38}$$

In fact, in the case of ALRs, d_b the characteristic length for mass transport. The resulting Sh ranges between 360 and 880 in bubble flow and between 4575 and 9800 in churn regime.

a can be also calculated as the product of the number of bubbles in the riser and the mean surface of the bubble divided by the volume of the riser. Thus, using the values obtained in this way, it assumes values comprised between 17 and 27 in bubble flow (the number of bubbles is available only for this regime). The relative range of values taken by k_{L} has 0.003 and 0.006 as its extrema, resulting in Sh equal to $450 \div 1200$.

Finally, by calculating the Sherwood number (in the riser) by the means of Eqn. 4.35, one obtains about 1010 for the bubble flow and the interval $1360 \div 1700$ for the heterogeneous churn flow.

If on the one hand a more than satisfactory agreement is found between the Sh calculated through the three different correlations in bubble flow, on the other some discrepancy is observed between the Sh estimated for churn regime using Eqn. 4.34 and that computed with Eqn. 4.35. This fact is to be expected, and strongly depends on the experimental errors other than on the adopted correlation, that depends only on Re and Sc numbers. Anyway, the ALR in the tested bubble regime seems to guarantee slightly lower mass transport characteristics than those obtained for the STRs; conversely, in churn regime mass transport was better than in the STRs. This could justify the adoption of the bubble regime, on the edge of transition to churn, for EL-ALRs devoted to biochemical processes as adopted in other works (Riegler et al., 2019).

4.3.7.3 Global kinetics of algae growth

Estimated parameters c_0, k_1 and k_a contribute to the determination of dimensionless groups $k_a c_0^{-1}$,$k_1 \mathrm{n}^{-1}$ and $\mathrm{DO_x} S^{-1}$. To thi end, it is important to notice how $k_1 \mathrm{n}^{-1}$, as demonstrated in Section 4.3.4, becomes $k_1 v_{\mathrm{G,riser}}^{-1} a^{-1}$ for the ALRs, as no impeller is present (it should be clear the reasoning according to which it is possible to switch D_c with a). To keep such dimensionless groups unaltered, one can exploit the available degrees of freedom. In practice, this task can be accomplished by choosing the appropriate initial concentration of microalgae, by diluting the exhaust gases with air and managing bubble sizes by varying the design of the diffuser.

Lastly, cc_0^{-1} is the dimensionless number representing the bioprocess yield and as such is designated as the target variable.

An adequate choice of time intervals for feeding with glycerol and for concurrent extraction and brought to volume can contribute to the optimal set-up of all these variables.

4.4 Scale-up of the polyphenols extraction process carried out in a DSTR

In Chapter 2, a procedure to evaluate the technological feasibility at pilot scale of the extraction process of polyphenols from olive pomace has been presented. The approach proposed there took into consideration the extended kinetic route coupled with mathematical simulation performed on the basis of detailed physically-based dynamic models. Hence, this represents one of the two main scaling approaches: a dynamic model-based scaling. In fact, it exploits the simulation of the process to transfer information across scales by altering input variables and parameter of the same model (Wu and Li, 2006). In order to attain a more general depiction of the process at hand, however, the second of the two possible main scaling routes was attempted as well: the one based on dimensional analysis. To this regard, the theoretical scale-up regards the case of the discontinuous process.

Furthermore, unlike what has been done for the study of Chapter 2, in this instance the line of thought that prefers greater yields, which are such in particular with regard to lower molecular weight polyphenols (Do et al., 2014), has been followed. This choice is not conceptually impacting, since the dissertation would not change if ethanol was employed as the organic solvent. Also, grape pomace was employed as dry mass as well.

4.4.1 Outlining of the relevance list for the polyphenols extraction process

Since the lab-scale reactor may be considered a semi-ideal isothermal DSTR, the scale-up is carried out under the hypothesis of a batch pilot-scale reactor.

When considering stirred reactors, it is crystal clear how transport phenomena such as mass and energy transfer play key roles, as well as fluid flow inside the reactor. The flow field can, in first approximation, be characterized on the basis of two material characteristics, density ρ and viscosity μ, geometric factors, such as the diameters of the reactor d and that of the impeller d_s, and on a process parameter, the speed of the impeller n.

Heat and mass transfer, in the considered framework, can be described by means of the effective diffusion coefficient D_{eff}, specific heat capacity c_p, thermal conductivity λ, convective heat transfer coefficient h, temperature difference ΔT between mixture and reactor walls, thermal power supplied by the heating system $\dot{Q}_{\text{syst}}$ and process temperature T. Regarding this latter parameter, the hypothesis of uniform and constant temperature is applied, as T is controlled by the self-regulating system. This entails that the process relationships obtained though dimensional analysis are valid for any constant process temperature to which the numerical values of the physical properties are related. Analogously, the mass concentration of total polyphenols inside the mixture, the target variable, is assumed uniform, due to the consideration of the reactor as well-mixed.

As a matter of fact, extraction and conversion of TP depend on their initial and final mass concentration c_{in} and c_{out}, and are regulated through kinetic constants K, consistent with the choice of modeling the extraction process using pseudo-first order reactions, and the parameter α, representing the effect of limiting phenomena on the extraction due to temperature (see Section 2.2.1). Since α results, at least in the direction of scaling, adimensional (see Eqn. 2.29), it is here considered as an a priori known dimensionless number.

Recapitulating, the relevance list turns out to be that reported in Table 4.14.

Table 4.14 Relevance list for the polyphenols extraction process carried out in a semi-ideal isothermal DSTR.

Geometric parameters		Diameter of the reactor d	[L]
		Diameter of the stirrer d_s	[L]
Physical properties	*Fluid dynamics*	Dynamic viscosity μ	$[M^1L^{-1}T^{-1}]$
		Density ρ	$[M^1L^{-3}]$
	Mass transfer	Effective diffusion coefficient D_{eff}	$[L^2T^{-1}]$
		Pseudo-first order kinetic constant K	$[T^{-1}]$
		Initial mass concentration c_{in}	$[M^1L^{-3}]$
		Final mass concentration c_{out}	$[M^1L^{-3}]$
	Heat transfer	Specific heat capacity c_p	$[M^{-1}\Theta^{-1}H^1]$
		Thermal conductivity λ	$[L^{-1}T^{-1}\Theta^{-1}H^1]$
		Convective heat transfer coefficient h	$[L^{-2}T^{-1}\Theta^{-1}H^1]$
		Process temperature T	$[\Theta]$
		Temperature difference ΔT	$[\Theta]$
Process parameters		Stirrer speed n	$[T^{-1}]$
		Heat power $\dot{Q}_{\mathrm{syst}}$	$[T^{-1}H^1]$

4.4.2 Determination of the dimensionless numbers for the polyphenols extraction process

The relevance list includes 15 physical quantities that refer to 4 fundamental SI units: length [L], mass [M], time [T] and temperature [Θ]. Consequently, the formation of $15-4=11$ dimensionless numbers is expected.

Note: to distinguish the dimensionless numbers from those previously identified in Section 4.3, instead of π they will be denoted with Π.

However, it has been shown (Zlokarnik, 2006) that adding the amount of heat [H] as a base quantity helps to reduce the space of the dimensionless groups (π-space). Therefore, 10 π-numbers will be present, or rather 11 if one recalls the presence of α, already anticipated to be one of the π-numbers for the problem. What is more, some other trivial dimensionless groups can be surmised as well: the purely geometrical ratio $d_s d^{-1}$, the temperature difference ratio $\Delta T T^{-1}$, the concentration ratio $c_{\mathrm{in}} c_{\mathrm{out}}^{-1}$ and $c_{\mathrm{out}} \rho^{-1}$. Thus, once the list

$$\left\{ \frac{d_s}{d}, \frac{c_{\mathrm{in}}}{c_{\mathrm{out}}}, \frac{c_{\mathrm{out}}}{\rho}, \frac{\Delta T}{T}, \alpha \right\} \tag{4.39}$$

is known, $11-5=6$ dimensionless numbers remain to be pinpointed. The dimensional matrix to be handled, having employed a characteristic length L in place of d or d_s for greater generality, is shrunk to

$$\begin{array}{|c|ccccc|cccccc|}
\hline
 & \rho & \mathrm{L} & \mathrm{n} & T & \dot{Q}_\mathrm{syst} & \mu & D_\mathrm{eff} & K & c_p & \lambda & h \\
\hline
M & 1 & 0 & 0 & 0 & 0 & 1 & 0 & 0 & -1 & 0 & 0 \\
L & -3 & 1 & 0 & 0 & 0 & -1 & 2 & 0 & 0 & -1 & -2 \\
T & 0 & 0 & -1 & 0 & -1 & -1 & -1 & -1 & 0 & -1 & -1 \\
\Theta & 0 & 0 & 0 & 1 & 0 & 0 & 0 & 0 & -1 & -1 & -1 \\
H & 0 & 0 & 0 & 0 & 1 & 0 & 0 & 0 & 1 & 1 & 1 \\
\hline
\end{array} \tag{4.40}$$

By row-reducing the matrix so that the core matrix becomes diagonal, one obtains (elementary operations carried out: $\mathtt{R}_2 \to \mathtt{R}_2 + 3\mathtt{R}_1$ and $\mathtt{R}_3 \to \mathtt{R}_3 - \mathtt{R}_5$ after having inverted the sign of $\mathtt{R}_3$):

$$\begin{array}{|c|ccccc|cccccc|}
\hline
 & \rho & \mathrm{L} & \mathrm{n} & T & \dot{Q}_\mathrm{syst} & \mu & D_\mathrm{eff} & K & c_p & \lambda & h \\
\hline
M & 1 & 0 & 0 & 0 & 0 & 1 & 0 & 0 & -1 & 0 & 0 \\
L & 0 & 1 & 0 & 0 & 0 & 2 & 2 & 0 & -3 & -1 & -2 \\
T & 0 & 0 & 1 & 0 & 0 & 1 & 1 & 1 & -1 & 0 & 0 \\
\Theta & 0 & 0 & 0 & 1 & 0 & 0 & 0 & 0 & -1 & -1 & -1 \\
H & 0 & 0 & 0 & 0 & 1 & 0 & 0 & 0 & 1 & 1 & 1 \\
\hline
\end{array} \tag{4.41}$$

whence

$$\Pi_1 = \frac{\mu}{\rho \mathrm{L}^2 \mathrm{n}} = \mathrm{Re}^{-1} \tag{4.42}$$

$$\Pi_2 = \frac{D_\mathrm{eff}}{\mathrm{L}^2 \mathrm{n}} = \mathrm{Sc}\,\mathrm{Re}^{-1} = \mathrm{Pe}^{-1} \tag{4.43}$$

$$\Pi_3 = \frac{K}{\mathrm{n}} \tag{4.44}$$

$$\Pi_4 = \frac{c_p \rho \mathrm{L}^3 \mathrm{n} T}{\dot{Q}_\mathrm{syst}} \tag{4.45}$$

$$\Pi_5 = \frac{\lambda \mathrm{L} T}{\dot{Q}_\mathrm{syst}} \tag{4.46}$$

$$\Pi_6 = \frac{h \mathrm{L}^2 T}{\dot{Q}_\mathrm{syst}} \tag{4.47}$$

Re is the Reynolds number, Sc the Schmidt number and Pe the Péclet number (for mass transfer). Π_5 relates the thermal power exchanged by conduction with that received from the heating system, as it can be rewritten as:

$$\Pi_5 \frac{\Delta T}{T} = \frac{\lambda \mathrm{L} \Delta T}{\dot{Q}_{\mathrm{syst}}} \cong \frac{\dot{Q}_{\mathrm{cond}}}{\dot{Q}_{\mathrm{syst}}} \tag{4.48}$$

Π_4 and Π_6 have a rather murky appearance; for that reason, it is advisable to try to reformulate them in a more understandable way. Then, one can notice how:

$$\frac{\Pi_6}{\Pi_5} = \frac{h\mathrm{L}}{\lambda} = \mathrm{Nu} \tag{4.49}$$

whilst

$$\frac{\Pi_4}{\Pi_5} = \frac{c_p \rho \mathrm{L}^2 \mathrm{n}}{\lambda} = \mathrm{NuSt}^{-1} \tag{4.50}$$

being Nu the Nusselt number and St the Stanton number ($\mathrm{St} = \mathrm{NuRe}^{-1}\mathrm{Pr}^{-1}$, where Pr is the Prandtl number).

Altogether, the π-space of the taken-up scale-up problem is spanned by:

$$\left\{ \mathrm{Re}, \mathrm{Pe}, \frac{K}{\mathrm{n}}, \mathrm{Nu}, \mathrm{St}, \frac{d_{\mathrm{s}}}{d}, \frac{c_{\mathrm{in}}}{c_{\mathrm{out}}}, \frac{c_{\mathrm{out}}}{\rho}, \frac{\Delta T}{T}, \frac{\dot{Q}_{\mathrm{cond}}}{\dot{Q}_{\mathrm{syst}}}, \alpha \right\} \tag{4.51}$$

4.4.3 Data-analysis and estimation of the relevance list parameters

Needless to say, in order to perform dimensional analysis and evaluate its results, actual values of the parameters cataloged in the relevance list are needed. Similarly to what has been done for the microalgae cultivation process case, in the following subsections a more detailed explanation on the rationale for the selection of the various variables and their quantification will be presented. Then, π-numbers for the lab-scale parameters will be computed.

4.4.3.1 Geometric data and fluid dynamics

When considering up-scaling a given device, the first thing that comes to mind is probably its length, height or diameter; anyhow, a geometric variable. Although all of them can be added to the relevance list, it is also true that each one can be turned dimensionless by dividing it for one of the other geometric parameters (Levin, 2001). This is the reason why in the dimensional matrix, a generic characteristic length L was used. Thus, it is convenient to pick possibly a single geometric variable as a characteristic geometric parameter, so as to not lose focus on the problem at hand. Since for the mixing to be effective, fluid circulated by the impeller must sweep the entire vessel in a reasonable time, choosing the diameter d of the reactor vessel as its characteristic geometric parameter seems reasonable in the same way as picking d_s is for the stirring. On the top of that, the velocity of the fluid moved by the stirrer has to be adequate to carry material to the peripheral areas of the tank. This leads to the identification of the stirrer speed n as another crucial variable. An appropriate rotational speed n determines the formation of turbulence, which strongly influences the phenomena of distribution, dispersion and diffusion. As turbulent regime in a flow field can be detected by taking into account viscosity and density of the fluid, ρ and μ are picked as material properties to be included in the relevance list.

Gravitational acceleration g, to which the appearance of the Froude number would be linked ($\mathrm{Fr} = \mathrm{n}^2 d_s g^{-1}$), could look like a relevant quantity. Nonetheless, it is specified in literature (Zlokarnik, 2001) that the effect of g on stirring in unbaffled reactor vessels is negligible. Oftentimes, the presence of the power number, i.e. Newton number $\mathrm{Ne} = \mathrm{P}\rho^{-1}\mathrm{n}^{-3}d_s^{-5}$, is expected. However, as the mixing power P was regarded as a factor influencing more the economic feasibility than the de facto scaling, it does not emerge from the scale-up procedure here proposed.

To perform the scaling, the values known beforehand were that of the diameter of the laboratory scale reactor and that of the impeller, equal to 0.051 m and 0.035 m respectively. Hence, the π-number $d_s d^{-1}$ is equal to 0.686. The scale-up factor ψ may be defined by the ratio between any characteristic length chosen to represent the pilot-scale device $\mathrm{L_P}$ and that $\mathrm{L_L}$ of the lab -scale one:

$$\psi = \frac{\mathrm{L_P}}{\mathrm{L_L}} \tag{4.52}$$

As an example, to have a scale-up such as one that would translate in an increase of the production about 100 folds, a commercial pilot-scale reactor having a diameter of 0.200 m and height 0.400 m was found. Hence, $\psi = 3.92$.

It has been already discussed how dimensionless numbers relative to transport phenomena, be it of mass, heat or momentum, that contain a characteristic length always refer to that of the considered transfer. The generation of regions of rotational flow, aiding the momentum transport and mass transfer through convection, are thus related in a stirred reactor to the impeller diameter d_s. This entails that the Reynolds number turns into the impeller Reynolds number (Eqn. 4.28).

Density of pure methanol (liquid phase) can be determined through DIPPR105 equation (Eqn. 2.37 while its viscosity can be individuated through the Vogel equation (Stachowiak and Batchelor, 2014)

$$\mu = \exp \mathrm{E} \frac{\mathrm{F}}{\mathrm{G} + T} \tag{4.53}$$

another empirical expression, dependent on temperature, that make use of tabulated fitting coefficients (E, F and G).

Note that when dealing with the properties of the mixture inside the reactor vessel, the contribute of the solid phase was not considered, an assumption that must be validated. Having that said, and knowing that the considered process temperatures are T = 150 °C for TP extraction process from grape pomace and T = 180 °C for that using olive pomace as dry mass (as for such values the greater yield is observed, see Section 2.2.1), ρ and μ of methanol are thus estimated to be, $643.955\,\mathrm{kg\,m^{-3}}$ and $1.168 \times 10^{-4}\,\mathrm{kg\,s^{-2}\,m^{-1}}$ respectively when dealing with grape pomace, while they tantamount $593.234\,\mathrm{kg\,m^{-3}}$ and $9.031 \times 10^{-5}\,\mathrm{kg\,s^{-2}\,m^{-1}}$ when using olive pomace. Then, since agitation was maintained constant for all the experiments conducted at lab-scale at n = 16.756 rad $\mathrm{s^{-1}}$, it follows that Re = 113167 at T = 150 °C and Re = 134833 at T = 180 °C.

4.4.3.2 Mass transfer

Fick's law of diffusion is oftentimes employed in synergy with kinetic equations for modeling mass transfer in extraction process (Chan et al., 2014). Since it implies the dependence on concentration and diffusion coefficient, these were chosen as fundamental variables for process description. Regardless of the type of biological resource chosen as the TP source, it can be considered a porous material; for this reason, an effective diffusion coefficient D_{eff} is used instead of the general one. Moreover, as the active compounds have to diffuse from the surface of the solid particles to the bulk of the fluid, external mass transfer resistance has to be overcome. To surmise if intraparticle diffusion is the controlling mechanism for mass transfer in the dry matter particles and Fick's law applies, it is necessary to analyze the relation between the effectiveness factor η and the Thiele modulus Φ, the first of which is a function of the second as manifested by Eqn. 4.54, valid for a first order reaction in a spherical particle:

$$\eta = \frac{1}{\Phi}\left(\frac{1}{\tanh(3\Phi)} - \frac{1}{3\Phi}\right) \tag{4.54}$$

However, this resistance can be circumvented whether the conditions on the surfaces of the dry matter particles are the same as that in the bulk phase. Since it is possible to achieve this by manipulating turbulence conditions, and that is doable by intervening on the stirrer speed n, no ulterior mass transfer-related variables where added to the relevance list.

In order to estimate the effective diffusion D_{eff}, relationship Eqn. 4.55 can be used.

$$D_{\mathrm{eff}} = \frac{\mathrm{Fo_m}}{t_{rr}} r_p^2 \tag{4.55}$$

r_p^2 is the spherical particle characteristic size, i.e. its mean radius, t_{rr} is the regular regime starting time and $\mathrm{Fo_m}$ is the mass Fourier number, which represents the ratio between the diffusive transport rate and the accumulation rate. Following the suggestion reported in (Seikova et al., 2004), $\mathrm{Fo_m} = 0.1$ was chosen as the Fourier number at the beginning of the regular regime. Assessment of r_p led to $r_p = 5 \times 10^{-4}$ m. The regular regime, defined as the time interval in which the influence of initial conditions on an unsteady diffusion phenomenon is negligible while the concentration is still time-dependent, is evaluated through Eqn. 4.56 (Shehata et al., 2015), in which $x_{\mathrm{TP}(s)}$ is the yield in total polyphenols at saturation (determined through an investigation of the tx_{TP}^{-1} curves as explained in (Shehata et al., 2015)) and K is the extraction rate (see Section 2.2.1.2 for more details).

$$t_{rr} = \frac{1}{Kx_{\mathrm{TP}(s)}} \tag{4.56}$$

Consequently, $D_{\mathrm{eff}} = 4.414 \times 10^{-8}\ \mathrm{m^2\,s^{-1}}$ for the extraction process carried out with methanol and olive pomace whilst $D_{\mathrm{eff}} = 1.050 \times 10^{-7}\ \mathrm{m^2\,s^{-1}}$ for that in which methanol and grape pomace were used.

Analogously to what has been said about the characteristic length for the computation of the Reynolds number, the Péclet number can hereby calculated setting $\mathrm{L} = d_s$ (with the usual mathematical justification). Thus $\mathrm{Pe} = d_s^2 \mathrm{n} D_{\mathrm{eff}}^{-1}$ = 195530 and 465005 for the extraction processes from grape and olive respectively.

In order to calculate the other dimensionless number purely related to the mass transfer characteristics of the process, i.e. Π_3, the kinetic constant K is needed. Referring to the results of the estimates in Chapter 2 (see Table 2.1 and Table 2.4), it was calculated that $K\mathrm{n}^{-1} = 3.161 \times 10^{-5}$ for the extraction process from olive pomace, whereas $K\mathrm{n}^{-1} = 5.012 \times 10^{-5}$ for the process exploiting grape pomace.

4.4.3.3 Extraction kinetics

The data on the extraction process was already gathered and reported in Chapter 2. For this reason, they are not here repeated. However, it is recalled for simplicity that $\alpha = 0.9317$ for the extraction process from olive pomace at 180 °C and $\alpha = 0.8867$ for that related to grape pomace.

Moreover, from the knowledge of the mass fraction x_{TP}, the concentration of polyphenols in liquid phase can be inferred by resorting to Eqn. 2.36. The final concentration of total polyphenols in liquid phase c_{out} is the target variable and its importance is self-evident. Its value was estimated from the experimental campaign and depends on temperature, extraction time and type of dry matter employed. The π-number given by the ratio between c_{out} and ρ can therefore assume the followed values: $c_{\mathrm{out}}\rho^{-1} = 0.0076$ for the extraction of olive pomace with methanol at 180 °C and 0.0216 for that from grape pomace, being $c_{\mathrm{out}} =$

4.52 kg m^3 for olive pomace andc_{out} = 13.94 kg m^3 for grape pomace. On the other hand, the initial concentration c_{in} is zero, as no polyphenol is present in the liquid phase before the start of the extraction process. Hence $c_{\mathrm{in}} c_{\mathrm{out}}^{-1}$.

4.4.3.4 Heat transfer

The modes of heat transfer to be taken into account when investigating the heat balance over the stirred reactor are conduction and convection. The driving force of both processes is the tendency of systems to balance temperature differences. Thus, ΔT and the process temperature T were appended to the relevance list. As already mentioned, we considered T = 150 °C when dealing with grape pomace as dry mass whilst T = 180 °C when the source from which polyphenols were extracted was olive pomace. Since ΔT was employed to modify the form of Π_5 (see Eqn. 4.48), yielding the ratio between the thermal power exchanged by conduction with that received from the heating system, ΔT refers to the difference between the temperature of the bulk of the fluid and that of the reactor walls. This latter was assumed to be that of the resistor wires, since for the heat transfer calculations this was the employed temperature difference (ideal reactor, no heat losses). Thus, ΔT = 125 °C for the extraction process with grape pomace and ΔT = 155 °C for that with olive pomace. Hence, $\Delta T T^{-1} = 0.295$ in the first case and 0.342 in the second.

Resuming the discussion on the thermal balance of the reactor seen in the Section 2.1.3, it is known that the heat flux that affects the reactor encompasses two heat transfer modes: conduction and convection. Accordingly, $\dot{Q}_{mathrmcond}$, referred to the heat conduction from the resistor wires to the reactor internal cylinder, can then be estimated through Fourier's law of heat conduction

$$\dot{Q}_{mathrmcond} = \lambda A_s \frac{T_{\mathrm{rw}} - T}{\delta} \tag{4.57}$$

where the cross-sectional area normal to direction of the heat flow A_s was calculated to be 0.008 m^2, wall thickness δ, meant as the distance between the reactor vessel and the coils, was 0.025 m and the coils temperature was 220 °C. Thermal conductivity λ, material property (stainless steel AISI 316) function of the temperature, amounts to 16.852 W m^{-1} K^{-1} when T = 423.15 K whilst $\lambda(T = 453.15\mathrm{K})$ = 17.242 W m^{-1} K^{-1}. Thus, it results that $\dot{Q}_{\mathrm{cond}}$ = 49.485 W with respect to the process with grape pomace and 27.636 W for that with olive pomace.

Regarding $\dot{Q}_{\mathrm{syst}}$, one can resort to the use R value $R_{\mathrm{th}}^{-1} = (UA_{s,\mathrm{hs}})^{-1}$, a resistance parameter which leads to Eqn. 4.58

$$\dot{Q}_{\mathrm{syst}} = UA_{s,\mathrm{hs}}(T_{\mathrm{rw}} - T) = \frac{T_{\mathrm{rw}} - T}{R_{\mathrm{th}}} \tag{4.58}$$

in which U is the overall heat transfer coefficient, $A_{s,\mathrm{hs}}$ the heat transfer area of the heating system and T_{rw} the temperature of the electric wires constituting the heat source for the reactor mantle.

Since R_{th}^{-1} resulted to be $0.478\,\mathrm{W\,K^{-1}}$ for the extraction process relative to olive pomace and $R_{\mathrm{th}}^{-1} = 0.521\,\mathrm{W\,K^{-1}}$ for that with grape pomace, the heating power supplied by the heating system was estimated to be 20.9 W in the first case and $\dot{Q}_{\mathrm{syst}} = 19.2\,\mathrm{W}$ in the second one.

These computations lead to $\dot{Q}_{\mathrm{cond}}\dot{Q}_{\mathrm{syst}}^{-1} = 0.330$ (olive pomace) and $\dot{Q}_{\mathrm{cond}}\dot{Q}_{\mathrm{syst}}^{-1} = 0.370$ (grape pomace).

Finally, the specific heat capacity, which embodies the ability of a substance to retain heat, is another obvious choice for the relevance list. The values of c_p for the employed solvent at the considered temperatures were individuated through linear interpolation from data found in literature (Goodwin, 1987): $c_p(T = 423.15\mathrm{K}) = 3464\,\mathrm{J\,kg^{-1}\,K^{-1}}$ and $c_p(T = 453.15\mathrm{K}) = 3982\,\mathrm{J\,kg^{-1}\,K^{-1}}$.

At this point, having introduced the values of all the parameters at the lab scale present in the relevance list, in the following the values of the π-numbers that have not yet been presented are reported, directly displaying them in the synoptic tables (Table 4.15 and Table 4.16).

A further note should however be specified: for the calculation of the Nusselt number it is necessary to use the thermal conductivity of the methanol and not that of the material constituting the inner walls of the reactor so as not to alter the physical meaning of this dimensionless number. Being $\lambda_{\mathrm{CH_3OH}}(T = 423.15\mathrm{K}) = 0.193\,\mathrm{W\,m^{-1}\,K^{-1}}$ and $\lambda_{\mathrm{CH_3OH}}(T = 453.15\mathrm{K}) = 0.191\,\mathrm{W\,m^{-1}\,K^{-1}}$, it was computed that $\mathrm{Nu} = 16.514$ in the first case and e $\mathrm{Nu} = 18.262$ for the second one.

Table 4.15 π-space for the extraction process carried out at T = 180 °C with methanol and olive pomace.

π-number	**Value**
Re	134833
Pe	195530
Kn^{-1}	3.161×10^5
Nu	18.262
St	0.0016
$d_s d^{-1}$	0.547
$c_{\text{out}} \rho^{-1}$	7.691
$c_{\text{in}} c_{\text{out}}^{-1}$	0
$\Delta T T^{-1}$	0.342
$\dot{Q}_{\text{cond}} \dot{Q}_{\text{syst}}^{-1}$	0.330
α	0.932

Table 4.16 π-space for the extraction process carried out at T = 150 °C with methanol and grape pomace.

π-number	**Value**
Re	113167
Pe	465010
Kn^{-1}	5.012×10^5
Nu	16.514
St	0.0022
$d_s d^{-1}$	0.547
$c_{\text{out}} \rho^{-1}$	16.2356
$c_{\text{in}} c_{\text{out}}^{-1}$	0
$\Delta T T^{-1}$	0.295
$\dot{Q}_{\text{cond}} \dot{Q}_{\text{syst}}^{-1}$	0.370
α	0.887

References

Bello, R.A., Robinson, C.W., Moo-Young, M., 1985. Prediction of the volumetric mass transfer coefficient in pneumatic contactors. Chem. Eng. Sci. 40, 53–58.

Beruto, D.T., Lagazzo, A., Frumento, D., Converti, A., 2014. Kinetic model of Chlorella vulgaris growth with and without extremely low frequency-electromagnetic fields (EM-ELF). J. Biotechnol. 169, 9–14.

BIPM, I., IFCC, I., IUPAC, I., ISO, O., 2008. The international vocabulary of metrology—basic and general concepts and associated terms (VIM), 3rd edn.

Catania, F., Massabò, M., Paladino, O., 2006. Estimation of transport and kinetic parameters using analytical solutions of the 2D advection-dispersion-reaction model. Environmetrics 17, 199–216.

Chan, C.-H., Yusoff, R., Ngoh, G.-C., 2014. Modeling and kinetics study of conventional and assisted batch solvent extraction. Chem. Eng. Res. Des. 92, 1169–1186.

Chisti, M.Y., 1989. Airlift bioreactors. Elsevier Applied Science, London, UK.

Curtis, W.D., Logan, J.D., Parker, W.A., 1982. Dimensional analysis and the pi theorem. Linear Algebra Its Appl. 47, 117–126.

Do, Q.D., Angkawijaya, A.E., Tran-Nguyen, P.L., Huynh, L.H., Soetaredjo, F.E., Ismadji, S., Ju, Y.-H., 2014. Effect of extraction solvent on total phenol content, total flavonoid content, and antioxidant activity of Limnophila aromatica. J. Food Drug Anal. 22, 296–302.

Farag, I., Price, K., 2013. Resources Conservation in Microalgae Biodiesel Production. " Int. J. Eng. Tech. Res. IJETR 1, 49–56.

Garcia-Ochoa, F., Gomez, E., 2009. Bioreactor scale-up and oxygen transfer rate in microbial processes: An overview. Biotechnol. Adv. 27, 153–176.

García-Ochoa, F., Gómez, E., 1998. Mass transfer coefficient in stirred tank reactors for xanthan gum solutions. Biochem. Eng. J. 1, 1–10.

Goodwin, R.D., 1987. Methanol Thermodynamic Properties From 176 to 673 K at Pressures to 700 Bar. J. Phys. Chem. Ref. Data 16, 799–892.

Krishna, R., Van Baten, J.M., 2001. Scaling up Bubble Column Reactors with the Aid of CFD. Chem. Eng. Res. Des., Particle Technology 79, 283–309.

Lee, E., Jalalizadeh, M., Zhang, Q., 2015. Growth kinetic models for microalgae cultivation: A review. Algal Res. 12, 497–512.

Levin, M., 2001. Pharmaceutical Process Scale-Up. CRC Press.

Riegler, P., Chrusciel, T., Mayer, A., Doll, K., Weuster-Botz, D., 2019. Reversible retrofitting of a stirred-tank bioreactor for gas-lift operation to perform synthesis gas fermentation studies. Biochem. Eng. J. 141, 89–101.

Seikova, I., Simeonov, E., Ivanova, E., 2004. Protein leaching from tomato seed—experimental kinetics and prediction of effective diffusivity. J. Food Eng. 61, 165–171.

Shehata, E., Grigorakis, S., Loupassaki, S., Makris, D.P., 2015. Extraction optimisation using water/glycerol for the efficient recovery of polyphenolic antioxidants from two Artemisia species. Sep. Purif. Technol. 149, 462–469.

Stachowiak, G., Batchelor, A., 2014. Engineering Tribology - 4th Edition, Fourth Edition. ed. Butterworth-Heinemann, Boston.

Szirtes, T., Rózsa, P., 2007. Applied dimensional analysis and modeling. Elsevier Butterworth-Heinemann.

Tamiya, H.E., Hase, E., Shibata, K., Mituya, A., Iwamura, T., Nihei, T., Sasa, T., 1953. Kinetics of growth of Chlorella, with special reference to its dependence on quantity of available light and on temperature, in: Burlew, J.S. (Ed.), Algal Culture from Laboratory to Pilot Plant. Carnegie Institution of Washington, pp. 205–232.

Versteeg, G.F., Blauwhoff, P.M.M., van Swaaij, W.P.M., 1987. The effect of diffusivity on gas-liquid mass transfer in stirred vessels. Experiments at atmospheric and elevated pressures. Chem. Eng. Sci. 42, 1103–1119.

Wu, J., Li, H., 2006. Perspectives and methods of scaling, in: Wu, J., Jones, K.B., Li, Habin, Loucks, O. (Eds.), Scaling and Uncertainty Analysis in Ecology: Methods and Applications. Springer, Dordrect, Netherlands, pp. 15–42.

Zlokarnik, M., 2006. Scale-up in Chemical Engineering. John Wiley & Sons.

Zlokarnik, M., 2001. Stirring: Theory and Practice. Wiley-VCH.

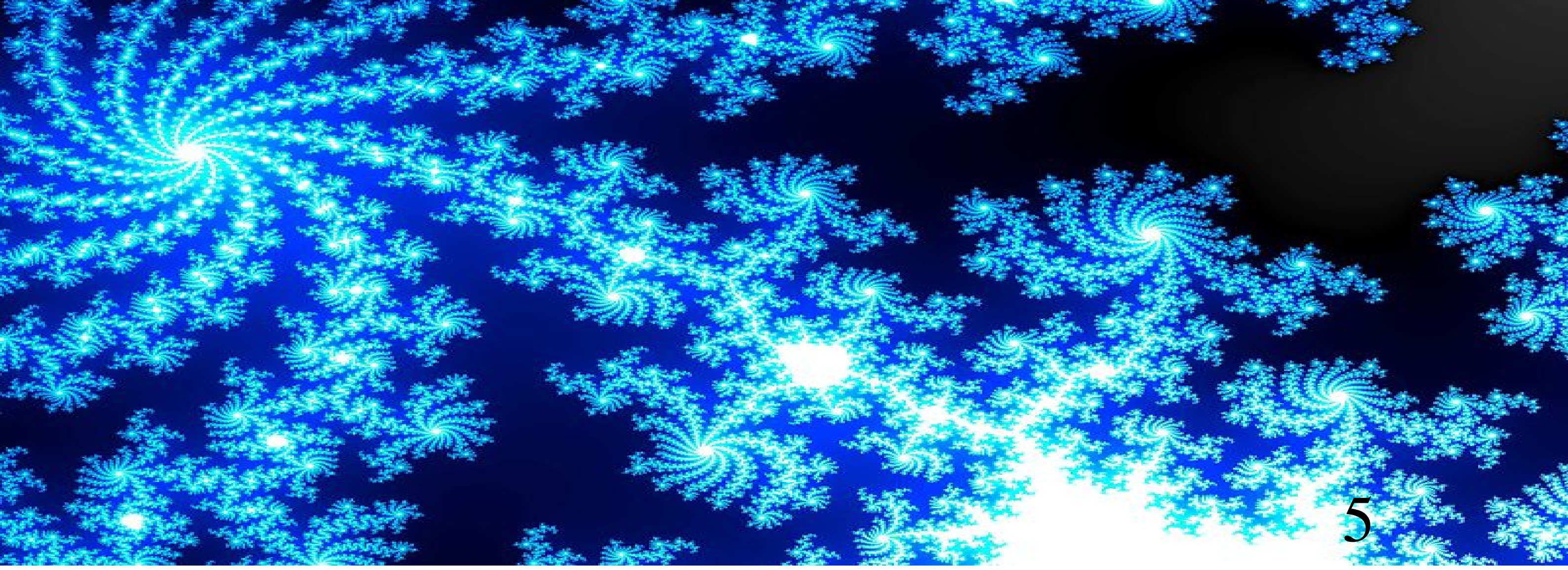

CHAPTER 5: CONCLUSIONS

Chronicled and forecasted detrimental effects of the climate change, world population growth and decrease of ecosystem resilience advocate an increase and improved use of renewable biological resources. These major impulses promote as a response a more sustainable production, the melioration of processing systems to render them more efficient, being able to products against minor inputs, thus lessening both wastes and GHGs emissions. The translation seems to be circular economy, with the design and realization of closed-loop systems and biorefineries at the forefront. Particular interest should be elicited as well by a waste management system that fully accounts and exploits the potential of agricultural, forestry and municipal (biogenic) wastes.

Olive oil industry is one of the main waste producers in Italian food sector. Olive pomace can reach up to 30% of olive oil manufacturing, depending on the milling process, and a large quantity of olive mill solid residue remains without actual application. Ditto can be said for the winery making industries. In the present thesis, the technological feasibility at pilot scale of a high temperature high pressure extraction process to produce polyphenols from waste olive and grape pomace has been demonstrated.

Experimental results obtained at lab scale were used both to evaluate the global extraction kinetics and to define the possible operating conditions for the process at pilot scale.

A pilot stirred reactor was designed and constructed. Dynamic simulation was used to set the values of the main operating variables and to test the possible control strategies at pilot scale.

Since the process adopted is a high temperature high pressure extraction, great importance is given to the definition of the parameters that influence heat exchange inside the reactor and to the choice between different possible heating systems. A subsequent economic feasibility study would make it possible to choose the less expensive heating system configuration.

Dynamic simulation has also proven to be a reliable tool to verify the sensitivity of the main model output, i.e. the yield in polyphenols, on the principal process parameters.

The technological feasibility of the process, operated both in discontinuous and in continuous, is confirmed. The quantity of product with high added value obtainable is high, as an estimated $16\,\mathrm{g\,h^{-1}}$ can be produced by employing the pilot CSTR with an input flowrate of $8\,\mathrm{L\,h^{-1}}$ circa and by processing $800\,\mathrm{g_{dry\ pomace}\,h^{-1}}$. This translates in an expected generation of about $350\,\mathrm{g\,d^{-1}}$, thus spelling the potential of the process for its industrial application.

Although from a deeper analysis of process economics Microwave-Assisted Extraction (MAE) or Ultrasound-Assisted Extraction (UAE) could show lower CAPEX and lower energy consumption than HPHTE, especially if methanol is used as solvent, the HPHTE process with water/ethanol most likely will show higher net present value of the relevant investment over the lifetime cycle.

The second topic on which the research work presented in this thesis was oriented concerns a pilot scale closed loop semi-continuous plant realizing an integrated process to produce biofuels from different organic wastes. The airlift photobioreactor destined to the *Chlorella Vulgaris* microalgae cultivation represents the most delicate device comprised in the system. Since its functioning relates to a multitude of parameters and variables on which it is possible to act so as to optimize its operation, the simulation of such phenomenon in detail is advised. Especially the shape, trajectory and size of the ascending bubbles has clear repercussions on mass transfer since they are related to permanence time and interfacial surficial area. Thus, their optimization positively influences microalgae growth as well as their recirculation. Excessive turbulence in the flow could spell damage to the cells. A precise understanding of the bubble flow regime is vital to improve the efficiency of the processes happening inside ALRs and the ability to opportunely manipulate the bubble flow would represent a major achievement for microalgae cultivation.

While classic CFD-based Euler-Euler and, sometimes, Euler-Lagrange methods have been extensively employed to model various types of reactors including bubble column ones, very few studies have been performed with front-tracking techniques, especially in conjunction with multiple, small bubbles. In the present work, both standard level set method and conservative level set methods (enriched with a correction technique aimed at dealing with the volume loss problem) were employed to simulate the vertical section of one of the external loop airlift reactors part of the biorefinery. Overall, the results confirm the good ability of the level set method to manage the complex dynamics of multiphase systems. Promising results were obtained using the standard level set method when considering the rise of a single bubble and bubble shapes coherent with those belonging to the classes found experimentally were identified. Nevertheless, when raising the complexity of the simulated system by considering multiple puffs of bubbles, the well-known volume loss problem proved to be too high of an obstacle to overcome and the switch to the conservative level set method was required. Effectively, it allowed to surmount the volume loss limitations: coalescence and breaking phenomena were successfully modeled as well, as evidenced by the formation of spherical caps as a result of bubble merging. In addition, the correct definition of the characteristics of the flow field highlighted the zig-zagging ascending trajectories desired and obtained in the experimental tests.

Anticipated future developments concern, on the one hand, the further optimization of the management of the computational domain and of the reinitialization, and, on the other hand, the implementation of mass balance equations apt to simulate the absorption of CO_2 in the liquid, central for the growth of microalgae. Furthermore, the definition of a cost functional useful to outline a proper optimization problem to formally infer the best shapes and trajectories of the bubbles could be devised.

Finally, extensive efforts were made to perform and investigate the rigorous scale-up of both the processes described and modeled. By resorting to Buckingham's π-theorem it is possible to identify the minimum set of suitable dimensionless parameters necessary for the complete description of the system. This procedure, that does not call for any knowledge of the equations ruling the phenomena that take place, provide a set of scale-invariant values, pure numbers that represent the relationships linking the main physical variables involved in the process.

In this way, 11 dimensionless groups were identified for the polyphenols extraction process. As expected, the set encompass geometric ratios, fluid dynamics dimensionless numbers (such as the impeller Reynolds number) were pinpointed as well as other well known groups describing the mass and heat transfer characteristics of the process (Péclet number, Nusselt number, Stanton number). All the π-numbers spanning the π-space were computed; the developing of an adequate physically-based mathematical model that covers all the considered aspects of the process is then needed in order to obtain a validation of the scaling results.

Instead, the scaling up of *C. Vulgaris* cultivation in photobioreactors was completed with experimental tests that were carried out on lab-scale STRs to investigate different operating conditions: the optimal obtained output values found at this scale are kept as desired in the ALRs at pilot scale by keeping fixed some dimensionless numbers. Mass transport, global kinetics and dimensionless numbers adopted to perform scale-up, based on the π-theorem, from 0.5 L DSTRs to semi-continuous 2.5 L STRs are obtained by experimental campaign.

A mixed approach coupled with fluid dynamics experimentation, is proposed to scale-up from semi-continuous 2.5 L STRs to semi-continuous 10 L ALRs.

It should be noted that, since scale-up also regards the operating mode, scaling from discontinuous to semi-continuous to continuous, some interesting dimensionless numbers arise other then $\mathrm{Re}, \mathrm{Sh}, \mathrm{Da}_{\mathrm{II}}$. These numbers are mainly related to the operating mode and are the ratio O_2/CO_2, the ratio between the final and the initial concentration, the ratio between the maximum increase in cell population and its initial concentration, the ratio between the estimated specific kinetic constant and a variable representing the characteristic time of mixing inside the chosen reactor.

APPENDIX A

POLYPHENOLS EXTRACTION PROCESS DATA

Experimental results of lab-scale polyphenols extraction process

Table A.1 TP yield extracted from olive pomace (Taggiasca cultivar) varying different operative parameters of the lab-scale HPHT stirred reactor.

Run	**Type of solvent**	**Solvent to dry pomace ratio (mL/g)**	**Extraction time (min)**	**Extraction temperature (°C)**	**TP (mg_{TP}/g)**
1	Methanol	10:1	15	100	8.2
2	Methanol	10:1	30	100	9.1
3	Methanol	10:1	60	100	10.6
4	Methanol	10:1	90	100	12.7
5	Methanol	10:1	120	100	11.7
6	Methanol	10:1	15	150	18.0
7	Methanol	10:1	30	150	19.4
8	Methanol	10:1	60	150	22.6
9	Methanol	10:1	90	150	23.9
10	Methanol	10:1	120	150	23.6
11	Methanol	10:1	15	180	21.2
12	Methanol	10:1	30	180	22.7
13	Methanol	10:1	60	180	31.9
14	Methanol	10:1	90	180	45.2
15	Methanol	10:1	120	180	39.3
16	H_2O	10:1	90	180	20.7
17	Ethanol	10:1	90	180	23.8
18	H_2O - Ethanol (75:25)	10:1	90	180	32.8
19	H_2O - Ethanol (50:50)	10:1	90	180	57.7
20	H_2O - Ethanol (25:75)	10:1	90	180	59.2
21	H_2O - Ethanol (75:25)	10:1	90	120	10.4
22	H_2O - Ethanol (50:50)	10:1	90	120	13.7
23	H_2O - Ethanol (25:75)	10:1	90	120	20.2

Table A.2 TP yield extracted from grape pomace (Croatina cultivar) varying different operative parameters of the lab-scale HPHT stirred reactor.

Run	**Type of solvent**	**Solvent to dry pomace ratio (mL/g)**	**Extraction time (min)**	**Extraction temperature (°C)**	**TP (mg_{TP}/g)**
1	Methanol	5:1	15	30	7.0
2	Methanol	5:1	30	30	8.1
3	Methanol	5:1	90	30	9.6
4	Methanol	5:1	150	30	10.5
5	Methanol	5:1	210	30	11.0
6	Methanol	5:1	270	30	11.5
7	Methanol	5:1	330	30	12.0
8	Methanol	5:1	15	120	20.4
9	Methanol	5:1	30	120	24.8
10	Methanol	5:1	90	120	25.2
11	Methanol	5:1	150	120	33.2
12	Methanol	5:1	210	120	36.0
13	Methanol	5:1	270	120	38.5
14	Methanol	5:1	330	120	39.7
15	Methanol	5:1	15	180	30.8
16	Methanol	10:1	30	150	51.6
17	Methanol	10:1	90	150	52.3
18	Methanol	10:1	150	150	59.0
19	Methanol	10:1	210	150	63.2
20	Methanol	10:1	270	150	69.7
21	Methanol	10:1	330	150	62.4
22	H_2O	10:1	150	270	15.5
23	Ethanol	10:1	150	270	67.7
24	H_2O - Ethanol (75:25)	10:1	150	270	27.4
25	H_2O - Ethanol (50:50)	10:1	150	270	70.6
26	H_2O - Ethanol (25:75)	10:1	150	270	73.8

APPENDIX B

MICROALGAE CULTIVATION IN PBRS. EXPERIMENTAL MATERIALS

Experimental materials used in the experimental tests employed in the study on the scale-up of microalgae cultivation in photobioreactors

The scale-up analysis presented in Chapter 4 is aimed at a biorefinery of the kind described in Section 1.5. Accordingly, the microalgae species employed were the same: *Chlorella Vulgaris*.

B.1 Microalgae culture

Chlorella Vulgaris was chosen due to its high versatility. It is a fast growing freshwater unicellular eukaryotic green algae belonging to the *Chlorophyta phylum* that can efficiently adapt to a wide-range of surrounding environments. Rich in lipid content, these microalgae can proliferate under conditions of high nutrient concentrations, effectively feeding also on wastewaters that can even enhance their growth (Hultberg et al., 2013; Ramesh Kumar et al., 2018). Studies highlight notable removal capabilities of N (up to about 90%), P (even complete elimination) and the ability to bind heavy metals (Mujtaba et al., 2018; Ruiz-Marin et al., 2010), with an average deletion efficiency of 72% for N and 28% for P (Rizwan et al., 2018). Chlorella Vulgaris can tolerate high CO_2 concentrations, showing good sequestration rates (Sadeghizadeh et al., 2017) with reasonable growth; for this reason it is often suggested for the treatment of exhaust gases in biofuel production processes (Frumento et al., 2013). *Chlorella* can withstand temperatures between 5 and 35 °C, with an optimal range between

25 and 30 °C (Enamala et al., 2018), and can absorb light energy at different wavelength ($420 \div 475$ nm, $630 \div 700$ nm (Atta et al., 2013; Blair et al., 2014)).

Chlorella Vulgaris CCAP 211 (Culture Collection of Algae and Protozoa, Argyll, UK) strain was used. It was cultivated in Bold's Basal Medium (BBM) (Bischoff and Bold, 1963), which has the following composition in distilled water: $250\,\mathrm{mg\,L^{-1}}$ $NaNO_3$, $75\,\mathrm{mg\,L^{-1}}$ MgSO4 × $7H_2O$, $25\,\mathrm{mg\,L^{-1}}$ NaCl, $75\,\mathrm{mg\,L^{-1}}$ K_2HPO_4, $175\,\mathrm{mg\,L^{-1}}$ KH_2PO_4, $25\,\mathrm{mg\,L^{-1}}$ $CaCl_2 \times 2H_2O$, $11.42\,\mathrm{mg\,L^{-1}}$ H_3BO_3, $8.82\,\mathrm{mg\,L^{-1}}$ $ZnSO_4 \times 7H_2O$, $1.44\,\mathrm{mg\,L^{-1}}$ $MnCl_2 \times 4H_2O$, $0.71\,\mathrm{mg\,L^{-1}}$ MoO_3, $1.57\,\mathrm{mg\,L^{-1}}$ $CuSO_4 \times 5H_2O$, $0.49\,\mathrm{mg\,L^{-1}}$ $Co(NO_3)_2 \times 6H_2O$, $50\,\mathrm{mg\,L^{-1}}$ Na_2 EDTA × $2H_2O$, $31\,\mathrm{mg\,L^{-1}}$ KOH, $4.98\,\mathrm{mg\,L^{-1}}$ $FeSO_4 \times 7H_2O$, $1.84\,\mathrm{mg\,L^{-1}}$ H_2SO_4.

The strain was stored in 250 mL Erlenmeyer flasks, kept at 25±1 °C and under a photon flux of $80\,\mathrm{\mu mol\,m^{-2}\,s^{-1}}$.

B.2 PBRs

B.2.1 Discontinuous cultivation at lab-scale

Open top cylindrical glass vessels, with internal diameter 100 mm and useful volume of 500 mL were adopted for discontinuous cultivation. Seed cultures were prepared by adding 50 mL of the stock culture in 450 mL of the same BBM medium. Batteries of six vessels were contemporary mixed by a Velp Scientifica FC 6S series flocculator, mixing speed ranging from 10 to 250 rpm, equipped with radial impellers with diameter of 80 mm. Air enriched by CO_2 was dispersed at the bottom of the reactor by a circular crown shaped ceramic diffuser with external diameter equal to 100 mm and internal diameter equal to 90 mm. CO_2 concentration was regulated by Brooks Instrument 5850S smart mass flow controllers. Water and glycerol were manually inserted at established time intervals, extraction was manually operated. Samples were daily collected for both dry cell weight measurements and spectrophotometric analysis. Temperature, pH, conductivity and dissolved oxygen were manually measured with a daily frequency.

B.2.2 Semi continuous cultivation at lab-scale

Two glass lined clamped top reactors with useful volume of 2500 mL and internal diameter 120 mm were adopted for semi-continuous lab-scale cultivation. The diameter/height ratio of the two reactors is 1:2, not in the range of classical stirred tanks, but specially designed in order to approximately keep at this scale the same light conditions of the discontinuous lab-scale. The reactors were equipped by a bottom central outlet nozzle (3/4" diameter) and four 1/4" couplings. The top had one drive central nozzle of 1" diameter (for impeller introduction) and three 3/4" nozzles for probes introduction. Mixing was performed by two PW overhead stirrers (Velp Scientifica) with speed ranging from 20 to 1200 rpm. Radial impellers with diameters ranging from 40 mm to 100 mm were available; no baffles were present into the reactors. Synthetic wastewater was inserted at chosen time intervals by peristaltic pumps and cyclic injection could be managed. Microalgae extraction could be cyclically operated. Air enriched by CO_2 was continuously dispersed at the bottom of the reactor by a circular crown shaped ceramic diffuser with external diameter equal to 120 mm and internal diameter equal to 150 mm. CO_2 concentration could be regulated. Seed cultures were prepared directly employing the stock culture into the BBM medium. One of the two reactors is shown in Figure B.1.

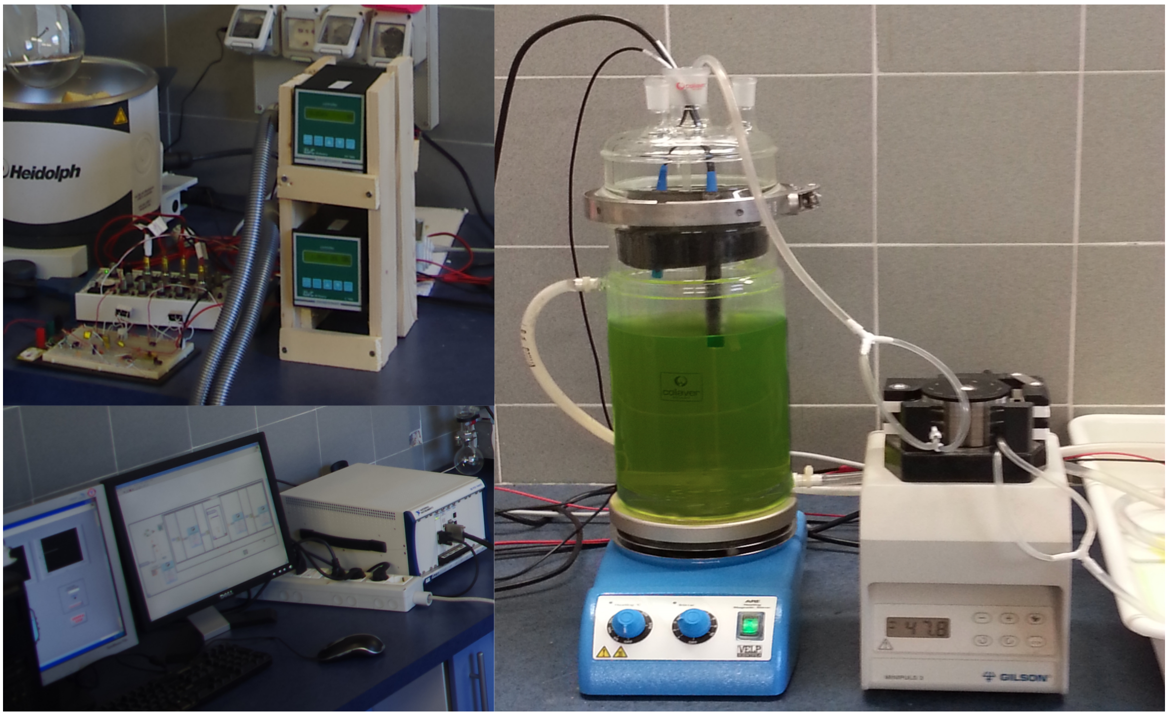

Fig. B.1 One of the semi-CSTRs used at lab-scale.

B.2.3 Continuous cultivation at pilot-scale

Four external loop airlift reactors were designed and assembled to conduct the experimental campaign.

Both the riser and the downcomer are made by transparent polymethyl methacrylate (PMMA), while the material adopted for the horizontal collectors is not-transparent PVC.

This choice allows a good dark/light cycles alternation at relatively short residence times, fact that plays a decisive role in improving algae growth. EL-ALRs are shown in Figure B.2.

The ratio between the riser and the downcomer diameter is 2.2, falling within the range $1.0 \div 3.0$ suggested as optimum for airlift bioreactors design (Hamood-ur-Rehman et al., 2013) and the total volume of each ALR is about 10.5 L. The main dimensions of each pilot ALR are reported in Table B.1.

Fig. B.2 Two of the ALRs employed at pilot-scale (Paladino and Neviani, 2018).

Air simulating flue gas is insufflated by a sparger installed into the base of the riser and made by a perforated stainless steel plate coupled with a porous sponge diffuser.

pH, conductivity and dissolved oxygen probes are installed in the midsection of the lower collector (see Figure B.4). pH measures were used during the hydrodynamic experimental tests as an indirect estimation of carbon dioxide dissolved in circulating water. Additional conductivity measures, collected at the top of both the riser and the downcomer, were used to estimate residence times by NaCl tracing.

Table B.1 Geometric data of the EL-ALRs.

Parameter	**Value**
Length of the riser	0.780 m
Diameter of the riser	0.110 m
Length of the downcomer	0.780 m
Diameter of the downcomer	0.050 m
Length of the horizontal collectors	0.385 m
Diameter of the horizontal collectors	0.050 m

B.3 Monitoring and automation

B.3.1 Discontinuous cultivation at lab-scale

B.3.1.1 Monitoring output variables

Microalgae concentration was measured through both direct dry cell weight measurements and spectrophotometric analysis. The former procedure was carried out by filtering the extracted samples (Buchner and 45 µm filters), then by drying the filters for 24 h at 70 °C into a Mechanical Convection Oven (Binder Microprocessor-Controlled WZ05012) and finally by weighing them by analytic balance (Mettler Toledo) to obtain the dry cell mass ($\mathrm{g\,L^{-1}}$). Spectrophotometric analysis was performed on daily collected algae samples by UV-VIS Hach DR-6000 spectrophotometer. Calibration curves constructed at different wavelengths (430, 434, 480, 550, 650, 663, 666, 680 nm) were used to correlate the measured absorbance with concentration measures. Microalgae growth was estimated by using concentration values obtained by both dry cell mass measures and absorbance measures. In the latter case, kinetic parameters were estimated at the different wavelengths, in order to choose the best ones, to test the robustness of the estimation procedure using spectrophotometric data and to obtain statistical information about measurement errors.

B.3.1.2 Monitoring internal variables

Internal variables as pH, conductivity (C), dissolved oxygen ($\mathrm{DO_x}$) and temperature (T) were off-line acquired by WTW multi-parameter portable system 340i and related probes SenTix 41, TetraCon 325, CellOx 325.

B.3.1.3 Operating mode and automation

The concentration of CO_2 mixed with air and simulating flue gas is regulated by Brooks Instrument 5850S smart mass flow controllers. Wastewater introduction and microalgae extraction are manually operated.

B.3.2 Semi-continuous cultivation at lab-scale

B.3.2.1 Monitoring output variables

Microalgae concentration was only indirectly measured by spectrophotometric analysis. Calibration curves were estimated at different wavelengths (430, 434, 480, 550, 650, 663, 666, 680 nm) to correlate the measured absorbance with concentration measures and daily spectrophotometric analysis of algae samples was carried out by UV-VIS Hach DR-6000 spectrophotometer. Kinetics parameters were estimated at all the considered wavelengths.

B.3.2.2 Monitoring internal variables

Internal variables as pH, C, DO_x and T were on-line acquired at 10 Hz frequency by B&C Electronics series 7685 Microcontrollers and related probes (inserted into the dedicated nozzles in the glass top of each reactor).

At this experimental stage the B&C systems wa not used as controllers but only adopted to acquire and convert the measures, show their values in the lab and to send the acquired values ($4 \div 20$ mA signal) to both a PXI National Instruments system and MEMO monitoring system, this one being a real-time, remotely accessible operating database that continuously collects, filters and stores the measures (ECPLab – University of Genoa, Italy).

B.3.2.3 Operating mode and automation

CO_2 concentration in the simulated flue gas (air enriched by CO_2) dispersed into the stirred tank reactors was regulated by Brooks Instrument 5850S smart mass flow controllers. Cyclic injection of secondary feed, i.e. simulated wastewater rich in glycerol, was regulated by the PXI National Instrument system plus Labview. The operator could set feed mass and injection intervals and the system could accordingly act on two inlet Gilson Minipuls 3 peristaltic pumps by manipulating the on-off switch and their flowrate. The same strategy was adopted to regulate microalgae extraction. A scheme is reported in Figure B.3.

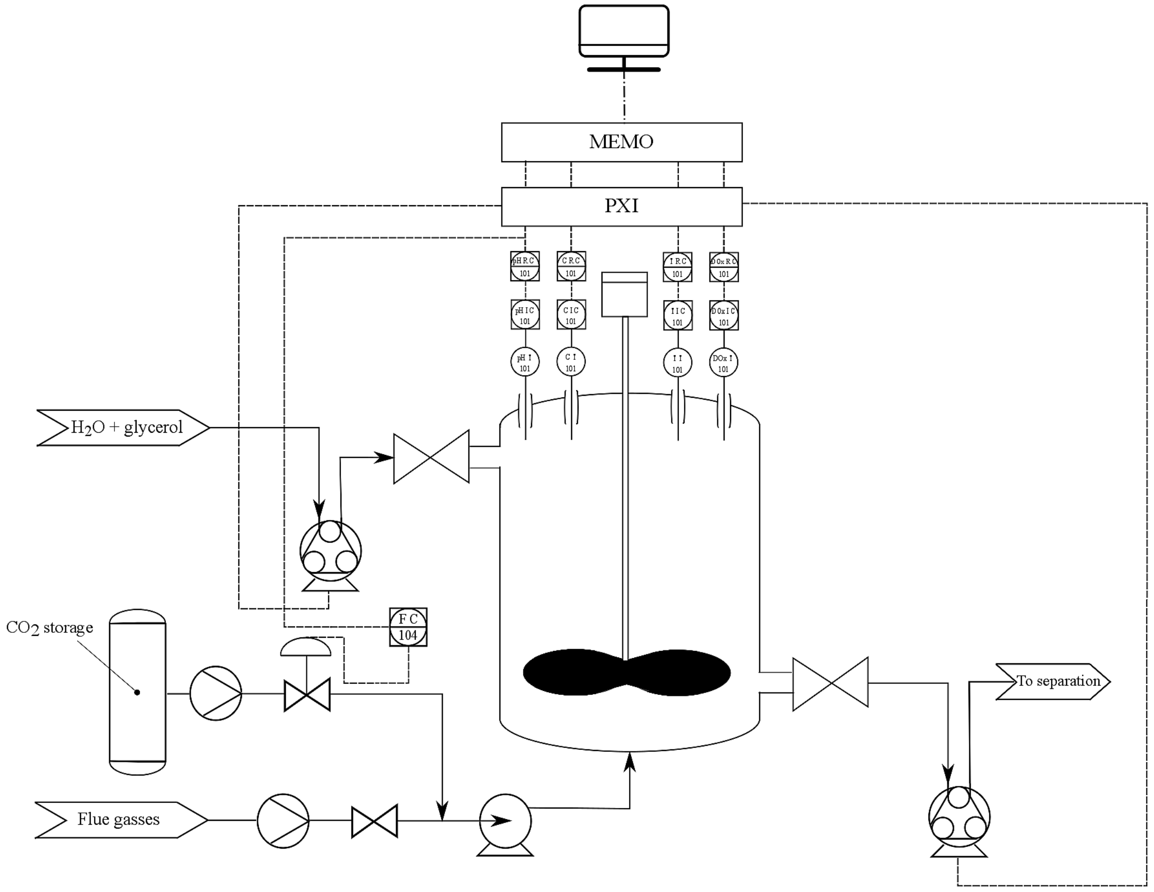

Fig. B.3 Representative scheme of one of the ALRs and related automation system.

B.3.3 Continuous cultivation at pilot-scale

B.3.3.1 Monitoring output variables

Daily spectrophotometric analysis of algae samples was performed by UV-VIS Hach DR-6000 spectrophotometer and only two wavelengths were used to construct the calibration curves to derive the concentration measures. Kinetics were estimated using data at the considered wavelengths.

B.3.3.2 Monitoring internal variables

At pilot scale the internal variables pH, C, DO_x and T were on-line acquired at 10 Hz by three B&C Electronics series 7685 Microcontrollers and related probes, that were inserted in the midsection of the lower collector. The B&C systems were used to acquire and convert the measures, to show their values in the lab and to send the acquired values ($4 \div 20$ mA signal) to both PXI National Instruments and MEMO monitoring system (ECPLab – University of Genoa, Italy). At this experimental stage the B&C conductivity controller and the pH controller were also used to respectively regulate the NaCl used as a tracer and pH into the ALRs.

B.3.3.3 Hydrodynamics and bubble dynamics measurements

Bubbles image acquisition was performed by a Canon EOS-10D camera and a self-developed software was adopted to process images (b/w transformation) and to evaluate bubble diameter and global G-L ratio. pH measurements carried out during bubbles acquisition (WTW multiparameter portable system 340i and B&C Electronics series 7685 pH Microcontroller respectively set at the top of the riser and the top of the downcomer) allowed to indirectly estimate dissolved carbon dioxide concentration in circulating water.

NaCl was used as a tracer to evaluate liquid residence times in the different sections of the ALRs; its concentration was evaluated by indirect conductivity measures at the top of both the riser and the downcomer and in the midsection of the lower collector (WTW multiparameter portable system 340i and B&C Electronics series 7685 Conductivity Microcontroller).

Different solid tracers are finally employed to simulate microalgae, whose movement is recorded by a Hamamatsu C5405 CCD camera, with a resolution of 752(H) × 582(V), a depth of 10 bits and a minimum object illumination of 0.3 lx. Tracers are flat reflective aluminum particles, polymers and TiO_2 particles (mean diameter range $0.5 \div 4$ mm).

B.3.3.4 Operating mode and automation

CO_2 concentration into the gas stream is regulated by a Brooks Instrument 5850S smart mass flow controller. During night CO_2 concentration could be set to zero and gas flowrate could be accordingly regulated by manipulating (through the PXI National Instrument system plus Labview) the pressure on the compressor valve in order to keep a constant gas velocity into the riser. Wastewater inlet and microalgae extraction were controlled with the same strategy adopted at the semi-continuous lab-scale and described in the previous subsection. In growing mode the B&C Microcontrollers were expected to work both as acquiring units for the MEMO monitoring system and as controllers. At pilot scale the MEMO system provided, in addition to the on-line filtering, also the gross errors elimination and alarms managing. A scheme is reported in Figure B.4.

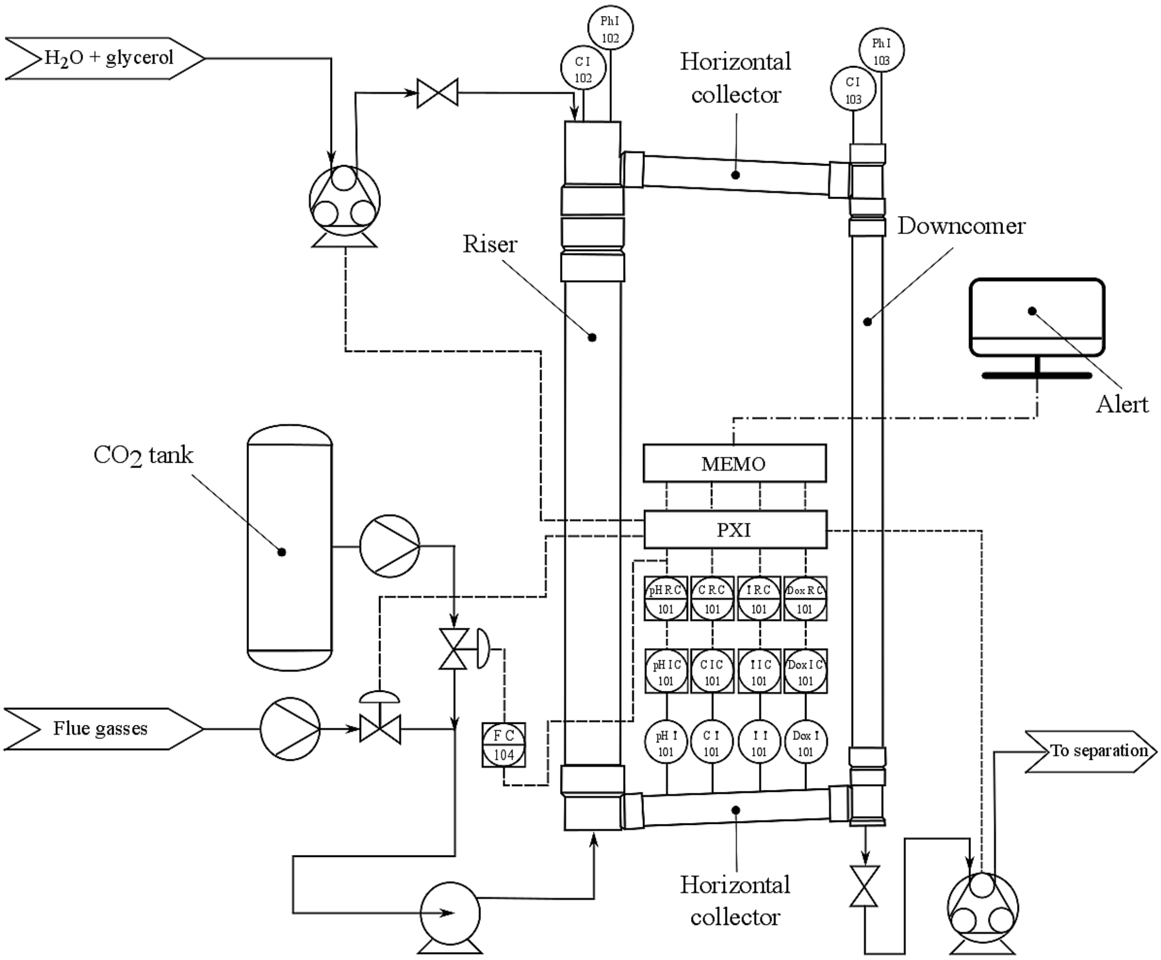

Fig. B.4 Representative scheme of one of the ALRs and related automation system.

References

Atta, M., Idris, A., Bukhari, A., Wahidin, S., 2013. Intensity of blue LED light: A potential stimulus for biomass and lipid content in fresh water microalgae Chlorella vulgaris. Bioresour. Technol. 148, 373–378.

Bischoff, H.W., Bold, H.C., 1963. Some soil algae from Enchanted Rock and related algal species, Texas University Phycological Studies. University of Texas, Austin, Texas.

Blair, M.F., Kokabian, B., Gude, V.G., 2014. Light and growth medium effect on Chlorella vulgaris biomass production. J. Environ. Chem. Eng. 2, 665–674.

Enamala, M.K., Enamala, S., Chavali, M., Donepudi, J., Yadavalli, R., Kolapalli, B., Aradhyula, T.V., Velpuri, J., Kuppam, C., 2018. Production of biofuels from microalgae - A review on cultivation, harvesting, lipid extraction, and numerous applications of microalgae. Renew. Sustain. Energy Rev. 94, 49–68.

Frumento, D., Casazza, A.A., Al Arni, S., Converti, A., 2013. Cultivation of Chlorella vulgaris in tubular photobioreactors: A lipid source for biodiesel production. Biochem. Eng. J. 81, 120–125.

Hamood-ur-Rehman, M., Ein-Mozaffari, F., Dahman, Y., 2013. Dynamic and local gas holdup studies in external loop recirculating airlift reactor with two rolls of fiberglass packing using electrical resistance tomography. J. Chem. Technol. Biotechnol.

Hultberg, M., Carlsson, A.S., Gustafsson, S., 2013. Treatment of drainage solution from hydroponic greenhouse production with microalgae. Bioresour. Technol. 136, 401–406.

Mujtaba, G., Rizwan, M., Kim, G., Lee, K., 2018. Removal of nutrients and COD through co-culturing activated sludge and immobilized Chlorella vulgaris. Chem. Eng. J. 343, 155–162.

Paladino, O., Neviani, M., 2018. A closed loop biowaste to biofuel integrated process fed with waste frying oil, organic waste and algal biomass: Feasibility at pilot scale. Renew. Energy, SI: Waste Biomass to Biofuel 124, 61–74.

Ramesh Kumar, V., Narendrakumar, G., Thyagarajan, R., Melchias, G., 2018. A comparative analysis of biodiesel production and its properties from Leptolyngbya sp. BI-107 and Chlorella vulgaris under heat shock stress. Biocatal. Agric. Biotechnol. 16, 502–506.

Rizwan, M., Mujtaba, G., Memon, S.A., Lee, K., Rashid, N., 2018. Exploring the potential of microalgae for new biotechnology applications and beyond: A review. Renew. Sustain. Energy Rev. 92, 394–404.

Ruiz-Marin, A., Mendoza-Espinosa, L.G., Stephenson, T., 2010. Growth and nutrient removal in free and immobilized green algae in batch and semi-continuous cultures treating real wastewater. Bioresour. Technol. 101, 58–64.

Sadeghizadeh, A., Farhad dad, F., Moghaddasi, L., Rahimi, R., 2017. CO2 capture from air by Chlorella vulgaris microalgae in an airlift photobioreactor. Bioresour. Technol. 243, 441–447.